Polymolecular and Unimolecular Micelles of Triblock Copolymers

by

Yang Gao

A thesis submitted to the Department of Chemistry
In conformity with the requirements for
the degree of Doctor of Philosophy

Queen's University
Kingston, Ontario, Canada
(September, 2011)

Abstract

Reported in this thesis are the studies of micellar aggregates of four triblock copolymers and the unimolecular micelles of a triblock copolymer.

The micelles were prepared from BCF and ACF copolymers. Here A, B, C, and F denote poly(acrylic acid), poly(*tert*-butyl acrylate), poly(2-cinnamoyloxylethyl methacrylate), and the liquid crystalline poly(perfluorooctylethyl methacrylate) block, respectively. At room temperature (21 ^{o}C) in solvents that were selective for the A or B blocks, three of the four copolymers formed exclusively cylindrical micelles regardless of their block ratios. Cylindrical micelles were formed because their geometries best accommodated the mesogen-ordering requirement of the core-forming F block, as supported by the results from wide angle X-ray scattering and differential scanning calorimetric studies. Mesogen-driven cylinder formation was further supported by the observation of ridges formed by collapsed coronal chains on the surfaces of dried cylinders. We also observed a morphological transformation from other micellar morphologies to cylindrical micelles at 70 ^{o}C, which is near the isotropic-to-smectic A phase transition temperature for the F blocks. This inter-conversion between the vesicular and cylindrical micelles of an ACF sample could be reversed repeatly by temperature cycling. These results provided additional evidence for the mesogen-driven micellization hypothesis.

Unimolecular micelles were prepared from CDC triblock copolymers, where D and C denote poly(dimethylaminoethyl methacrylate) and poly(2-cinnamoyloxylethyl methacrylate), respectively. In selective solvents for the D block at high dilutions, the D chain formed a loop, and the terminal C blocks of the isolated unimer chain associated together as a globule, thus closing the loop and rendering a cyclic structure. Alternatively, the terminal C blocks formed individual globules, thus yielding a pompom-coil-pompom structure. To lock in these structures, the globules were photo-crosslinked. The D block chain was subsequently enlarged for AFM observation through a quaternization step, which increased the chain's diameter and introduced cations to the chain. The semi-flexible thickened polymer chains and the globules were observed by AFM, confirming unambiguously the hypothesized architectures of the unimolecular micelles. The AFM images also allowed the quantification of the macrocyclic structures, and a correlation between the direct AFM results and determined from a traditional size exclusion chromatography technique.

.

Acknowledgements

First, I would like to thank Dr. Guojun Liu for inviting me to work in his lab. Without this opportunity, I wouldn’t become who I am today. I appreciated all his inspiration and guidance in the years that supported me overcame the difficulties in the study. He has taught me a great deal about the polymer physics and chemistry in general.

I would also like to express thanks to:

Dr. Dehui Han and Dr. Liangzhi Hong for providing block copolymers.

Dr. Gabriel Njikang, Dr. John Dupont and other group members whose discussion and friendship has meant a lot.

Jian Wang for doing AFM and other support as a lab technician. Mr. Alan Grant for doing the XRD study. Dr. De’an Xiong for doing XPS measurement. Dr. Hugh Horton for providing information on the XPS analysis.

Dr. Ian Wyman for proofreading this thesis.

Xiaoyu Li, whose loving support has helped make my dream reality.

I would also like to thank my parents, who have always encouraged me to be the best I can.

Finally, I would like to acknowledge the financial assistance from NSERC, Queen’s University, Faculty of Graduate Studies and the Department of Chemistry.

Statement of Originality

I hereby certify that all of the work described within this thesis is the original work of the author. Any published (or unpublished) ideas and/or techniques from the work of others are fully acknowledged in accordance with the standard referencing practices.

(Yang Gao)

(September, 2011)

Table of Contents

List of Figures

List of Tables

List of abbreviations

Å	angstrom (1 Å = 10^{-10}m)
χ	Flory-Huggins interaction parameter
η	viscosity
σ	standard deviation
AFM	atomic force microscopy
ATRP	atom transfer radial polymerization
BBBV	benzyl (4-bromomethylbenzyl)viologen
BBC	4’-bromomethyl-2-biphenylcarbonitril
$CDCl_3$	deuterated chloroform
CMC	critical micellization concentration
cryo-TEM	cryogenic transmission electron microscopy
d_h	hydrodynamic diameter
DLS	dynamic light scattering
DMF	dimethylformamide
dn_r/dc	refractive index increment
DSC	differential scanning calorimetry
EtOH	ethanol
HCl	hydrochloric acid
^{1}H NMR	proton nuclear magnetic resonance
iPrOH	isopropanol
LC	liquid crystalline
L_n	end-to-end distance
LS	light scattering
M	mole/L
MA	micelle-like aggregate
MeOH	methanol
mg	milligram

mL	millilitre
M_n	number average molecular weight
mPEG	methoxy poly(ethylene glycol)
M_w	weight average molecular weight
nm	nanometer
OsO_4	osmium tetraoxide
P2VP	poly(2-vinyl pyridine)
PAA	poly(acrylic acid)
PAChol	poly(cholesteryl acryloyloxyethyl carbonate)
PAMA	poly(2-aminoethyl methacrylate)
PB	polybutadiene
PBMA	poly(n-butyl methacrylate)
PBuA	poly(n-butyl acrylate)
PCEMA or C	poly(2-cinnamoyloxyethyl methacrylate)
PCL	polycaprolactone
P(CL-LLA)	poly(caprolactone-b-l-lactide)
PCP	pompom-coil-pompom
PDI or M_w/M_n	polydispersity index
PDMAEMA or D	poly(dimethylaminoethyl methacrylate)
PDMS	poly(dimethylsiloxane)
PE	polyelectrolyte
PEHA	poly(2-ethylhexylacrylate)
PEO	poly(ethylene glycol)
PF or F	poly(perfluorooctylethyl methacrylate)
PFA	poly(1H,1H,2H,2H-perfluorodecyl acrylate)
PFS	Poly(ferrocenylsilanes)
PGMA	poly(glyceryl monomethacrylate)
PHEMA or H	poly(hydroxylethyl methacrylate)
P(HEMA-TMS)	poly(trimethylsiloxyethyl methacrylate)

PI	polyisoprene
PMA	poly(methyl methacrylate)
PMAA	poly(methacrylic acid)
PMAChol	poly(cholesteryl methacryloyloxyethyl carbonate)
PMMA	poly(methyl methacrylate)
POEGA	poly((oligoethylene glycol) acrylate)
PPQ	poly(phenylquinoline)
PS	polystyrene
PSGMA	poly(succinated glyceryl monomethacrylate)
PtBA or B	poly(*tert*-butyl acrylate)
PTFE	poly(tetrafluoro ethylene)
RI	refractive index
SEC	size exclusive chromatography
TEM	transmission electron microscopy
TFT	α,α,α-trifluoro toluene
THF	tetrahydrofuran
$UO_2(Ac)_2$	uranyl acetate
μm	micrometer
WAXS	wide angle x-ray scattering

Chapter 1

Introduction and Literature Review

1.1 Thesis Organization

Two types of self-assembly behaviors among linear triblock copolymers in block-selective solvents were studied in this thesis, including interchain micellization and unimolecular micellization. In the first project, the formation of cylindrical micelles from the ABC triblock terpolymers poly(acrylic acid)-*block*-poly(2-cinnamoyl-oxylethyl methacrylate)-*block*-poly(perfluorooctylethyl methacrylate) (PAA-*b*-PCEMA-*b*-PF) and poly(*tert*-butylacrylate)-*block*-poly(2-cinnamoyloxylethyl methacrylate)-*block*-poly(perfluorooctylethyl methacrylate) (PtBA-*b*-PCEMA-*b*-PF) in solvent mixtures of α,α,α,-trifluorotoluene and methanol were studied. The structures of these polymers are shown in Figure 1.1. It was found that the mesogen-ordering of the PF block was the driving force for the formation of the cylindrical micelles, which also led to the sparsely-distributed corona chains on the cylindrical micelles.

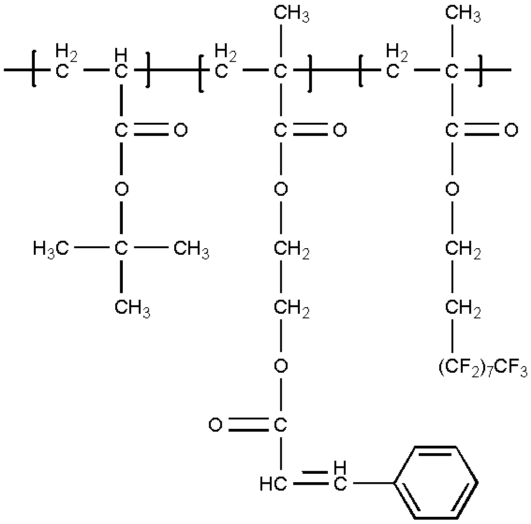

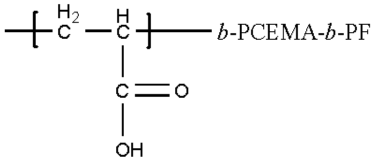

poly(acrylic acid)-*block*-poly(2-cinnamoyl oxylethyl methacrylate)-*block*-poly(perfluoro octyl ethyl methacrylate)
(PAA-*b*-PCEMA-*b*-PF)

poly(tert-butyl acrylate)-*block*-poly(2-cinnamoyl oxylethyl methacrylate)-*block*-poly(perfluorooctyl ethyl methacrylate)
(PtBA-*b*-PCEMA-*b*-PF)

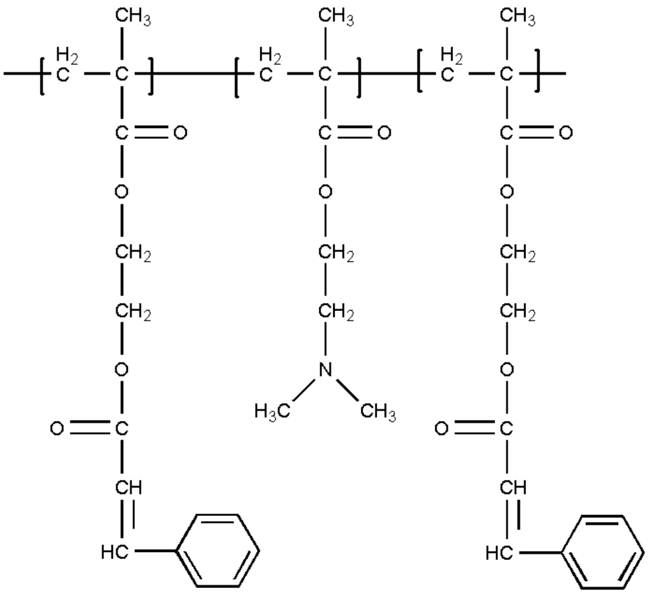

poly(2-cinnamoyloxylethyl methacrylate)-*block*-poly(dimethylaminoethyl methacrylate)-*block*-poly(2-cinnamoyloxylethyl methacrylate)
(PCEMA-*b*-PDMAEMA-*b*-PCEMA)

Figure 1.1. Chemical structures of the triblock copolymers studied in this thesis.

Investigated in the second study was atomic force microscopy (AFM) imaging of the hydrophobically end-functionalized poly(dimethylaminoethyl methacrylate) (PDMAEMA) polymer, which is also shown in Figure 1.1, and its cyclized product. The hydrophobically end-functionalized PDMAEMA block consisted of two short end PCEMA blocks and one long central block PDMAEMA. It was found that under different solvation conditions, through the collapse and association of the PCEMA end-blocks, the polymer formed macrocycles and pompom-coil-pompom (PCP) structures. If the two PCEMA end-blocks on the same polymer chain collapse together, a macrocyclic structure is formed. Meanwhile, if the two PCEMA end-blocks collapse separately, a PCP structure is formed. The pH effect on the ratio of the cycles/PCP was studied. The macrocyclic product was then observed by AFM after modification of the central PDMAEMA block. The results from AFM characterization were compared with those from size exclusion chromatography (SEC), which was the traditional method for polymer characterization. It was found that the cyclization yields obtained from both characterization methods shared similar trends, while the SEC method would overestimate the yield of the macrocycles. The overestimation of the cyclization yield from SEC measurements suggested that it was not a reliable method for macrocycle characterization. In contrast, the cyclization yield obtained from AFM observation was more reliable, since it allowed direct observation of the unimer chains.

This thesis is organized in the following manner: Chapter 1 will summarize the relevant literature and give a brief introduction to the objectives of my Ph.D. research.

Chapter 2 will describe the physical and analytical methods used in this thesis to characterize the polymers and micelles. Chapter 3 focuses on the formation of cylindrical micelles from four triblock copolymers. The effect of the mesogen-ordering of the PF block on cylindrical micelle formation will be discussed in detail. The morphologies of nanostructures formed in solvent mixtures with different selectivities for the copolymer blocks will be analyzed. AFM imaging of single polymer chains with cyclic or linear structures will be the main subject of Chapter 4. The cyclization yield obtained from SEC and AFM characterization methods will also be correlated and discussed. The final chapter will summarize the conclusions of this research and propose some ideas for future work.

This chapter will begin with a review of block copolymer self-assembly behavior, including the self-assembly behavior of diblock copolymers, triblock copolymers, and block copolymers containing fluorinated blocks in selective solvents. The preparation and characterization of macrocycles from single polymer chains will then be summarized in this context. This chapter will conclude with a brief introduction to the objectives of my research.

1.2 Phase Segregation of Block Copolymers

Block copolymers are a class of polymers formed by covalently connecting two or more different homopolymer subunits.[1] Block copolymers can be classified as diblock, triblock, tetrablock, pentablock or multiblock copolymers based on their number of component blocks. They can also be categorized as linear or branched block copolymers according to their architectures. The development of controllable synthetic strategies, such as anionic polymerization[2-4] or controlled free radical polymerization,[5-7] makes it possible to synthesize these polymers and to understand their physical behavior.

In the field of block copolymers, most studies have focused[8-11] on their ability to undergo microphase separation, leading to nanostructures with controllable morphologies and domain sizes. Generally, two different polymers will segregate from each other into different phases. This can be explained qualitatively in terms of Gibbs free energy (Equation 1.3).[12] Among the small molecule blends, the positive energy contribution arising from the interaction of two components can be offset by the large negative free energy contribution provided by the entropy of mixing (Equation 1.2). In contrast to small molecule blends, the entropy of mixing between two different polymer chains (Equation 1.1) is very small, and the enthalpic interaction between the two components dominates the phase behavior of the polymer blends. The interaction between two dissimilar polymer chains can be represented as the Flory-Huggins interaction parameter (χ).[12] Practically, when the product of total number of repeating units of a polymer (N) multiplied by χ (χN) is greater than 10.5, the two polymers undergo phase segregation. Typically, χ values between different polymer pairs range between approximately 0.01 and 0.1. Some reported χ values (at 25 °C unless otherwise indicated) from various literature reports[13-16] between polystyrene and other polymer chains are shown in Table

1.1. For example, the typical χ value between polystyrene and polyisoprene is approximately 0.1,[15] and thus these polymers will become phase-segregated from each other when N is larger than 105 units. Among polymers with very similar chemical structures, e.g. deuterated polystyrene and poly(α-methylstyrene), the average χ value can be as low as 5.0×10^{-3}.[17] Therefore, these two polymers will undergo phase segregation when N exceeds 2100. Thus phase segregation between different polymers is a common characteristic among most polymer mixtures, except for those having specific interactions, such as ion pairing or hydrogen-bonding. As briefly mentioned above, the entropy of mixing among polymers, among small molecules, and the free energy of mixing are described as Equations 1.1, 1.2, and 1.3, respectively:

$$\Delta S_{mix-polymers} = k_B \left({}^{N_1}\!/_{n_1} \, ln\emptyset_1 + {}^{N_2}\!/_{n_2} \, ln\emptyset_2 \right) \tag{1.1}$$

$$\Delta S_{mix-small\ molecules} = k_B (N_1 ln x_1 + N_2 ln x_2) \tag{1.2}$$

$$\Delta G_{mix} = \Delta H_{mix} - T\Delta S_{mix} \tag{1.3}$$

where ΔS_{mix} is the mixing entropy, k_B is the Boltzmann constant, N_1 and N_2 are the total numbers of monomer units or corresponding small molecules, n_1 and n_2 are the repeating units of each block. Meanwhile, $\emptyset_1$ and $\emptyset_2$ are the volume fractions of each block, x_1 and x_2 are the mole fractions of the corresponding molecules, ΔG_{mix} is the Gibbs free energy of mixing and ΔH_{mix} is the enthalpy of mixing.

Table 1.1. Experimentally determined Flory-Huggins interaction parameters χ between polystyrene and other polymers.

	Polyisoprene[15]	Polycarbonate[14]	Poly(2-vinylpyridine)[13]	Poly(4-vinylpyridine)[13]	Poly(methyl methacrylate)[16]
χ	0.15	0.038 at 250 °C	0.09~0.11	0.30~0.35	0.041

In the case of block copolymers, phase separation is spatially-limited due to the covalent bonds between the different blocks. Consequently, block copolymers undergo microphase segregation, but not macrophase segregation, which occurs among polymer blends. Thus, they are phase-segregated microscopically or undergo microphase separation. In the bulk phase, block copolymers can form nanostructures having long-range order, such as the cubic arrays of spheres, hexagonally-packed cylinders, lamella and gyroid structures with characteristic domain sizes ranging from 10 to 100 nm.[18] Careful selection of the block compositions and volume fraction ratios between the different blocks allows preparation of nanostructures with different sizes and morphologies in a controllable and predictable manner.[1,8,19]

1.3 Block Copolymer Self-Assembly in Block-Selective Solvents

When a block copolymer is dispersed into a block-selective solvent, which is a good solvent for one block (the solvophilic block) and a precipitant for another block (a solvophobic block), micelles or micelle-like aggregates are formed as a result of the association of the solvophobic blocks. The aggregation number (number of polymer chains) per micelle will become larger than one when the critical micelle concentration (CMC) is reached. The micelle or micelle-like aggregate morphologies of diblock copolymers, as the simplest models for block copolymer assemblies, have been extensively studied experimentally and theoretically.[20-24] Various micellar morphologies, such as spherical, cylindrical and vesicular micelles or micelle-like aggregates have been observed among diblock copolymer aggregates. Here, micelles are thermodynamically-favored aggregates while micelle-like aggregates are kinetically-trapped aggregates. In recent years, even more interesting morphologies have been reported from micelles prepared from triblock copolymers.[54,57-62] In this context, previous results will be reviewed for the diblock and triblock copolymer micelles.

1.3.1 Theoretical and Experimental Studies on Diblock Copolymer Micelles in Selective Solvents

In a block-selective solvent, the aggregation behavior of an AB diblock copolymer closely resembles that of a low molecular weight surfactant. When an AB diblock copolymer is present in a block-selective solvent S, that is selective for the A block, the copolymer chains spontaneously organize themselves into core-shell structures, with the A block and S in the shell, and core region composed of the collapsed

B block. The core-shell structure consists of a single polymer chain when the concentration of the block copolymer is below the CMC, or of an aggregate of polymer chains when the concentration is above the CMC. In comparison with low molecular weight surfactants, block copolymers usually possess much lower CMC values. In addition, the chain exchange dynamics between different micelles are much slower among block copolymer micelles than among micelles of small surfactants. The slower chain exchange rate derives from the higher molecular weight, lower CMC, greater chain entanglement in the micellar core, and lower mobility typically encountered among polymers. The sizes of the core and shell domains are dependent on the degrees of polymerization of the B and A blocks, respectively.

The thermodynamic theories of diblock copolymer micelles have been constructed by de Gennes[20] and developed later by Leibler,[21] Halperin,[22,23] and Noolandi[24] and coworkers. The ideal micelle model is assumed to consist of a fully segregated core, a sharp interface between the core and shell, and a shell with uniform penetration of solvent molecules. Thus, the free energy of a single micelle can be approximated as:

$$F_{micelle} = F_{core} + F_{interface} + F_{corona} \tag{1.4}$$

where F_{core} accounts for the change in the configuration entropy of the B chains upon aggregation, $F_{interface}$ represents the decrease in the interfacial energy due to micellization, and F_{corona} reflects the loss of free energy for the confinement arising from the A chains being grafted onto the interface. By minimizing the amount of free energy per chain with respect to the aggregation number in an isolated micelle, the characteristic dimensions of the micelle, e.g. the core radius R_{core}, the micellar radius R, and the aggregation number f can be related to the number of repeating units in the A and B blocks. This model, proposed by de Gennes,[20] is best suited for micelles with thin and densely-packed shells, such as crew-cut micelles. The model predicted that when the interfacial energy is large $R_{core} \propto N_B^{2/3}$ and $f \propto N_B$. N_B is the number of repeating units in block B. Meanwhile, when the interfacial energy is small $R_{core} \propto N_B^{1/2}$ and $f \propto N_B^{1/2}$. These predictions were in close agreement with experimental data.[20]

Later, changes were made to update this model. For example, Halperin presented a star micelle model, describing micelles having a large corona and a small core. In this case, the repulsion between the corona chains could not be ignored. The scaling relations he obtained predicted that $R_{core} \propto N_B^{3/5}$, $f \propto N_B^{4/5}$, and $R \propto N_B^{4/25} N_A^{3/5}$ for star micelles. Meanwhile, for crew-cut micelles having large shells and small cores, Halperin's model predicted $R \propto R_{core} \propto N_B^{2/3}$, and that $f \propto N_B$. Leibler and coworkers[21] developed the theory further by taking into account the free energy of single dispersed copolymer chains in addition to the total free energy. Thus, the total free energy of the system was minimized with respect to the number of chains, rather than the free energy of the micelle. Their model predicted that among block copolymer micelles with the weakly incompatible blocks, $R_{core} \propto N_B^{0.53}$ and $f \propto {N_B}^{0.60}$.

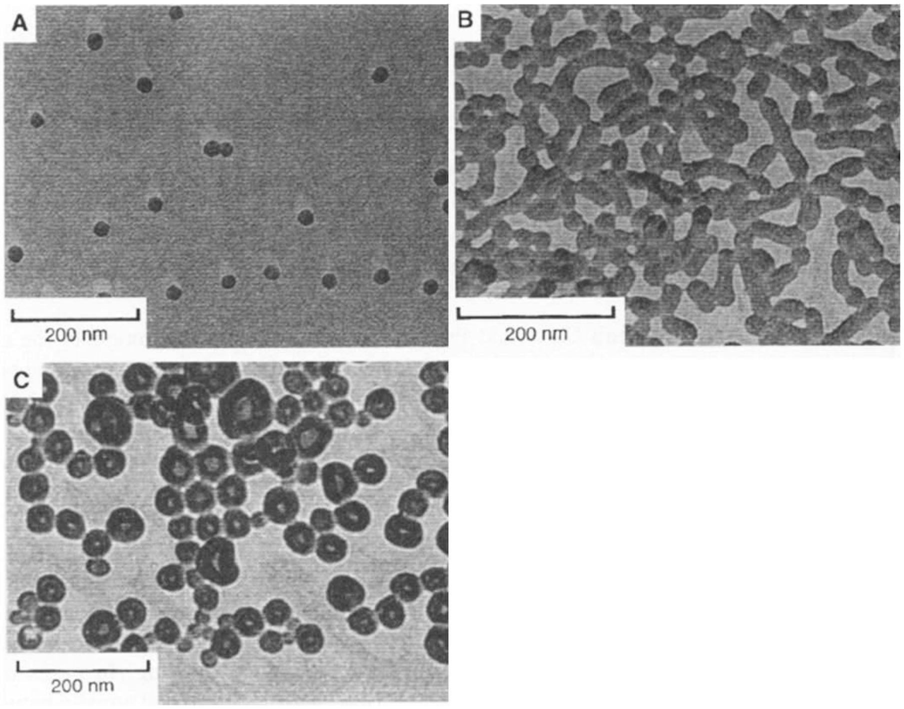

Figure 1.2. Multiple morphologies of crew-cut aggregates of PS-*b*-PAA block copolymers with different block ratios in a binary solvent mixture of DMF and water. PS_{200}-*b*-PAA_{21} formed spherical micelles (image a), PS_{200}-*b*-PAA_{15} formed worm-like or rod-shaped micelles (image b), and PS_{200}-*b*-PAA_{8} formed vesicles or bilayers (image c). The PAA block was soluble in this solvent mixture, while the PS block was insoluble.[25]

Since the morphologies of block copolymer micelles are determined by the aforementioned three free energies, parameters that control their morphological transitions can be predicted. Generally, two cases can be considered. One case involves changes to the volume fraction of the solvent-compatible block while the solvent composition is kept constant. The other case involves changes to the volume fraction of the selective-solvent in a binary solvent system while the polymer composition is kept constant. The first systematic study on the morphological changes among diblock copolymer micelles was conducted by Eisenberg and coworkers.[25] Morphological transitions from spheres, to worm-like micelles, and to vesicles were observed (as shown in Figure 1.2a, b and c, respectively).

The polymer studied in this work was polystyrene-*block*-poly(acrylic acid) (PS-*b*-PAA) and the binary solvent was a mixture of dimethylformamide (DMF) and water, in which the PS block was solvophobic. As the length of the solvophilic PAA block decreased, the repulsive interactions between the coronal chains decreased, and thus the aggregation numbers of the micelles increased. When the aggregates grew larger, the entropic penalty arising from the stretching of the core blocks increased. The stretching energy of the PS block and repulsion energy from the PAA chains were balanced by the interfacial energy and the total free energy of the aggregation across the morphological transitions, as shown in Figure 1.3. In the image, “rods” and “bilayers” refer to cylinders and vesicles, respectively. Cylinders were thus formed with decreased core size to relieve the PS stretching in the core. Similarly, cylinders transformed into to vesicles to accommodate the greater number of chains in the aggregates. The roles of other parameters, such as solvent composition, the presence of salt and scaling relations between these parameters were also studied.[26]

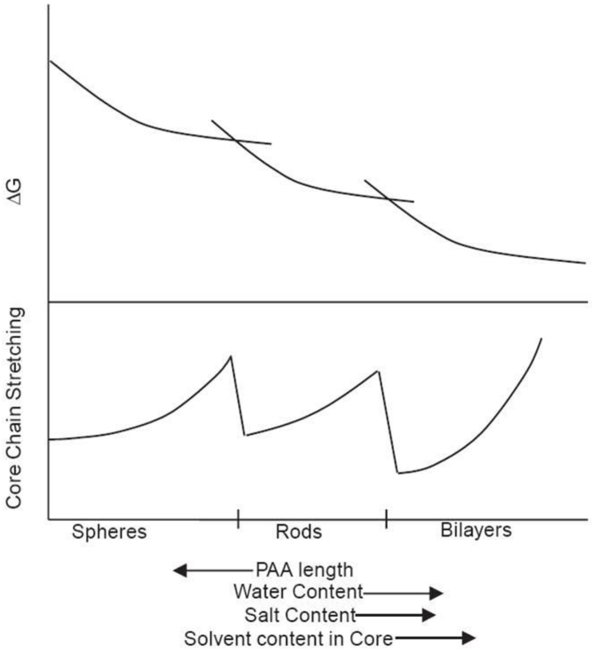

Figure 1.3. Schematic plot of relative free energies and degree of core–chain stretching to indicate morphological boundaries as a function of morphogenic parameters.[26]

Spherical micelles are readily prepared from coil-coil block copolymers in solvents that are selective for one of the component blocks. Non-spherical block copolymer micelles, e.g. cylinders and vesicles (or bilayers), can only be produced in the "crew-cut" regime, which prevails when the thickness of the corona is much less than that of the core.[49-51] From the practical experience gained from preparing micelles of amphiphilic diblock copolymers in aqueous solution, Eisenberg has proposed a unifying rule for the relation between the weight ratio of the hydrophilic block $f_{\text{hydrophilic}}$ compared to the total molecular weight of the copolymer ($f_{\text{hydrophilic}}$) and the observed micellar morphologies (Table 1.2).[52]

Table 1.2. The relationship between the weight ratio of the hydrophilic block and the predicted micellar morphologies.[52]

Micellar Morphologies	Spherical	Cylindrical	Vesicular	Inverted
$f_{\text{hydrophilic}}$	>45%	<50%	~35%	<25%

Symmetrical ABA triblock copolymers behave in a similar manner as AB diblock copolymers in selective solvents. These copolymers can assembly into core-shell structures in selective solvents for the A block, or into flower-like aggregates in selective solvents for the B block, with the B block forming loops in solvent phase.[27]

1.3.2 Review of the Morphologies of ABC Triblock Copolymer Micelles in Selective Solvents

In comparison with AB diblock copolymers, ABC triblock copolymers (Figure 1.5a) are influenced by more variables, including two independent compositional variables (volume fractions $f_A, f_B, f_C = 1 - f_A - f_B$) and three χ parameters (χ_{AB}, χ_{AC} and χ_{CB}). In comparison with AB diblock copolymer micelles, ABC triblock copolymer micelles can provide greater functionality, because more functional groups can be incorporated into the third block.

As mentioned in the previous section, a morphological transition can be observed from the crew-cut diblock copolymer micelles. According to the volume fractions of the blocks and solvent composition, the micellar morphologies can change from sphere to cylinder and vesicles. Similarly, ABC triblock copolymers have also been observed to form the same morphological trend, when changing the block ratios. For example, Liu et al. reported micelle-like aggregates with morphological transition from spheres to vesicles from poly(*tert*-butyl acrylate)-*block*-poly(2-cinnamoyloxylethyl methacrylate)-*block*-poly(glyceryl monomethacrylate) (PtBA-*b*-PCEMA-*b*-PGMA) in a mixture of pyridine and methanol.[37] Under these solvent conditions, only PCEMA was insoluble. However, instead of forming a homogenous surface in the case of diblock copolymer vesicles, the corona chains of this triblock copolymer vesicles were composed of two kinds of blocks, which were PtBA and PGMA. The outer surface of the vesicles consisted mainly of PGMA chains and some PtBA chains, with the PtBA chains forming circular patches. Thus, segregated surface chains were observed on the surface of the vesicles by both TEM and AFM (Figure 1.4).

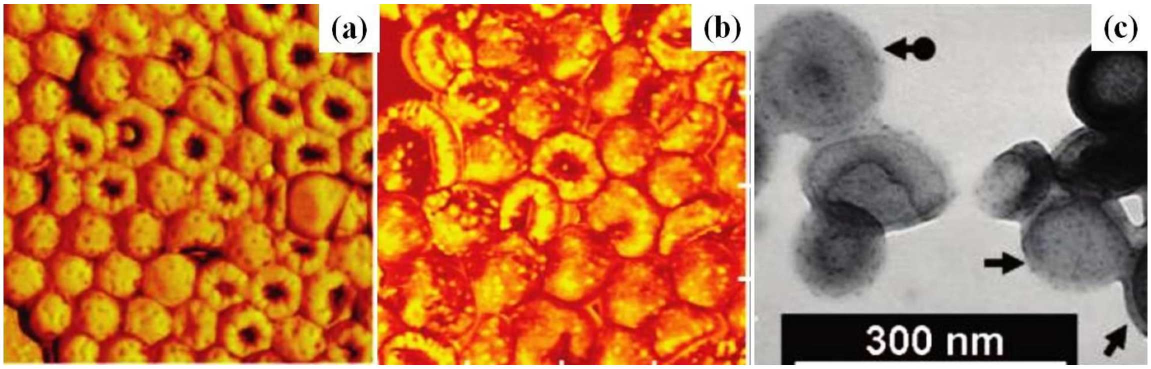

Figure 1.4. AFM phase images of vesicles formed by PtBA-*b*-PCEMA-*b*-PGMA in MeOH/pyridine with f_{MeOH} = 95% (a), and vesicles with PtBA chains hydrolyzed to PAA (b). Also shown is a TEM image of PAA-*b*-PCEMA-*b*-PGMA vesicles (c). The TEM specimens were stained with uranyl acetate, which selectively stained the PAA domains.[37]

Although the triblock copolymer micelle system is complicated, it can be simply divided into two different cases[32]: firstly, when only one block is insoluble, and secondly when two blocks are insoluble.

In the first case, the insoluble block may be either a terminal block such as blocks A or C, or the central B block. When a terminal A or C block is incompatible with the solvent, micellar morphologies with core-shell-corona structures (Figure 1.5b) are formed. Gohy and coworkers have reported pH-responsive spherical micelles formed by polystyrene-*block*-poly(2-vinyl pyridine)-*block*-poly(ethylene glycol) (PS-*b*-P2VP-*b*-PEO) triblock copolymers in water, with PS forming core, PEO forming the corona and P2VP serving as a pH-responsive shell.[33] Liu and coworkers have produced spherical and cylindrical micelles from the triblock copolymer polyisoprene-*block*-poly(2-

cinnamoyloxylethyl methacrylate)-*block*- poly(*tert*-butyl acrylate) (PI-*b*-PCEMA-*b*-PtBA). These micellar structures were structurally locked through their UV cross-linkable PCEMA block, and subsequently hollow spheres and tubes were prepared by etching the PI core.[34]

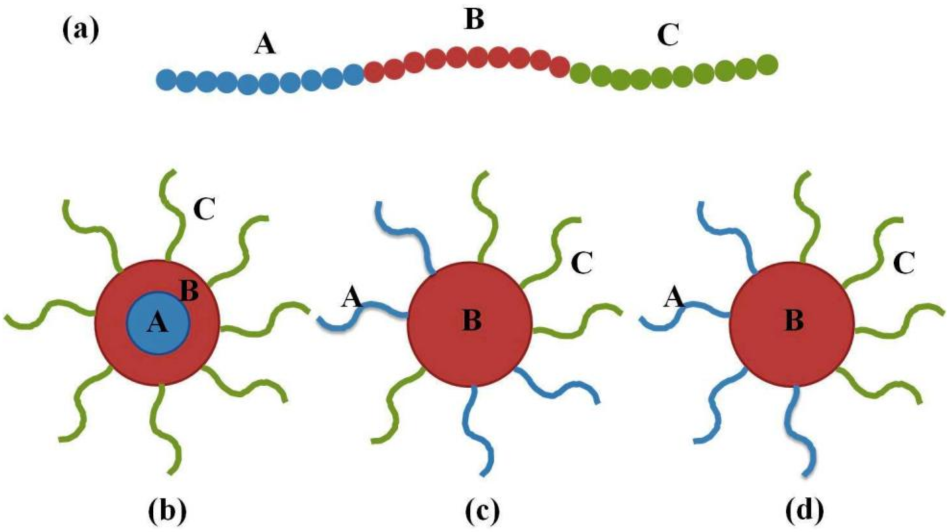

Figure 1.5. Schematic representation of ABC triblock copolymer (a) morphologies including: a core-shell-corona micelle (b) a micelle with a segmented corona (a patched micelle, c), and a Janus micelle (d).

If the central B block is insoluble, micelles with a heterogeneous corona and a homogeneous core will form. If the A and C chains in the corona are strongly segregated from each other, Janus particles with phase-segregated hemispheres consisting of A and C domains will arise (Figure 1.5d). Meanwhile, if the corona chains are only mildly incompatible, aggregates with segregated chain surfaces (patchy micelles) can be observed (Figure 1.5c). The concept of patchy micelles was first uncovered by Liu et al. in 2003, with a triblock copolymer poly(n-butyl methacrylate)-*block*-poly(2-cinnamoyloxylethyl methacrylate)-*block*-poly(*tert*-butyl acrylate) (PBMA-*b*-PCEMA-*b*-PtBA).[36] In a selective solvent for PBMA and PtBA, spherical micelles were observed, with PCEMA forming the micellar core and the PBMA and PtBA blocks forming the corona. Because PBMA and PtBA chains were phase-segregated from each other in the corona, patched particles were observed by TEM. Using a similar triblock copolymer, PGMA-*b*-PCEMA-*b*-PtBA, with different block lengths,[38] Liu and coworkers prepared core-shell-corona cylindrical micelles in water with the insoluble PtBA and PCEMA blocks comprising the core and shell, respectively, and the soluble PGMA block forming the corona. In a further step, twisted cylinders were obtained by dialyzing the cylinders in water against methanol, which solubilized not only PGMA, but also PtBA, and caused the PtBA chains to burst out from the core.[38] In selective solvents, patched micelles were also produced by our group from mixtures of two diblock copolymers, which shared the same solvophobic block and had different solvophilic blocks.[39,40]

Janus paticles have been produced by Erhardt et al.[41,42] by the dissolution of polystyrene-*block*-polybutadiene-*block*-poly(methyl methacrylate) (PS-*b*-PB-*b*-PMMA) from the bulk morphology. PB formed spheres at the interface between PS and PMMA layers. The segregation between the corona chains PS and PMMA was enhanced greatly by the hydrolysis of the hydrophobic PMMA chains into hydrophilic poly(methacrylic acid) (PMAA) chains. Similarly, Müller and coworkers obtained Janus cylinders from dissolution of PS-*b*-PB-*b*-PMMA thin films.[43] Recently, Armes et al. made patchy and Janus micelles in water from poly(ethylene glycol)-*block*-polycaprolactone-*block*-poly(2-aminoethyl methacrylate) (PEO-*b*-PCL-*b*-PAMA).[44] The segregation between the PEO and PAMA corona chains drives the formation of Janus micelles.

In the second case, when two of the blocks are insoluble, micelles with either core-shell-corona structures or compartmental cores were obtained from triblock copolymers. For example, the two insoluble A and B blocks were phase-segregated in the radial direction with A forming the core and B forming a shell surrounding the core.[45,46]

Another case that is also interesting occurs when one of the blocks is in a marginally-soluble state, and the other two blocks are soluble and insoluble, respectively. In some studies, multiamine small molecules were added into the triblock copolymer solutions to complex with one of the polymer blocks, which leads to the complexed polymer blocks marginal soluble in the solvent. Micelles or micelle-like aggregates with interesting morphologies,[28] such as double helix structures,[29] hamburger-like structures,[30] and many other compartment micelles can be generated from ABC triblock copolymers.[31]

Liu et al. have reported core segmented spheres and cylinders from poly(*tert*-butyl acrylate)-*block*-poly(2-cinnamoyloxyethyl methacrylate)-*block*-poly(succinated glyceryl monomethacrylate) (PtBA-*b*-PCEMA-*b*-PSGMA) in selective solvents for the PtBA and

PSGMA blocks in the presence of sparteine, a diamine which can complex with PSGMA, causing the PSGMA block to become marginally soluble in this solvent.[30] The hamburger-like structures were subsequently hydrolyzed to yield Janus particles.

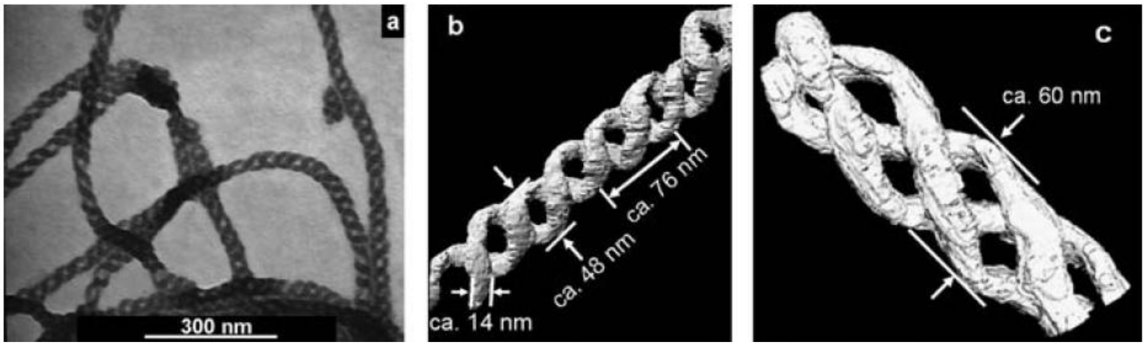

Figure 1.6. A TEM image of PBMA-*b*-PCEMA-*b*-PtBA double helices sprayed from THF/MeOH at f_{MeOH} = 79% (a), and TEM tomography images of a double (b) and a triple helix (c) sprayed from CH_2Cl_2/MeOH at f_{MeOH} = 82%.[48]

Liu and coworkers have also reported double helical structures (Figure 1.6) from PBMA-*b*-PCEMA-*b*-PtBA.[29,48] The copolymer was dispersed into solvent mixtures composed of methanol and either dichloromethane, THF, or chloroform. In such solvent mixtures, PBMA was marginally soluble and PCEMA was insoluble. The PCEMA block formed the core of the cylindrical micelles, and the PBMA and PtBA blocks formed the corona. Since PBMA was marginally soluble and tended to associate, this caused the cylinders to bend. Eventually different cylinders became twisted around one another to minimize contact between PBMA and the solvent (Figure 1.7).

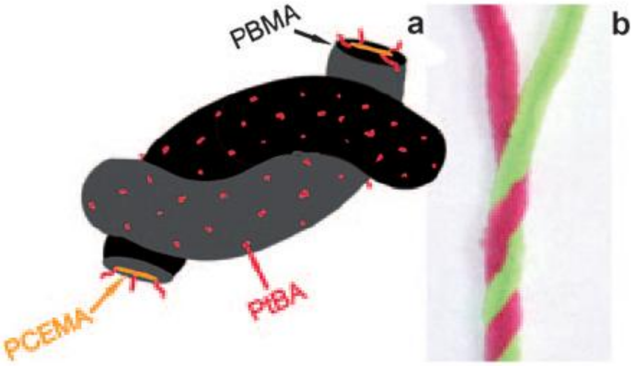

Figure 1.7. Schematic representation of the chain packing in a double-helix section (a). Photograph of two pipe cleaners twisted into a double helix (b). [31]

Wooley et al.[35] reported toroidal micelles (Figure 1.8) prepared from polystyrene-block-Poly(methyl methacrylate)-block-poly(acrylic acid) (PS-*b*-PMA-*b*-PAA) in a mixture of tetrahydrofuran (THF) and water in the presence of diamine. The toroidal micelles were formed by the cylinder-forming triblock copolymer in a solvent mixture of THF and water in the presence of a chelating cation, 2,2'-(ethylenedioxy)diethylamine. The hydrophobic PS and PMA blocks formed the core, and PAA formed the corona. The interaction between the negatively charged PAA chains and the positively charged diamine promoted a self-association among the cylindrical micelles, which was a key for the formation of the toroidal morphology. Similarly, Wooley and Pochan studied the self-assembly of PAA-*b*-PMA-*b*-PS in mixtures of THF and water.[47] The PS and PMA blocks were both insoluble and formed the core and shell of the cylindrical micelles, respectively. In the presence of different multiamines, which complex with the PAA corona chain, single and double helical structures were observed.

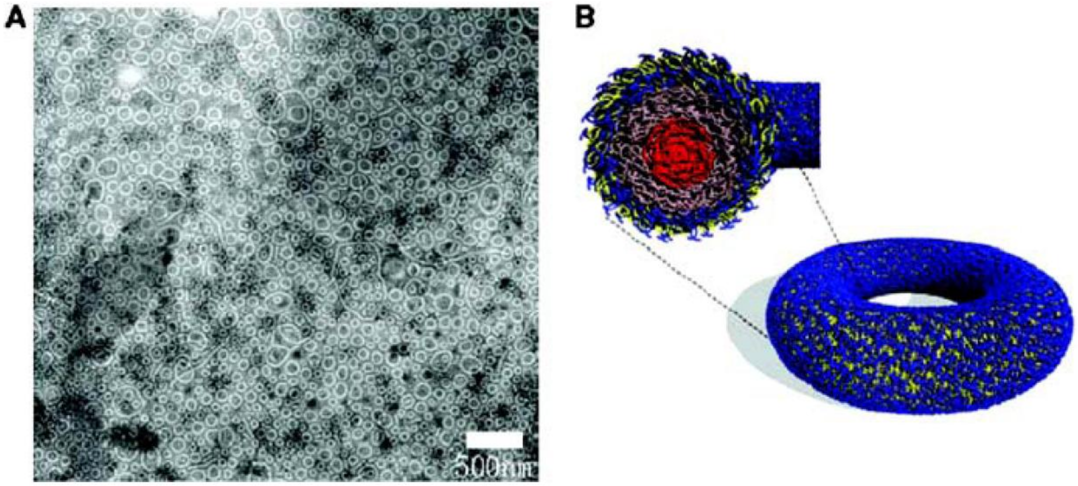

Figure 1.8. TEM image of toroidal micelles obtained from a PAA-*b*-PMA-*b*-PS triblock copolymer (A). The cast film was negatively stained with uranyl acetate. A schematic representation of theses micelles is also shown (B). [35]

Although a significant progress has been made on understanding the self-assembly of triblock copolymers in selective solvents, it is still much more difficult to predict the self-assembly behaviors of triblock copolymers than that of the diblock copolymers. The problem is mainly arisen from the complexity of triblock copolymer systems, which have a lot more variables can be tuned. However, the triblock copolymer micelles can be very useful with the addition of a third block. For example, functional groups, which can be attached to the third block, make the corresponding micelles more controllable (with temperature or pH sensitive blocks) and processible (with crosslinkable blocks). Besides, triblock copolymers containing blocks with special properties, e.g. crystalline or liquid crystalline properties, might have different micellar behaviors. These unusual self-assembly behaviors are resulted from the additional crystal/liquid crystal energy competing with the traditional micellization energy of amorphous block copolymers. Previous studies on several diblock copolymer systems containing crystalline/liquid crystalline blocks in selective solvent have been performed and the results are summarized in the following section.

1.4 Morphological Studies on the Self-Assembly of Block Copolymers Containing Liquid Crystalline/Crystalline Blocks in Solution

The main factors that control the morphologies of crystalline or rod-coil block copolymer aggregates include the enthalpy of fusion of crystalline (or rod) block, the interfacial free energy between the crystalline or liquid crystalline core and the solvent, and the conformational entropy of the amorphous block.[53] The interplay between these factors determines the final morphologies. Among aggregates with a semicrystalline core, thin platelet-like structures are favored, with the folded crystalline domain sandwiched between the brush-like layers of the soluble block. This morphology yields a minimized lateral interface. The 2-D folding of PEO blocks, for example, triggered the formation of "platelet" morphologies, with the PEO chains folded in the center and PS chains stretched outward to the organic solvent.[54]

Crystalline or rod-coil block copolymers provide an alternative route toward non-spherical micellar morphologies. Cylindrical micelles are observed among some semicrystalline block copolymers.[57-62] Meanwhile, rod-coil block copolymers can readily form cylindrical morphologies due to their specific packing, as opposed to chain folding of crystalline block, of the rod block in the micellar core. The formation of cylindrical micelles, as induced by the crystallinity or liquid crystallinity of their block copolymer building blocks, will be reviewed in the following section.

1.4.1 Cylindrical Morphologies from Rod-Coil or Semicrystalline Block Copolymers

In selective solvent for the rod block, the rod-coil block copolymers can form regular micelles as the coil-coil block copolymers do. For example, Jenekhe and Chen prepared spherical and tubular aggregates[55] from poly(phenylquinoline)-*block*-polystyrene (PPQ-*b*-PS), when the solvent was selective for the rod block PPQ. In contrast, in selective solvent for the coil block, the rod-coil block copolymers are promising building blocks for cylinders and vesicles (or also bilayers). For instance, Müllen and coworkers reported micrometer-long ribbon-like structures prepared from rod-coil oligomers in a solvent which was selective for the coil block.[56] Besides, Li and coworkers reported the formation of cylindrical aggregates in water from diblock copolymers consisting of liquid crystalline hydrophobic blocks such as poly(cholesteryl methacryloyloxyethyl carbonate) (PMAChol) or poly(cholesteryl acryloyloxyethyl carbonate) (PAChol). Cylinders were observed for PMAChol-containing block copolymers with a wide range of volume fractions, with which the coil-coil block copolymers would form non-cylindrical morphologies.[57] The image of cylinders from high resolution TEM showed that the PMAChol block formed the smectic layer in the core of cylinders. However, the effect of the formation of liquid crystalline phase on the micellar morphologies was not discussed in this work. Thus, this study raised a question: whether the cylinder was formed before the formation liquid crystalline phase of PMAChol block or the formation of cylinder was driven by the liquid crystal formation of the PMAChol block.

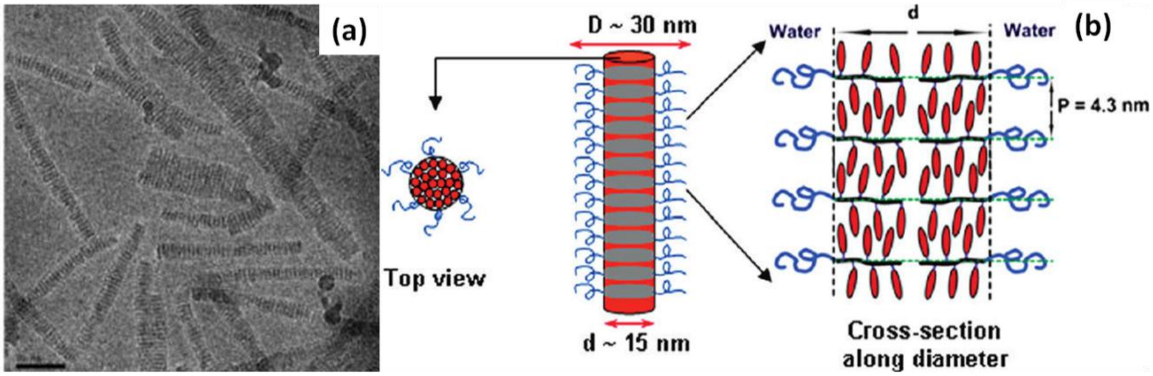

Figure 1.9. Cryo-TEM images (a) and schematic representation (b) of mesogenic cylinders prepared from poly-(cholesterylmethacryloyloxyethyl carbonate)-*b*-poly(*N*,*N*-diethylacrylamide), (PMAChol-*b*-PDEAAm) in water. The layered structures shown in the cryo-TEM images represented the smectic layer of PMAChol blocks in the core of the cylinder. The chain arrangement in the cylindrical core is illustrated in the schematic diagram, with the red ellipses representing the mesogenic cholesteryl side-chain.[57]

Semicrystalline block copolymers (SBCs) are block copolymers that possess a crystalline block. When the crystalline block is the core-forming block, the SBCs behave in a similar manner as rod-coil block copolymers in solution. The energy of crystallization drives the crystalline block to fold into highly ordered structures, and thus the morphologies of SBC micelles differ from those of common block copolymers composed of coil blocks under similar conditions. There have been several studies[54,57-62] focused on micelle formation among SBCs in selective solvents for the coil blocks. And cylinders were reported to form from those SBCs.

Winnik and Manners reported the preparation of rod-like aggregates from Poly(ferrocenylsilanes)-*block*-poly(dimethylsiloxane) (PFS-*b*-PDMS) in hexane at elevated temperature.[58-60] They demonstrated that the crystallinity of the core-forming PFS block played an important role in the self-assembly and organization of the diblock copolymer into cylindrical micelles. In a later development, they discovered that the cylinders grew longer if more copolymer was added. Dynamic light scattering (DLS) was used to demonstrate the living growth of the cylinders. Furthermore, block cylinders (Figure 1.10) were obtained by adding another PFS-containing copolymer into the cylinder seed solution. Wang et al.[61] reported formation of extended cylindrical micelles from block copolymers based on methoxy poly(ethylene glycol) (mPEG) and crystalline poly(caprolactone-b-l-lactide) (P(CL-LLA)). They also claimed that the crystallinity of the P(CL-LLA) block in the micellar core was the main driving force for the formation of these cylindrical micelles. Lazzari and coworkers[62] reported micrometer-scale cylindrical micelles from diblock copolymers composed of either PAN-*b*-PS or PAN-*b*-PMMA. The extraordinary contour length of these cylinders was attributed to the crystal growth of the core-forming PAN chains.

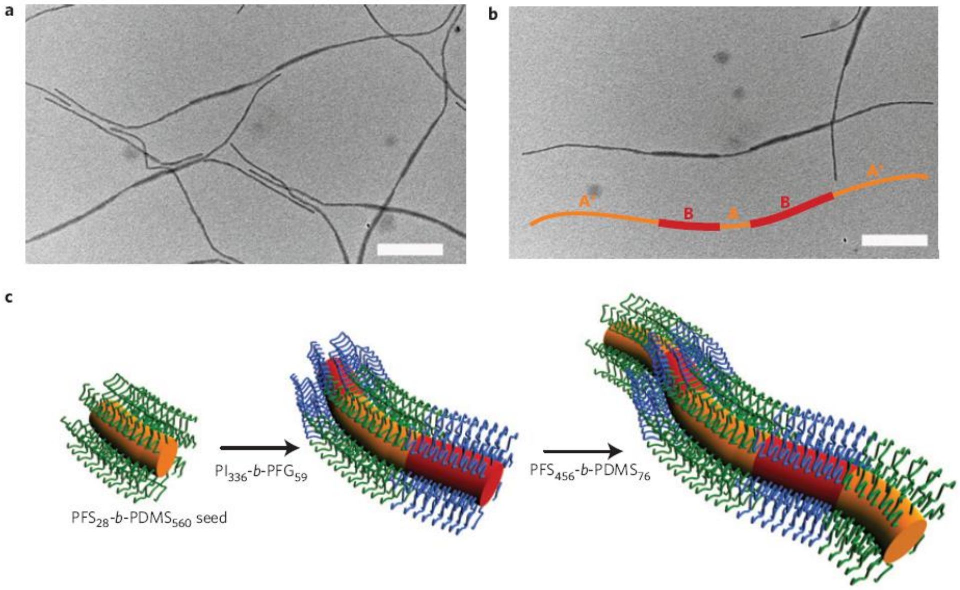

Figure 1.10. TEM micrographs of heteroepitaxially grown pentablock co-micelles (a and b), and schematic representation of the formation of the pentablock co-micelles with different core-forming blocks (c).[58]

Coil-coil diblock copolymers can form cylinders in a very narrow weight ratio range, with typical values of $f_{\text{hydrophobic}}$ between 50% and 65%. However, block copolymers containing a crystalline block can form cylinders within a wide range of weight ratios. For example, the PAN-bearing diblock copolymers exclusively formed cylinders with $f_{\mathrm{hydrophoic}}$ = 11%~65%.[62] Similarly, among diblock copolymers bearing a crystalline P(CL-LLA) block, cylinders were observed with $f_{\mathrm{hydrophoic}}$ = 54%~90%.[61] Cylinders were only observed among PFS-bearing diblock copolymers with low hydrophobic block ratios, such as 1/7 ($f_{\mathrm{hydrophoic}}$ = 27%). If the block ratio of PFS and the hydrophilic block were near 1:1 ($f_{\mathrm{hydrophoic}}$ = 71%), layered structures or "platelet" morphologies were formed.[42] Data in Table 1.2 shows that coil-coil diblock copolymers will form spherical micelles when $f_{\mathrm{hydrophobic}}$ is low (<55%) and vesicles when $f_{\mathrm{hydrophoic}}$ is high (~65%). However, block copolymers containing a crystalline block formed cylinders in a wide range of volume fractions, which would otherwise yield spherical or vesicular micelles from coil-coil diblock copolymers.

Based on the previous experimental results, the self-assembly behaviors of the rod-coil or semicrystalline block copolymers is different from the traditional coil-coil block copolymers. Thus, the theories developed for the coil-coil block copolymer micelles are not applicable for micelles formed by the rod-coil or semicrystalline block copolymers. However, studies on micellar morphologies of the rod-coil or semicrystalline block copolymers are still limited, especially on the rod-coil block copolymer systems. And the effect of liquid crystallinity on the micellar morphology has not been clearly addressed yet.

1.4.2 Self-Assembly and Mesogen-Ordering of Block Copolymers Bearing Fluorinated Blocks

Fluorinated polymers are generally hydrophobic and oleophobic, and are thus immiscible with most hydrocarbon polymers and solvents. Considering the properties of fluorinated polymers,[63] including their resistance to aggressive chemicals and solvents, their low dielectric properties, low coefficients of friction, high surface activities, and liquid crystallinity, the self-assembly of block copolymers bearing fluorinated blocks is very interesting and could lead to many applications.[64]

Block copolymers containing fluorinated pendent groups tend to aggregate in solution, since fluorine-bearing blocks are usually immiscible with common solvents. Imae and coworkers reported ellipsoidal micelles from the diblock copolymers poly(methacrylic acid)-*block*-poly(perfluorooctylethyl methacrylate) (PMAA-*b*-PFMA) and poly(*t*-butyl methacrylate)–*block*–poly(perfluorooctylethyl methacrylate) (PtBMA-*b*-PFMA).[65] The long and short axis lengths of the ellipsoidal micelles were measured from the TEM images, and the size distributions are summarized in Figure 1.11. According to the measured long and short axis length of the micelles, which are apparently different from each other, the micelles are of ellipsoidal shape.

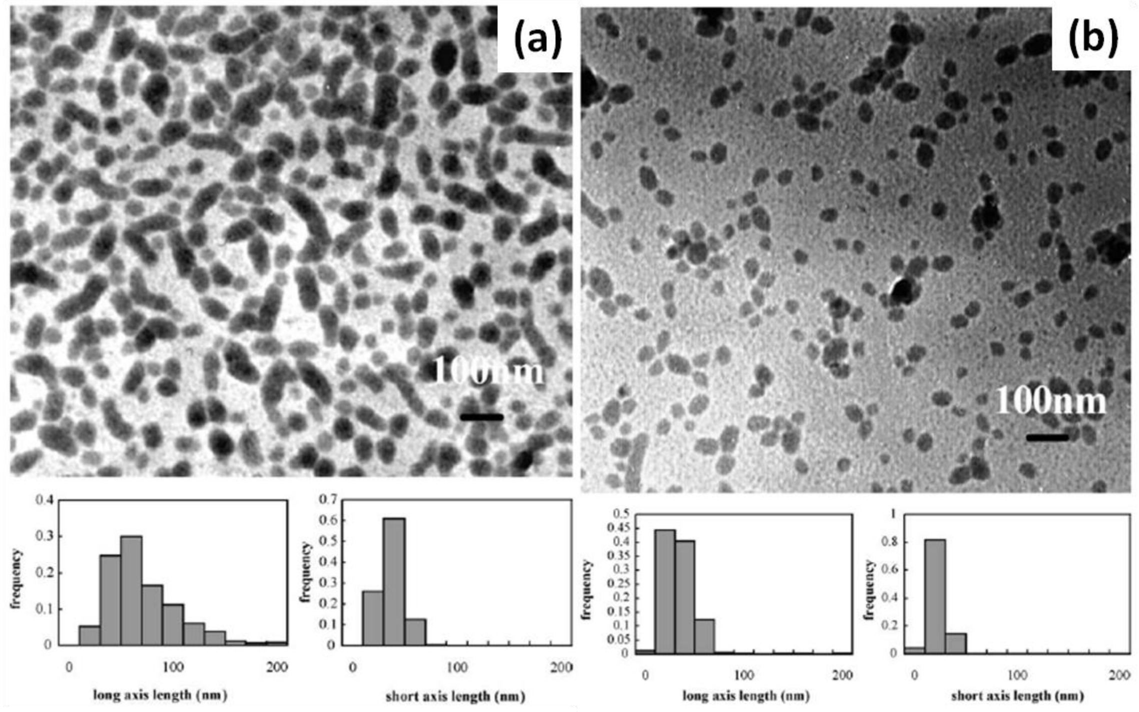

Figure 1.11. TEM images of a film cast onto a carbon grid from ethanol solutions of PMAA-*b*-PFMA (a) and PtBMA-*b*-PFMA (b) at a concentration of 1.0 mg/cm^3. The graphs at the bottom display the size distribution.[65]

The ellipsoidal shapes of the micelles were caused by the special shape of the PFMA block. For the core-forming block of spherical micelles, an ideal circular cone structure is normally adopted. However, due to the crowding of the side-chain, the PFMA block can be considered as a rigid cylinder (Figure 1.12 left). The steric hindrance of the PFMA block in the center of the core (dashed line in the right image in Figure 1.12)[65] resulted in the roughness of the core-shell interface. Furthermore, the aggregation number of the micelles (thousands of chains per micelle) is larger than that of hydrocarbon diblock copolymer analogues (~ 20 chains).[66] This is due to the much greater solvophobicity of the fluorinated block. The micellization of diblock copolymer poly(methyl methacrylate-*block*-1H,1H,2H,2H-perfluorooctyl methacrylate) (PMMA-*b*-PF_6H_2MA) was studied by the Seiko group in THF, which was a selective solvent for the PMMA block.[67] The presence of PMMA homopolymer was claimed to be responsible for the morphological transition from cylinders to spheres. Diblock copolymers of PEO-*b*-PDHFOMA (where DHFOMA is an abbreviation for 1H,1H-perfluorooctyl methacrylate) with different block lengths were synthesized and their self-assembly in water or chloroform was studied by Lim and coworkers,[68] who observed spherical and cylindrical morphologies.

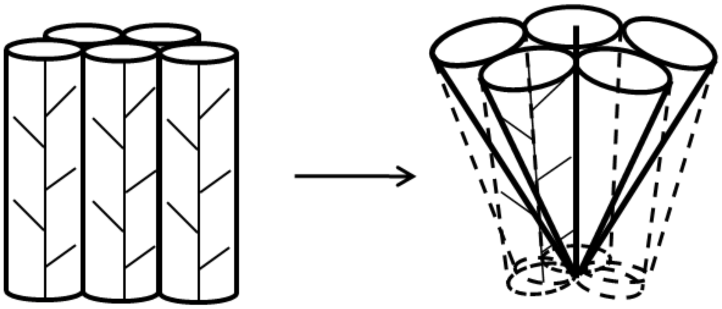

Figure 1.12. Schematic images for the PFMA blocks as rigid cylinders (left) and their chain arrangement in the micelle core (dashed line in the right image).[65] The circular cone in the right image represents the shape of coil polymer chain in the micelle core.

Triblock copolymers composed of hydrophilic, hydrophobic, and fluorinated blocks can undergo strong phase separation in solution. Laschewsky and coworkers produced micelles with compartmented cores from triblock copolymers in water. The triblock copolymers consisted of hydrophilic, lipophilic, and fluorophilic blocks in different sequences. The three kinds of blocks hydrophilic, lipophilic, fluorophilic blocks included, and poly((oligoethylene glycol) acrylate) (POEGA), poly(n-butyl acrylate) or poly(2-ethylhexyl acrylate) (PBuA or PEHA), and poly(1H,1H,2H,2H-perfluorodecyl acrylate (PFA), respectively.[69] The chemical structures of the monomers are shown in Figure 1.13.

The PFA block apparently is semicrystalline with melting points ranging from 75 to 80 ^{o}C. The micelles formed in water had a shell composed of POEGA, while PEHA or PBuA and PFA were segregated in the core. The micellar morphologies changed according to the block volume fractions and the sequences of the copolymer blocks. Interesting morphologies, such as patched micelles and soccer ball micelles were observed.

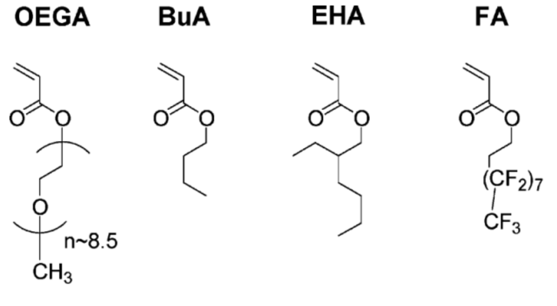

Figure 1.13. The chemical structures OEGA, FHA, BuA, and FA.

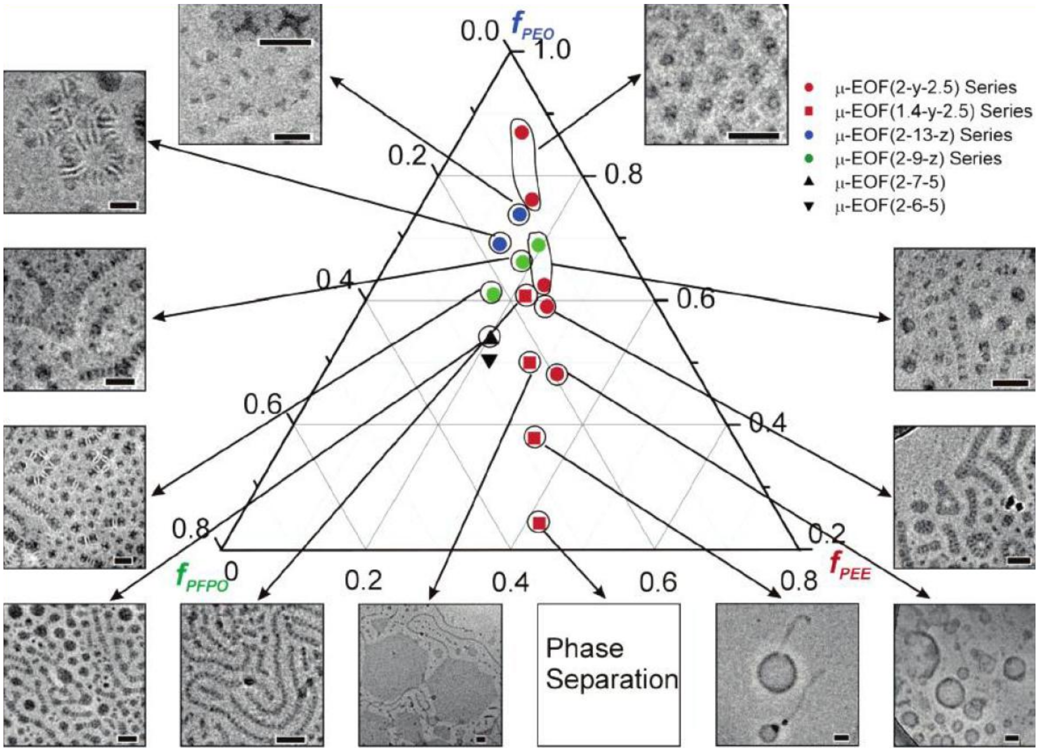

Figure 1.14. Multicompartment micelle morphology diagram for μ-EOF miktoarm star terpolymers in dilute aqueous solution as a function of their composition. The terms f_E, f_O, and f_F represent the volume fractions of the E, O, and F blocks, respectively.[31] The scale bars in the inset images represents 50 nanometers.

Hillmyer and Lodge reported a morphological study on μ-ABC miktoarm copolymers incorporating three mutually immiscible blocks. Their copolymer was abbreviated as μ-EOF and incorporated poly(ethylene oxide) (O), polyethylethylene (E) and poly(perfluoropropylene oxide) (F).[70] Multicompartmental micelles with phase-segregated cores were observed in aqueous solutions of these polymers. An extensive study[31] was performed on the morphology dependence on the molecular weight and composition of a series of μ-EOF copolymers. As shown in Figure 1.14, when the F block composition was low, compartmental micelles such as segmented hamburgers, ribbons, and networks were preferred (insert images on the upper left side). When the fraction of the F block increased, raspberry-like spherical and cylindrical micelles (insert images on the lower left side) were formed. The raspberry-like structure was formed with the F block forming the matrix in the phase-segregated core, providing the smallest interfacial area with the O corona.

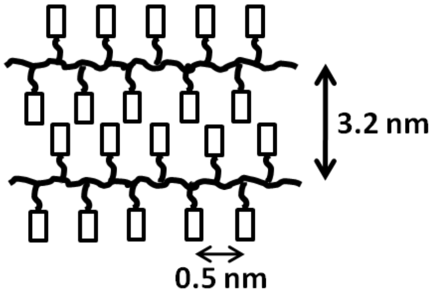

Figure 1.15. Schematic images for the smectic phase of PF polymer.[56]

Polymers with fluorinated side-chains are much more rigid than coil chains, due to the crowded arrangement of the fluorine atoms on the side-chains. Block copolymers with fluorinated side-chains containing more than 7 CF_2 units have been reported to show liquid crystalline properties.[64,69,71,72] The isotropization temperature of poly(perfluorooctylethyl methacrylate) (PF) from the smectic phase to the isotropic state is reported to be between 70 and 80 ^{o}C.[64,69,71,72] The PF block formed a smectic-A phase, and the side-chain organized in layered structures with a spacing of 3.2 nm. Another characteristic distance is ~ 0.5 nm for the distance between two adjacent pendant perfluorooctylethyl methacrylate (FO) units (schematic images for the smectic phase of PF polymer is shown in Figure 1.15, this image was reproduced from literature[56]).

Side-chain liquid crystalline (SCLC) block copolymers have been shown to generate hierarchical structures.[64,73-80] The hierarchical structures resulted from the interplay of different energies in the system, including interfacial free energy, chain stretching energy and mesogenic ordering energy that is associated with the ordering packing of mesogenic components. Competition among these energies results in ordering at two different scales in the final structures:[81,82] microphase segregation of different segments at scales of tens of nanometres and ordered packing of mesogenic segments at the scale of a few nanometres. Many interesting morphologies have been reported for LC block copolymers in selective solvents,[83] in which the LC blocks are the insoluble block. For instance, spheres,[84] nanofibers,[57,84] vesicles,[85,86] nanoribbons,[87] and polyersomes[88] were reported and the ordering at these two scales studied with TEM, small-angle X-ray scattering (SAXS), and other characterization techniques.

However, systematic studies on fluorine-containing block copolymer self-assembly behaviors have not yet been reported. The micellar morphology of such block copolymers is still unpredictable, and more experimental results are needed to fully understand this field.

1.5 Macrocycle Preparation and Characterization

Macromolecules with different topologies are of interest because of the challenges involved in synthesizing numerous polymers with well-defined architectural complexity, and the prospect of discovering new physical properties resulting from their topologies. Cyclic macromolecules,[89] which are also referred as macrocycles, are among the most exciting macromolecular topologies. Their unique properties, such as their reduced viscosity[90] and lower hydrodynamic volume[89] comparing with their linear analogs, are intriguing and generate growing research interest.[91,92]

1.5.1 Background and Literature Review of the Preparation of Macrocycles

The first macromolecule found to have a cyclic conformation was the DNA belonging to a natural microorganism in 1962.[93] Along with the development of synthetic polymerization methods,[2-4] thousands of linear polymers have been obtained, with one or more type of monomer repeated in a polymer chain. In some cases, a small amount of macrocyclic polymers were produced along with the linear polymers. For example, this occurs during the condensation polymerization of polydimethylsiloxane (PDMS).[94] The probability of forming a macrocycle, $W_x(0)$, decreases as the unperturbed mean-square end-to-end length $< r_x^2 >$ decreases. This trend as found by utilizing simulations of Gaussian chains:[95]

$$W_x(0) = (2/2\pi < r_x^2 >)^{2/3} \tag{1.5}$$

where *x* is a vector. Inspired by this discovery, special strategies taking advantage of the equilibrium between macrocycles and linear polymer chains in very dilute solution were designed to prepare macrocycles.[96-106]

Generally speaking, macrocycles can be obtained following two routes. One route utilizes a one-step polymerization, such as a condensation polymerization.[96-98] Theoretical studies by Jacobson and Stockmayer[96] have shown that the fraction of the macrocycles obtained from a condensation polymerization increases with dilution and molecular weight. They also claimed that macrocycles could be obtained with a 100% theoretical yield if the dilution exceeds a critical point by driving the condensation to completion. Several kinds of cyclic oligomers (usually with < 10 repeat units) such as carbonates,[99] aryl esters,[100-103] and ethers[104-106] were obtained by condensation polymerization or ring opening polymerization (Figure 1.16).

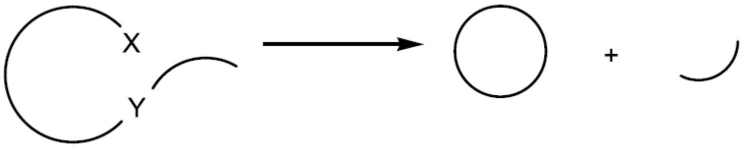

Figure 1.16. Scheme of the backbiting cyclization of one-step polymerization.

However, the macrocycles with high molecular weights are difficult to prepare by this route, as this procedure requires high dilution conditions, and thus the monomer concentrations are extremely low. Even though the high dilution conditions are utilized during the synthesis to increase the fraction of macrocycles produced, an appreciable portion of linear polymers are always present. This route has been improved by Grubbs et al.,[107] who used a cyclic metathesis catalyst to aid the synthesis of macrocycles from cyclooctene (Figure 1.17). Macrocycles with high purity were prepared in large quantities, but they had a polydispersity index (PDI), of ~ 2. However, since this approach uses the same catalyst for ring expansion metathesis polymerization (REMP), this strategy is limited to the polymerization of ring-like monomers, such as cyclooctene.

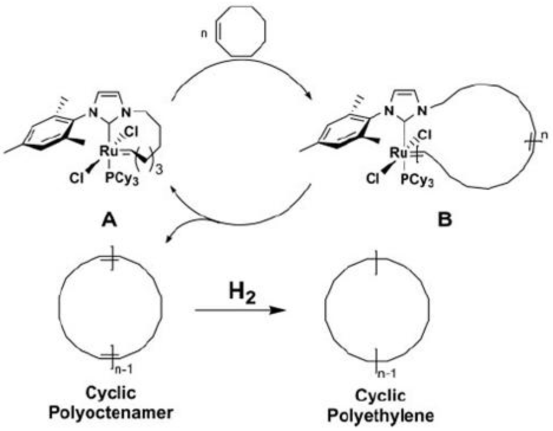

Figure 1.17. Synthesis of macrocycles using ring-opening metathesis polymerization.[107]

Another route involves the coupling pre-made linear polymers with difunctional end groups.[108,109] Two strategies have been demonstrated by Höcker, Rempp and Reffieux,[108,109] which are shown in Figure 1.18. In the bimolecular process, ring closure is achieved by reacting bifunctional polymer chains with small bifunctional molecules having complimentarily reactive groups. The unimolecular process involves the coupling between two end-groups of a heterobifunctional pre-made polymers chains. Narrowly distributed macrocycles could be obtained under high dilution conditions.

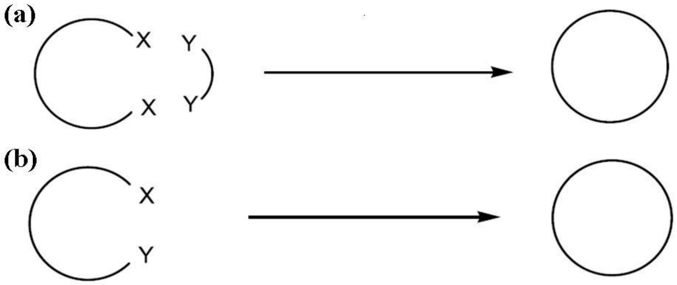

Figure 1.18. Scheme showing the cyclization of pre-made bifunctional polymer chains via coupling reaction. In part (a) a bimolecular process is shown, which involves the coupling between the end-groups of a bifunctional polymer and complimentary end-groups of a small bifunctional bridging molecule. In part (b) a unimolecular process is shown, which involves end-coupling between two reactive end-groups of a bifunctional polymer.

This route was recently improved lately by utilizing more efficient end-coupling reactions, such as click chemistry (Figure 1.19).[110] Macrocycles made by this route are of high purity. However, this strategy requires that the end-groups of the pre-made polymers be amenable to modification . The preparation of high molecular weight macrocycles following this route not yet been reported.

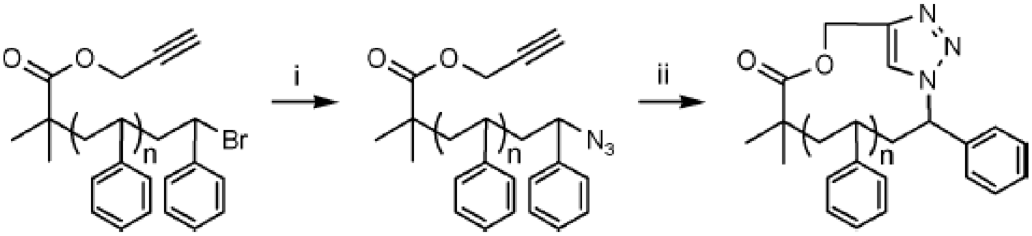

Figure 1.19. Cyclization of polystyrene via click chemistry.

Polymers with highly reactive telechelic dianions[111-113] obtained directly from anionic polymerization have also been used and coupled with bifunctional agents, such as $(CH_3)_2SiCl_2$, to produce macrocycles. However, the stability of the dianion at low concentrations was an issue, since the dianions degrade rapidly under dilute conditions ($[P^{2-}] < 10^{-3}$ M).[114]

1.5.2 Recent Improvements in Macrocycle Synthesis

Obviously, high dilution conditions are crucial for both macrocycle preparation routes, to prevent intermolecular coupling and decrease the percentage of linear impurities. The end-to-end distance of a polymer chain increases with the number of monomer units, or the degree of polymerization (DP). Therefore, the preparation of high molecular weight macrocycles becomes even more difficult, due to the decreasing probability of one chain end finding the other end. Jacobson and Stockmayer[115] have discussed the probability (P_r) at any given instant for finding chain ends within a given area (ν_e) as:

$$P_r = \left(3/2\pi\right)^3 \nu_e / R_n^3 \tag{1.6}$$

where R_n is the root-mean-square end-to-end distance, and ν_e is the reaction volume within which the end coupling reaction occurs effectively.

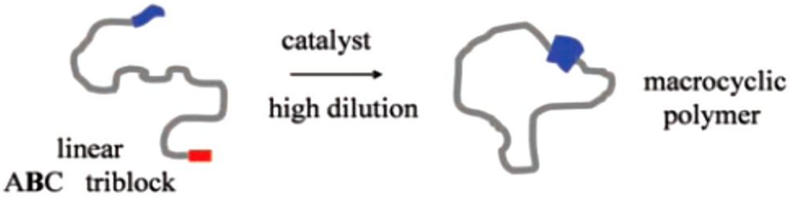

Figure 1.20. Scheme showing the preparation of a high molecular weight macrocycle from a linear ABC triblock copolymer precursor.[116]

For the preparation of macrocycles by click chemistry, ν_e is increased by utilizing a more efficient reaction than the traditional esterification or amidization reactions. Similarly, one can use a pair of reactive end-blocks, rather than end-groups, to increase the probability of macrocycle formation and increase ν_e. This has been demonstrated recently by Schappacher and Deffieux (Figure 1.20).[116] By using an ABC triblock copolymer and end-coupling the terminal A and C blocks, they successfully prepared macrocycles in high yield and in large quantities. The DP of the A and C blocks were both approximately 5, while the DP of the central B,block was much higher, at around 1000. This cyclization was performed under highly dilute conditions. However, an appreciable amount of linear precursor and linear dimers indicated the occurrence of side reactions.

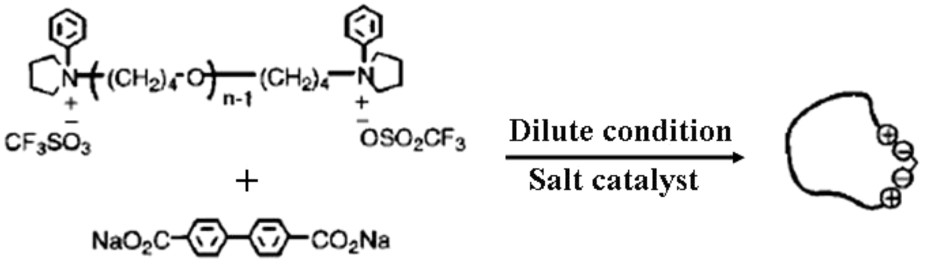

Figure 1.21. Preparation of macrocycles via electrostatic self-assembly of a polymer precursor under dilute conditions.

An alternative way to increase the end-coupling probability is to decrease R_n. Tezuka and coworkers[117] used electrostatic interactions between the end-blocks to aid the ring closure reaction (Figure 1.21). The polymers with cationic end groups were mixed with the small coupling agent with anions. Under the dilute condition, the polymer chains tend to self-assemble to ring conformations due to the electrostatic interactions. Different macromolecular topologies, such as star-shaped, balloon-shaped and multicycles (such as figure-eight shaped structures), were obtained by using different polymer precursors and small molecular coupling agents.[117]

1.5.3 Characterization

Although preparation of the macrocycles has been successfully achieved by following different strategies, their purity is still an issue. Side reactions, such as intermolecular reactions, can produce dimers and higher molecular weight linear polymers. Separation of the macrocycles from the linear polymers is always required. Purifications by fractionation precipitation and preparative chromatography are mostly used. Therefore, although the quantitative characterization of macrocycle purity is important, it is still challenging.

1.5.3.1 Size Exclusion Chromatography

Size exclusion chromatography (SEC),[118,119] until now, is the most frequently used method to differentiate the macrocycles from the by-products and to examine their purity. The working mechanism of SEC is based on entropic exclusion, and the retention time is directly related to the hydrodynamic volume (V_P).[120] Shown below is the relationship between V_P and the molecular weight (M_P) of a monodisperse PS sample:

$$V_p = \frac{[\eta]_p M_p}{2.5} \tag{1.7}$$

where $\left[\eta\right]_P$ is the intrinsic viscosity of a hypothetical monodisperse sample.

Theoretical calculation and some experimental evidence has shown that[121] SEC can be used to determine M_P of different macromolecular topologies according to the differences of their retention volumes. Based on the universal SEC calibration, the apparent molecular weight M_{app} of a macrocycle is predicted by the following equation:

$$M_{app} = M\left(\frac{\eta_r}{\eta_l}\right)^{\frac{1}{1+a}} \tag{1.8}$$

where M is the actual molecular weight of the macrocycle or linear precursor, η_r is the intrinsic viscosity of the macrocycle, η_l is the intrinsic viscosity of the linear precursors, and a is the exponent of the Mark-Houwink relationship.[121] The value of the ratio η_r/η_l is usually taken as ~0.7 (a detailed discussion is provided in the Appendix I) and a is ~0.72 in a good solvent. Based on the above values, the apparent molecular weight of a macrocycle is calculated to be ~80% of the true molecular weight.[113,122] This value could be used to examine the purity of macrocycle samples.

However, in practice, SEC usually cannot provide sufficient peak resolution between the peaks of polydisperse cyclic polymers and their linear precursors. Figure 1.22 shows an example of SEC traces for a macrocycle sample of polystyrene and its linear precursor. The two peaks are obviously not well resolved.

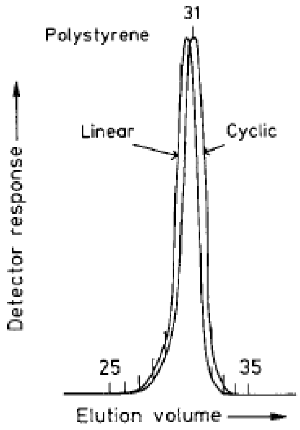

Figure 1.22. Size exclusion chromatographic elution curves for linear and cyclic polystyrene samples of the same molecular weight and low polydispersity.[122]

1.5.3.2 Matrix Assisted Laser Desorption/Ionization Time-of-Flight Mass Spectrometry

Matrix Assisted Laser Desorption/Ionization Time-of-Flight Mass Spectrometry (MALDI-TOF-MS) is a promising method for analyzing polymers with low or moderate molecular weights, ranging up to ~ 10^4 Daltons.[123] Absolute molar mass and the distributions of synthetic polymers could be obtained by this method due to the absence of molecular decomposition. Many investigations have demonstrated the characterization of macrocyclic oligmers utilizing MALDI-TOF-MS.[124-129] Generally, MALDI-TOF-MS spectra of macrocycles show a uniform series of peaks corresponding to the molecular weights of the macrocycles with a mass increment corresponding to the exact monomer molar mass, if the sample has a single charge. The linear contaminants are identified by their differences of molar mass from their cyclic analogues. Taking macrocycles prepared by polycondensation reactions as an example, the molecular weight of a linear contaminant with functional end-groups will differ from that of a macrocycle, which lacks these end-groups. The molar mass of a macrocycle shown in a MALDI-TOF MS spectrum will solely represent the sum of the masses of the monomer units. Meanwhile, that of a linear contaminant will include the total mass of the monomer units, along with the masses of the end-groups.[128]

However, the ionization and detection mechanism used by MALDI-TOF-MS encounters problems among high molecular weight polymers, and consequently they are underrepresented in MALDI-TOF-MS spectra. The ionization of polymers with high molecular weights usually requires a high-powered laser, which will reduces the mass resolution.[123] In addition, among polymers with high polydispersity, the polymer chains of high molar mass may not be detectable when polymers of lower molar mass are allowed to reach the detector.[130] Furthermore, detection of macrocycles with high molecular weight is even more difficult, because of the reduced sensitivity of MS for macrocycles.[125]

1.5.3.3 Atomic Force Microscopy Characterization

Macromolecules of different topologies but of identical DP have very similar SEC retention times, and thus it is very difficult to distinguish the topologies of the product from those of the impurities. Optical microscopy[131] is usually used to visualize the micrometer-sized objects. However, due to its limited magnification, only large biomolecular chains are visible. Atomic force microscopy (AFM) is a scanning probe microscopy technique with very high resolution.[132] It can provide spatial resolution down to the subnanometer scale, and strong contrast of physical properties as well. Its remarkable features in imaging, measuring and manipulating material at the nanometer scale have been widely used.

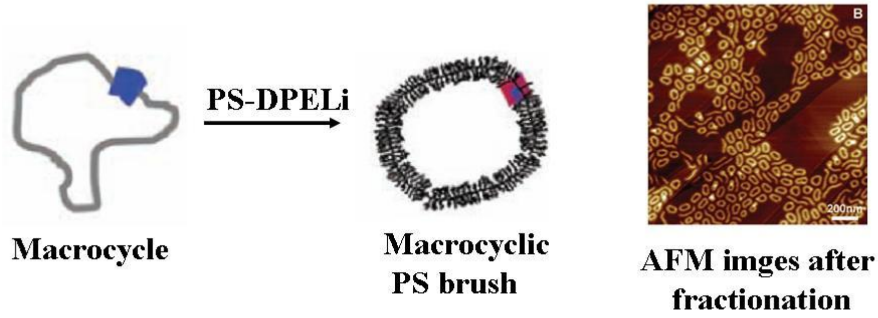

Figure 1.23. Scheme showing the preparation of a macrocyclic brush (Left) and an AFM image of the macrocyclic brush after fractionation (Right).[116]

Recently, direct visualization of modified polymer rings has been demonstrated by Deffieux and coworkers using AFM.[116] Pendant oligomers groups were grafted onto a macrocycle, yielding a macrocyclic brush, which was visible by AFM. However, such graft reaction was difficult to perform. Also, the addition of the long pendant groups increases the constraints upon the ring, and thus changes its conformation from that of the original macrocycle. Consequently, *in situ* analysis of the macrocycle conformations becomes inaccessible.

1.6 Thesis Objectives

1.6.1 Self-Assembly of Triblock Copolymers Bearing a Fluorinated Block

The self-assembly behavior of amphiphilic block copolymers in block-selective solvents has attracted great attention in recent decades. The richness and complexity of the nanostructures produced,[25,133] and the substantial applications of these nanostructures[19] are very appealing, both to scientists and to society. Among diblock copolymer systems, both the theoretical understanding and experimental knowledge have gained great depth. Polymer scientists have an intimate knowledge of the preparation and control of micellar structures. Spherical, cylindrical and vesicular structures have been prepared from diblock copolymers. The self-assembly of triblock copolymers, comparing with that of diblock copolymers, is much more complex, and understanding of the self-assembly of triblock copolymers is still limited.

Fluorinated polymers are unique, as they are both hydrophobic and oleophobic. Thus, they are highly immiscible with ordinary non-fluorinated polymers and they are insoluble in most organic solvents, except for fluorinated solvents. Block copolymers bearing fluorinated blocks are thus expected to behave differently from their non-fluorinated analogs. Furthermore, fluorinated side-chains yield polymers that are much more rigid than their analogous hydrocarbon-based coil-like polymer chains, due to the crowding of the fluorine atoms in the side-chain. Block copolymers with long fluorinated side-chains (with numbers of fluorinated units on the side-chains > 7) have been reported to have liquid crystalline properties.[64,69,71,72] The features of fluorinated polymers, i.e. high surface activity, low immiscibility, rod-like backbones and liquid crystallinity, make the self-assembly of block copolymers containing fluorinated blocks all the more interesting.

Therefore, the micellization of ABC triblock copolymers bearing fluorinated blocks is of great fundamental interest and previous studies on such polymers have been rarely reported.[31,69,70] The first project (Chapter 3), studied the formation of cylindrical morphologies of the ABC triblock copolymers PAA-*b*-PCEMA-*b*-PF and PtBA-*b*-PCEMA-*b*-PF (the structures of these polymers are shown in Figure 1.1) in solvent mixtures of α,α,α,-trifluorotoluene and methanol. The mesogen-ordering of the PF block was found to be crucial for the formation of the cylindrical morphologies. A systematic study was performed as well on the micellar morphologies of PtBA-*b*-PCEMA-*b*-PF in various solvent systems (Appendix B). In different solvent compositions, the morphologies of micelles or micelle-like aggregates were analyzed by TEM. Interesting structures, such as elliptical spheres and hamburger-like aggregates were studied in detail.

1.6.2 AFM Imaging of Macrocyclic Products of ABA Triblock Copolymers

If the concentration of a block copolymer in solution is extremely low (lower than the critical micelle concentration), the polymer will prefer to form unimer micelles instead of aggregate micelles. When a diblock copolymer is dissolved in a block-selective solvent at such a low concentration, the solvophobic block will collapse and the solvophilic block will stretch outward from the solvophobic block, and thus tadpole-like unimer micelles will form. Meanwhile, if a linear ABA triblock copolymer is dissolved in a selective solvent for the central B block, the solvophobic A block can either collapse separately, forming a pompom-coil-pompom structure, or fuse together forming a macrocyclic structure. Cyclic polymers can be produce by permanently locking the macrocyclic structures through crosslinking the A end-blocks together.

The synthesis of the well-defined macrocycles with long chain lengths has been a challenge for polymer chemists for over 60 years.[94,97,99,101,103,104,109,110,116,117,134] Although the preparation of macrocyclic topologies with low molecular weights has been realized, only a few of the reported macrocycles have very high molecular weights. The cyclization of long polymer chains is difficult because the probability for the polymer chain ends to contact one another is much lower, and intramolecular cyclization has to compete with inter-chain coupling. The competition between intra-chain and inter-chain reactions determines the composition of the final product. Thus, linear impurities will always be present as a by-product of the cyclization reaction. Therefore distinguishing the linear impurities from the target macrocycles becomes essential for the characterization of a macrocyclic product.

SEC is the most commonly used method to isolate macrocycles from their by-products and determine their purity,[118,119] by comparing the hydrodynamic volumes of the macrocycles with those of their linear precursors. However, distinguishing the impurities from the macrocycles by SEC is very difficult, due to the small differences between the hydrodynamic volume of macrocycle and those of the impurities. A method was developed in this work that uses AFM to directly image the crosslinked product composed of macrocyclic and linear unimer chains.

Investigated in the second study (Chapter 4) was the single chain self-assembly of an ABA triblock copolymer, (PCEMA-*b*-PDMAEMA-*b*-PCEMA) in a block-selective solvent. It was found that under different solvation conditions, the polymer formed macrocycles or pompom-coil-pompom structures, which were arose from the association of the PCEMA end-blocks. The two PCEMA end-blocks of a unimer chain associated either together or seperately, yielding the macrocycles or pompom-coil-pompom structures, respectively. Those structures could be fixed permanently by photo-crosslinking the PCEMA blocks. The long central polyelectrolyte block of the triblock copolymer precursor led to a considerable amount of the linear species remaining in the macrocyclic product. The macrocyclic product was then observed with AFM after modification. The results from AFM analysis were compared with those from SEC, which was the traditional polymer characterization method. It was found that the cyclization yields determined from both methods shared similar trends, while the SEC method gave a relatively higher cyclization yield. The unreliable SEC separation and detection methods might explain the overestimation of the cyclization yield from SEC.

References

(1) Hamley, I. W. e. *The Physics of Block Copolymers*; Oxford Science Publications: Oxford, **1998**.

(2) Morton, M. *Anionic Polymerization: Principles and Practice*; Academic: New York, **1983**.

(3) Hsieh, H. Q., R. *Anionic Polymerization: Principles and Practice*; Marcel Dekker: New York, **1996**.

(4) Hadjichristidis, N. P., S.; Floudas, G. *Block Copolymers: Synthetic Strategies, Physical Properties, and Applications*; Wiley: New York, **2003**.

(5) Wang, J. S.; Matyjaszewski, K. *Macromolecules* **1995**, *28*, 7901-7910.

(6) Benoit, D.; Chaplinski, V.; Braslau, R.; Hawker, C. J. *J. Am. Chem. Soc.* **1999**, *121*, 3904-3920.

(7) Braunecker, W. A.; Matyjaszewski, K. *Prog. Polym. Sci.* **2007**, *32*, 93-146.

(8) Bates, F. S.; Fredrickson, G. H. *Phys. Today* **1999**, *52*, 32-38.

(9) Fredrickson, G. H.; Helfand, E. *J. Chem. Phys.* **1987**, *87*, 697-705.

(10) Matsen, M. W.; Bates, F. S. *Macromolecules* **1996**, *29*, 1091-1098.

(11) Bates, F. S. *Science* **1991**, *251*, 898-905.

(12) Flory, P. J. *Principles of Polymer Chemistry*; Cornell University Press: Ithaca, **1953**.

(13) Alberda van Ekenstein, G. O. R. M., R.; ten Brinke, G.; Ikkala, O. *Macromolecules* **2000**, *33*, 3752-3756.

(14) Kim, W. N. B., C. M. *J. Appl. Polym. Sci.* **1987**, *34*, 945-967.

(15) Rounds, N. A., *Ph.D. thesis*, University of Akron, **1970**.

(16) Russell, T. P. H., Jr., R. P.; Seeger, P. A. *Macromolecules* **1990**, *23*, 890-893.

(17) Rameau, A. G., Y.; Marie, P.; Farnoux, B. *Polymer* **1989**, *30*, 386-392.

(18) Bates, F. S.; Fredrickson, G. H. *Annu. Rev. Phys. Chem.* **1990**, *41*, 525-557.

(19) Khandpur, A. K.; Forster, S.; Bates, F. S.; Hamley, I. W.; Ryan, A. J.; Bras, W.; Almdal, K.; Mortensen, K. *Macromolecules* **1995**, *28*, 8796-8806.

(20) de Gennes, P.-G. *Solid State Physics*; Academic: New York, **1978**.

(21) Leibler, L.; Orland, H.; Wheeler, J. C. *J. Chem. Phys.* **1983**, *79*, 3550-3557.

(22) Halperin, A.; Alexander, S. *Macromolecules* **1989**, *22*, 2403-2412.

(23) Halperin, A. *Macromolecules* **1987**, *20*, 2943-2946.

(24) Noolandi, J.; Hong, K. M. *Macromolecules* **1983**, *16*, 1443-1448.

(25) Zhang, L. F.; Eisenberg, A. *Science* **1995**, *268*, 1728-1731.

(26) Cameron, N. S.; Corbierre, M. K.; Eisenberg, A. *Can. J. Chem.* **1999**, *77*, 1311-1326.

(27) Booth, C. Y., G.E.; Nace, V.M. *Block Copolymers of Ethylene Oxide and 1,2-butylene oxide*; Elsevier: Amsterdam, **1997**.

(28) Ma, Z. W.; Yu, H. Z.; Jiang, W. *J. Phys. Chem. B* **2009**, *113*, 3333-3338.

(29) Dupont, J.; Liu, G. J.; Niihara, K.; Kimoto, R.; Jinnai, H. *Angew. Chem. Int. Ed* **2009**, *48*, 6144-6147.

(30) Dupont, J.; Liu, G. *Soft Matter* **2010**, *6*, 3654-3661.

(31) Li, Z. B.; Hillmyer, M. A.; Lodge, T. P. *Langmuir* **2006**, *22*, 9409-9417.

(32) Gohy, J. F. In *Block Copolymers* **2005**; Vol. 190, p 65-136.

(33) Gohy, J. F.; Willet, N.; Varshney, S.; Zhang, J. X.; Jerome, R. *Angew. Chem. Int. Ed* **2001**, *40*, 3214-3216.

(34) Liu, G.; Stewart, S. *Abstracts of Papers of the ACS* **1999**, *218*, 6-PMSE.

(35) Pochan, D. J.; Chen, Z. Y.; Cui, H. G.; Hales, K.; Qi, K.; Wooley, K. L. *Science* **2004**, *306*, 94-97.

(36) Hoppenbrouwers, E.; Li, Z.; Liu, G. J. *Macromolecules* **2003**, *36*, 876-881.

(37) Njikang, G.; Han, D. H.; Wang, J.; Liu, G. J. *Macromolecules* **2008**, *41*, 9727-9735.

(38) Hu, J. W.; Njikang, G.; Liu, G. J. *Macromolecules* **2008**, *41*, 7993-7999.

(39) Zheng, R. H.; Liu, G. J.; Yan, X. H. *J. Am. Chem. Soc.* **2005**, *127*, 15358-15359.

(40) Yan, X. H.; Liu, G. J.; Hu, J. W.; Willson, C. G. *Macromolecules* **2006**, *39*, 1906-1912.

(41) Erhardt, R.; Boker, A.; Zettl, H.; Kaya, H.; Pyckhout-Hintzen, W.; Krausch, G.; Abetz, V.; Mueller, A. H. E. *Macromolecules* **2001**, *34*, 1069-1075.

(42) Erhardt, R.; Zhang, M. F.; Boker, A.; Zettl, H.; Abetz, C.; Frederik, P.; Krausch, G.; Abetz, V.; Muller, A. H. E. *J. Am. Chem. Soc.* **2003**, *125*, 3260-3267.

(43) Walther, A.; Drechsler, M.; Rosenfeldt, S.; Harnau, L.; Ballauff, M.; Abetz, V.; Muller, A. H. E. *J. Am. Chem. Soc.* **2009**, *131*, 4720-4728.

(44) Du, J. Z.; Armes, S. P. *Soft Matter*, **2010**, *6*, 4851-4857.

(45) Kriz, J.; Masar, B.; Plestil, J.; Tuzar, Z.; Pospisil, H.; Doskocilova, D. *Macromolecules* **1998**, *31*, 41-51.

(46) Ishizone, T.; Sugiyama, K.; Sakano, Y.; Mori, H.; Hirao, A.; Nakahama, S. *Polym. J.* **1999**, *31*, 983-988.

(47) Zhong, S.; Cui, H. G.; Chen, Z. Y.; Wooley, K. L.; Pochan, D. J. *Soft Matter* **2008**, *4*, 90-93.

(48) Dou, H. J.; Liu, G. J.; Dupont, J.; Hong, L. Z. *Soft Matter* **2011**, *6*, 4214-4222.

(49) Tao, J.; Stewart, S.; Liu, G. J.; Yang, M. L. *Macromolecules* **1997**, *30*, 2738-2745.

(50) Ding, J. F.; Liu, G. J. *Macromolecules* **1997**, *30*, 655-657.

(51) Won, Y. Y.; Davis, H. T.; Bates, F. S. *Science* **1999**, *283*, 960-963.

(52) Discher, D. E.; Eisenberg, A. *Science* **2002**, *297*, 967-973.

(53) Schmalz, H.; Schmelz, J.; Drechsler, M.; Yuan, J.; Walther, A.; Schweimer, K.; Mihut, A. M. *Macromolecules* **2008**, *41*, 3235-3242.

(54) Lin, E. K.; Gast, A. P. *Macromolecules* **1996**, *29*, 4432-4441.

(55) Jenekhe, S. A.; Chen, X. L. *Science* **1998**, *279*, 1903-1907.

(56) Leclere, P.; Calderone, A.; Marsitzky, D.; Francke, V.; Geerts, Y.; Mullen, K.; Bredas, J. L.; Lazzaroni, R. *Adv. Mater.* **2000**, *12*, 1042-1046.

(57) Boisse, S.; Rieger, J.; Di-Cicco, A.; Albouy, P. A.; Bui, C.; Li, M. H.; Charleux, B. *Macromolecules* **2009**, *42*, 8688-8696.

(58) Gadt, T.; Ieong, N. S.; Cambridge, G.; Winnik, M. A.; Manners, I. *Nat. Mater.* **2009**, *8*, 144-150.

(59) Massey, J. A.; Temple, K.; Cao, L.; Rharbi, Y.; Raez, J.; Winnik, M. A.; Manners, I. *J. Am. Chem. Soc.* **2000**, *122*, 11577-11584.

(60) Wang, X. S.; Guerin, G.; Wang, H.; Wang, Y. S.; Manners, I.; Winnik, M. A. *Science* **2007**, *317*, 644-647.

(61) Zhang, J.; Wang, L. Q.; Wang, H. J.; Tu, K. H. *Biomacromolecules* **2006**, *7*, 2492-2500.

(62) Lazzari, M.; Scalarone, D.; Vazquez-Vazquez, C.; Lopez-Quintela, M. A. *Macromol. Rapid Commun.* **2008**, *29*, 352-357.

(63) Drobny, J. G. *Macromol. Symp.* **2001**, *170*, 149-156.

(64) Al-Hussein, M.; Serero, Y.; Konovalov, O.; Mourran, A.; Moller, M.; de Jeu, W. H. *Macromolecules* **2005**, *38*, 9610-9616.

(65) Ito, H.; Imae, T.; Nakamura, T.; Sugiura, M.; Oshibe, Y. *J. Colloid Interface Sci.* **2004**, *276*, 290-298.

(66) Ravi, P.; Wang, C.; Tam, K. C.; Gan, L. H. *Macromolecules* **2003**, *36*, 173-179.

(67) Krupers, M. J.; Sheiko, S. S.; Moller, M. *Polym. Bull.* **1998**, *40*, 211-217.

(68) Lim, K. T.; Lee, M. Y.; Moon, M. J.; Lee, G. D.; Hong, S. S.; Dickson, J. L.; Johnston, K. P. *Polymer* **2002**, *43*, 7043-7049.

(69) Skrabania, K.; von Berlepsch, H.; Bottcher, C.; Laschewsky, A. *Macromolecules*, **2010**, *43*, 271-281.

(70) Li, Z. B.; Kesselman, E.; Talmon, Y.; Hillmyer, M. A.; Lodge, T. P. *Science* **2004**, *306*, 98-101.

(71) Martinelli, E.; Fantoni, C.; Galli, G.; Gallot, B.; Glisenti, A. *Mol. Cryst. Liq. Cryst. Sci. Technol., Sect. A* **2009**, *500*, 51-62.

(72) Sheiko, S.; Lermann, E.; Moller, M. *Langmuir* **1996**, *12*, 4015-4024.

(73) Muthukumar, M.; Ober, C. K.; Thomas, E. L. *Science* **1997**, *277*, 1225-1232.

(74) Hamley, I. W.; Castelletto, V.; Lu, Z. B.; Imrie, C. T.; Itoh, T.; Al-Hussein, M. *Macromolecules* **2004**, *37*, 4798-4807.

(75) Anthamatten, M.; Wu, J. S.; Hammond, P. T. *Macromolecules* **2001**, *34*, 8574-8579.

(76) Xu, B.; Pinol, R.; Nono-Djamen, M.; Pensec, S.; Keller, P.; Albouy, P. A.; Levy, D.; Li, M. H. *Faraday Discuss.* **2009**, *143*, 235-250.

(77) Yamada, M.; Itoh, T.; Nakagawa, R.; Hirao, A.; Nakahama, S.; Watanabe, J. *Macromolecules* **1999**, *32*, 282-289.

(78) Kasko, A. M.; Heintz, A. M.; Pugh, C. *Macromolecules* **1998**, *31*, 256-271.

(79) Kato, T.; Mizoshita, N.; Kishimoto, K. *Angew. Chem. Int. Ed.* **2006**, *45*, 38-68.

(80) Mao, G. P.; Wang, J. G.; Clingman, S. R.; Ober, C. K.; Chen, J. T.; Thomas, E. L. *Macromolecules* **1997**, *30*, 2556-2567.

(81) Kato, T. *Science* **2002**, *295*, 2414-2418.

(82) Schneider, A.; Zanna, J. J.; Yamada, M.; Finkelmann, H.; Thomann, R. *Macromolecules* **2000**, *33*, 649-651.

(83) Olsen, B. D.; Segalman, R. A. *Mater. Sci. Eng., R* **2008**, *62*, 37-66.

(84) Tu, Y. F.; Graham, M. J.; Van Horn, R. M.; Chen, E. Q.; Fan, X. H.; Chen, X. F.; Zhou, Q. F.; Wan, X. H.; Harris, F. W.; Cheng, S. Z. D. *Polymer* **2009**, *50*, 5170-5174.

(85) Loos, K.; Boker, A.; Zettl, H.; Zhang, A. F.; Krausch, G.; Muller, A. H. E. *Macromolecules* **2005**, *38*, 873-879.

(86) Li, M. H.; Keller, P. *Soft Matter* **2009**, *5*, 927-937.

(87) Kim, K. T.; Park, C.; Vandermeulen, G. W. M.; Rider, D. A.; Kim, C.; Winnik, M. A.; Manners, I. *Angew. Chem. Int. Ed.* **2005**, *44*, 7964-7968.

(88) Mabrouk, E.; Cuvelier, D.; Pontani, L. L.; Xu, B.; Levy, D.; Keller, P.; Brochard-Wyart, F.; Nassoy, P.; Li, M. H. *Soft Matter* **2009**, *5*, 1870-1878.

(89) Zimm, B. H.; Stockmayer, W. H. *J. Chem. Phys.* **1949**, *17*, 1301-1314.

(90) Yamakawa, H. *Modern Thoery of Polymer Solution*; Harper and Row: New York, **1969**.

(91) Klein, J. *Macromolecules* **1986**, *19*, 105-118.

(92) Rubinstein, M. *Phys. Rev. Lett.* **1986**, *57*, 3023-3026.

(93) Fiers, W.; Sinsheimer, R. L. *J. Mol. Biol.* **1962**, *5*, 424-&.

(94) Brown, J. F.; Slusarcz.Gm *J. Am. Chem. Soc.* **1965**, *87*, 931-&.

(95) Flory, P. J. *Statistical mechanics of chain molecules*; Interscience publisher: New York, **1969**.

(96) Jacobson, H.; Stockmayer, W. H. *J. Chem. Phys.* **1950**, *18*, 1600-1606.

(97) Jones, F. R.; Scales, L. E.; Semlyen, J. A. *Polymer* **1974**, *15*, 738-742.

(98) Andrews, J. M.; Jones, F. R.; Semlyen, J. A. *Polymer* **1974**, *15*, 420-424.

(99) Brunelle, D. J.; Shannon, T. G. *Macromolecules* **1991**, *24*, 3035-3044.

(100) Hubbard, P.; Brittain, W. J.; Simonsick, W. J.; Ross, C. W. *Macromolecules* **1996**, *29*, 8304-8307.

(101) Jiang, H. Y.; Chen, T. L.; Xu, J. P. *Macromolecules* **1997**, *30*, 2839-2842.

(102) Brunelle, D. J.; Bradt, J. E.; Serth-Guzzo, J.; Takekoshi, T.; Evans, T. L.; Pearce, E. J.; Wilson, P. R. *Macromolecules* **1998**, *31*, 4782-4790.

(103) Qi, Y. H.; Chen, T. L.; Jiang, H. Y.; Bo, S. Q.; Xing, Y.; Lin, Y. H.; Xu, J. P. *Macromol. Chem. Phys.* **1999**, *200*, 2407-2410.

(104) Wang, J. Z.; Chen, C. H.; Xun, X. M.; Wang, S. Y.; Wu, Z. W. *J. Polym. Sci., Part A: Polym. Chem.* **1999**, *37*, 1957-1967.

(105) Teasley, M. F.; Wu, D. Q.; Harlow, R. L. *Macromolecules* **1998**, *31*, 2064-2074.

(106) Wang, Y. F.; Chan, K. P.; Hay, A. S. *Macromolecules* **1996**, *29*, 3717-3726.

(107) Bielawski, C. W.; Benitez, D.; Grubbs, R. H. *Science* **2002**, *297*, 2041-2044.

(108) Hild, G.; Kohler, A.; Rempp, P. *Eur. Polym. J.* **1980**, *16*, 525-527.

(109) Deffieux, A.; Beinat, S.; Schappacher, M. *Macromol. Symp.* **1997**, *118*, 247-253.

(110) Laurent, B. A.; Grayson, S. M. *J. Am. Chem. Soc.* **2006**, *128*, 4238-4239.

(111) Hogen-Esch, T. E. *J. Polym. Sci., Part A: Polym. Chem.* **2006**, *44*, 2139-2155.

(112) Iatrou, H.; Hadjichristidis, N.; Meier, G.; Frielinghaus, H.; Monkenbusch, M. *Macromolecules* **2002**, *35*, 5426-5437.

(113) Roovers, J.; Toporowski, P. M. *Macromolecules* **1983**, *16*, 843-849.

(114) Szwarc, M. *Carbanions, Living Polymers and Electron Transfer Processer*; Wiley: New York, **1968**.

(115) Jacobson, H.; Beckmann, C. O.; Stockmayer, W. H. *J. Chem. Phys.* **1950**, *18*, 1607-1612.

(116) Schappacher, M.; Deffieux, A. *Science* **2008**, *319*, 1512-1515.

(117) Oike, H.; Imaizumi, H.; Mouri, T.; Yoshioka, Y.; Uchibori, A.; Tezuka, Y. *J. Am. Chem. Soc.* **2000**, *122*, 9592-9599.

(118) Dodgson, K.; Sympson, D.; Semlyen, J. A. *Polymer* **1978**, *19*, 1285-1289.

(119) Dagger, A. C.; Semlyen, J. A. *Polymer* **1999**, *40*, 3243-3245.

(120) Young, R. J. L., P. A. *Introduction to Polymers.* 2nd Ed.; Chapman&Hall: London, **1991**.

(121) Vakhrushev, A. V.; Gorbunov, A. A.; Tezuka, Y.; Tsuchitani, A.; Oike, H. *Anal. Chem.* **2008**, *80*, 8153-8162.

(122) Lutz, P.; McKenna, G. B.; Rempp, P.; Strazielle, C. *Makromol. Chem. Rapid Commun.* **1986**, *7*, 599-605.

(123) Rader, H. J.; Schrepp, W. *Acta Polym.* **1998**, *49*, 272-293.

(124) Blais, J. C.; Tessier, M.; Bolbach, G.; Remaud, B.; Rozes, L.; Guittard, J.; Brunot, A.; Marechal, E.; Tabet, J. C. *Int. J. Mass Spectrom. Ion Processes* **1995**, *144*, 131-138.

(125) Montaudo, G.; Montaudo, M. S.; Puglisi, C.; Samperi, F. *J. Polym. Sci., Part A: Polym. Chem.* **1996**, *34*, 439-447.

(126) Pasch, H.; Gores, F. *Polymer* **1995**, *36*, 1999-2005.

(127) Adachi, K.; Takasugi, H.; Tezuka, Y. *Macromolecules* **2006**, *39*, 5585-5588.

(128) Tezuka, Y.; Ohtsuka, T.; Adachi, K.; Komiya, R.; Ohno, N.; Okui, N. *Macromol. Rapid Commun.* **2008**, *29*, 1237-1241.

(129) Wollheim, T.; Kricheldorf, H. R.; Altstadt, V.; Koning, C. E.; Buning, G. H. W. *High Perform. Polym.* **2001**, *13*, 119-132.

(130) McEwen, C. N.; Jackson, C.; Larsen, B. S. *Int. J. Mass Spectrom. Ion Processes* **1997**, *160*, 387-394.

(131) Bradbury, S. *The Optical Microscope in Biology*; Edward Arnold: London, **1976**.

(132) Cicoira, F. e. a. *STM and AFM Studies on (Bio)molecular Systems: Unravelling the Nanoworld*; Springer: Berlin, **2008**.

(133) Zhang, L. F.; Eisenberg, A. *J. Am. Chem. Soc.* **1996**, *118*, 3168-3181.

(134) Ge, Z. S.; Zhou, Y. M.; Xu, J.; Liu, H. W.; Chen, D. Y.; Liu, S. Y. *J. Am. Chem. Soc.* **2009**, *131*, 1628-1629.

Chapter 2

Experimental Methods for Preparing and Studying the Polymers, Macrocyclic Polymer Chains, and Cylindrical Micelles

This section discusses the instrumental techniques used to characterize the polymers and micelles. The properties that were characterized include the composition, molecular weight, and molecular weight distribution of the polymers. Nuclear magnetic resonance (NMR) spectroscopy was used to determine the chemical composition of the copolymers and the molar ratios between the different blocks. The apparent molecular weight and distribution of the polymers and macrocycles were analyzed by size exclusion chromatography (SEC). The structures of the macrocyclic products were observed by atomic force microscopy (AFM). Meanwhile, the morphologies of the cylindrical micelles were analyzed by both transmission electron microscopy (TEM) and AFM. Dynamic light scattering (DLS) was used to monitor the growth of the cylindrical micelles. The surface composition of the cylindrical micelles was analyzed by X-ray photoelectron spectroscopy (XPS). The crystallinity of the fluorinated block was determined by wide angle X-ray scattering (WAXS) and differential scanning calorimetry (DSC).

2.1 Characterization of Polymers and Macrocycles

2.1.1 ^{1}H NMR Spectroscopy

^{1}H NMR is a spectroscopic technique routinely used by chemists to study the composition of compounds. The nuclei of certain isotopes have an intrinsic spin, which is represented by the spin quantum number (I). If I is not zero, the nucleus should have two or more spin states, which correspond to different magnetic quantum numbers (m).[1] The nucleus of a proton, for example, has a spin quantum number of $I = \frac{1}{2}$ and two spin states with magnetic quantum numbers of $m = +\frac{1}{2}$ and $m = -\frac{1}{2}$. In the absence of a magnetic field, the nuclei with different spin states occupy the same energy level. However, when they are placed into an external magnetic field, the nuclei with different spin states will split into different energy levels. In a ^{1}H NMR spectrometer, electromagnetic radiation is applied to the nuclei. If the photon energy ($h\nu_0$) of the radiation matches the energy gap (ΔE) between the different spin states of the nuclei, the radiation will be absorbed and then the nuclei at the lower energy level will be excited to the higher energy level (Figure 2.1). This process is called nuclear magnetic resonance.

The energy required is proportional to the strength of the magnetic field. The relationship between the frequency (ν_0) and the magnetic field (H_0) is given by[1]:

$$\nu_0 = \frac{gH_0}{2\pi} \tag{2.1}$$

where g is the magnetogyric ratio and ν_0 is called Larmor frequency. The frequency required for a photon to bring a nucleus into resonance is affected by the chemical environment of the nucleus.[1] Therefore, NMR spectra can provide information about the chemical environments surrounding the nuclei.

After a nucleus is excited, it will relax from the higher energy level to the lower energy level mainly through a non-irradiative relaxation process, which includes spin-lattice relaxation and spin-spin relaxation. In the spin-lattice relaxation process, the loss of energy occurs through the vibration and rotation of the nucleus as it transfers its absorbed energy to the surrounding environement. The average lifetime of a nucleus at a higher energy level is defined as the spin-lattice relaxation time (T_1), which is dependent on the magnetic ratio of the nucleus and the mobility of the lattice. T_2 is defined as the spin-spin relaxation time (also called the transverse relaxation time), which involves a transfer of energy from one nucleus to another. For polymer samples, the mobility is much lower than that of the small molecules, and longer relaxation times are required.

In this study, ^{1}H NMR was used to analyze the structures of the block copolymers. The ratios among the different blocks of the triblock copolymers were measured by comparing the integrations of peaks assigned to the functional groups attached to different blocks as side-chains. Since polymer chains generally have lower mobility than small molecules,[2] the relaxation delay time was adjusted to 3 seconds (usually 1 second is used for small molecules) in all of the NMR measurements performed in this thesis.

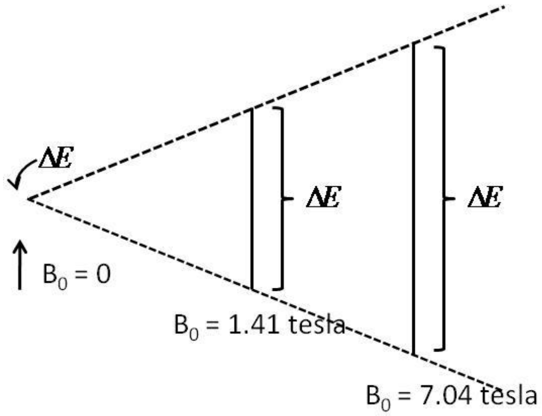

Figure 2.1. The energy difference between the two spin states of a proton depends on the strength of the external magnetic field, B_0. $B_0 = 1.41$ Tesla and 7.04 Tesla corresponds to that of electromagnetic radiation of 60 and 300 MHz, respectively.

2.1.2 Size Exclusion Chromatography

Size exclusion chromatography (SEC) is a technique used to determine the relative molecular weight, as well as the molecular weight distributions of polymer samples. Instead of directly measuring the molecular weight, SEC measures the hydrodynamic volumes (V_h) of polymers, which are related to the molecular weight. The intrinsic viscosity $[\eta]$ is given as:[3]

$$[\eta]M \sim V_h \tag{2.2}$$

where M is the molecular weight of the polymer. Another useful equation is the Mark-Houwink equation:

$$[\eta] = K\, M^a \tag{2.3}$$

where terms a and K are constant for a given polymer in a particular solvent and at a given temperature. Combining Equations 2.2 and 2.3 gives the relationship between the hydrodynamic volume and the molecular weight:[3]

$$V_h \sim KM^{1+a} \tag{2.4}$$

In a good solvent for the polymer, the coefficient a is close to 0.8.

A typical SEC system includes a solvent pump, a set of chromatography columns, and detectors. The packing materials of the columns are gels with the desired size distributions of pores, and they can separate polydisperse polymer samples by size. When a polymer sample passes through the columns, polymers with smaller volumes require more time to pass through the columns, because the number of available pores in the gel in which they may be retained is greater than for polymers with larger volumes. The time between when the sample is introduced to the columns and when the the analyte reaches the detector is defined as the retention time (t_R). A shorter t_R usually indicates that a polymer has a larger volume, a longer polymer chain, and thus a higher molecular weight.

To correlate either t_R or the retention volume (V_R, where $V_R = t_R \times$ effluent rate) with the molecular weight of an unknown polymer, the columns are calibrated using a series of monodisperse polymer standards. For example polystyrene standards are typically used a standards for calibration. A calibration curve can be obtained by plotting the logarithm of their molecular weights ($\log M$) of the polymer standards against their peak retention times or volumes. Theoretically, the relationship between the molecular weight and the retention volume is:

$$\log M = A + BV_R + CV_R^2 + DV_R^3 \tag{2.5}$$

where A, B, C, and D are experimentally determined constants. Therefore, the molecular weight of an unknown sample can be calculated in terms of the standards by inserting the retention volume into Equation 2.5.

A detector is used to record the concentration changes of the solute in the column effluent. Refractive index (RI) detectors are the most popular detectors used in SEC systems. These detectors measure the differential refractive index between the mobile phase and the column effluent containing the solute, which is considered to be proportional to the concentration of the solute.[3] The molecular weight distribution can be obtained based on the molecular weight of a certain polymer fraction and its concentration, and combining these results with those obtained from all of the fractions.

2.1.3 Atomic Force Microscopy

AFM is a technique that provides high resolution images of a sample in three dimensions, and can be used to observe a nanostructure's morphology.[4] Usually an AFM system consists of three main components: a cantilever, a sample holder and a signal detector. A schematic diagram of an AFM device is shown in Figure 2.2. The tip, which interacts with the sample, is mounted at the end of a cantilever. The resonance of the cantilever is monitored with the detector. Based on the kinds of interactive forces between the tip and the sample during the scanning, AFM can be classified into three modes: contact mode, non-contact mode, and tapping mode.[4] For analyzing soft materials such as polymers, tapping mode is most frequently used, since it can be performed under ambient conditions and minimizes sample deformation. All of the AFM images shown in this thesis were obtained using the tapping-mode.

In tapping mode AFM, the cantilever is driven to oscillate up and down near its resonance frequency above the surface of a sample. The tip is located at an intermediate distance from the sample's surface, so that they are always within the domain of attractive forces. During scanning, the driving frequency (ω) of the cantilever is fixed, and the driving amplitude (A) and phase angle of the frequency (ϕ) change according to the interactions between the cantilever and the surface of the sample (Figure 2.3).

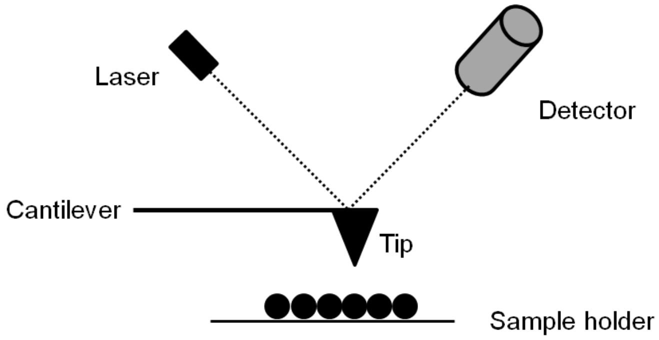

Figure 2.2. Simple schematic diagram of an AFM system.

To obtain a height image, the cantilever is brought to the sample surface and the amplitude A_0 is changed to A_t. Here, A_0 and A_t are the amplitude of the cantilever at time 0 and t. The amplitude of the cantilever is maintained at A_t by changing the height of the cantilever. The height change of the cantilever provides the surface topography of the sample. The phase image is obtained by measuring the phase angle change of the cantilever frequency (Figure 2.4). For example, when the cantilever approaches the surface, the attractive force gradient between the cantilever and the surface will act as a spring that is attached to the tip, and will reduce the cantilever frequency, which ‘drags’ the phase of the tip (Figure 2.4).

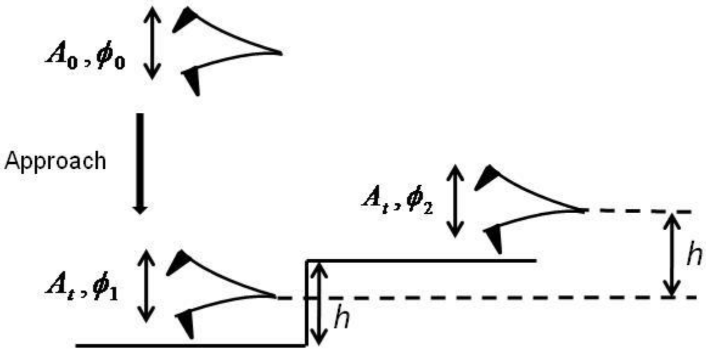

Figure 2.3. Scheme of the AFM mechanism for height and phase images.

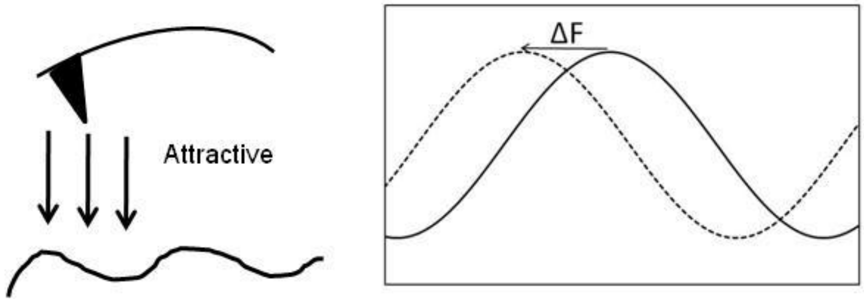

Figure 2.4. Scheme of the phase displacement of a cantilever's oscillating frequency when the cantilever approaches a surface.

In this thesis, tapping mode AFM was used to observe single polyelectrolyte chains. The high resolution of AFM, which reaches down to fractions of a nanometer in scale, enables imaging of single polymeric chains, with heights of several nanometers. The accuracy of the vertical axis is even better than that in the horizontal axis, since the horizontal accuracy can be influenced by the shape of the tip. Furthermore, in tapping mode the AFM tip does not come into direct contact with the surface of the samples, which minimizes damage to the morphologies that are being scanned.

2.2 Characterization of Cylindrical Micelles

2.2.1 Transmission Electron Microscopy

Transmission electron microscopy (TEM) is a direct method used to observe structures at the nanometer scale.[5] The outstanding resolution of TEM is attributed to the short electron wavelength. According to the Rayleigh criterion, the resolution of an imaging technique is limited to approximately half of the wavelength of the probing radiation used in the device.[5]

When an electron beam passes through a sample, the electrons can be scattered, absorbed, or they can penetrate through the sample, depending on the sample's electron density. Samples with higher electron density will scatter more of the electrons. Therefore, an image can be obtained by capturing the permeated electrons using a fluorescence screen. The image reveals the differences of electron density across an inspected region of a sample and areas with higher electron density appear darker in the TEM image.

In this thesis, solution samples were directly sprayed onto copper grids covered with an ultrathin carbon film. Since the electron densities between different polymer domains are quite similar to each other, heavy metals were used to selectively stain particular polymer domains to enhance the contrast of the electron densities between the different domains. In this context, the PCEMA domains (which contain double bonds) can be selectively stained by OsO_4, and the PAA domains (containing carboxyl groups) can be selectively stained with uranyl acetate.

2.2.2 X-ray Photoelectron Spectroscopy

X-ray photoelectron spectroscopy (XPS) is a surface analysis technique used to determine the elemental composition on a sample's surface. When an incident X-ray photon encounters a core electron of the sample, the energy of the photon (E_{photon}) is transferred to the core electron, which causes the core electron to escape from the attraction of its nuclei. This energy, which pulls a core electron from the nucleus and yields a free electron, is called the electron binding energy ($E_{binding}$). The energy difference between E_{photon} and $E_{binding}$ becomes the kinetic energy of a free electron ($E_{kinetic}$). The relationhip between the three energies is:

$$E_{binding} = E_{Photon} - (E_{kinetic} + \phi) \tag{2.6}$$

where ϕ is an instrument-dependent constant. Therefore, by measuring the magnitude of $E_{kinetic}$, $E_{binding}$ can be obtained. $E_{binding}$ is a characteristic energy for each element. Therefore, XPS can identify the elements by determining $E_{binding}$. Generally, the penetration depth for an X-ray photon into a sample is several millimeters in approximate scale, but electrons escaping from the sample surface can only be detected to a depth of 0.5-5 nanometers. This is because the electrons from the inner layers of a sample will collide with electrons in the upper layers. This collision causes the electron to lose energy, so that it will no longer exhibit the characteristic energy of the atom that it escaped from.

XPS is a good technique for analyzing polymer samples. Firstly, it generates soft X-ray photons, which are considered to be non-destructive to the sample. Secondly, XPS can provide quantitative information about the same element in different chemical environments.

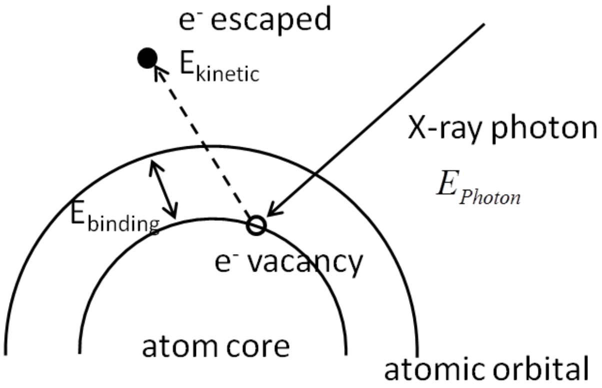

Figure 2.5. Scheme showing the mechanism of XPS.

2.2.3 Dynamic Light Scattering

In dynamic light scattering (DLS)[6] or photon correlation spectroscopy (Figure 2.6), the fluctuation of scattered light is measured. Ideally, when a monochromic beam of light, such as a laser beam, encounters particles in solution that exhibit Brownian motion, the light is scattered in all directions with a time-dependent fluctuation in the light intensity. Since the Brownian motion of a particle is dependent on the particle's size, the fluctuation of the scattered light includes dynamic information which is also particle size-dependent. DLS determines the the diffusion coefficient (D) by using an auto-correlation function to analyze the fluctuation of the scattered light intensity, which is recorded by a photomultiplier (Figure 2.6). If the particle is an ideal sphere, the hydrodynamic radius (R_h) is given by the Einstein-Stokes equation[6]:

$$R_h = \frac{k_B T}{6\pi\eta D} \quad \text{or} \quad D = \frac{k_B T}{6\pi\eta R_h} \qquad (2.7)$$

where k_B is the Boltzmann's constant, T is the absolute temperature of the solvent expressed in Kelvins, η is the viscosity of the solvent. Under certain conditions, the lower the value of D, the lower the mobility of the micelles, and the larger the volume of the micelles.

In this thesis, DLS was used to monitor the *in situ* growth of cylindrical micelles. Since the diameters of the cylinders are quite uniform in a large scale, the apparent hydrodynamic radius (R_h) reveals the relative sizes of the cylindrical micelles. In other words, if the cylinders become longer, R_h becomes larger.

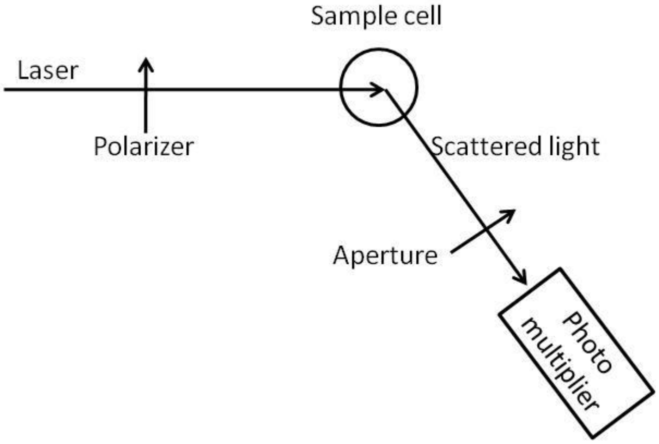

Figure 2.6. Schematic diagram of a DLS system.

2.2.4 Wide Angle X-ray Scattering

Diffraction is the constructive interference that occurrs when an incident X-ray beam is scattered by the periodic atomic structure of crystals at certain angles. X-ray diffraction is a non-destructive technique used to determine the position, intensity and width of diffraction peaks of crystalline materials. Wide angle X-ray scattering (WAXS) is typically used to measure the average spacing between layers of atoms of small-molecule crystals. When an X-ray beam passes through a crystalline sample, it will be scattered by the orderly periodic atomic array of the crystal. The scattered light will form a diffraction pattern, which is then recorded by the instrument (Figure 2.7).

Bragg's law was used to explain the X-ray diffraction pattern, derived by the English physicists Sir W. H. Bragg and his son, Sir W. L. Bragg, who were awarded the Nobel Prize in physics in 1915 for their work. Bragg's law demonstrated that the space between the diffracting planes of atoms determines the peak position or diffracting angle, and is expressed as:

$$n\lambda = 2d \sin \theta \tag{2.8}$$

where λ is the wavelength of the incident X-ray beam, d is the spacing between the layers of periodic atomic array, and θ is the angle of incidence at which the diffraction occurs. A simple model is shown in Figure 2.8 to illustrate Bragg's law. When the incident X-ray beams labeled as 1 and 2 are scattered by atoms in adjacent layers, the scattered beams can exhibit constructive interference when the light path difference OA + OB is an integer multiple of the wavelength of the incident X-ray (Figure 2.8). Since $OA = OB = dsin\theta,\ OA + OB = 2\sin\theta = n\lambda$ (Figure 2.8).

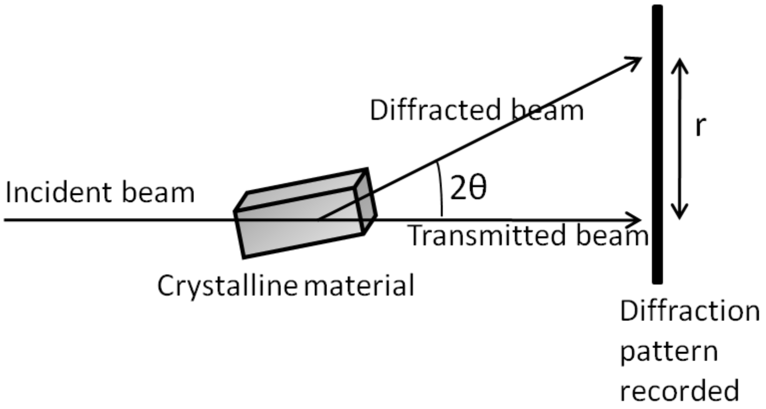

Figure 2.7. Schematic diagram of the X-ray diffraction process.

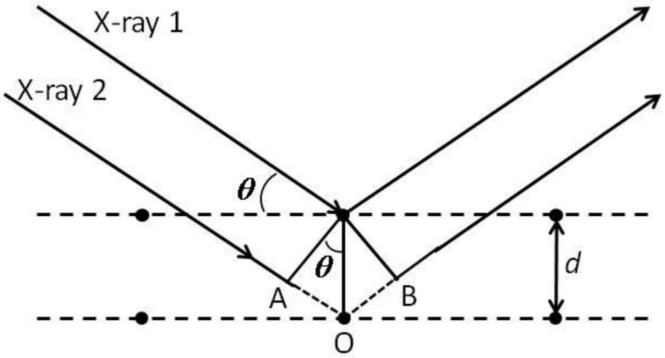

Figure 2.8. A simple model of the derivation of Bragg's law. Constructive interference occurs only when $OA + OB = n\lambda$, where n is integer.

WAXS has been used to study the structures of semi-crystalline polymers or liquid crystalline polymers for decades.[7,8] In comarison with small molecular crystals, polymeric crystals are generally less ordered and contain some non-crystalline defects, which may be subject to changes of temperature, pressure, chain defects, and other factors. Those defects in the polymeric crystals cause their diffraction patterns to be more complex than those of small molecules. In this thesis, isotropic powder was obtained from solutions of cylindrical micelles by centrifugation and drying. The supernatant was decanted after the centrifugation and the residue was transferred to a glass plate and allowed to dry under vacuum. Only the magnitude of the mesogen spacing is of interest here, and this was calculated according to Bragg's law using θ obtained from the instrument.

References

(1) Staurt, B. H. *Polymer Analysis*; Wiley: Chichester, **2002**.

(2) Bovey, F. A. M., P.A. *NMR of Polymers*; Academic Press: San Diego, **1996**.

(3) Sadao, M. H., G. Barth *Size Exclusion Chromatography*; Springer: New York, **1999**.

(4) Magonov, S. N. W., M.-H. *Surface Analysis with STM and AFM*; VCH: Weinheim, **1996**.

(5) Born, M. W., E. *Principles of Optics*; Cambridge Univ. Press: Cambridge, U.K., **1999**.

(6) Berne, B. J. P., R. *Dynamic Light Scattering: With Application to Chemistry, Biology and Physics*; Wiley: New York, **1976**.

(7) Vonk, F. J. B.-C. a. C. G. *X-ray Scattering of Synthetic Polymers*; Elsevier Science Publishers B.V.: New York, **1989**; Vol. 8.

(8) Alexander, L. E. *X-Ray Diffraction Methods in Polymer Science*; John Wiley & Sons, Inc.: New York, **1969**.

Chapter 3

Mesogen-Driven Formation of Triblock Copolymer Cylindrical Micelles with Sparse Coronal Chains

3.1 Introduction

Cylindrical micelles have many potential applications. They are particularly suitable for drug delivery applications because their circulation times, in animals, are much longer than those of spherical micelles.[1] They have also been shown to be superior to spherical micelles when used to toughen plastics.[2] Core-shell-corona cylindrical micelles of block terpolymers are of fundamental interest. For example, crosslinking the intermediate shell yields “permanent” nanofibers, which can be viewed as a macroscopic counterpart of polymers chains.[3] The study of the dilute solutions of block copolymer nanofibers has helped validate the classical viscosity[4,5] and light scattering theories[6,7] of wormlike polymer chains at a different size scale. The decomposition of the cores of these triblock copolymer nanofibers yields nanotubes,[8-10] whose tubular cavities can subsequently be filled with magnetic and semi-conducting inorganic nanoparticles yielding solvent-dispersible polymer/inorganic hybrid nanofibers. [11-13]

Despite their utility and interesting properties, cylindrical micelles can be difficult to obtain, even from coil-coil diblock copolymers. This difficulty is encountered because cylindrical micelles form only within a narrow block copolymer composition window.[14-18] Core-shell-corona cylindrical micelles are even more difficult to obtain from coil-coil-coil block terpolymers,[19-21] because these polymers can form segmented cylinders,[22-25] looped cylinders,[26] helical cylinders,[27-29] and Janus cylinders[30-32] beside core-shell-corona cylinders. Manners, Winnik, and coworkers discovered that cylindrical micelles[33] were readily prepared from block copolymers bearing crystalline blocks, and this led to many other wonderful applications[34-37] arising from this crystallization-driven micellization process. With this in mind, we were curious if a liquid crystalline block, possessing a weaker ordering driving force than a crystalline block, could be used to direct block copolymer-based cylindrical micelle formation, and thus initiated this investigation. Reported in this chapter is our success in this venture.

For this project four block terpolymers were designed, synthesized, and characterized, and these included $B_{53}C_{44}F_{13}$, $B_{105}C_{86}F_{19}$, $A_{53}C_{44}F_{13}$, and $A_{105}C_{86}F_{19}$, respectively. Here A, B, C, and F denote poly(acrylic acid), poly(*tert*-butyl acrylate), poly(2-cinnamoyloxylethyl methacrylate), and poly(perfluorooctylethyl methacrylate), respectively. The chemical structure of the ACF block terpolymer is shown in Scheme 3.1. The subscripts refer to the repeat unit numbers for the different blocks. The ACF polymers were derived from the BCF polymers via the selective hydrolysis of the B blocks. The F blocks were chosen because the rod-like perfluorooctyl (FO) groups were known to form a smectic A phase at room temperature.[38-41] Meanwhile, the C blocks were used because they could be photo-crosslinked if required for later applications.[42]

Our study has so far indicated that $B_{53}C_{44}F_{13}$, $A_{53}C_{44}F_{13}$, and $A_{105}C_{86}F_{19}$ readily formed cylindrical micelles in various selective solvents for the A or B blocks. Also, evidence gathered so far suggests that the formation of a liquid crystalline phase from the F blocks has been the main driving force for this micellization process. Interestingly, the cylindrical MAs of these copolymers all show rugged surfaces in the dry state, which is due to their sparsely-distributed corona chains. We also demonstrate that these structures are thermodynamically stable. For traditional thermodynamic micelles or MAs, their surface will always be fully covered by the solvent-selective block, so that the interfacial energy between the core block and solvent would be minimized. Thus, the sparse distribution of the corona chains provides additional evidence that the formation of the cylindrical structures is mesogen-driven. We believe these findings are unique and interesting.

The micellization of block terpolymers containing fluorinated blocks has been reported by various groups.[22,41,43,44] The micellization of poly(perfluorooctylethyl methacrylate)-bearing[45] or poly(perfluorohexylethyl methacrylate)-bearing[46,47] diblock copolymers has also been studied. Despite past studies, we do not believe that the strong morphology-directing effect, as observed by us, has been reported for a fluorinated block.

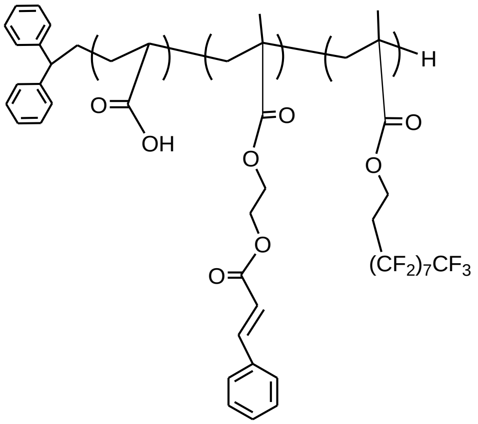

Scheme 3.1. Structure of the triblock copolymer abbreviated as ACF.

3.2 Experimental

Materials. Anhydrous diethyl ether (99.9%), chloroform (99.9%), methanol (99.8+%), and isopropanol (99.5%) were purchased from Fisher Scientific and were used without further purification. Ethanol (95%) was purchased from Commercial Alcohols and used as received. THF was purchased from Sigma-Aldrich and distilled over sodium and benzophenone before use. The initiator *sec*-butyllithium (1.3 M in cyclohexane) and the monomers *tert*-butyl acrylate (98%), perfluorooctylethyl methacrylate (FOEMA) (97%) were obtained from Aldrich. 1,1-Diphenylethylene was purchased from PCI. Cinnamoyl chloride (98%, predominantly *trans*), hexafluorobenzene (99.5%), triethylsilane (99%), trifluoroacetic acid (99%), and α,α,α-trifluorotoluene (TFT, 99%) were purchased from Aldrich and used as received. The staining agents osmium tetroxide (OsO_4) and uranium acetate dihydrate ($UO_2(Ac)_2$ $2H_2O$) were purchased from Electron Microscopy Sciences and were used without further purification. Pyridine (Fisher Scientific) was refluxed and distilled over CaH_2 under nitrogen.

Polymer Synthesis. The precursors to the BCF terpolymer were prepared by the sequential living anionic polymerization[48] of *tert*-butylacrylate (tBA),[49] 2-trimethylsiloxyethyl methacrylate (HEMA-TMS),[42,50] and perfluorooctylethyl methacrylate (FOEMA)[51] in THF at -78 °C. The initiator used was 1,1-diphenyl-3-methylpentyllithium, which was generated *in situ* from the reaction of *sec*-butyllithium with 1.3 molar equivalents of 1,1-diphenylethylene.[52] The polymerization time used for each block was 3 h. HEMA-TMS was prepared and purified following a literature method,[42,50] and tBA was initially distilled over CaH_2, and then over triethylaluminium. FOEMA was purified by distillation over CaH_2 before use. The trimethylsilyl protecting group was removed from the P(HEMA-TMS) block to yield poly(2-hydroxyethyl methacrylate) (PHEMA) by stirring the PtBA-*b*-P(HEMA-TMS)-*b*-PFOEMA terpolymer in THF/methanol/water (v/v/v = 30/13/5) overnight. The BCF samples were obtained by reacting PtBA-*b*-PHEMA-*b*-PFOEMA with cinnamoyl chloride,[42] at 1.5 molar equivalents relative to the PHEMA hydroxyl groups, and subsequently purified by precipitation from methanol/water = 9/1, v/v. The selective hydrolysis of the B block was achieved by treating the BCF terpolymer in dichloromethane with trifluoroacetic acid,[53] yielding the ACF terpolymer.

Micelle Preparation. Micelles were prepared by directly dispersing a polymer at 1.0 mg/mL at 70 ^{o}C for 2 h into a mixture consisting of α,α,α -trifluorotoluene (TFT) and methanol (MeOH), ethanol (EtOH), or isopropanol (iPOH). The dispersion was then cooled stepwise by 5 ^{o}C increments, and maintained for 30 min at each newly-set temperature until it reached room temperature.

Size Exclusion Chromatography (SEC) and Nuclear Magnetic Resonance (NMR) Spectroscopy. The molecular weights and polydispersity indices of the polymers used were determined by an Agilent size-exclusion chromatograph (SEC) system equipped with a Wyatt Dawn Helios-II light scattering detector, and an Optilab rEX refractive index detector. The wavelength of the light source was 658 nm for both detectors. The SEC columns used were Waters Styragel HR 5E, HT 4E and μ-Styragel HT 500 Å. The system was calibrated with monodisperse polystyrene standards. Chloroform was used as the eluent, at a flow rate of 1.0 mL/min. The ratios between the numbers of repeat units for the different blocks were determined in deuterated pyridine or hexafluorobenzene from ^{1}H NMR by comparing the ratios of the integrals of the appropriate proton peaks from the different blocks in both spectra.

Dynamic Light Scattering (DLS). DLS measurements were carried out at 90 ℃ using a Brookhaven BI-200 SM instrument equipped with a BI-9000AT digital correlator and a He-Ne laser (632.8 nm). To obtain the hydrodynamic diameter (d_h) of an $A_{105}C_{85}F_{19}$ micelle sample in TFT/MeOH at a TFT weight fraction (f_{TFT}) of 44% at different temperatures, the temperature was decreased by increments of 5 °C. This was done by regulating the temperature of a circulating water bath, which was used to thermostat the sample holder. After each temperature decrease, the micelles were allowed to equilibrate for 8 h and reach their new sizes before DLS measurements were recorded. The data were treated by a Cumulant method[54] to determine the hydrodynamic diameters (d_h) of the particles and their polydispersity, K_2^2/K_4. The refractive index (n_r) of a TFT/MeOH mixture was estimated from:[55]

$$n_r = n_{r1}f_{MeOH} + n_{r2}(1 - f_{MeOH}) \tag{3.1}$$

where n_{r1} and n_{r2} are the refractive indices of MeOH and TFT, respectively. The refractive indices were considered to remain constant across the temperatures tested. The viscosity (η) of a solvent mixture was calculated[56] using the relationship:

$$ln\eta = \phi_1 ln\eta_1 + \phi_2 ln\eta_2 \tag{3.2}$$

with η_1 and η_2 representing the viscosities of Solvents 1 and 2, respectively. Meanwhile, $\phi_1$and ϕ_2 represented the molar fractions of Solvents 1 and 2. The viscosities of TFT and MeOH at different temperatures were retrieved from literature sources.[57,58]

Transmission Electron Microscopy (TEM). Specimens for transmission electron microscopy (TEM) were prepared by aero-spraying micellar solutions onto carbon-coated copper grids using a home-built device.[59] To stain the PCEMA domains, the specimens were equilibrated with OsO_4 vapor for 1 h before TEM observation. To stain the PAA domains, a specimen was equilibrated with one drop of a 20 mg/mL $UO_2(Ac)_2$ solution in MeOH for 20 min. After the residual solution was gently wiped off with filter paper, the excess staining agent was rinsed with MeOH droplets, which were applied by a disposable pipette and gently wiped off with filter paper, five times in succession. Images were recorded using a Hitachi-7000 instrument operated at 75 kV.

Wide-angle X-ray Scattering (WAXS) and Differential Scanning Calorimetry (DSC). $A_{105}C_{86}F_{19}$ cylindrical micelles (10 mL at 3.0 mg/mL) in TFT/MeOH solvent mixtures at f_{TFT} = 44% and 10% were settled by ultracentrifugation at 17,000 *g* for 10 min. The settled cylinders were then separated from the supernatant by decantation.

For wide-angle X-ray scattering (WAXS) measurements, the settled cylinders were transferred onto a glass holder to form a thin film. The sample was then vacuum-dried at room temperature for 48 h. WAXS analysis was performed at room temperature on a Rigaku Ru 200b instrument using the Cu Kα radiation at $\lambda = 0.15418$ nm.

For differential scanning calorimetric (DSC) studies, the settled cylinders (~3 mg) were vacuum-dried and then transferred to a Tezo pan before measurement. A bulk $B_{105}C_{86}F_{19}$ sample was prepared by evaporating a TFT solution of the polymer in an aluminum-foil-covered Tezo pan over three days and then drying the sample under vacuum overnight. DSC analyses were performed on a Q2000 series TA instrument at a heating rate of 5 ^{o}C/min, and the samples were heated from 0 to 100 ^{o}C. The traces reported were those from the first heating cycle to confirm that the liquid crystalline phase already existed in the as-prepared dried samples.

Atomic Force Microscopy (AFM). Specimens were prepared by aero-spraying micellar solution samples onto silicon surfaces. All samples were analyzed by tapping-mode AFM using a Veeco multimode instrument equipped with a Nanoscope IIIa controller.

X-Ray Photoelectron Spectroscopy (XPS). X-ray photoelectron spectroscopic **(**XPS) measurements were performed using a Thermo Instruments Microlab 310F surface analysis system (Hastings, U.K.) under ultrahigh vacuum conditions, using a Mg Kα X-ray source (1486.6 eV) with a 15 kV anode potential and a 20 mA emission current. Scans were acquired in the Fixed Analyzer Transmission (FAT) mode, with a pass energy of 20 eV and a surface/detector take-off angle of 75 °. All spectra were calibrated to the C 1s line at 285.0 eV. The same method that was used to prepare samples for WAXS and DSC measurements was also used to procure the powder samples used here. The settled cylinders (~15 mg) were transferred onto a cover glass to form a thin layer, and subsequently dried under vacuum for 48 h. The cover glass was then mounted on the sample holder before analysis.

3.3 Results and Discussion

3.3.1 Triblock Copolymer Characterization.

Four samples, including the $A_{105}C_{86}F_{19}$, $A_{53}C_{44}F_{13}$, $B_{105}C_{86}F_{19}$, and $B_{53}C_{44}F_{13}$ terpolymers were used in this study. Since the ACF terpolymers were derived from the BCF terpolymers,[53] only $B_{105}C_{86}F_{19}$ and $B_{53}C_{44}F_{13}$ were characterized.

Table 3.1 shows the characteristics of the $B_{105}C_{86}F_{19}$ and $B_{53}C_{44}F_{13}$ terpolymers. The ratios between the repeat unit numbers of different blocks ($l/m/n$) were obtained by ^{1}H NMR analysis by comparing the signal integrations corresponding to the B, C, and F blocks. The weight- and number-average molecular weights (M_w and M_n) and polydispersity indices (M_w/M_n) were obtained from SEC analysis, which was calibrated with polystyrene standards. The number-average repeat unit numbers l, m, and n for the B, C, and F blocks, respectively, were calculated using the corresponding$l/m/n$ values obtained by ^{1}H NMR analysis and the M_n values obtained by SEC analysis. These l, m, and n values matched reasonably closely with their targeted values which were 120, 100, and 22, respectively, for $B_{105}C_{86}F_{19}$, and were 65, 54, and 16 for $B_{53}C_{44}F_{13}$.

The B and F block weight fractions (w_B and w_F, respectively) were calculated to be 29% and 22%, respectively, for $B_{105}C_{86}F_{19}$, based on the l, m, and n values. Meanwhile, w_B and w_F were found to be 27% and 27%, respectively, for $B_{53}C_{44}F_{13}$. For $A_{105}C_{86}F_{19}$, the weight fraction of the A block (w_A) was calculated to be 19%, while w_F

was calculated as 25%. These values changed to 17% and 31%, respectively, for $A_{53}C_{44}F_{13}$.

Table 3.1. Molecular characteristics of the BCF terpolymer samples.

Terpolymer	SEC M_n (g/mol)	SEC M_w/M_n	^{1}H NMR $l/m/n$	l	m	n	w_B	w_F
$B_{105}C_{86}F_{19}$	4.6×10^4	1.04	5.5/4.5/1.0	105	86	19	29%	22%
$B_{53}C_{44}F_{13}$	2.6×10^4	1.04	4.1/3.4/1.0	53	44	13	27%	27%

3.3.2 Solubility Test for the Polymer Blocks

To further understand the solubility of each terpolymer block, the solubilities of homopolymers with identical chemical compositions and similar molecular weights as their corresponding blocks were tested. All of the homopolymers were synthesized by anionic polymerization. The refractive index increments and weight average molecular weights of the homopolymers were determined using the batch-mode of a Wyatt Optilab rEX refractive index detector and a Wyatt Dawn Helios-II light scattering detector, respectively. The measurements were performed in chloroform for the B and C homopolymers (*h*B and *h*C, respectively), while the F polymer (*h*F) was measured in TFT. Results were summarized in Table 3.2.

Table 3.2. Characteristics of the homopolymers used for the solubility tests.

Homopolymer	dn_r/dc (mL/g)	M_w/M_n	SEC-LS M_w g/mol	Number of repeating units
hB	0.053	1.05	1.4×10^4	105
hC	0.163	1.02	5.0×10^4	190
hF	-0.028	-	7×10^3	14

The solubility tests were performed in pure solvents or solvent mixtures of TFT and MeOH. Visual inspection revealed that the hB_{105} homopolymer was soluble in a TFT/MeOH mixture with f_{TFT} ranging from 0 to 100%. The hC_{190} homopolymer, however, was insoluble in TFT/methanol in the full range of f_{TFT}.

Table 3.3. Solubility tests for various homopolymers in TFT and MeOH.

Homopolymer	hA	hB	hC	hF
TFT	Insoluble	Soluble	Insoluble	Soluble
MeOH	Soluble	Soluble	Insoluble	Insoluble
TFT/MeOH mixtures	Insoluble when $f_{TFT} > 65\%$	Soluble	Insoluble	Insoluble when $f_{TFT} < 74\%$

To determine f_{TFT}, below which hF became insoluble, the following protocol was used. The hF homopolymer was firstly dissolved in TFT, and then MeOH was slowly added into the solution. The value of f_{TFT} was determined to be 74% when the solution became turbid. Similarly, hA (derived from hydrolysis of hB) was initially dissolved in MeOH, and TFT was then slowly added into the solution. It was determined that when $f_{TFT} > 65\%$, when hA became insoluble. The results of these solubility tests are summarized in Table 3.3.

3.3.3 Facile Formation of Cylindrical Micelles.

The micelles of the ACF terpolymers were prepared by initially dispersing the ACF terpolymer into TFT/MeOH at 70 ^{o}C, which was selective towards the A block. The dispersion was then cooled to room temperature. The samples were initially heated to 70 ^{o}C, so that the F block was in the isotropic phase.[60] The samples were slowly cooled, providing sufficient time for the F block to form a liquid crystalline phase.

The ACF copolymers were directly dispersed into TFT/MeOH, rather than being dissolved into a solvent that was good for all of the blocks, because such a solvent could not be found. The homopolymer solubility tests (Table 3.3) indicated that F became insoluble in TFT/MeOH after the TFT volume fraction f_{TFT} was decreased below ~74%.

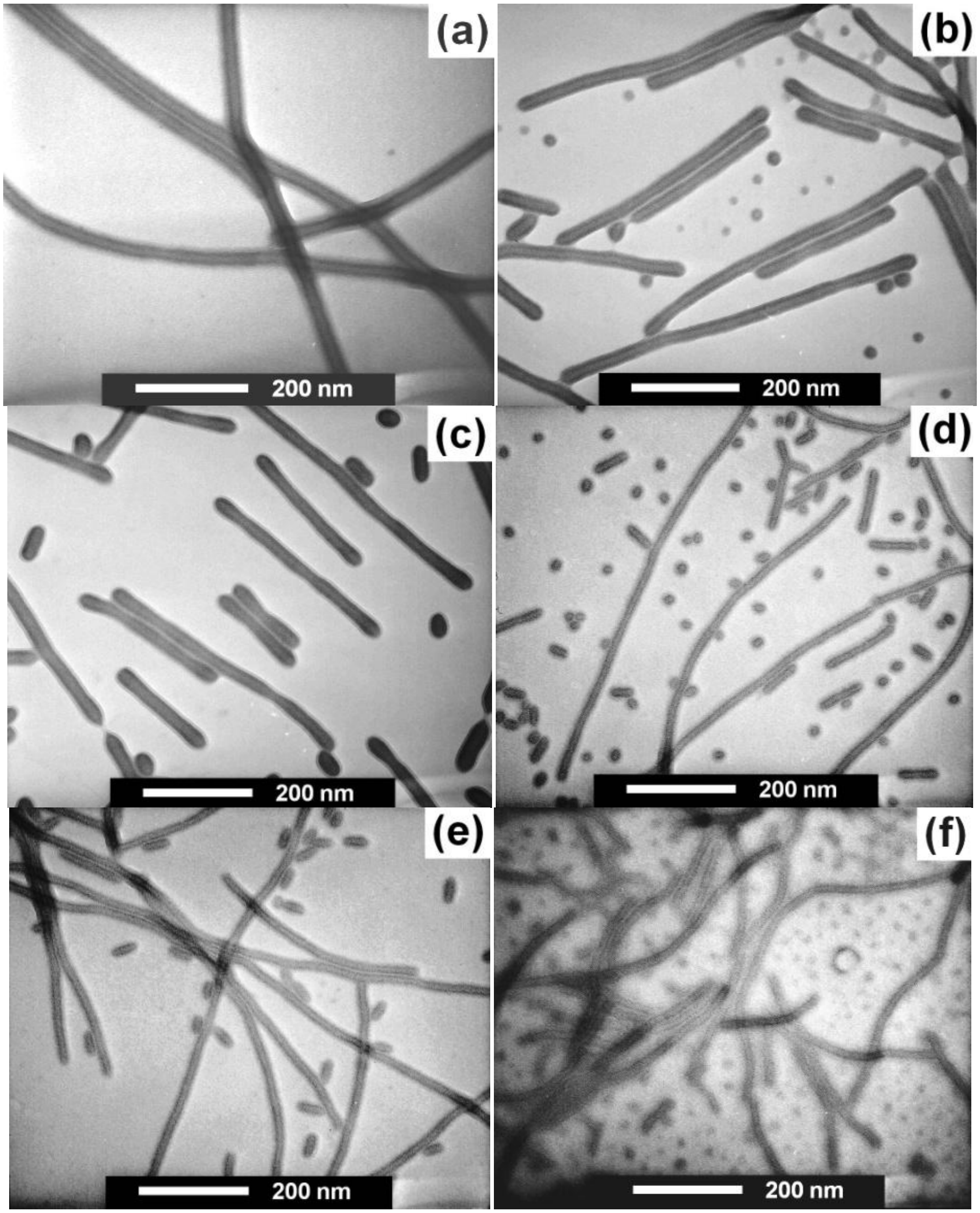

Figure 3.1. TEM images of $A_{105}C_{86}F_{19}$ (a-c) and $A_{53}C_{44}F_{13}$ (d-f) micelles that were aero-sprayed from TFT/MeOH. Images (a), (b), and (c) show $A_{105}C_{86}F_{19}$ micelles that were sprayed from TFT/MeOH at f_{TFT} =44%, 30% and 10%, respectively. Images (d), (e), and (f) show $A_{53}C_{44}F_{13}$ micelles that were sprayed from TFT/MeOH mixtures at f_{TFT} = 44%, 30%, and 10%, respectively. The samples were prepared by a slow cooling method and were stained with OsO_4.

Shown in Figure 3.1 are the TEM images of the aero-sprayed cylindrical micellar samples of the $A_{105}C_{86}F_{19}$ and $A_{53}C_{44}F_{13}$ terpolymers. All of the micelles seemed to have a core-shell-corona structure. In the TEM images the core appeared gray, the shell was dark, and the corona was also gray, and visible only in certain sections. Since the samples were stained with OsO_4, which reacted selectively with the C double bonds, the dark shell consisted of the C block. The F blocks must have formed the cores because they were insoluble under these solvation conditions. Meanwhile, the A block apparently constituted the ill-defined corona.

Previous studies of micelles formed from coil-coil diblock copolymers[14,15,61] and coil-coil-coil block terpolymers[62] have revealed that an increase in the block-selective content of a binary solvent mixture normally causes a micellar morphological transition. This occurs because the interfacial tension between the solvent and the insoluble cores of the core-corona diblock copolymer micelles, or between the solvent and the shells of the triblock core-shell-corona micelles, increases with the block-selective solvent content. The increased interfacial tension initially causes the micelles to expand, and eventually leads to a morphological transition, because the core and corona chains become more stretched and energetically unstable in the larger micelles.

The cylindrical morphology of the ACF polymers was insensitive to the f_{TFT} changes. Two factors could be responsible for the stability of the cylindrical micelles of these polymers. Firstly, the interfacial tension between the C shell and the solvent phase probably changed little among the different solvent mixtures, because the C block dissolved in neither TFT nor any of the alcohols. Secondly, the liquid crystalline phase formation of the F block dictated the morphology of the ACF micelles, so that this morphology was not readily altered by varying the block-selective solvent composition.

We believe that the second factor had greater influence on the stability of the cylindrical micelles of ACF, because f_{TFT} variation did trigger a morphological transition among the $B_{105}C_{86}F_{19}$ micelles in TFT/MeOH (discussed later in Section 3.3.12 and Figure 3.18). This effect was unleashed in the $B_{105}C_{86}F_{19}$ system probably because this polymer had the lowest F block weight fraction and the highest soluble block weight fraction. Therefore this system had the lowest driving force for liquid crystalline phase formation. Furthermore, mesogen-driven formation of cylindrical[63,64] and vesicular micelles[63,65] has been observed for diblock copolymers bearing multi-phenyl rod-shaped liquid crystalline pendant groups.

For coil-coil diblock copolymers, a decrease in the weight fraction of the soluble block can also trigger a morphological transition.[14,61,66] This is also true for coil-coil-coil block terpolymers.[21] The same cylindrical morphology was observed for $A_{53}C_{44}F_{13}$, $A_{105}C_{86}F_{19}$, and $B_{53}C_{44}F_{13}$ (which will be discussed later in section 3.3.12 and Figure 3.19) under all tested conditions despite the differing soluble block weight fractions of 17%, 19%, and 27%, respectively. This may be again due to mesogen-driven formation of cylindrical micelles.

3.3.4 Mesogen-Ordering of the Core-Forming F Block.

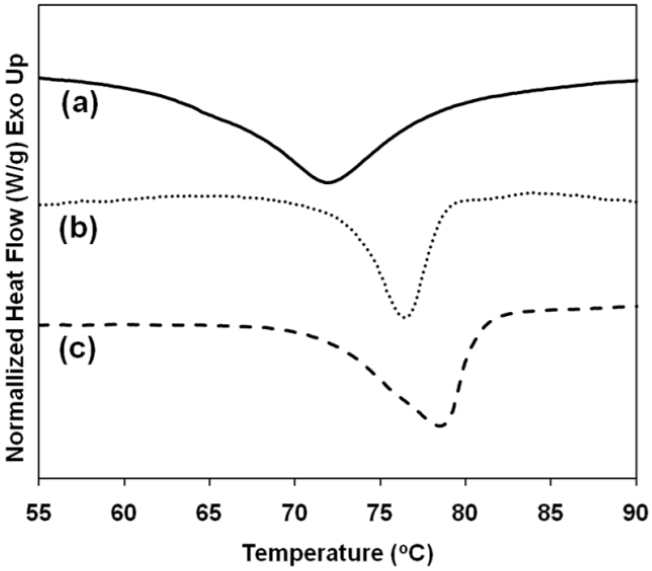

Figure 3.2. DSC traces of a bulk $B_{105}C_{86}F_{19}$ sample (a), and of $A_{105}C_{86}F_{19}$ micelles that were centrifuged from TFT/MeOH at f_{TFT} = 44% (b) and 10% (c) and subsequently vacuum-dried at room temperature. The well depths of the DSC traces were normalized to facilitate shape comparison.

Figure 3.2 compares the first-heating DSC traces of a bulk $B_{105}C_{86}F_{19}$ sample and those of $A_{105}C_{86}F_{19}$ micelles that were centrifuged from TFT/MeOH solvent mixtures at f_{TFT} = 44% and 10%, and subsequently dried. In each case, an endothermic peak was observed near 76 °C, which is the reported smectic A-to-isotropic phase transition temperature for the F block.[38] Therefore, the F block of the dried cylindrical micelle samples and of the bulk sample existed as a liquid crystalline phase at room temperature.

Our quantitative analysis of the DSC traces yielded enthalpy values of 3.2, 4.3, and 7.6 J/g of F (for the F block alone) for the phase transitions of the bulk $B_{105}C_{85}F_{19}$ sample and the $A_{105}C_{86}F_{19}$ micelles settled from TFT/MeOH at f_{TFT} = 44% and 10%, respectively. These values are comparable to those reported by Ober and coworkers[39,40] among polymers bearing perfluorooctyl groups. They are, however, much smaller than the melting enthalpies of crystalline polymers. Linear polyethylene, for example, exhibits decreasing melting enthalpies, ranging between 30 and 69 J/g, as its molecular weight is decreased.[67]

Among the three samples, the bulk $B_{105}C_{85}F_{19}$ sample had the lowest formation enthalpy and the broadest phase transition peak for its liquid crystalline phase. These suggest a less complete segregation of the F block, and a broader size distribution for the F domains in this sample than for those in the other samples. The less-defined block segregation observed for the bulk sample was reasonable, because this sample was prepared by evaporating a $B_{105}C_{85}F_{19}$ solution from TFT. Both the F and B blocks were solvated by TFT, and thus they were probably not well-segregated from one another.

A study on the bulk morphologies of $B_{105}C_{85}F_{19}$ and $B_{53}C_{44}F_{13}$ was performed on film slowly evaporated from TFT solutions of the corresponding copolymers. Results and discussion on the bulk morphologies were given in Section 3.3.13. The F and B blocks segregated from one another during solvent evaporation in bulk state. As the polymer concentration and matrix viscosity increased, the block segregation could become kinetically hindered, leading to incomplete block segregation and a broad F domain size distribution. In constrast, the F blocks of the micellar samples were already segregated from the other blocks, even before the solvent was evaporated.

We further note that the formation enthalpy was lower for micelles settled from TFT/MeOH mixtures with f_{TFT} = 44% than those with f_{TFT} = 10%. This probably arose due to the partial memory retained of the loosely-held and less ordered packing of the F phase in the TFT/MeOH solvent mixture at f_{TFT} = 44%. The lower liquid crystalline phase stabilization energy and its change with f_{TFT} clearly explain why the $B_{105}C_{86}F_{19}$ cylindrical micelle underwent morphological changes (Section 3.3.12) as f_{TFT} was increased in the TFT/MeOH solvent mixture.

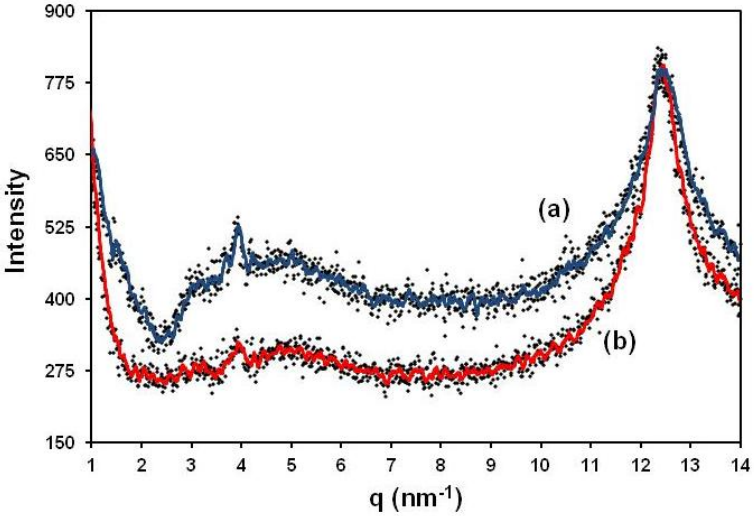

Figure 3.3. WAXS data of $A_{105}C_{85}F_{19}$ in TFT/MeOH mixtures at f_{TFT} = (a) 44% and (b) 10%. Samples were prepared by a slow cooling method.

Both bulk and thin film structures of diblock copolymers analogues containing F block have been studied with WAXS previously, and the F block are known to be liquid crystalline in the solid state.[38] Figure 3.3 shows WAXS spectra of the dried $A_{105}C_{86}F_{19}$ cylindrical micelles that were settled from TFT/MeOH solvent mixtures at f_{TFT} = 44% and 10%. Each sample showed a peak at q = 12.3 nm^{-1}, where q is the scattering vector length and given by Equation 3.3.

$$q = 4\pi sin\theta/\lambda \tag{3.3}$$

where θ is the angle of scattered light and λ is the wavelength of the incident light. The interplanar spacing d of the liquid crystalline structure of F block can be obtained from Equation 3.4.

$$d = 2\pi/q \tag{3.4}$$

Thus, according to Equation 3.4, q of 12.3 nm^{-1} was corresponding to a periodic spacing d of 0.51 nm. This value was similar, within experimental error, to the spacing of 0.50 nm reported by Al-Hussein et al.[38] for the average perfluorooctyl (FO) spacing in a smectic A layer (Scheme 3.2), thus confirming unambiguously that the F block formed a liquid crystalline phase in the both the dry cylindrical micelles and probably also in the solvated cylindrical micelles.

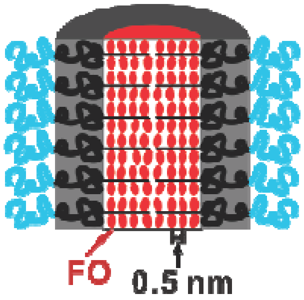

Scheme 3.2. Schematic drawing showing the packing of the perfluorooctyl (FO) units in the smectic A layers and the average spacing between the different FO units.

3.3.5 Core and Shell Dimensions

The $A_{105}C_{86}F_{19}$ and $A_{53}C_{44}F_{13}$ micelles prepared from TFT/MeOH were closely investigated. We measured the core and shell diameters of more than 70 cylinders for each sample and obtained their average diameters and their deviations. These diameters are shown in Table 3.4 for selected samples. Table 3.4 shows that the core diameters of the $A_{53}C_{44}F_{13}$ or $A_{105}C_{86}F_{19}$ cylindrical micelles were constant at ~8 and ~11 nm, respectively, regardless of f_{TFT} or changes to the binary solvent combination. Due to the large size of the pendant FO groups, the F blocks should be almost fully stretched. With 19 and 13 repeat units, the F blocks should have the end-to-end distances of 4.8 and 3.3 nm, respectively. These were comparable with, but slightly smaller than, the corresponding TEM radii of 5.5 and 4 nm, suggesting that only the longer chains stretched to the centers of the cylindrical micellar cores.

Table 3.4. TEM diameters of cylindrical micelles sprayed from different TFT/selective solvent mixtures.

Solvent Core	f_{TFT}	Core Diameter (nm)	Shell Diameter (nm)	Overall Diameter (nm)
$A_{105}C_{86}F_{19}$ Cylindrical Micelles				
TFT/MeOH	10%	11 ± 2	23 ± 2	32 ± 4
TFT/MeOH	30%	11 ± 2	24 ± 2	36 ± 3
TFT/MeOH	44%	12 ± 2	24 ± 2	33 ± 3
$A_{53}C_{44}F_{13}$ Cylindrical Micelles				
TFT/MeOH	10%	8 ± 2	13 ± 2	18 ± 3
TFT/MeOH	30%	8 ± 1	15 ± 2	21 ± 2
TFT/MeOH	44%	8 ± 1	13 ± 1	23 ± 2
$A_{105}C_{86}F_{19}$ Cylindrical Micelles				
TFT/EtOH	44%	12 ± 2	26 ± 2	
TFT/iPOH	44%	12 ± 2	26 ± 2	

Also based on the characteristic ratio of 12.6 for C recently reported by our group,[68] we calculated unperturbed root-mean-square end-to-end distances of 7.2 nm and 5.1 nm for the C blocks of $A_{105}C_{86}F_{19}$ and $A_{53}C_{44}F_{13}$, respectively. These calculations were based on Equation 3.5.

$$< r^2 >^{1/2} = \sqrt{2mC_\infty}\, l_0 \tag{3.5}$$

where $< r^2 >^{1/2}$ is the root mean square end-to-end distance, m is the number of repeating units of the C block, l_0 is the carbon-carbon bond length of a freely jointed single bond, which is usually taken as 0.154 nm. Meanwhile, C_∞ is the characteristic ratio of the C block. Using the core and shell diameters from Table 3.4, we calculated the average shell thicknesses of 6.0 and 3.0 nm, respectively, for the $A_{105}C_{86}F_{19}$ and $A_{53}C_{44}F_{13}$ cylindrical micelles.

To decrease the interfacial area between the core and shell, and also that between the shell and the solvent, the core, shell, and corona chains of coil-coil-coil triblock copolymer micelles are normally stretched radially relative to their unperturbed dimensions. As mentioned earlier, the F chains were indeed fully stretched in the cores of the ACF cylindrical micelles. The average respective shell thicknesses were 6.0 and 3.0 nm for the $A_{105}C_{86}F_{19}$ and $A_{53}C_{44}F_{13}$ cylindrical micelles, respectively. The unperturbed root-mean-square end-to-end distances for the C chains of $A_{105}C_{86}F_{19}$ and $A_{53}C_{44}F_{13}$ were calculated as 7.2 and 5.1 nm, respectively. Thus, the C chains were apparently compressed. Furthermore, the coronal chains were abnormally sparse (this will be discussed in greater details in Section 3.3.6). These trends suggest that the mesogen packing of the F chains dictated the formation of the cylindrical micelles and that the shell and corona did not maintain their typical thicknesses found in coil-coil-coil triblock copolymer micelles.

3.3.6 Cylinders Bearing Ridged Coronas.

Staining the coronal A chains of the ACF micelles with $UO_2(Ac)_2$ allowed their direct visualization by TEM. Figure 3.4 shows TEM images of $A_{105}C_{86}F_{19}$ micelles that were sprayed from TFT/MeOH solvent mixtures at f_{TFT} = 30% and 44%, respectively. Figure 3.5 displays the height and phase AFM images of the $A_{105}C_{86}F_{19}$ micelles sprayed from a TFT/MeOH solvent mixture at f_{TFT} = 10%. To our great surprise, the outer surfaces of these cylindrical micelles were not smooth but quite bumpy.

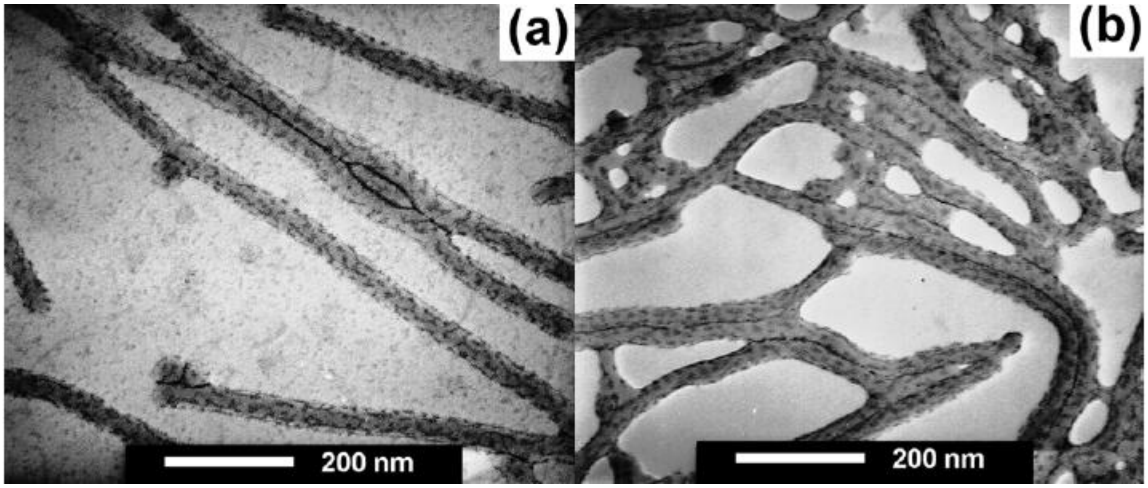

Figure 3.4. TEM images of $A_{105}C_{86}F_{19}$ micelles sprayed from TFT/MeOH solvent mixtures at f_{TFT} = 30% (a) and 44% (b). The samples were stained with $UO_2(Ac)_2$.

For conventional micelles or MAs of triblock copolymers, the micellar surfaces are normally fully covered by the coronal chains. The shell or core chains of a MA are usually shielded from the solvent by a brush layer of corona chains. Theoretically, this fully covered core-shell-corona structure will be favored since it can provide a lower interfacial energy between the solvent and the solvophobic shell or core blocks, and thus should provide a thermodynamically stable structure.

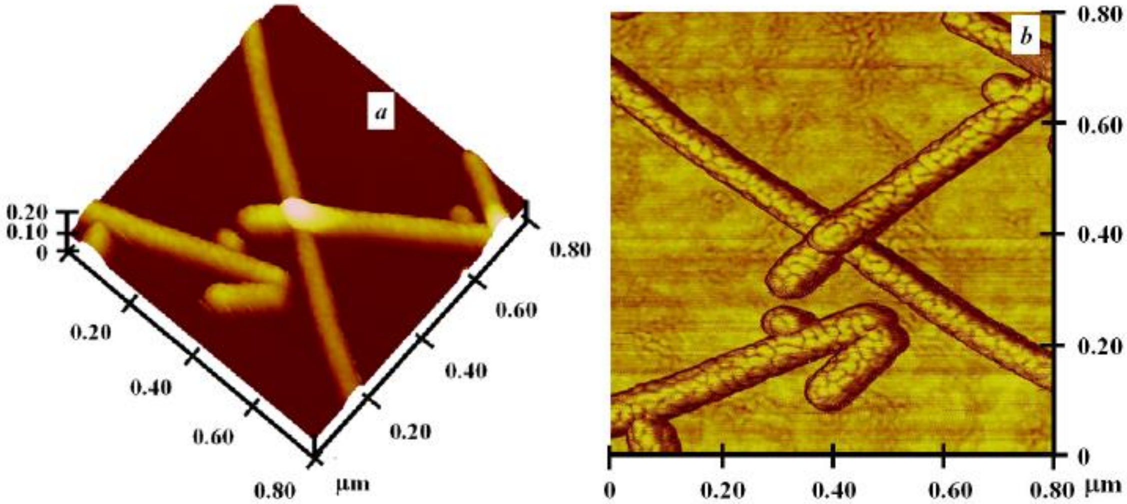

Figure 3.5. AFM topography (a) and phase (b) images of $A_{105}C_{86}F_{19}$ micelles sprayed from a TFT/MeOH solvent mixture at f_{TFT} = 10%.

Figure 3.4 and Figure 3.5 clearly show that the PAA chains formed ridges on the C shell of the dried ACF micelles. The ridges appeared wider in the AFM images than in the TEM images, due to contributions from the size of the AFM tip. This also explained why the AFM diameter of 73 ± 6 nm was larger than the corresponding TEM diameter, while the average AFM height of 30 ± 3 nm was comparable with the overall TEM diameter of 33 ± 3 nm (Figure 3.4) of the $A_{105}C_{86}F_{19}$ cylinders sprayed from a TFT/MeOH mixture at f_{TFT} = 10%.

If the PAA chains are distributed uniformly on the surfaces of the cylindrical MAs in the dry state, a uniform dark layer should be seen on the exteriors of the MAs.[69] The cylindrical MAs from $A_{53}C_{44}F_{13}$ showed the same rugged surface when stained with $UO_2(Ac)_2$ and characterized by TEM analysis (Figure 3.6). Another feature worth noting is that when the cylindrical MAs of $B_{105}C_{86}F_{19}$ (Figure 3.7) were characterized by AFM, they showed less rugged surfaces than the MAs of the $A_{105}C_{86}F_{19}$ and $A_{53}C_{44}F_{13}$ terpolymers. This might be due to the fact that a B chain occupies a much larger volume than an A chain, so that the surfaces of the cylindrical MAs were better covered by the B corona chains.

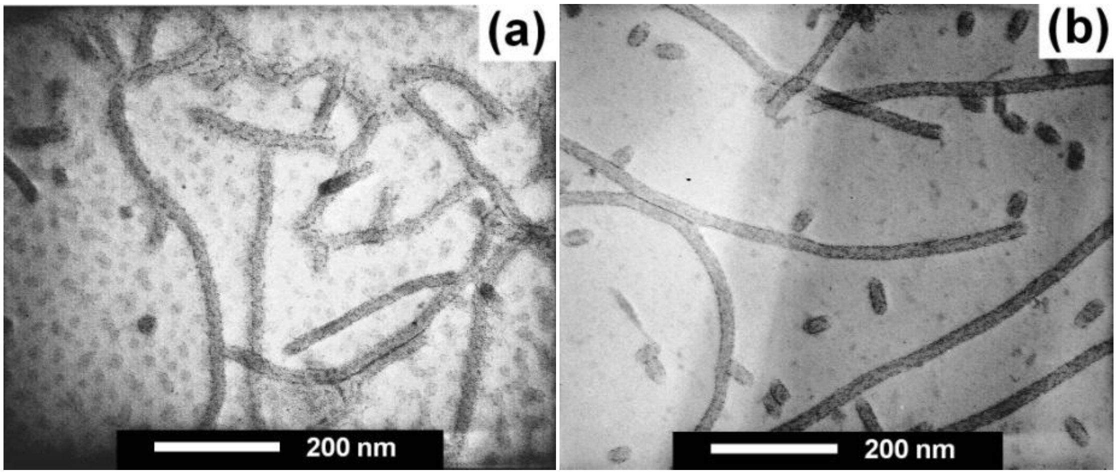

Figure 3.6. TEM images of $A_{53}C_{44}F_{13}$ micelles sprayed from TFT/MeOH solvent mixtures at f_{TFT} = 10% (a), and 30% (b). The TEM samples were stained with $UO_2(Ac)_2$.

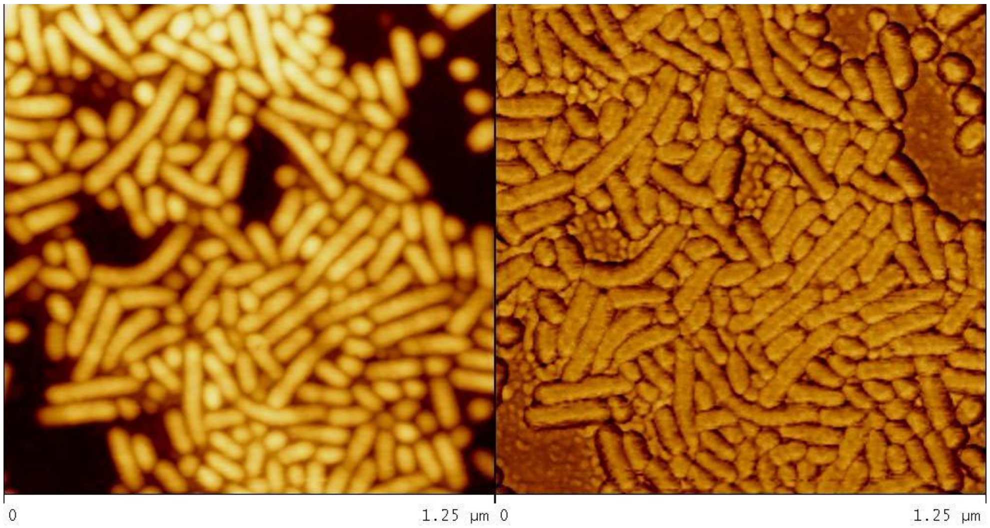

Figure 3.7. AFM images of $B_{105}C_{86}F_{19}$ micelles sprayed from a TFT/MeOH solvent mixture at f_{TFT} = 10%.

Two factors could have caused the coronal ridges to form. Firstly, the surface tension of the A block could be much larger than that of the C block. Also, the interfacial tension between the A and C domains was sufficiently large so that the A film dewetted the C shell. These factors would be very similar to those causing discrete domains, such as cylinders, to sometimes form in the solid state from the central block of a block terpolymer between the domains of the terminal blocks.[70,71] However, we reject this hypothesis, because uniform A layers have been observed covering C cylinders of AC diblock cylindrical micelles.[69,72]

Secondly, the coronal A chains were sparsely distributed, and thus could not form a continuous thin layer. The scarcity of the coronal chains could be readily appreciated by considering the following calculation: The F core of the $A_{105}C_{86}F_{19}$ micelles was ~11 nm (Table 3.4). Using the respective densities of 1.85,[73] 1.25,[6] and 1.0 g/cm^3 and respective weight fractions of 25%, 56%, and 19% for the F, C, and A blocks of dry $A_{105}C_{86}F_{19}$ micelles, we calculated, from geometric considerations, diameters of 22.8 and 26.3 nm for the core-shell cylinders and the core-shell-coronal cylinders, respectively. While the calculated value of 22.8 nm agreed with the observed TEM shell diameter of 23 ± 2 nm, the second number (26.3 nm) suggested that a uniform PAA layer would have been only 1.7 nm thick. This was much smaller than the calculated unperturbed root-mean-square end-to-end distance of 5.8 nm for the A chains, which have a characteristic ratio of 6.7.[74] Thus, the formation of a thin uniform layer, in this case, would have required substantial energy to compress the A chains.[75] Therefore, the A chains formed ridges on the surfaces of the C domain to avoid excessive configurational entropy loss. Thanks to ridge formation, the apparent diameter of the core-shell-corona cylinders was 32 ± 4 nm, which was thus larger than the anticipated diameter of 26.3 nm for cylinders possessing a hypothetical uniform A corona.

While there have been several reports on the formation of ridged coronas from the segregation of two types of chains on the surface of nanospheres,[76,77] it is rare to observe bump formation from one type of chain on nanoparticle surfaces.[78] To the best of our knowledge, this is the first report on the preparation of block copolymer cylindrical micelles possessing nanometer-scale surface roughness. This might be useful for the creation of super-hydrophobic and -oleophobic coatings[79,80] if block copolymer cylindrical micelles or nanofibers are ever used in such an application.[78]

3.3.7 "Grafting Density" Calculations

Due to the surprising finding of the ridged surfaces of the cylindrical MAs, we suspect that this behaviour might be related to the grafting density of the corona chains on the outer side of the cylindrical MAs. To test this, a calculation was performed based on Minko's study.[81] In this calculation the term polymer brush refers to a layer with densely grafted polymer chains. The reduced tethering density (Σ) is defined as

$$\Sigma = \sigma \pi R_g^2 \tag{3.6}$$

where R_g is the radius of gyration of a tethered chain under specific experimental conditions. Meanwhile, σ is the grafting density and is determined by:

$$\sigma = (h \rho N_A)/M_n \tag{3.7}$$

where h is the brush thickness (Figure 3.8a), ρ is the bulk density of the tethered polymer, N_A is Avogadro's number and M_n is the number average molecular weight of the tethered polymer. The term σ is sometimes determined in a simplified manner, using the equation:

$$\sigma = 1/D^2 \tag{3.8}$$

where D is the distance between the grafting points (Figure 3.8a).

The Σ term provides a reliable parameter to define the brush-like character of a grafted film. In practical terms, three regimes are recognized in brush formation (Figure 3.8b).[81]: The first regime is the mushroom regime, where $\Sigma < 1$, in which the grafted chains are distributed far apart from one another and interact weakly with each other. The second regime is the crossover regime or mushroom-to-brush transition regime, in which $1 < \Sigma < 5$, occurs when the grafted chains have an intermediate density. Meanwhile, the brush regime, where $\Sigma < 5$, occurs when the polymer chains are distributed very closely together so that they are highly stretched and interact strongly with each other.

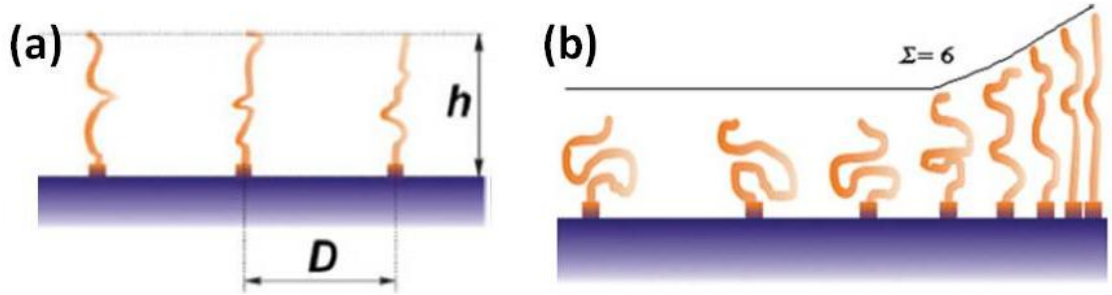

Figure 3.8. Image (a) shows characteristic parameters of a polymer brush. The term h represents the height of the grafted chains and D represents the distance between grafting points.81 Image (b) shows the transition between the mushroom regime and the true brush regime, as observed by Genzer et al.[81] when they changed the grafting densities of polyacrylamide brushes.

We carried out a simple calculation based on the the diameter of $A_{105}C_{86}F_{19}$ cylinders obtained from TEM images. From TEM negatives, thickness of F domain is 11 nm, C domain is 24 nm.

$$
\begin{aligned}
& m_F = \rho V = 1.847\ \mathrm{g/cm}^3 \times \pi \times (5.5\ \mathrm{nm})^2 L \\
& n_F = n_A = {m_F}\big/{M_F} = 1.847\ \mathrm{g/cm}^3 \times \pi \times (5.5\ \mathrm{nm})^2 L \big/ 532\ \mathrm{g/mol} \times 19 \\
& A_A = 2\pi r L / n_A = 2\pi \times (12\ \mathrm{nm}) L / n_A = 4.3e6\ \mathrm{m}^2/\mathrm{mol} \\
& \mathrm{R_n} = \sqrt{2nC_\infty l} : n = 105, l = 0.154nm, C_\infty = 6.7 \\
& \mathrm{R_G} = \mathrm{R_n} \big/ \sqrt{6} \\
& A^0 = N_A \pi R_G^2 = 1.2e7\ \mathrm{m}^2/\mathrm{mol} \\
& \therefore A^0 \big/ A_A \approx 2.8,
\end{aligned}
$$

We found that for $A_{105}C_{86}F_{19}$ and $A_{53}C_{44}F_{13}$, the grafting density of the A chains is near 2.8 and 1.6, respectively. According to the definition of a polymer bush by Brittain and Minko,[81] the A chains are in the mushroom-to-brush transition regime on the external surface.[81] This “crossover regime” means that the polymer chains attached to the substrate are not highly dense, and thus there is free space between adjacent brush chains so that the surface of the substrate is not fully covered by the brush layer.

This theoretical consideration agrees with our finding, that the C-based shell of the cylindrical MAs were not densely covered by the A corona chains. Thus, the proposed structure of the cylindrical micelles is a core-shell-corona structure, with the F block forming the core, the C block forming the shell and the A corona chains distributed sparsely on the surface of the cylinders. Scheme 2 depicts our proposed structure for the core-shell-corona cylindrical micelles. In the solvated state, the coronal A chains should stretch into the solvent phase, as depicted in Scheme 3.3a. Upon solvent evaporation, these chains collapsed and aggregated into ridges (Scheme 3.3b).

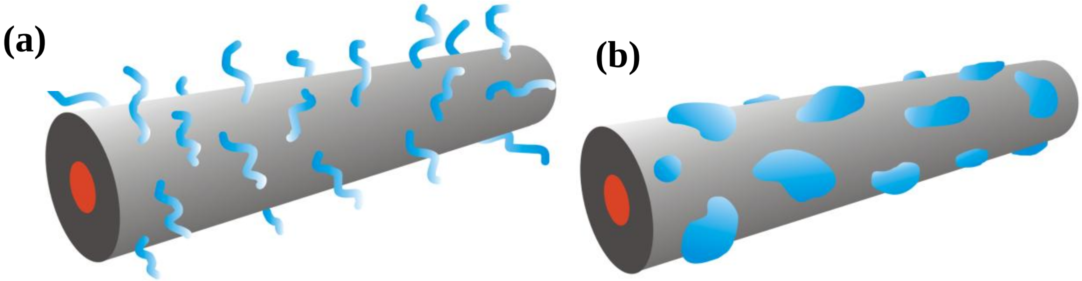

Scheme 3.3. Proposed schematic illustration of the cylindrical MAs in solution (a) and in a dried state (b). The blue, gray and red domains represent A/B , C and F domains, respectively.

However, the A or B chains are very unlikely to form separated domains on the surfaces of cylindrical MAs, which decreases the entropy of the system and is not favored. Our belief is that the A or B chains were distributed randomly and sparsely on the surfaces of the cylindrical MAs, as shown in Scheme 3.3a. When the MAs were aero-sprayed for AFM and TEM analysis, the corona chains aggregated together during the drying process due to the swelling of the residue solvents, as shown in Scheme 3.3b. On the contrary, among the MAs with a dense brush layer, the corona chains were so dense that the chains became stretched so that the beading seepage of the residual solvent did not cause significant fluctuation in the density of the corona chains.

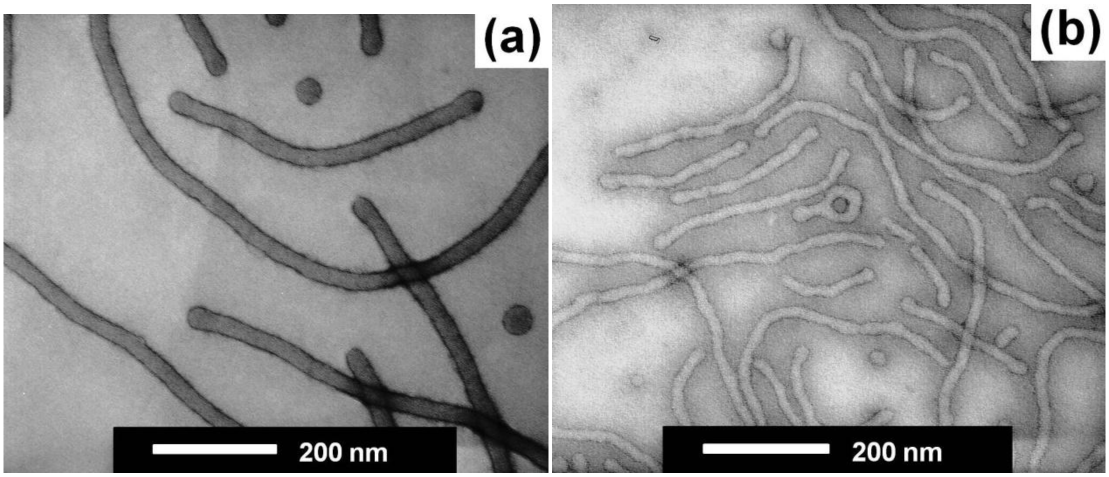

Figure 3.9. TEM images of cylindrical MAs from (a) diblock copolymer PCEMA-*b*-PtBA,[69] and (b) the triblock copolymer PtBA-*b*-PCEMA-*b*-PDMAEMA.[72] The TEM PtBA domains were selectively hydrolysed into PAA before they were stained with $UO_2(Ac)_2$.

To compare the surface coverage values with those of other cylindrical MA systems, two calculations were performed based on the results from previous studies from our group. In the first example, cylinders were prepared by firstly dissolving a diblock copolymer, PCEMA-*b*-PtBA, in THF and then removing the solvent via rotary-evaporation. The resultant polymer film was subsequently redispersed into methanol.[69] After photo-crosslinking the PCEMA block, the *tert*-butyl group was hydrolyzed, yielding PAA. In the second example, a triblock copolymer, PtBA-*b*-PCEMA-*b*-PDMAEMA, was directly dispersed into methanol to produce cylindrical MAs.[72] To investigate the distribution of the PtBA and PDMAEMA blocks on the micellar surface, the cylinders were photo-crosslinked and *tert*-butyl group was hydrolyzed, yielding PAA. In both cases, both of the cylinders showed uniform outer layers under TEM when $UO_2(Ac)_2$ was used to stain the samples. The TEM images are shown in Figure 3.9. According to the characteristic numbers we obtained (Table 3.5), the surface coverage Σ calculated for the cylinders by the PtBA block is calculated to be ca. 9 and 8, respectively. Generally, surfaces with $\Sigma > 5$ are considered to be in the brush regime. This is theoretically plausible for the micelles, because the surface chains are densely packed and thus shield the solvent from contacting the core chains, which can reduce the interfacial free energy between the solvent and the solvophobic blocks.

Table 3.5. The characteristic numbers of polymers and cylinders from the two examples.[69,72]

Example	Number of PtBA units	Number of PCEMA units	Core Diameter (nm)	Calculated Σ
PCEMA-*b*-PtBA [69]	560	175	20	9
PtBA-*b*-PCEMA-*b*-PDMAEMA [72]	160	135	14	8

3.3.8 XPS Studies on the Chemical Composition of the Cylinder Surface.

Fluorinated units are known to creep toward surfaces to reduce surface tension among polymer samples.[39] We ruled out the possibility of ridge formation due to the phase separation between the A domains and escaped F domains by performing an XPS study of the dried cylindrical micelles. Figure 3.10 compares the XPS spectra of the cylindrical micelles and a bulk $A_{105}C_{86}F_{19}$ sample in the C 1s spectral region.

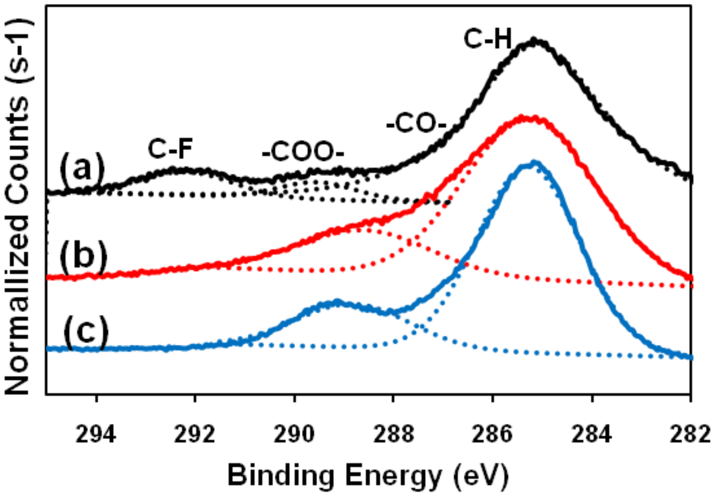

Figure 3.10. XPS C 1s spectra of a bulk $A_{105}C_{86}F_{19}$ sample (a), and $A_{105}C_{86}F_{19}$ micelles prepared from TFT/MeOH at f_{TFT} = 10% (b), and 44% (c).

For the bulk sample, all of the four peaks for the -CF-, -COO-, -CO- and -CH groups are clearly visible.[83] In addition, their relative intensities are very close to the theoretical values calculated based on their numbers of repeat units, as shown in Table 3.6. However, for the two cylindrical micellar samples, the -CF- peak at 292.2 eV disappeared. Since XPS is a surface analysis technique and detects elements that are within several nanometers of a sample's surface, this result demonstrated that the F block was buried inside the cylindrical micellar core, even after the samples were dried. Also two extreme cases were considered, and it is shown in Table 3.6 that either only the A chains are on the surface, or both the A and C chains are on the micellar surface. However, it was found that the calculated percentage values were similar in the two extreme cases. Thus, we can only conclude from this calculation that for the cylindrical MAs, the percentage values of the carboxyl bond were comparable with the values from the two extreme cases. Another feature worth noting is that the percentages of the C-H, CO and COO peaks from MA samples were exactly the same, suggest that although the solvent compositions differed greatly, the surface compositions of the cylindrical MAs remained the same. This unusual finding again can be explained by considering that the formation of these cylindrical MAs was driven by the mesogen-ordering of the F block. As long as the structure of the core remains the same, the composition of the outer layer will remain fixed as well.

Table 3.6. Relative concentrations of C1s components of $A_{105}C_{86}F_{19}$ on the surfaces of bulk polymer and micelles under different micelle conditions.

Binding Energy (eV)	C-H and CO (285.0 nm)	COO (288.8 nm)	C-F (292.2 nm)
Bulk calc.*	75.2%	14.9%	9.9%
Bulk experimental	78.1%	10.2%	11.7%
f_{MeOH} = 90%	78.9%	21.1%	-
f_{MeOH} = 56%	79.2%	20.8%	-
Calc.* PAA only	83.3%	16.7%	-
Calc.* PAA & PCEMA only	83.3%	16.7%	-

* Calculated based on the block ratios of the polymer $A_{105}C_{86}F_{19}$.

3.3.9 Mesogen-Driven Cylindrical Micelle Formation.

Heating the micellar solutions above the smectic A-to-isotropic transition temperature should convert the liquid crystalline F block into to a coil block. Therefore the ACF micelles formed at such a high temperature should be those of coil-coil-coil triblock copolymers. Figure 3.11 shows TEM images of $A_{105}C_{86}F_{19}$ and $A_{53}C_{44}F_{13}$ micelles that were sprayed from a TFT/MeOH (f_{TFT} = 44%) solvent mixture at 70 ^{o}C. While $A_{105}C_{86}F_{19}$ apparently formed mostly "large compound micelles",[14] $A_{53}C_{44}F_{13}$ mainly yielded vesicles. While the elucidation of the exact structures of these micelles was beyond the scope of this work, the micelles observed at 70 ^{o}C for the coil-coil-coil copolymers were certainly not cylindrical. Thus, the cylinders were formed at lower temperatures, most likely to facilitate formation of a liquid crystalline phase from the F block.

This data suggests that the smectic A-to-isotropic phase transition temperature was lower than 70 ^{o}C, and definitely lower than 76 ^{o}C, which was that determined for the dried ACF cylindrical micelles. The lower transition temperature probably arose from the plasticizing of the F block by TFT that was sorbed from the TFT/MeOH mixture.

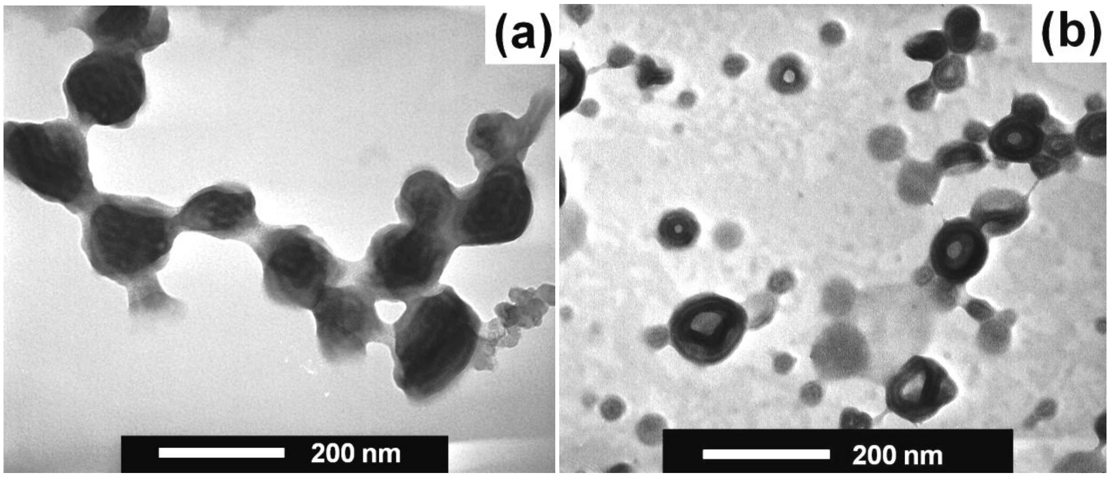

Figure 3.11. TEM images of MAs from $A_{105}C_{86}F_{19}$ (a) and $A_{53}C_{44}F_{13}$ (b) in a TFT/MeOH (f_{MeOH} = 56%) mixture at 70 °C. The samples were stained with OsO_4.

More interestingly, the $A_{53}C_{44}F_{13}$ vesicles and cylinders could be repeatedly inter-converted by cycling the system's temperature. The solution was firstly heated up to and kept at 70 °C for 20 min before sprayed on TEM grids, and then slowly cooled to 21 °C in 6 hrs. After going through the heating/cooling or vesicle/cylinder cycle once (Figure 3.12a and b) for the $A_{53}C_{44}F_{13}$ micelles in TFT/MeOH at f_{TFT} = 44%, we repeated the cycle between temperature of 70 and 21 °C for another time. The samples taken at the different temperatures in the second cycle were analyzed by TEM, yielding images (c) and (d) in Figure 3.12.

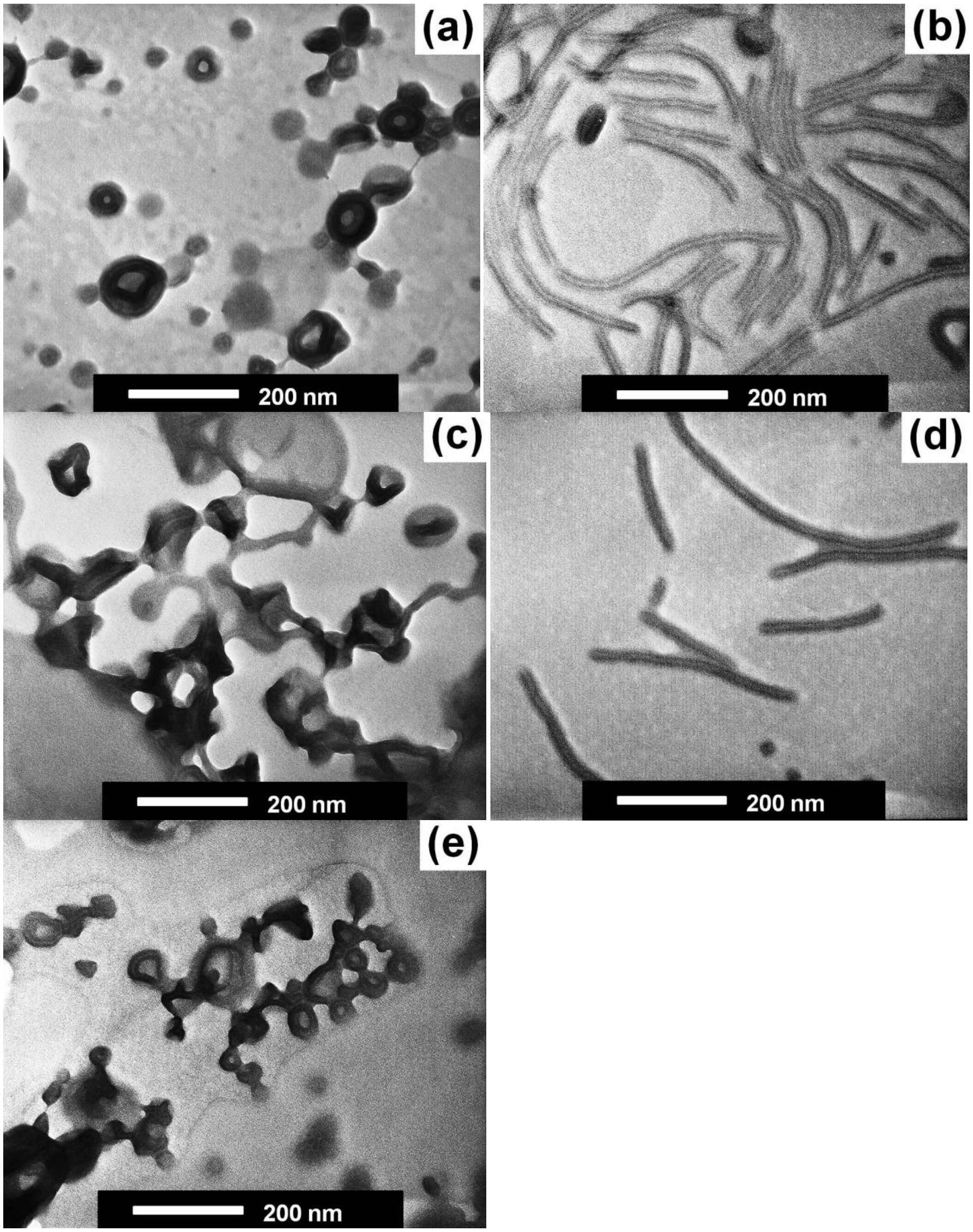

Figure 3.12. TEM images of $A_{53}C_{44}F_{13}$ micelles sprayed from TFT/MeOH at $f_{TFT} = 44\%$ which were sprayed after being heated once to 70 ^{o}C (a), after being heated to 70 °C and then slowly cooled to room temperature (b), after being heated for a second cycle to 70 ^{o}C (c), after being heated to 70 °C for a second cycle and then slowly cooled to room temperature (d), and after being heated for a third cycle to 70 ^{o}C (e).

Analysis of a sample collected from a solution heated for a third cycle to 70 °C yielded the image shown as Figure 3.12e. The vesicle-cylinder interconversion was clearly being repeated during the temperature cycling process. After cooling the solution to room temperature, cylindrical morphologies with open-ends on both sides of the cylinders were observed. Furthermore, the open-ends of the cylinders may have indicated that the growth of the cylinders along the cylinder's axis was still taking place when the solution was sprayed onto the TEM grids.

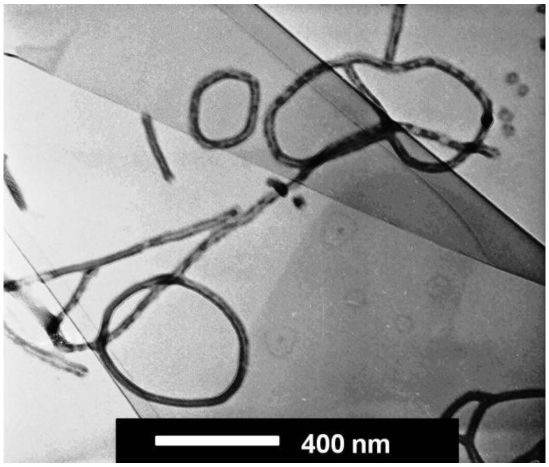

Figure 3.13. The TEM images of cylindrical and toroidal morphologies. The sample was sprayed from $A_{105}C_{86}F_{19}$ cylindrical micelle in TFT/MeOH at f_{TFT} = 44% at elevated temperature (second cycle at 70 °C).

For the $A_{105}C_{86}F_{19}$ micelles, however, the reversibility of the morphologies was not observed. When the $A_{105}C_{86}F_{19}$ cylinder solution was heated to 70 °C again, no composite spherical aggregates like shown in Figure 3.11a was found. Instead, cylinders and toroidal micelles (Figure 3.13) were observed in the TEM images.

The toroidal morphologies might have been formed by end-fusion of the cylinders. For the cylinders with open-ends on both sides, there are two types of interfaces: the cylinder growth interface and the lateral interface. At low temperature, the F block of free triblock copolymer chain was growing continuously onto the growth interface along the lateral direction. Due to the rigidity of the liquid crystalline F core, the cylinders are much straighter when compared to cylindrical MAs from coil-coil-coil triblock copolymers.[84,85] When such cylinders were heated up to the smectic A-to-isotropic phase transition temperature of the F block, the rigidity of the mesogen core was reduced and the cylinders became more flexible. This more flexible conformation of the cylinders made the “back-biting” of one cylinder end onto the other possible, which can minimize the interfacial energy between the F core and the solvent.

Furthermore, the relatively high molecular weight of the insoluble domain of the polymer, especially for the C block, can prohibit the morphological transition at different temperatures. Halperin and Alexander have performed a theoretical study on the relaxation kinetics on polymeric micelles.[86] They claimed that the fast chain exchange rate (τ_1) is exponentially proportional to $N_B^{2/3}$, where N_B is the core block’s degree of polymerization. Lodge and Bates also verified that the single chain exchange rate is hypersensitive to the core chain length using the diblock copolymer micelles.[87]

According to their experimental results, the core block length leads to an approximately logarithmic chain exchange rate. Considering that the C block is insoluble in either TFT or MeOH, the core-shell-corona micelles observed in our case can be simplified as a core-shell structure by ignoring the F domain. In this simplified model, the C block forms the core and the A blocks forms the micellar shell. A longer C block (the core-forming block) reduces the chain exchange rate between different aggregates. This might "lock" the cylindrical morphologies, even if the solution is heated to the transitional temperature for the F block.

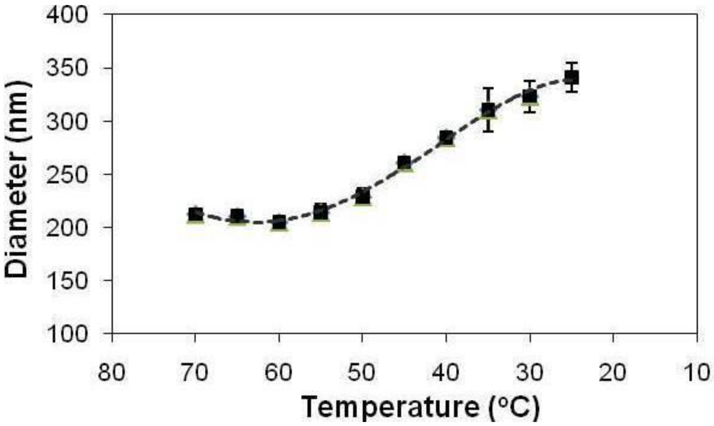

Figure 3.14. Hydrodynamic diameters (d_h) of $A_{105}C_{86}F_{19}$ micelles in TFT/MeOH at f_{TFT} = 44% at various temperatures.

DLS was used to monitor changes to the hydrodynamic diameter (d_h) of an $A_{105}C_{86}F_{19}$ sample in a TFT/MeOH solvent mixture at f_{TFT} = 44% as it was cooled from 70 °C. The cooling was achieved in 5 °C increments, and new temperature was maintained for 8 h before d_h measurement. The d_h values remained relatively constant at T > ~55 °C (Figure 3.14). however, the d_h values grew once T was decreased below 60 °C. This was probably due to the formation of cylinders, which thus had larger d_h values because of their length.

Another noticeable feature is that the transition temperature is approximately 60 °C, which is lower than the melting temperatures of the F block measured by DSC analysis. This might be due to the incorporation of some fluorine-affinity solvent, such as TFT, in the F-based cores of the cylindrical MAs.

3.3.10 Room Temperature Morphologies and Thermodynamically-Favoured Structures.

We also attempted to disperse the copolymer directly in the solvent mixture at room temperature (Figure 3.15), which yielded similar cylindrical MAs. However, these cylindrical MAs formed at room temperature were not well-defined. Many branched cylinders were observed in the samples, and the diameters of the cylindrical MAs were not uniform. The formation of branched MAs and aggregates with non-uniform diameters is very common when MAs are produced by direct dispersion into selective solvents.[84,85] However, the similarity of the cylindrical structures and their dimensions still suggests that the cylindrical MAs were the thermodynamically stable structure.

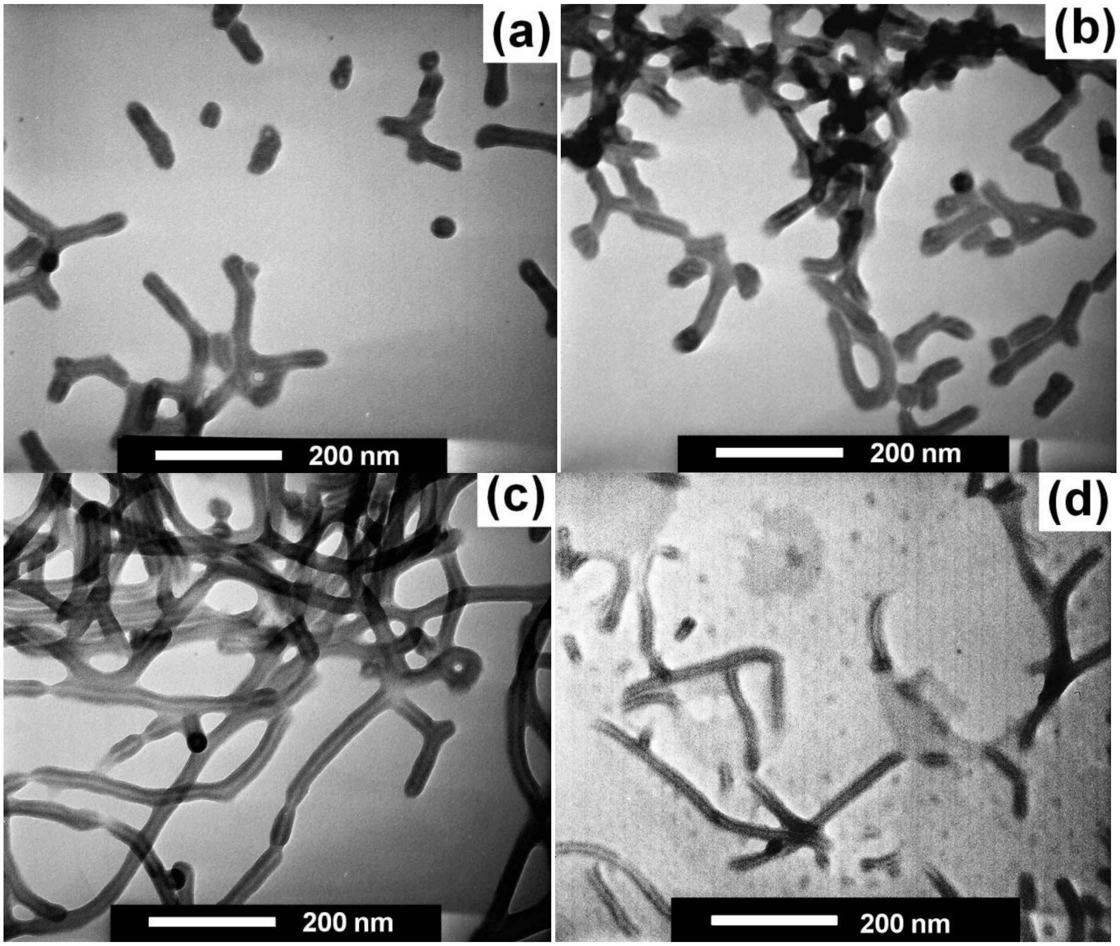

Figure 3.15. TEM images of OsO_4 stained cylindrical MAs formed by $A_{105}C_{86}F_{19}$ copolymer samples that were sprayed from TFT/MeOH solvent mixtures with f_{TFT} at: 10% (a), 30% (b), and 44% (c), Image (d) shows cylindrical MAs formed by $A_{53}C_{44}F_{13}$, which was sprayed from a TFT/MeOH solvent mixture with at f_{TFT} = 44%. The samples were stained with OsO_4 before TEM observation.

3.3.11 Robustness of the Method to Produce Cylindrical MAs.

It has been shown above that the $A_{105}C_{86}F_{19}$ and $A_{53}C_{44}F_{13}$ copolymers can form cylindrical MAs at many f_{TFT} values in TFT/MeOH mixtures through the slow cooling method (Figure 3.16) and direct dispersion method (Figure 3.17). In addition, when MeOH was replaced with EtOH and iPOH, it is found that $A_{105}C_{86}F_{19}$ formed similar cylindrical MAs as well. Figure 3.16 shows the TEM images of the cylindrical MAs in TFT/EtOH and TFT/iPOH with f_{TFT} at 44% that were prepared by the slow cooling method. The diameters of these cylindrical MAs were measured from the TEM images and are summarized in Table 3.4. These values were comparable with the values of the cylindrical MAs from the TFT/MeOH experiments. This is reasonable, since the core diameter is not determined by the solvophilic or solvophobic interactions, but instead by the liquid crystalline structure of the PFOEMA block. These two sets of experiments again confirmed our assumption that this cylindrical morphology is induced by the mesogen-ordering of the PFOEMA block.

Two additional block terpolymers, $B_{105}C_{86}F_{19}$ and $B_{53}C_{44}F_{13}$, were also used to produce similar cylindrical MAs in TFT/MeOH solvent mixtures. The $B_{105}C_{86}F_{19}$ and $B_{53}C_{44}F_{13}$ terpolymers are the precursors of $A_{105}C_{86}F_{19}$ and $A_{53}C_{44}F_{13}$ before the hydrolysis of *tert*-butyl groups of the B (or PtBA) block. In the solvent mixtures of TFT/MeOH, $B_{105}C_{86}F_{19}$ yields similar cylindrical MAs from the slow cooling method at f_{TFT} = 10% as obtained from $A_{105}C_{86}F_{19}$, as shown in Figure 3.18c. Meanwhile, at f_{TFT} = 30%, the $B_{105}C_{86}F_{19}$ terpolymer formed both cylindrical and spherical MAs (Figure 3.18b) and yielded mainly irregular aggregates at f_{TFT} = 44% (Figure 3.18a).

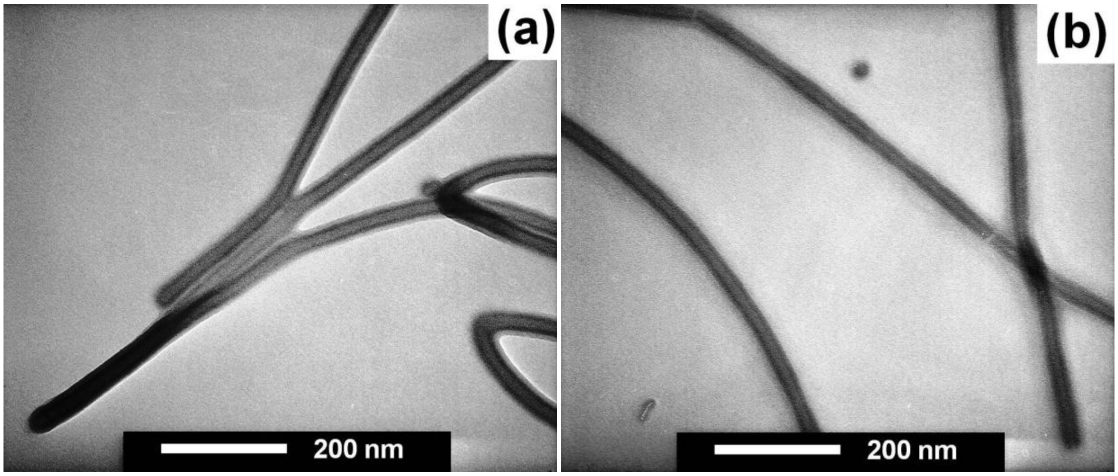

Figure 3.16. TEM images of MA samples sprayed from $A_{105}C_{86}F_{19}$ copolymer samples dispersed into a TFT/EtOH solvent mixture (a) and a TFT/iPOH solvent mixture (b). In both solvent mixtures f_{TFT} = 44%. The samples were prepared by the slow cooling method and were stained with OsO_4.

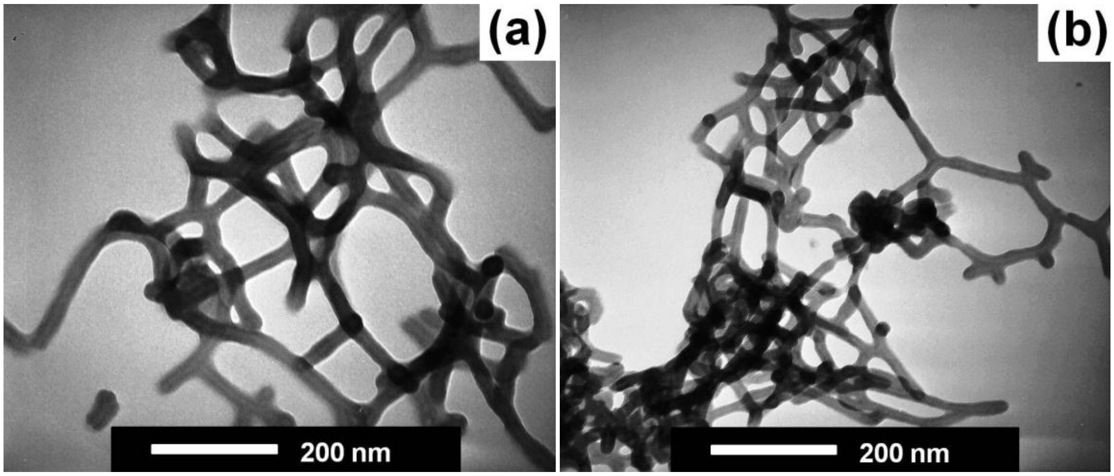

Figure 3.17. TEM images of MAs prepared from $A_{105}C_{86}F_{19}$ in solvent mixtures of TFT/EtOH (a), and TFT/iPOH (b). In both solvent mixtures f_{TFT} = 44%. The samples were prepared by directly dispersing the $A_{105}C_{86}F_{19}$ copolymer into the desired solution at room temperature for approximately 4 days. The samples were stained with OsO_4.

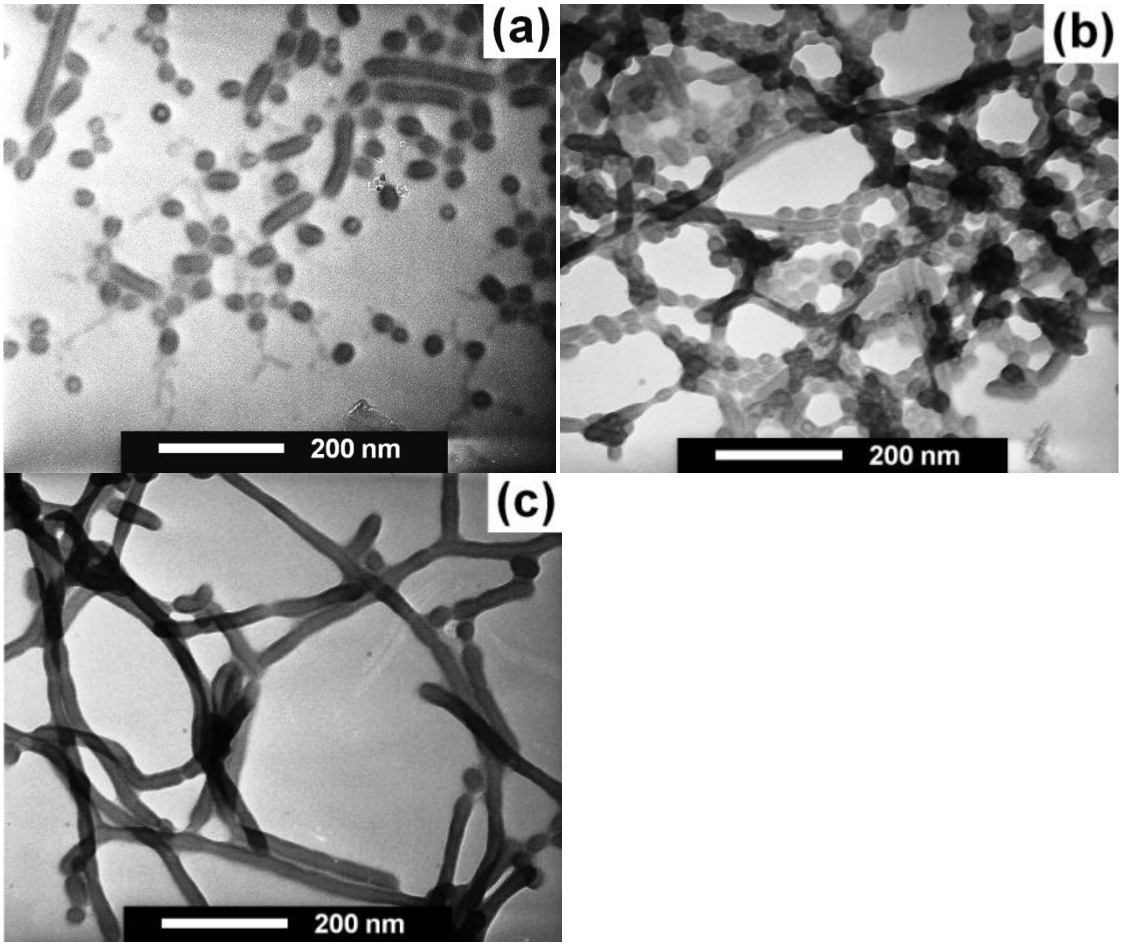

Figure 3.18. TEM images of MA samples sprayed from solutions of $B_{105}C_{86}F_{19}$ in TFT/MeOH solvent mixtures at f_{TFT} = 44% (a), 30% (b), and 10% (c). The samples were prepared by the slow cooling method and were stained with OsO_4.

Since TFT is a good solvent for both the B and F blocks, but not the A block, the different micellization behaviours of the $A_{105}C_{86}F_{19}$ and $B_{105}C_{86}F_{19}$ copolymers is understandable. Because the resultant morphology is a delicate balance between the liquid crystalline structure of the F block and the interactions between the blocks and the solvent, the spherical core-shell-corona MAs very likely resulted from the stronger solvophobic and solvophilic interactions. A consideration of the energy competition is included in the following context. The $B_{53}C_{44}F_{13}$ copolymer produced cylindrical MAs in TFT/MeOH solvent mixtures at f_{TFT} = 44%~10% using the slow cooling method, as shown in Figure 3.19. Besides cylindrical MAs, it can be seen that there were some smaller structures in the sample as well. By examining the TEM images closely, it was found that some of these small MAs were not really spherical MAs as shown in Figure 3.18b, but were actually very short cylindrical MAs. An enlarged image of the smaller MAs is shown in the inset image. It is very clear that the two ends of the MAs were open and the core appeared to be a short cylinder instead of a sphere. Since the cylindrical MAs could be produced from different solvent systems of the same polymer, and also from different polymers in the same solvent system, it was again confirmed that the cylindrical structure is the thermodynamically stable morphology.

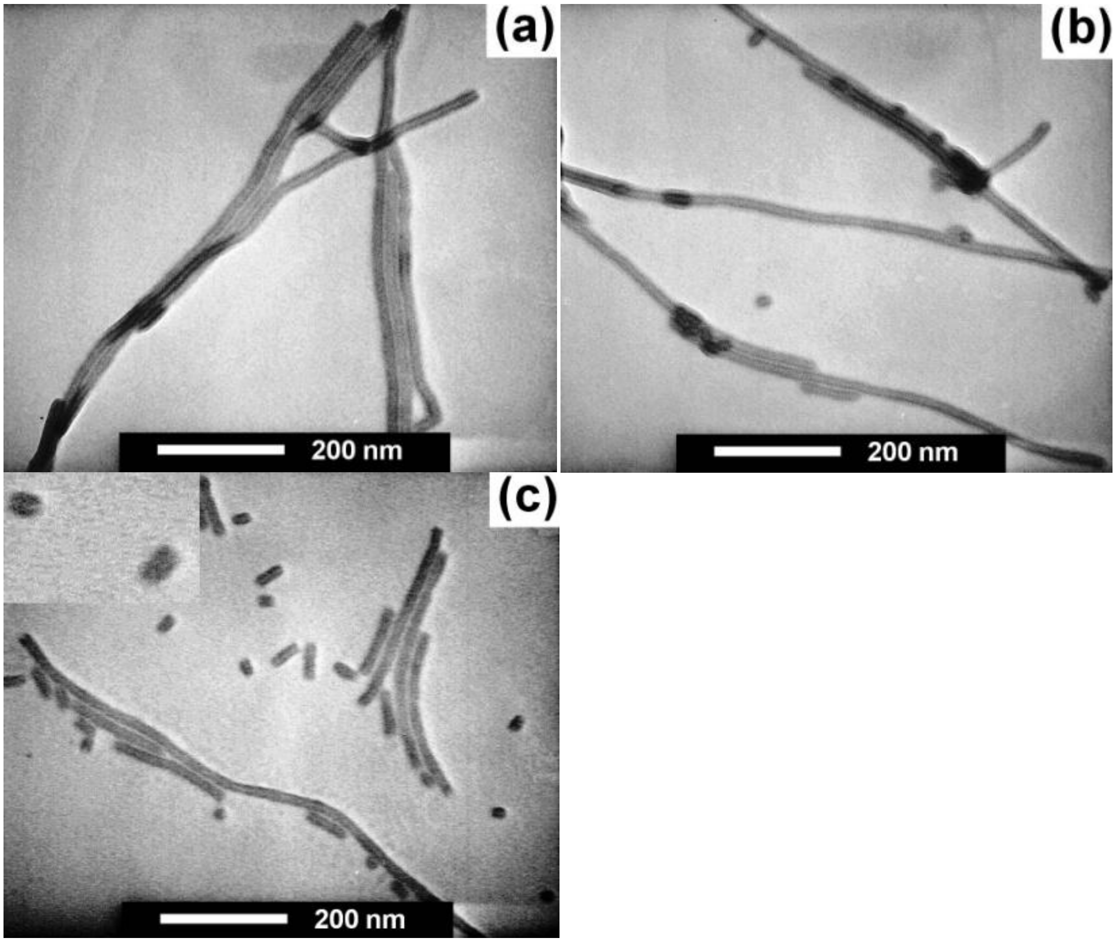

Figure 3.19. TEM images of MAs from $B_{53}C_{44}F_{13}$ in TFT/MeOH solvent mixtures at f_{MeOH} = 56% (a), 70% (b), and 90% (c). The samples were prepared by the slow cooling method and were stained with OsO_4.

3.3.12 Bulk Morphologies of $B_{105}C_{86}F_{19}$ and $B_{53}C_{44}F_{13}$.

One item that needs to be mentioned is that the bulk morphologies of the $B_{105}C_{86}F_{19}$ and $B_{53}C_{44}F_{13}$ copolymers were also monitored by TEM, as shown in Figure

3.20 and Figure 3.21, respectively. Two different methods were used to prepare films of the $B_{105}C_{86}F_{19}$ terpolymer. The first method involved dissolving $B_{105}C_{86}F_{19}$ into TFT at a high concentration (~10 mg/mL) and then allowing the solution to slowly evaporate in a sealed glass desiccator for one week. The second method was similar to the first method, except that once all of the solvent had evaporated, the film was then heated to 120 ^{o}C under high vacuum for an additional week. From Figure 3.20, films obtained from the two methods formed similar morphologies. The morphology is very similar to that proposed by Wei and Wang,[88] with C and F blocks forming cylindrical morphologies and the B block forming the matrix (Figure 3.22a). For TEM observation of the $B_{53}C_{44}F_{13}$ films prepared from the first method, OsO_4 was used to stain the C domains (Figure 3.21a). Meanwhile, the B domains (Figure 3.21b) were stained with $UO_2(Ac)_2$ after hydrolysis of *tert*-butyl groups to yield carboxyl groups. The morphology obtained from $B_{53}C_{44}F_{13}$ appeared to be similar to the lamella-cylinder phase described by Wei and Wang (Figure 3.22b),[88] with the C and B blocks forming lamellar phase and the F block forming cylinder phase arranged alternatively with the B block. The phase separation between the C and F blocks in the lamellar phase is not quite clear, as the structure was too small to be identified from the TEM images (Figure 3.21). These findings suggest that neither the cylindrical MAs formed at room temperature, the irregular spherical MAs, nor the double-walled vesicles represented were the kinetically trapped morphology.

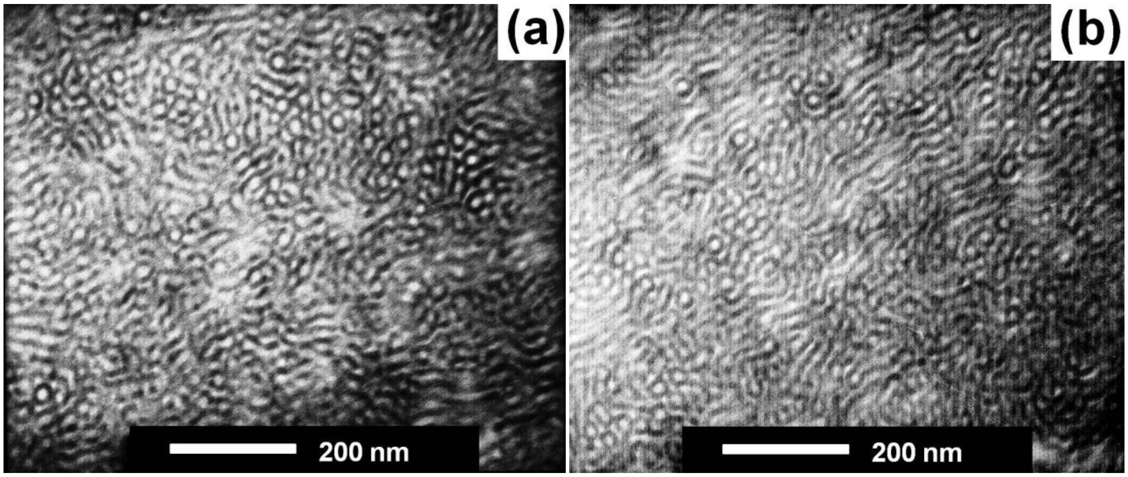

Figure 3.20. Cross-sectional TEM images of bulk samples of the $B_{105}C_{86}F_{19}$ terpolymer prepared by: the slow evaporation of $B_{105}C_{86}F_{19}$ from a TFT solution (a), and by annealing at 120 °C for an additional week (b). The samples were stained with OsO_4.

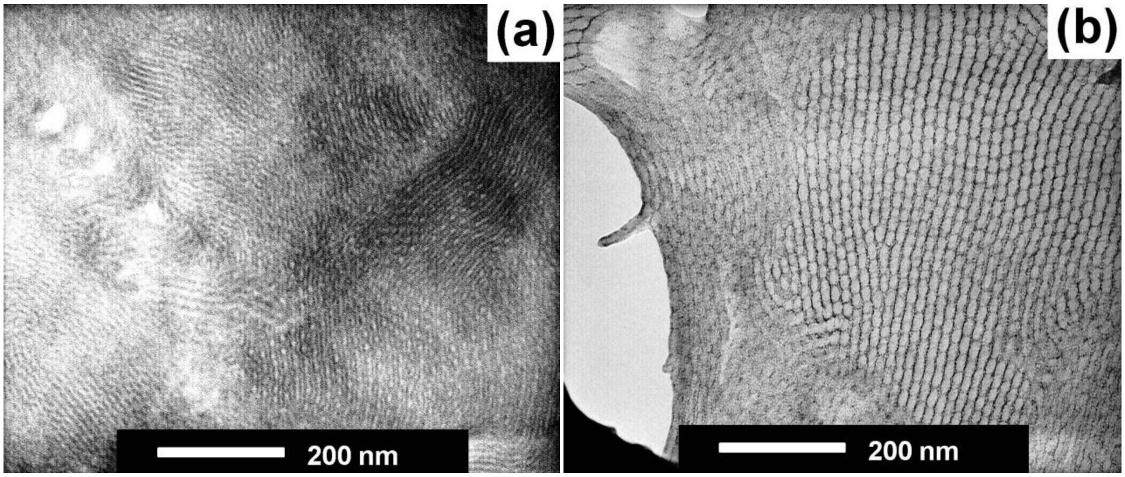

Figure 3.21. Cross-sectional TEM images of bulk samples of the $B_{53}C_{44}F_{13}$ copolymer prepared by: the slow evaporation of $B_{53}C_{44}F_{13}$ from a TFT solution, and staining the sample with OsO_4 (a), and by subjecting the B block to selective hydrolysis with trifluoroacetic acid and subsequently staining the sample with $UO_2(Ac)_2$ (b).

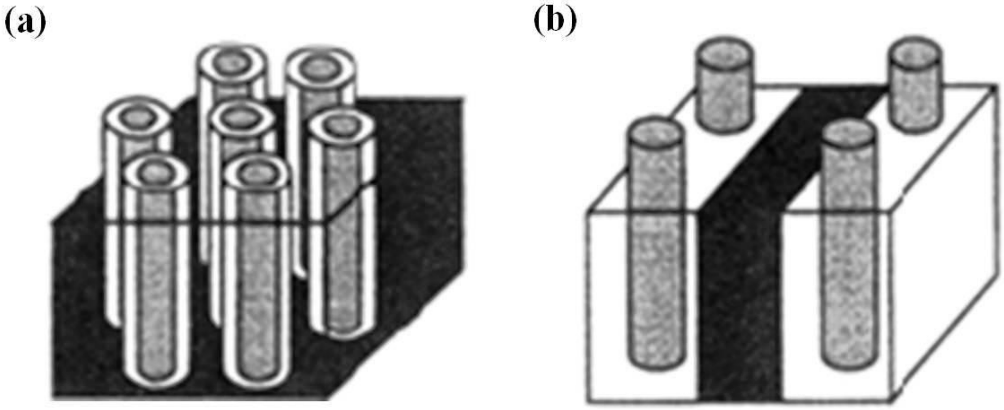

Figure 3.22. Schematic representation of possible phase morphologies of the $B_{105}C_{86}F_{19}$ terpolymer with a coaxial cylindrical phase (a), and the $B_{53}C_{44}F_{13}$ terpolymer with a mixed lamellar-cylindrical phase.[88]

3.3.13 A Consideration of Competing Energetic Contributions.

Among MAs formed from coiled \`ABC\` triblock copolymers in \`A\`- or \`C\`-selective solvents, core-shell-corona structures are the most commonly adopted morphologies. Therefore, it is very surprising to find that the cylindrical MAs were not fully covered by the corona chains. Energetically speaking, this observed structure is unfavourable, since the solvent is a precipitant for the C shell, which would prefer to be isolated from solvent by a layer of corona chains. However, the F core-forming block requires ordering with a specific pattern that forces the C chains to become stretched along the cylindrical MAs. This leads to the sparsely distributed A or B corona chains. Due to the liquid crystalline properties of the PFOEMA block, below the isotropization temperature, the regular packing of the fluorocarbon side-chains leads to the formation of a smectic mesophase. The phase-transition energy obtained from DSC measurements is approximately 3~7 J/g per polymer chain, and a typical polymer-solvent surface tension is on the order of tens of mN/m.[89] According to our calculations (an example is shown below), the interfacial energy is approximately similar to the phase-transition energy of the PFOEMA block. Therefore, the resultant morphology is very likely a delicate balance between the polymer-solvent interactions and the liquid crystalline ordering of the PFOEMA block. In most the cases among these systems, the liquid crystalline effect dominates, leading to the cylindrical MAs with sparsely-distributed corona chains. In some other cases, the polymer-solvent interaction predominates, yielding conventional core-shell-corona structures. A more detailed study of the latter systems will be provided in Appendix B. The polymer-solvent interactions was estimated using the equations shown below:

$$\epsilon = \frac{1}{\rho * \pi r^2} * (2\pi r) * \gamma \tag{3.9}$$

$$\epsilon = \frac{1}{1.847\text{g/cm}^3 * \pi(5.5\text{nm})^2} * \pi * (24\text{nm}) * 5\text{mJ/m}^2$$

$$\epsilon = 2.1\ \text{J/g}$$

where ρ is the density of PFOEMA block, r is the radius of the PFOEMA core of the cylindrical MAs, and γ represents the surface tension between the PFOEMA block and solvent, which was assumed to be 10 mJ/m^2 for a rough estimation.

3.3.14 Conclusions

Four F-bearing block terpolymers $A_{53}C_{44}F_{13}$, $A_{105}C_{86}F_{19}$, $B_{53}C_{44}F_{13}$, and $B_{105}C_{86}F_{19}$, and their respective micelles were prepared and characterized. The first three block copolymers readily formed cylindrical micelles at room temperature in TFT/MeOH solvent mixtures at f_{TFT} = 44%, 30%, and 10%. The $A_{53}C_{44}F_{13}$ and $A_{105}C_{86}F_{19}$ terpolymers also self-assembled into cylindrical micelles in either TFT/EtOH or TFT/iPOH solvent mixtures at f_{TFT} = 44%. The only exception was $B_{105}C_{86}F_{19}$, which had the lowest F weight fraction and the highest soluble block weight fraction among the four copolymers. Meanwhile, $B_{105}C_{86}F_{19}$ formed cylindrical micelles in TFT/MeOH solvent mixtures at f_{TFT} = 10%, a mixture of cylindrical and spherical micelles at f_{TFT} = 30%, and spherical micelles at f_{TFT} = 44%. All of the micelles possessed an F core, a C shell, and an A or B corona. Our detailed analysis of the TEM images of these micelles indicated that the C shell chains of the ACF cylindrical micelles were radially compressed relative to their unperturbed dimensions. Also, the coronal A chains were so thin that they did not form a uniform film covering the C shells. Rather, they formed ridges to reduce their radial compression and to avoid excessive configurational entropy loss. These structural features all arose from the F block-driven micellization, which yielded cylinders possessing abnormal thicknesses for the shell and corona layers. Aside from the indirect evidence, the smectic A layer formation was confirmed by our DSC and WAXS studies of dried micelles. More interestingly, the ACF micelles underwent morphological transitions from large compound micelles or vesicles at high temperatures to cylinders when they were cooled below the isotropic-to-smectic A phase transition temperature for the F blocks. For $A_{53}C_{44}F_{13}$, this morphological transition was reversible via temperature cycling, proving unambiguously that mesogen-order-driven cylindrical micelle formation occurs at room temperature for these polymers. This mesogen-driven process should provide a facile and versatile route for the controlled preparation of useful block copolymer cylindrical micelles.

References

(1) Geng, Y.; Dalhaimer, P.; Cai, S. S.; Tsai, R.; Tewari, M.; Minko, T.; Discher, D. E. *Nat. Nanotechnol.* **2007**, *2*, 249-255.

(2) Liu, J.; Thompson, Z. J.; Sue, H. J.; Bates, F. S.; Hillmyer, M. A.; Dettloff, M.; Jacob, G.; Verghese, N.; Pham, H. *Macromolecules*, **2010**, *43*, 7238-7243.

(3) Liu, G. J. In *Self-Assembled Nanomaterials I: Nanotubes* **2008**; Vol. 220, p 29-64.

(4) Liu, G. J.; Yan, X. H.; Duncan, S. *Macromolecules* **2003**, *36*, 2049-2054.

(5) Yan, X. H.; Liu, G. J. *Langmuir* **2004**, *20*, 4677-4683.

(6) Liu, G. J.; Ding, J. F.; Qiao, L. J.; Guo, A.; Dymov, B. P.; Gleeson, J. T.; Hashimoto, T.; Saijo, K. *Chem. Euro. J.* **1999**, *5*, 2740-2749.

(7) Liu, G. J.; Yan, X. H.; Qiu, X. P.; Li, Z. *Macromolecules* **2002**, *35*, 7742-7747.

(8) Stewart, S.; Liu, G. *Angew. Chem., Int. Ed.* **2000**, *39*, 340-344.

(9) Liu, G. J.; Yan, X. H.; Li, Z.; Zhou, J. Y.; Duncan, S. *J. Am. Chem. Soc.* **2003**, *125*, 14039-14045.

(10) Yan, X. H.; Liu, G. J.; Li, Z. *J. Am. Chem. Soc.* **2004**, *126*, 10059-10066.

(11) Yan, X. H.; Liu, G. J.; Liu, F. T.; Tang, B. Z.; Peng, H.; Pakhomov, A. B.; Wong, C. Y. *Angew. Chem., Int. Ed.* **2001**, *40*, 3593-+.

(12) Yan, X. H.; Liu, G. J.; Haeussler, M.; Tang, B. Z. *Chem. Mater.* **2005**, *17*, 6053-6059.

(13) Li, Z.; Liu, G. J. *Langmuir* **2003**, *19*, 10480-10486.

(14) Zhang, L. F.; Eisenberg, A. *Science* **1995**, *268*, 1728-1731.

(15) Shen, H. W.; Eisenberg, A. *J. Phys. Chem. B* **1999**, *103*, 9473-9487.

(16) Srinivas, G.; Discher, D. E.; Klein, M. L. *Nat. Mater.* **2004**, *3*, 638-644.

(17) Jain, S.; Bates, F. S. *Macromolecules* **2004**, *37*, 1511-1523.

(18) Jain, S.; Bates, F. S. *Science* **2003**, *300*, 460-464.

(19) Hayward, R. C.; Pochan, D. J. *Macromolecules*, **2010**, *43*, 3577-3584.

(20) Qian, J. S.; Zhang, M.; Manners, I.; Winnik, M. A. *Trends Biotechnol.* **2010**, *28*, 84-92.

(21) Fustin, C. A.; Abetz, V.; Gohy, J. F. *Eur. Phys. J. E* **2005**, *16*, 291-302.

(22) Li, Z. B.; Kesselman, E.; Talmon, Y.; Hillmyer, M. A.; Lodge, T. P. *Science* **2004**, *306*, 98-101.

(23) Dupont, J.; Liu, G. *Soft Matter* **2010**, *6*, 3654-3661.

(24) Cui, H. G.; Chen, Z. Y.; Zhong, S.; Wooley, K. L.; Pochan, D. J. *Science* **2007**, *317*, 647-650.

(25) Zhu, J. T.; Jiang, W. *Macromolecules* **2005**, *38*, 9315-9323.

(26) Pochan, D. J.; Chen, Z. Y.; Cui, H. G.; Hales, K.; Qi, K.; Wooley, K. L. *Science* **2004**, *306*, 94-97.

(27) Zhong, S.; Cui, H. G.; Chen, Z. Y.; Wooley, K. L.; Pochan, D. J. *Soft Matter* **2008**, *4*, 90-93.

(28) Dupont, J.; Liu, G. J.; Niihara, K.; Kimoto, R.; Jinnai, H. *Angew. Chem., Int. Ed.* **2009**, *48*, 6144-6147.

(29) Dou, H. J.; Liu, G. J.; Dupont, J.; Hong, L. Z. *Soft Matter*, **2011**, *6*, 4214-4222.

(30) Hu, J. W.; Njikang, G.; Liu, G. J. *Macromolecules* **2008**, *41*, 7993-7999.

(31) Liu, Y. F.; Abetz, V.; Muller, A. H. E. *Macromolecules* **2003**, *36*, 7894-7898.

(32) Walther, A.; Drechsler, M.; Rosenfeldt, S.; Harnau, L.; Ballauff, M.; Abetz, V.; Muller, A. H. E. *J. Am. Chem. Soc.* **2009**, *131*, 4720-4728.

(33) Massey, J. A.; Temple, K.; Cao, L.; Rharbi, Y.; Raez, J.; Winnik, M. A.; Manners, I. *J. Am. Chem. Soc.* **2000**, *122*, 11577-11584.

(34) Qian, J. S.; Guerin, G.; Cambridge, G.; Manners, I.; Winnik, M. A. *Macromol. Rapid Commun.*, **2010**, *31*, 928-933.

(35) Wang, X. S.; Guerin, G.; Wang, H.; Wang, Y. S.; Manners, I.; Winnik, M. A. *Science* **2007**, *317*, 644-647.

(36) Gadt, T.; Ieong, N. S.; Cambridge, G.; Winnik, M. A.; Manners, I. *Nat. Mater.* **2009**, *8*, 144-150.

(37) Gilroy, J. B.; Gadt, T.; Whittell, G. R.; Chabanne, L.; Mitchels, J. M.; Richardson, R. M.; Winnik, M. A.; Manners, I. *Nat. Chem.* **2010**, *2*, 566-570.

(38) Al-Hussein, M.; Serero, Y.; Konovalov, O.; Mourran, A.; Moller, M.; de Jeu, W. H. *Macromolecules* **2005**, *38*, 9610-9616.

(39) Wang, J. G.; Mao, G. P.; Ober, C. K.; Kramer, E. J. *Macromolecules* **1997**, *30*, 1906-1914.

(40) Xiang, M. L.; Li, X. F.; Ober, C. K.; Char, K.; Genzer, J.; Sivaniah, E.; Kramer, E. J.; Fischer, D. A. *Macromolecules* **2000**, *33*, 6106-6119.

(41) Hirao, A.; Hayashi, M.; Loykulnant, S.; Sugiyama, K. *Prog. Polym. Sci.* **2005**, *30*, 111-182.

(42) Guo, A.; Liu, G. J.; Tao, J. *Macromolecules* **1996**, *29*, 2487-2493.

(43) Skrabania, K.; von Berlepsch, H.; Bottcher, C.; Laschewsky, A. *Macromolecules* **2010**, *43*, 271-281.

(44) Li, Z. B.; Hillmyer, M. A.; Lodge, T. P. *Langmuir* **2006**, *22*, 9409-9417.

(45) Imae, T.; Tabuchi, H.; Funayama, K.; Sato, A.; Nakamura, T.; Amaya, N. *Colloids Surf., A* **2000**, *167*, 73-81.

(46) Lim, K. T.; Lee, M. Y.; Moon, M. J.; Lee, G. D.; Hong, S. S.; Dickson, J. L.; Johnston, K. P. *Polymer* **2002**, *43*, 7043-7049.

(47) Krupers, M. J.; Sheiko, S. S.; Moller, M. *Polym. Bull*, **1998**, *40*, 211-217.

(48) Nakahama, S.; Hirao, A. *Prog. Polym. Sci.* **1990**, *15*, 299-335.

(49) Henselwood, F.; Liu, G. J. *Macromolecules* **1997**, *30*, 488-493.

(50) Hirao, A.; Kato, H.; Yamaguchi, K.; Nakahama, S. *Macromolecules* **1986**, *19*, 1294-1299.

(51) Ishizone, T.; Sugiyama, K.; Sakano, Y.; Mori, H.; Hirao, A.; Nakahama, S. *Polymer J.* **1999**, *31*, 983-988.

(52) Hirao, A.; Sugiyama, K.; Yokoyama, H. *Prog. Polym. Sci.* **2007**, *32*, 1393-1438.

(53) Zheng, R. H.; Wang, J. D.; Liu, G. J.; Jao, T. C. *Macromolecules* **2007**, *40*, 7601-7608.

(54) Berne, B. J. P., R. *Dynamic Light Scattering with Applications to Chemistry, Biology, and Physics;*; Dover Publications, Inc.: Mineola, NY, **1976**.

(55) Huglin, M. B. *Light Scattering from Polymer Solutions*; Academic Press: London, **1972**.

(56) Jouyban, A.; Khoubnasabjafari, M.; Vaez-Gharamaleki, Z.; Fekari, Z.; Acree, W. E. *Chem. Pharm. Bull.* **2005**, *53*, 519-523.

(57) Grocholski, B.; Jeanloz, R. *J. Chem. Phys.* **2005**, *123*.

(58) DeLorenzi, L.; Fermeglia, M.; Torriano, G. *J. Chem. Eng. Data* **1996**, *41*, 1121-1125.

(59) Ding, J. F.; Liu, G. J. *Macromolecules* **1999**, *32*, 8413-8420.

(60) Corpart, J. M.; Girault, S.; Juhue, D. *Langmuir* **2001**, *17*, 7237-7244.

(61) Ding, J. F.; Liu, G. J.; Yang, M. L. *Polymer* **1997**, *38*, 5497-5501.

(62) Njikang, G.; Han, D. H.; Wang, J.; Liu, G. J. *Macromolecules* **2008**, *41*, 9727-9735.

(63) Xu, B.; Pinol, R.; Nono-Djamen, M.; Pensec, S.; Keller, P.; Albouy, P. A.; Levy, D.; Li, M. H. *Faraday Discuss.* **2009**, *143*, 235-250.

(64) Pinol, R.; Jia, L.; Gubellini, F.; Levy, D.; Albouy, P. A.; Keller, P.; Cao, A.; Li, M. H. *Macromolecules* **2007**, *40*, 5625-5627.

(65) Jia, L.; Cao, A.; Levy, D.; Xu, B.; Albouy, P. A.; Xing, X. J.; Bowick, M. J.; Li, M. H. *Soft Matter* **2009**, *5*, 3446-3451.

(66) Cameron, N. S.; Corbierre, M. K.; Eisenberg, A. *Can. J. Chem.* **1999**, *77*, 1311-1326.

(67) Mandelke.L; Allou, A. L.; Gopalan, M. *J. Phys. Chem.* **1968**, *72*, 309-&.

(68) Hong, L. Z.; Liu, G. J. *Macromolecules,* **2010**, *43*, 3941-3946.

(69) Li, X. Y.; Liu, G. J. *Langmuir* **2009**, *25*, 10811-10819.

(70) Breiner, U.; Krappe, U.; Abetz, V.; Stadler, R. *Macromol. Chem. Phys.* **1997**, *198*, 1051-1083.

(71) Bates, F. S.; Fredrickson, G. H. *Phys. Today* **1999**, *52*, 32-38.

(72) Li, X. Y. a. L., G. J. *Soft Matter* **2011**.

(73) Kim, J.; Efimenko, K.; Genzer, J.; Carbonell, R. G. *Macromolecules* **2007**, *40*, 588-597.

(74) Xu, Z. D.; Hadjichristidis, N.; Fetters, L. J.; Mays, J. W. In *Physical Properties of Polymers* **1995**; Vol. 120, p 1-50.

(75) de Gennes, P. J. *Scaling Concepts in Polymer Physics*; Cornell University Press: Ithaca, **1979**.

(76) Zheng, R. H.; Liu, G. J.; Yan, X. H. *J. Am. Chem. Soc.* **2005**, *127*, 15358-15359.

(77) Zhou, Z. H.; Liu, G. J.; Hong, L. Z. *Biomacromolecules,* **2010**, *12,* 813-823.

(78) Xiong, D. A.; Liu, G. J.; Zhang, J. G.; Duncan, S. *Chem. Mater.*, **2011**, *23*, 2810-2820.

(79) Tuteja, A.; Choi, W.; Ma, M. L.; Mabry, J. M.; Mazzella, S. A.; Rutledge, G. C.; McKinley, G. H.; Cohen, R. E. *Science* **2007**, *318*, 1618-1622.

(80) Gao, X. F.; Jiang, L. *Nature* **2004**, *432*, 36-36.

(81) Brittain, W. J.; Minko, S. *J. Polym. Sci., Part A: Polym. Chem.* **2007**, *45*, 3505-3512.

(82) Wu, T.; Efimenko, K.; Genzer, J. *J. Am. Chem. Soc.* **2002**, *124,* 9394-9395.

(83) Kassis, C. M.; Steehler, J. K.; Betts, D. E.; Guan, Z. B.; Romack, T. J.; DeSimone, J. M.; Linton, R. W. *Macromolecules* **1996**, *29*, 3247-3254.

(84) Liu, G. J.; Yan, X. H.; Duncan, S. *Macromolecules* **2002**, *35*, 9788-9793.

(85) Tao, J.; Stewart, S.; Liu, G. J.; Yang, M. L. *Macromolecules* **1997**, *30*, 2738-2745.

(86) Halperin, A.; Alexander, S. *Macromolecules* **1989**, *22*, 2403-2412.

(87) Choi, S. H.; Lodge, T. P.; Bates, F. S. *Phys. Rev. Lett.*, **2010**, *104*, 0470802.

(88) Wei, Z.; Wang, Z. G. *Macromolecules* **1995**, *28*, 7215-7223.

(89) *Polymer Handbook*; Fourth Edition ed.; Wiley: New York, **1999**.

Chapter 4

AFM Imaging of End-Functionalized PDMAEMA and Its End-Cyclized Products

4.1 Introduction

Although the preparation of macrocyclic polymers or macrocycles has been successfully achieved by various strategies, the monitoring of product purity remains an issue. The competition between intra-chain and inter-chain reactions decides the composition of the product. Side reactions, such as intermolecular reactions, produce dimers and higher molecular weight linear polymer contaminants. Small amounts of linear polymers will interfere with the physical properties of a bulk macrocyclic product.[1] Therefore, distinguishing the two classes of species becomes essential for the characterization of macrocyclic products.

SEC is the most commonly used method to distinguish macrocycles from their by-products and determine their purity.[2,3] This is achieved by comparing the hydrodynamic volumes of the macrocycles with those of their linear precursors. Based on universal SEC calibrations, the apparent molecular weight (M_{app}) of a macrocycle is typically about 80% of its true molecular weight.[4,5] However, the resolution of SEC is limited so that large difference in molecular weight is required for complete resolution.[6] Furthermore, the axial dispersion of the column and partition and adsorption effect, e.g. non-size exclusive interactions between the columns and sample molecules, will also jeopardize the results.[7-10] In addition, the usage of RI detecting system, which is a universal detector for SEC, leads to a lower reproducibility of the calculated molecular weight. This occurs because the system needs to be calibrated with narrow standards to determine molecular weight values using a SEC system equipped with a RI detector. The combination of the calibration curve and the retention time of the sample provide the calculated molecular weight. A 0.1% change of eluent flow rate can cause a 10% error in the calculated molecular weight.[11] These disadvantages diminish the reliability of SEC for distinguishing polydisperse macrocyclic polymers from their linear precursors. Macrocyclic polymers were also characterized by other techniques, such as matrix-assisted laser desorption/ionization time-of-flight mass spectrometry (MALDI-TOF MS)[12-17]. Linear impurities are identified by their molar masses, which differ from those of their macrocyclic analogues. However, this method works only for polymers with low or moderate molecular weights, ranging up to ~10^4 Daltons.[18]

Atomic force microscopy (AFM) is a scanning probe microscopy technique with a spatial resolution on the subnanometer scale, which can differentiate materials with different physical properties.[19-21] AFM has been used to record images of samples at very low scales, for example, single DNA molecules,[22,23] and more recently individual polyelectrolyte (PE) chains.[24] In most of these studies, samples were deposited onto solid substrates, such as mica or graphite, from dilute solutions. However, visualization of flexible single-chain polymers is still challenging,[25-27] due to their high mobility and small size. For samples to be resolved by AFM, they must be immobilized onto substrates. To visualize charged polymeric chains, a substrate with a complimentary charge is used to immobilize the polymer chains via electrostatic interactions. In some cases,[28,29] strong van der Waals interactions are also used for the adsorption of the PE onto weakly charged surfaces or onto a surface with the same charge as the PE. In addition, magnification of the polymer chain is necessary to obtain clear AFM images. Polymeric combs prepared by grafting linear or dendron-like polymeric chains onto the polymer backbone are typically used for this purpose.[21] Mineralization of PE chains was another technique to enhance the contrast between the polymeric chains and the substrate.[30] Despite all of these reported examples, AFM was only occasionally used to record images of macrocyclic polymers bearing grafted chains.[31,32]

This chapter focuses on the AFM imaging of hydrophobic end-functionalized PDMAEMA chains and their cyclized products. The triblock copolymer PCEMA-*b*-PDMAEMA-*b*-PCEMA (CDC, Scheme 4.1) bearing short PCEMA (C) end-blocks and a long central PDMAEMA (D) block, are used in this study. To facilitate the imaging of single polymer chains, stronger interactions between the polyelectrolyte and the substrate and a longer polyelectrolyte chain with a stiffer back-bone is preferred. For this very reason, we chose the D block as the central block, as will be discussed in greater detail in Section 4.3.1. Three different compounds were used to react with the tertiary amine groups in the D blocks, to magnify the chains. The magnification effects of these three compounds were studied and compared. The compound exhibiting the best effect was chosen for the next step to modify the chains for AFM imaging.

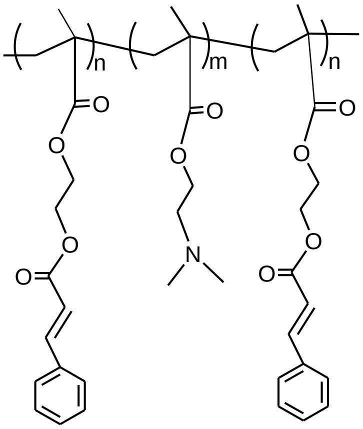

Scheme 4.1. Structure of the copolymer PCEMA-*b*-PDMAEMA-*b*-PCEMA (CDC).

The C block is photo-crosslinkable. The macrocycles could be prepared by the association of C blocks in a selective solvent for the D block, in which the C blocks collapsed together to decrease the interfacial energy. The end-coupling reaction was performed in aqueous HCl solutions at different pH values. The polymer concentration was kept below its CMC, which to prevent inter-chain coupling. Meanwhile, the pH effect on the cyclization yield was also studied. SEC was be used to determine M_{app} or the retention time of the crosslinked products. Since the area of SEC peaks is related to the concentration of the copolymer, and the macrocyclic and linear products share the same molecular weight, the ratio of the macrocycles to the linear chains of the crosslinked products can be obtained by comparing the integration of the areas of the peaks assigned to the linear and macrocyclic chains. Meanwhile, the population of the macrocyclic product and its linear precursor would be determined from AFM images by counting the macrocycles and linear impurities observed in the AFM images. Based on these populations, the cyclization yield may be determined and can subsequently be compared with obtained from SEC analysis.

4.2 Experimental

Materials. Benzyl bromide (98%), *p*-xylene dibromide (98%), 4’-bromomethyl-2-biphenylcarbonitril (BBC, 97%), cinnamoyl chloride (98%), 4,4’-dipyridyl (98%), and nitromethane (95+%) were purchased from Aldrich and used as received. Pyridine (Fisher Scientific) was refluxed and distilled over CaH_2 under nitrogen. Triethylamine (TEA, Aldrich, 99.5%) was refluxed in the presence of *p*-toluensulfonyl chloride for 8 h and then distilled. Naphthalene (Aldrich, 99%) was purified by vacuum sublimation.

1,1-Diphenylethylene was distilled sequentially over calcium hydride and *n*-butyllithium. Benzyl(4-bromomethylbenzyl)viologen (BBBV) was synthesized following a literature method.[33]

Synthesis of PHEMA-*b*-PDMAEMA-*b*-PHEMA. The precursor CDC, PHEMA-*b*-PDMAEMA-*b*-PHEMA, was derived from the hydrolysis of P(HEMA-TMS)-*b*-PDMAEMA-*b*-P(HEMA-TMS), which was prepared by sequential anionic polymerization of DMAEMA and HEMA-TMS with the difunctional initiator 1,4-dilithio-1,1,4,4-tetraphenylbutane.[34] Anionic polymerization was performed following standard procedures in THF at -78 ^{o}C.[35] The diinitiators were prepared *in situ* by reacting lithium naphthalenide with 1,1-diphenylethylene at a molar ratio of 1 to 1.5, respectively. DMAEMA and HEMA-TMS were polymerized for 3.0 h and 2.5 h, respectively. PHEMA-*b*-PDMAEMA-*b*-PHEMA was obtained by the hydrolysis of P(HEMA-TMS)-*b*-PDMAEMA-*b*-P(HEMA-TMS) in a solvent mixture of THF/water (v/v/v = 3/1/0.05). After the copolymer was precipitated with *n*-hexane and dried under vacuum, it was collected as a foamy white solid in an essentially quantitative yield.

Preparation and Purification of the linear precursors PCEMA-*b*-PDMAEMA-*b*-PCEMA (CDC). The terpolymer PCEMA-*b*-PDMAEMA-*b*-PCEMA was synthesized by the reaction of the precursors PHEMA-*b*-PDMAEMA-*b*-PHEMA with cinnamoyl chloride. The polymer was abbreviated as $C_{60}D_{476}C_{60}$, with the subscripts representing the number of repeat units of each block. The HEMA block was reacted with cinnamoyl chloride, yielding CEMA.

In a typical preparation, 500.0 mg of PHEMA-*b*-PDMAEMA-*b*-PHEMA (containing 0.86 mmol of hydroxyl groups for both PHEMA block), was dissolved into 20 mL of dry pyridine, and 0.4 mL of triethylamine (2.87 mmol) was then added. Into this solution, 300 mg (1.80 mmol) of cinnamoyl chloride was added under vigorous stirring. After the solution was stirred overnight at room temperature, it was then dialyzed against methanol, using a dialysis tube with a 12 000-14 000 g/mol cut-off. The solvent was then removed via rotary evaporation and dried under vacuum. Approximately 450 mg of yellow powder-like product was obtained.

All of the final products contained impurities with lower molecular weights, which might have resulted from a one-sided initiation of the diinitiator during the polymerization. The polymers were fractioned by SEC to obtain the purified product. The yield of the SEC fractionation was ~ 60%.

Critical Micelle Concentration (CMC) Determination of $C_{60}D_{476}C_{60}$. The CMC of $C_{60}D_{476}C_{60}$ was determined with dynamic light scattering (DLS) in HCl/water mixtures with the HCl concentration $C_{HCl} = 0.4$ M. DLS measurements were performed using a Brookhaven BI-200 SM instrument equipped with a BI-9000AT digital correlator and a He-Ne laser (632.8 nm). Measurements were performed at angle 90° at ambient temperature.

Fabrication of the Macrocyclic $C_{60}D_{476}C_{60}$. The triblock copolymer $C_{60}D_{476}C_{60}$ was dissolved in an aqueous hydrochloric acid solution with pH between 0.4 and 1.5. Under these conditions, the PDMAEMA block was protonated and soluble, while the PCEMA blocks were insoluble in this solvent. The concentration of the copolymer was ~ 0.05 mg/mL. The solution was then transferred into a solvent reservoir, which was subjected to constant stirring and irradiation. The reactor temperature was regulated to 25 °C. After photolysis, the solution was neutralized by sodium hydroxide until precipitate appeared (pH~11). The solid samples were obtained in quantitative yield after chloroform extraction, which was followed by rotary-evaporation of solvent.

The focused irradiation beam was from a 500 W mercury lamp in an Oriel 6140 lamp housing, which was powered by an Oriel 6128 power supply. The beam was filtered by a 270 nm cut-off filter to remove short-wavelength light. The CEMA double bond conversion was monitored by measuring the CEMA absorbance decrease at 276 nm, by UV-visible spectroscopy.[36] After UV-irradiation, the CEMA double bond conversions were ~ 60%.

Size Exclusion Chromatography (SEC) and Nuclear Magnetic Resonance. SEC analysis was performed on a system consisting of a 1200 series Agilent isocratic pump, a Wyatt Wish-01 high-pressure injector equipped with a 20 μL loop, a Wyatt DAWN HELLOS-II multiangle laser light scattering, or LS, detector (658 nm, 120 mW) and a Wyatt Optilab rEX refractometer (658 nm). The μ-Styragel columns used were

Waters HT 5, HT 4, and 500 Å columns. Chloroform, with a 2% volume fraction of triethylamine, was used as the eluent. The flow rate was 1.00 mL/min. All samples were analyzed at comparable polymer concentrations of 6-8 mg/mL and were filtered through 0.1 μm Whatman PTFE syringe filters before injection.

All ^{1}H NMR measurements were carried out on a Bruker Avance-400 instrument in deuterated pyridine.

Molecular Weight Determination. The weight-average molecular weight (M_w) of $C_{49}D_{391}C_{49}$ and $C_{60}D_{476}C_{60}$ were determined in THF using a Wyatt DAWN HELEOS-II multiangle LS detector in batch mode. To determine the specific refractive index increments dn_r/dc, the refractive index differences Δn_r between a series of $C_{49}D_{391}C_{49}$ and $C_{60}D_{476}C_{60}$ solutions and the THF solvent THF were measured using a Wyatt Optilab rEX refractometer. The Δn_r data were then plotted against the polymer concentration c, and the dn_r/dc values were obtained from the slopes of these linear plots. Before LS measurements were recorded, the samples were clarified by filtering them through 0.1 μm Whatman PTFE syringe filters.

Quaternization of D. Three compounds were used to quaternize the D block. They were benzyl bromide, BBC and BBBV. BBBV was synthesized following a literature procedure.[33] The procedure for reacting BBC or benzyl bromide with the D block is as follows. The linear precursor or the macrocyclic $C_{60}D_{476}C_{60}$ copolymer was dissolved in nitromethane at a concentration of 5.0 mg/mL. To this solution, BBC or benzyl bromide (BBC/benzyl bromide:DMAEMA = 1.5:1, molar ratio) was added. The solution was stirred overnight at room temperature. The resultant solution was then precipitated from diethyl ether. The obtained precipitate was then washed with chloroform and THF. The resulted product quaternized with BBC was vacuum dried and analyzed by ^{1}H NMR, which is included in supporting information.

Quaternization of the D block by BBBV followed a similar procedure as that for BBC, except methanol was used as the solvent instead of nitromethane. After the reaction, the solution was then dialyzed three times against methanol using a dialysis tube with a 12 000-14 000 g/mol cut-off. ^{1}H NMR spectra of the product is included in the Appendix.

Atomic Form Microscopy (AFM) Sample Preparation and Analysis. Tapping mode atomic force microscopy (AFM) studies were performed using a Veeco Multimode Microscope equipped with a Nanoscope IIIa Controller. For AFM measurements, silicon tips with a force constant and oscillating frequency of approximately 40 N/m and 300 kHz, respectively, were used. Specimens were prepared by depositing the quaternized PDMAEMA molecules onto freshly-cleaved mica from a very dilute (0.0005 mg/mL) methanol solution. Drops of the examining solution were set on the substrate for 10 s, and then were removed with a flow of air.

4.3 Results and Discussions

4.3.1 Polymer Design and Synthesis

For this study, four triblock copolymers were designed, synthesized, and characterized, and these copolymers included $C_{12}D_{246}C_{12}$, $C_{17}D_{414}C_{17}$, $C_{49}D_{391}C_{49}$ and $C_{60}D_{476}C_{60}$. The chemical structure of the triblock copolymer CDC is shown in Scheme 4.1. The subscripts refer to the number of repeat units for the different blocks. The CDC polymers were obtained by reacting PHEMA-*b*-PDMAEMA-*b*-PHEMA with cinnamoyl chloride,[36] at 1.5 molar equivalents relative to the PHEMA hydroxyl groups. The product was purified by dialysis with dialysis tube against MeOH, and the dialysis solvent was changed three times at 8 h intervals to remove the low molecular weight impurities.

The C block was chosen because it could be photo-crosslinked.[36] Macrocycles were made firstly by the pre-association of the linear precursor CDC into a ring-conformation through the intra-chain aggregation of the C end-blocks in a poor solvent. The polymer concentration was dilute (0.05 mg/mL) to prevent the inter-chain association of the C blocks. The macrocyclic structures of polymer chains were then permanently locked by photo-crosslinking the CEMA units of the C block. There are two reasons to choose D as the central block. Firstly, the tertiary amine groups of the D chains can be quaternized, thus yielding cationic chains that could be immobilized onto the surfaces of mica plates through strong electrostatic interactions. Secondly, using a bulky compound to quaternize D block could enlarge the dimensions of the polymer chain. These two properties of the D block would facilitate the use of AFM to visualize the individual macrocyclic chains.

The four copolymers we designed to possess similar D block lengths (except for $C_{12}D_{246}C_{12}$) of ~400 units and various C block lengths ranging from 10 to 60 units. The length of the C block was varied for these copolymers, because we initially wanted to test the effect of the C block length on the cyclization yield. However, the cyclization yields of the four copolymers were not found to vary substantially. In this chapter, only the cyclization yield obtained for the $C_{60}D_{476}C_{60}$ copolymer will be discussed. Some of the results for the other three polymers $C_{12}D_{246}C_{12}$, $C_{17}D_{414}C_{17}$ and $C_{49}D_{391}C_{49}$, will be included in the Appendix D.

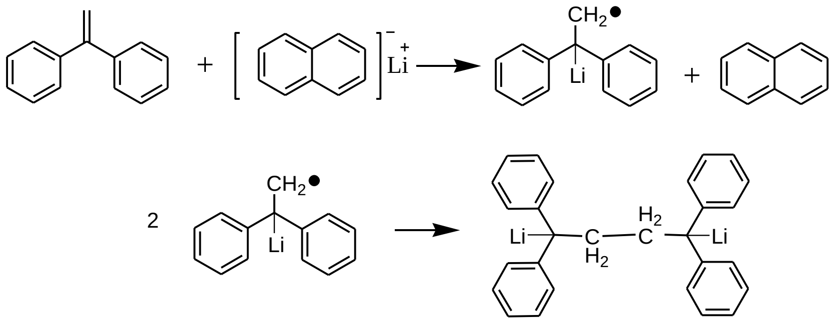

Scheme 4.2. Reaction used for producing the diinitiator.

To synthesize P(HEMA-TMS)-*b*-PDMAEMA-*b*-P(HEMA-TMS), the initiator was prepared *in situ* from the reaction between diphenylethylene and lithium naphthalide (Scheme 4.2).[37] P(HEMA-TMS)-*b*-PDMAEMA-*b*-P(HEMA-TMS) was prepared from the sequential polymerization of DMAEMA and HEMA-TMS. After removal of the TMS group, $H_{60}D_{476}H_{60}$ was produced.

4.3.2 Polymer Purification and Characterization

The resultant $C_{60}D_{476}C_{60}$ copolymer obtained after cinnamation was characterized by SEC (chloroform with a 2% volume fraction of triethylamine as the eluent) and the SEC trace (solid line) is shown in Figure 4.1. Evidently, shoulders representing impurities were visible in the high and low molecular weight ends of the main peak. The high molecular weight shoulder may be due to the oxidization of the D block, since it was occasionally observed for $H_{60}D_{476}H_{60}$ as well. Based on conventional calibration calculations, the molecular weight of the low molecular weight impurity was approximately half of that of the targeted copolymer (middle peak). Therefore, this might represent a diblock copolymer impurity, which would form during the polymerization from the diinitiator if one of the initiating points was killed by impurities.

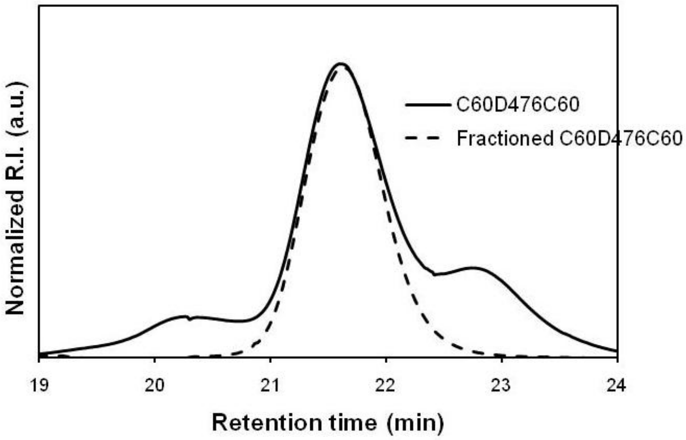

Figure 4.1. SEC curves for the crude product (solid line), $C_{60}D_{476}C_{60}$, and of the product obtained after SEC fractionation (dashed line).

Much effort has been devoted to the fractionation of the copolymer products. However, it seems very difficult to obtain pure product by the fractional precipitation method, since the copolymer and its impurities have very close block ratios. The samples were fractioned by SEC in a small scale, and the SEC trace of the purified product is shown in Figure 4.1(as a dashed line). The SEC traces for the three portions of the copolymer fraction are shown in Figure AC.1 of Appendix C. Since the three peaks were very close to each other in the SEC trace, some of the triblock copolymer $C_{60}D_{476}C_{60}$ would be lost with the high and low molecular weight impurities during the fractionation. The total yield of the SEC fractionation is approximately 60%. The effect of the loss of the low molecular weight $C_{60}D_{476}C_{60}$ on the cyclization yield will be discussed later in Section 4.3.8.

Table 4.1 shows the characteristics for the fractionated $C_{60}D_{476}C_{60}$ copolymer. The ratios between the repeat unit numbers of different blocks (n/m) were obtained from ^{1}H NMR spectra by comparing the signal integrals corresponding to the C and D blocks. The weight-average molecular weights (M_w) and polydispersity indices (M_w/M_n) were obtained from static light scattering measurements in THF. The weight-average repeat unit numbers (n and m for the C and D blocks, respectively) were calculated using the n/m values obtained by ^{1}H NMR spectroscopy and the M_w values obtained by LS measurements, respectively. These n and m values matched reasonably well with their targeted values, which were 70, 400, and 70 for $C_{60}D_{476}C_{60}$.

Table 4.1. Characterization of $C_{60}D_{476}C_{60}$.

Polymer	D/C[a]	dn_r/dc (mL/g)	M_w	$n/m/n$	PDI
$C_{60}D_{476}C_{60}$	4/1	0.083 ± 0.002	1.05 e5[b]	60/476/60	1.05

[a]Determined from ^{1}H NMR analysis. [b]Determined from static LS.

4.3.3 Optimization of the Cyclization Conditions

A new methodology to prepare the macrocycles was recently proposed by our group.[38] Theoretically, if the triblock copolymer CDC was dissolved in a selective solvent for the central block D, polymer chains with a pompom-coil-pompom (or PCP) structure would be formed (Scheme 4.3), with the collapsed terminal C blocks forming individual pompoms. If the solvent was even worse for the C end-block, a closed ring-like structure would form (Scheme 4.3). Energetically, the PCP structure was more entropically favourable than the macrocyclic structure. The driving force for the structural to change from PCPs to macrocycles was the reduction of interfacial free energy when the two pompom structures fused together to form a globule. Therefore, two classes of species would be obtained after the photo-irradiation of CDC in selective solvents for the D block: PCPs and macrocycles.

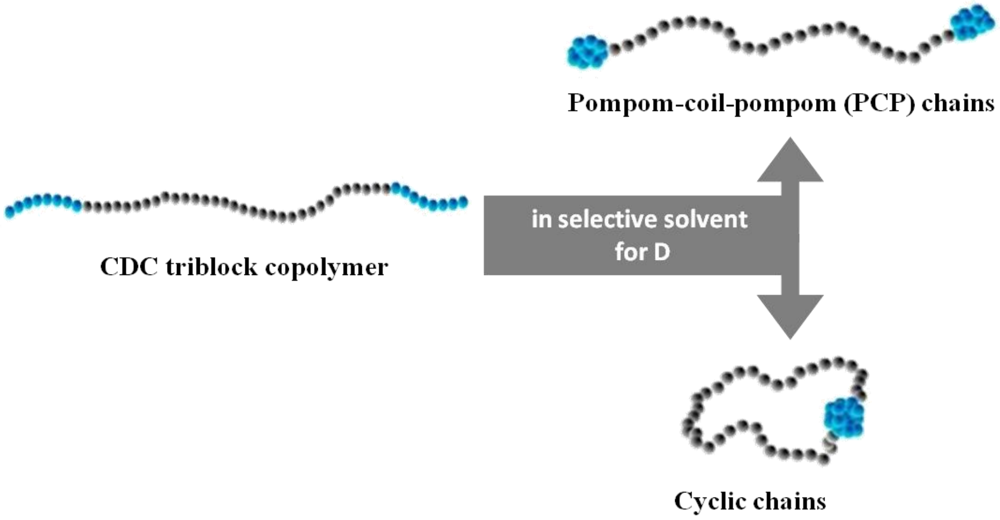

Scheme 4.3. Scheme for pompom-coil-pompom (PCP) and cyclic CDC chains in selective solvent for D.

The solvent system must meet two general criteria for macrocycles of CDC to form. Firstly, the solvent should be poor for the terminal C blocks, but good for the central D block. Therefore, the C blocks may collapse together into a single globule to minimize the surface energy if the solution is sufficiently dilute (in concentrated solutions, the polymer chains would form micelles). However, an assumption made in this ideal situation is that the central D block is a coiled chain. Otherwise, if the central block is rigid, the increased bending energy encountered during the transformation of the central block from a random coil chain to a macrocyclic structure will greatly overwhelm the decrease of the interfacial energy resulting from the fusion of the end blocks. Therefore, the second requirement is that the D block should behave as a coil chain in the selective solvent.

$C_{49}D_{391}C_{49}$ was initially used to find the optimal cyclization conditions. Efforts were made to find solvents, or solvent mixtures, in which $C_{49}D_{391}C_{49}$ gave the highest cyclization yield after crosslinking was performed. Cyclization of the $C_{49}D_{391}C_{49}$ copolymer was tested in several different organic solvents and solvent mixtures. However, only PCP structures were produced according to the SEC results. However, it was found that in aqueous HCl solutions with pH values near 0, a longer retention time was observed, indicating the formation of macrocyclic chains. Some of these SEC results are included in Appendix D. As water generally has a higher interfacial tension with the C block than most organic solvents, it is reasonable to anticipate that macrocycles would form in aqueous HCl solutions rather than in organic solvent mixtures. The reason HCl was added to water was to solubilise the D block, since it could be protonated and form cationic chains under acidic conditions when the pH was below 5.5.[39] The high ionic strength of the solution would screen the charges on the D block, causing the polyelectrolyte chain to become less stiff.

4.3.4 Macrocycle Fabrication and Characterization via SEC

$C_{60}D_{476}C_{60}$ was used as a precursor to fabricate macrocycles. The polymer was firstly dissolved into aqueous hydrochloric acid solutions at different pH values. In the aqueous solution, the C blocks were insoluble and tended to collapse together and form a globule. To prevent the C blocks of different polymer chains from associating with one another, the concentration of the polymer chain (0.05 mg/mL) was kept below the critical micelle concentration (CMC, which will be discussed later in this Section). Thus, polymers in macrocyclic conformations were formed by the intra-chain aggregation of the C end-blocks. The structures were then locked by photo-crosslinking the C-blocks.

To determine the CMC of the $C_{60}D_{476}C_{60}$ copolymer in aqueous HCl solutions with C_{HCl} = 0.4 M (pH = 0.4), DLS was used to investigate the intensity change (Figure 4.2). The CMC of $C_{60}D_{476}C_{60}$ was determined as 0.057 mg/mL, at which point the light scattering intensity increased dramatically. The dramatic increased light scattering intensity indicated the formation of larger scale aggregates, such as dimers, trimers, or micelles.

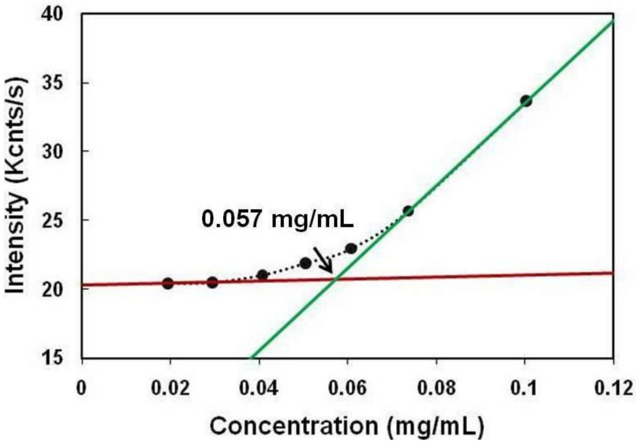

Figure 4.2. Dynamic light scattering intensity versus the concentration of $C_{60}D_{476}C_{60}$ in hydrochloride acid aqueous solution with C_{HCl} = 0.4 M.

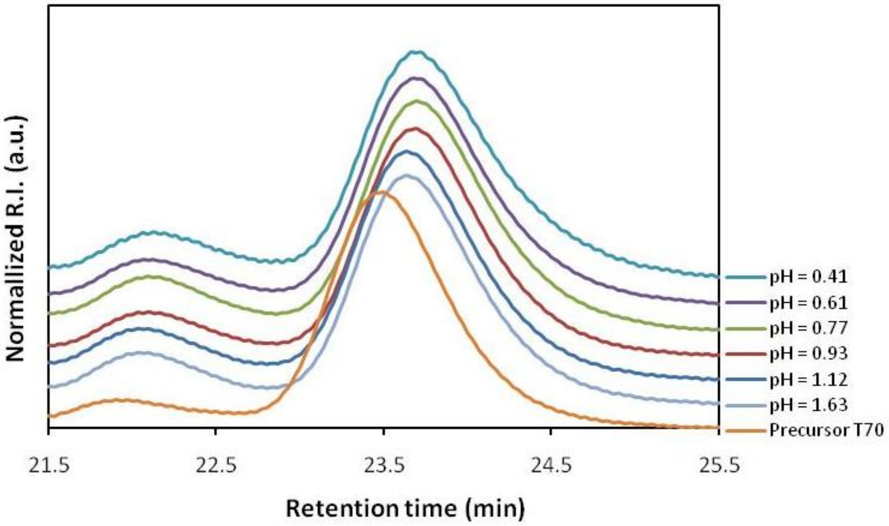

Figure 4.3. SEC curves of the precursory $C_{60}D_{476}C_{60}$ copolymer chain and its crosslinked products.

The crosslinked products, which were prepared under various solvent conditions, were characterized by SEC. As mentioned earlier in Chapter 1, the apparent molecular weight of a macrocycle, was calculated to be 80% of the molecular weight of its linear precursor.[4,5] In a previous study conducted by our group, we found that the apparent molecular weight of a macrocyclic chain is approximately 75% of that of its precursor.[38]

The SEC traces of the crosslinked $C_{60}D_{476}C_{60}$ product are shown in Figure 4.3. The peaks observed at the higher molecular weight region (with shorter retention times) might be due to oxidation of the D block. The main peak involved polymer chains in two different topologies, as PCPs and macrocycles. As discussed earlier, the apparent molecular weights of the macrocyclic chains are lower than those of the PCP chains. From Figure 4.3, it was clear that the peaks shifted toward the lower molecular weights (with longer retention times) as the acidity of the aqueous solution was increased. This shift toward lower molecular weights indicated that the composition of macrocyclic chains increased among the crosslinked products with decreasing pH.

Based on the working mechanism of refractive index (RI) detector, the differential signal is proportional to the concentration. Thus:

$$R_i \propto C_i \propto n_i W_i / \Delta V \tag{4.1}$$

where R_i, C_i, n_i and W_i are the detector signal, the concentration of the solute, the number of moles, and the molecular weight of the polymer, respectively, at the interval i. Meanwhile, ΔV is the elution volume at interval i.

The area of the SEC peak R_{i-area} can be derived from the sum of the R_i values in the elution range:

$$R_{i-area} = \sum_i R_i \cdot \Delta V \propto \sum_i C_i \cdot \Delta V \propto \sum_i n_i W_i \tag{4.2}$$

In this project, the molecular weights and the differential refractive indices, dn_r/dC, of the PCPs and macrocycles were considered to be similar. Therefore, the area ratio of the RI signal can be approximated as being proportional to the ratio of the total number of the chains. If the polymer is monodisperse, this relationship is:

$$R_{i-PCP-area}/R_{i-macrocycle-area} = \sum_i n_{i-PCP}/\sum_i n_{i-\mathrm{macro}cycle} = n_{PCP}/n_{macrocycle} \tag{4.3}$$

Since the SEC elution curve resembled a Gaussian distribution, the area of the SEC peaks was obtained by curve fitting according to Gaussian distribution. The Gaussian function is determined by the following equation:[40]

$$f(x) = \frac{1}{\sqrt{2\pi\sigma^2}} e^{-\frac{(x-\mu)^2}{2\sigma^2}} \tag{4.4}$$

where μ is the peak position of the Gaussian distribution curve and σ^2 is the width of the curve. In this approach, only the peak values corresponding to the PCPs and macrocyclic chains was fixed when fitting the curves. The width of the curve was automatically fitted by the software. The peak positions of peaks on the higher molecular weight side were simply assigned as the maximum values. An example of the curve fitting approach followed is shown in Figure 4.4. From the main peak, two peaks positions were assigned for the PCPs and the macrocycles. For chains with PCP structures, the peak position could be determined based on the crosslinked product observed in HCl/water mixtures with relatively higher pH values, such as at pH = 1.53. It was later verified by AFM that such a sample contained absolutely no macrocycles. Macrocycles were absent in less acidic solutions, because the cations of the protonated D blocks were not fully screened, and thus the protonated D block was not flexible enough to allow the C end-blocks to fuse together. Therefore, only PCP chains formed after UV-crosslinking of the C block. From the SEC curves, the main peak of the precursor was observed at 23.45 min. Meanwhile, the main peak corresponding to the PCP eluted at 23.63 min, which was determined from the crosslinked products prepared in aqueous HCl solutions at pH = 1.53. However, assigning the peak position of the macrocyclic chains by the curve fitting approach was difficult and involved uncertainty. The peak position of the macrocyclic chain was assigned as 24.43 min, which has a delay time of 0.8 min compared with the precursor peak. The delay time of 0.8 min for the peak of macrocycles was estimated from a calibration plot of log$M$t versus the SEC retention times for four standard polystyrene samples (Figure 4.6). This experiment reveals that 25% reduction in the M_w of $C_{60}D_{476}C_{60}$ results in a retention time delay of ~0.8 min.

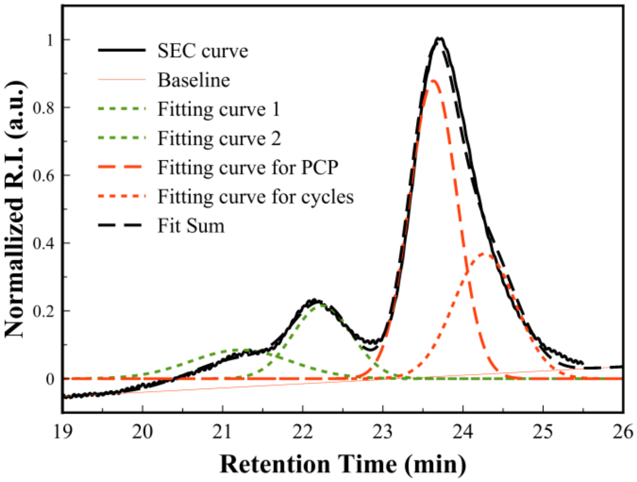

Figure 4.4. An example of an experimental SEC trace, and calculated Gaussian-fitting curves. The fitting curves 1 and 2 are assigned to fit the peaks of the higher molecular weight products. The fitting curves for the PCP and macrocycles are red dashed and dotted line. The sum of the fitting curves from baseline, 1, 2, PCP and macrocycles is shown as the black dotted line, which matches the original SEC curve closely.

Figure 4.5 shows how the delay times of the crosslinked products changed with the acidity of the aqueous solution in which the polymer was crosslinked. When the pH is above ~0.9 (C_{HCl} = 0.13 M), the ionic strength of the solvent is not sufficient to screen the charges on the polymer chains. Consequently, the PDMAEMA block behaves as a semi-rigid chain, due to the ionic repulsion of charges on the protonated D block. Therefore, it is difficult for the PCEMA end-blocks to fuse together. Instead, they collapse individually, and PCP product is obtained after crosslinking. This was confirmed by the small delay time (~ 0.2 min) observed among the SEC traces of the

PCP structures. As the pH decreases or ionic strength increases, more charges on the polymer chains are screened. Thus the ionic repulsion along the protonated D block gets reduced and the D block becomes softer accordingly. The softer the D block, the higher possibility that the end C blocks meet each other to form cycles. Consequently, the ratio of macrocycles in the crosslinked product increases with lower pH of water. Therefore, the optimum solvation conditions for the cyclization of the $C_{60}D_{476}C_{60}$ triblock copolymer is in acidic aqueous media, with pH < 0.9. Further evidence was provided in this context, in which AFM was used to characterize the crosslinked and modified products.

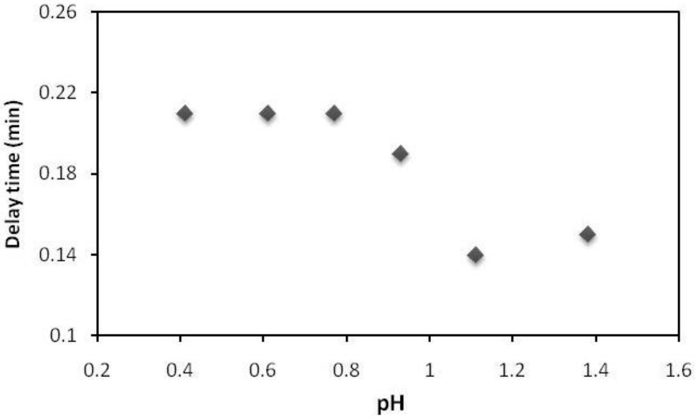

Figure 4.5. Graph of the delay time (retention times of the crosslinked products minus the retention time of the precursor) of crosslinked $C_{60}D_{476}C_{60}$ copolymers versus the pH of the aqueous solution, in which the products were crosslinked.

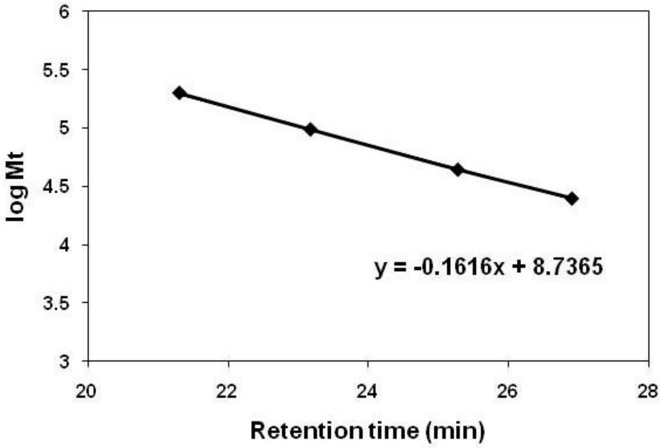

Figure 4.6. Plot of log*M*t versus the SEC retention time for four polystyrene standards.

According to the fitting curve used for both the linear and macrocyclic peaks, the area ratio between the two peaks can be calculated for a sample prepared at each pH value. The calculated area ratios were plotted against the pH values of the acidic solution, as shown in Figure 4.7. The area ratio of the macrocyclic chains suddenly decreased at pH = ~1.0, which coincides with the trend observed from the delay time of the SEC peak. It was shown that the yield of the macrocyclic chains at lower pH values is ~40%, while at higher pH values above ~1.0, the yield of , the macrocyclic chains decreased to ~20%.

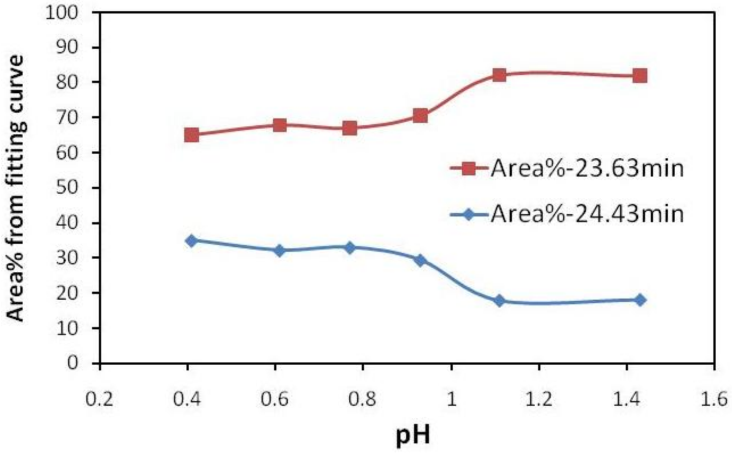

Figure 4.7. Percentage area of the fitting curves with peaks at 23.63 min and 24.43 min from SEC traces of crosslinked products at different pH.

4.3.5 AFM Visualization of Quaternized Single-Chain PHEMA-*b*-PDMAEMA-*b*-PHEMA.

Minko and coworkers reported that AFM could be used for imaging single PE chains on a solid substrate.[24,30,41] The contrast between the polymer chains and the solid substrate could be further enhanced by mineralization of the PE chains.[26] To verify the existence of the macrocycles, AFM provides a direct method, which is superior to SEC analysis.

To observe macrocycles by AFM, the polymeric chain should have sufficient thickness.[42] We used three different reagents, including benzyl bromide, BBC, and BBBV to enlarge the macrocyclic chain via quaternization of the tertiary amine groups in the D block. The quaternized products were confirmed by ^{1}H NMR spectroscopy (Appendix C Figure AC.2, Figure AC.3).

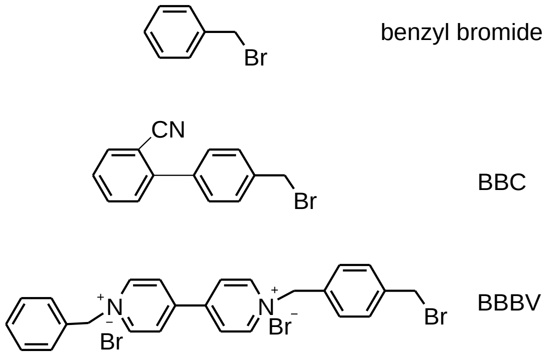

Scheme 4.4. Structures of the quaternization reagents employed in this study.

The triblock copolymer $H_{60}D_{476}H_{60}$ was quaternized via reaction with the three different compounds shown in Scheme 4.4. The AFM images of the quaternized products are shown in Figure 4.8. All of the AFM samples were prepared following the same protocol, and they characterized using the same AFM tip on the same day. As shown in Figure 4.8a, when benzyl bromide was to quaternize $H_{60}D_{476}H_{60}$, the chain-like structures were poorly resolved. This would make it very difficult to distinguish the macrocyclic and linear chains from each other in subsequent step. Meanwhile, when BBC was used as the quaternization reagent (Figure 4.8b), clear chain-like structures were observed. When BBBV was used, products with even better contrast were observed by AFM (Figure 4.8c). The extra cationic center introduced by BBBV enhanced the repulsion between the side chains. This, to some extent, stiffens the polymer chains and eliminates the appearance of the artificial "macrocyclic" chains (the end-blocks of such polymer chains contact one another, but are not connected together covalently).

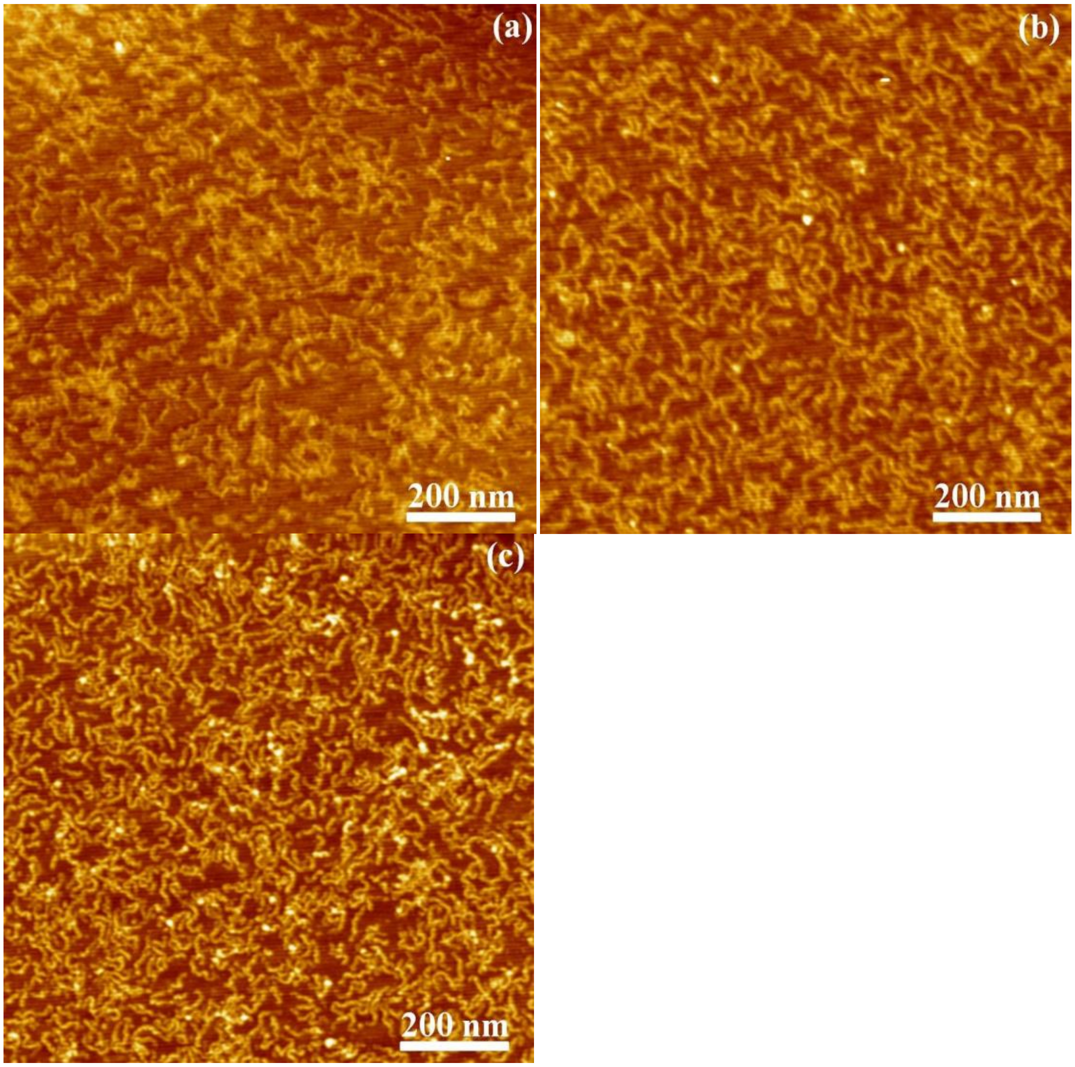

Figure 4.8. AFM images of quaternized $C_{60}D_{476}C_{60}$ with different quaternization reagents benzyl bromide (a), BBC (b), and BBBV (c). The z-scale of all the AFM images was set at 3 nm.

To examine the feasibility of this method, the end-to-end distance of the polymer chains obtained from AFM height images were compared with their theoretical values. The conformations of the PE chains that we observed by AFM were the kinetically frozen structures. The end-to-end distances of each chain observed in the AFM image shown in Figure 4.8c were measured, and are summarized in Figure 4.9. From Figure 4.8c, by measuring over 200 chains, the average end-to-end distance of the quaternized $H_{60}D_{476}H_{60}$ copolymer was found to be ~64 nm. The end-to-end distance (L_n) of a fully stretched chain can be estimated by the equation:

$$L_n = m \times l \tag{4.5}$$

where *m* is the number of repeat units of the DMAEMA block, and *l* is the length of each unit. For $C_{60}D_{476}C_{60}$, m is 476 and *l* is 2 × 0.15 × sin(109.28^{o}/2) nm, which is ~0.25 nm. Thus the end-to-end distance of a fully stretched $C_{60}D_{476}C_{60}$ chain is 476 × 0.25 nm = 119 nm. Meanwhile, the average end-to-end distance of an ideal coil chain can be estimated as $L_n = \sqrt{2mC_\infty}l_0 = \sqrt{2 \times 476 \times 11} \times 0.154\, nm = 15.8\, nm$. The measured length of a $C_{60}D_{476}C_{60}$ chain after quaternization with BBBV is about half of the length of a corresponding fully stretched chain, but is much higher than the length of an ideal coil chain. Thus, the measured chain length of ~50 nm is reasonable for this semi-rigid polymer chain after quaternization with the BBBV reagent. The comparable lengths obtained from experimental measurements and theoretical calculations further confirmed that the chain-like structures observed in the AFM images matched the structures that we expected the single polymer chains to form.

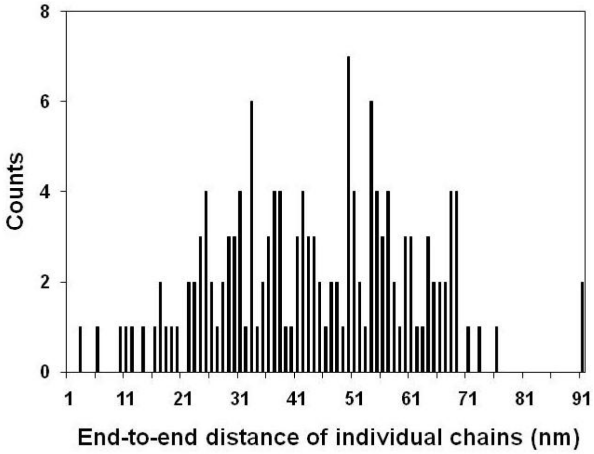

Figure 4.9. Distribution of the end-to-end distances of individual chains measured from the AFM image shown in Figure 4.8c.

The widths of the chains shown in Figure 4.8 can be inaccurate due to a contribution from the size of the AFM tip, but the heights of the chains observed by AFM should be comparable to their actual height, since it is independent of the shape of the AFM tip. The cross-sectional heights of the $C_{60}D_{476}C_{60}$ derivatives prepared from the quaternization reactions were obtained from the AFM height images, and are summarized in Table 4.2. When the heights of the PE chains obtained following the reaction with the three quaternization reagents were compared, it was apparent that the height increased sequentially when larger quaternization reagents were used.

Table 4.2. Average heights of chains obtained from AFM height images of $C_{60}D_{476}C_{60}$ derivatives prepared from different quaternization reagents.

Quaternization reagent	Benzyl bromide	BBC	BBBV
Avg. chain height (nm)	0.2 ± 0.1	0.3 ± 0.1	0.5 ± 0.1

4.3.6 AFM Imaging of Single Polymer Chains.

To enlarge the polymer chain for AFM imaging, the crosslinked products from $C_{60}D_{476}C_{60}$ in aqueous HCl solutions with different pH values were quaternized by BBBV. An AFM image is shown in Figure 4.10 for quaternized $C_{60}D_{476}C_{60}$ derivative, which was crosslinked in aqueous HCl at pH = 0.41. The macrocyclic chains visible in the AFM images are highlighted with green arrows. The linear chains usually adopted relatively stretched morphologies.

The probability of the linear chains forming artificial macrocyclic structures were considered to be very small, because the semi-rigid polymer chain would pay a very high entropic penalty to adopt a macrocyclic structure. Thus, the chains showing ring-like structures in the AFM images should solely represent the macrocyclic chains. The height and phase images of some of the macrocycles in Figure 4.10 were magnified and are shown in Figure 4.11. As can be seen, the AFM phase images gave better contrast for the single polymer chains than the height images.

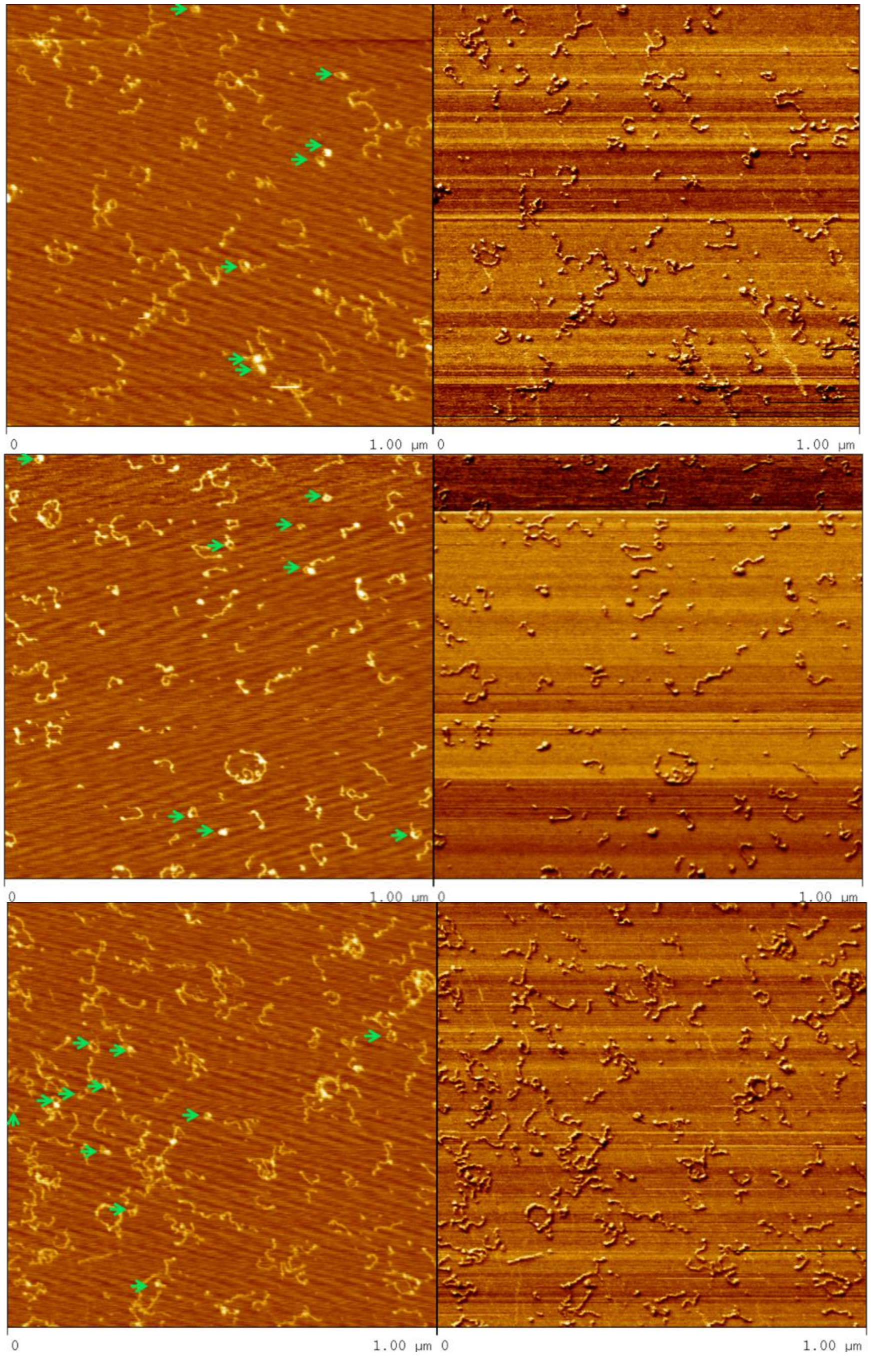

Figure 4.10. AFM height (left) and phase (right) images of a specimen prepared by dropping a methanol solution of the crosslinked $C_{60}D_{476}C_{60}$ copolymer that was modified by BBBV onto a mica substrate. The crosslinked products were obtained from aqueous solutions with a pH of 0.41. The images were obtained by scanning different positions on the same mica substrate. Macrocyclic chains are shown by the green arrows.

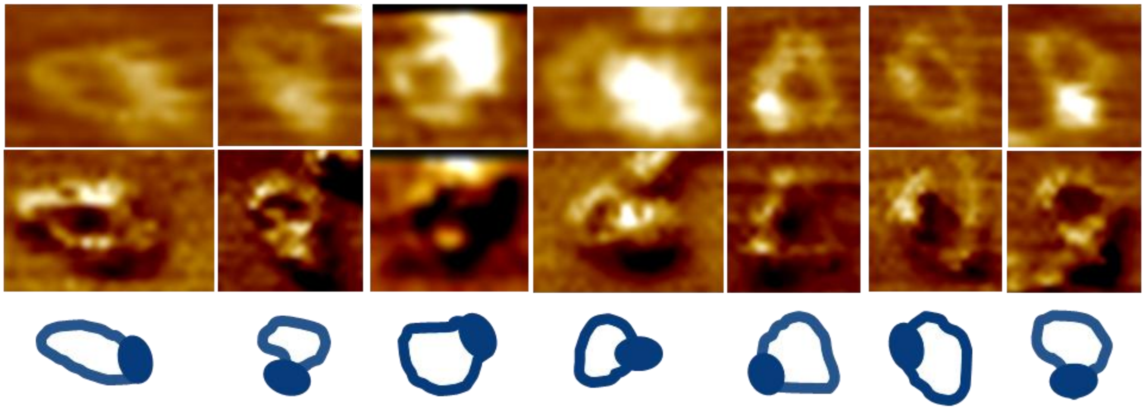

Figure 4.11. Magnified AFM height (upper level) and phase (middle level) images of macrocyclic $C_{60}D_{476}C_{60}$ chains, and their schematic diagrams (lower level).

AFM images of some of the $C_{60}D_{476}C_{60}$ PCP chains were also magnified, and are shown in Figure 4.12. Firstly, we could see they formed dumbbell structures (as shown in the schematic illustration in Figure 4.12) with the terminal C block collapsed and crosslinked at the end of the chains separately. Secondly, some linear chains formed artificial “back-biting” structures, such as the last two AFM images shown in Figure 4.12. These structures appeared similar to macrocycles in the AFM height images, but they could be distinguished from real cycles with the AFM phase images. Therefore, a combination of both the height and phase images should be used to distinguish the macrocycles from the linear chains.

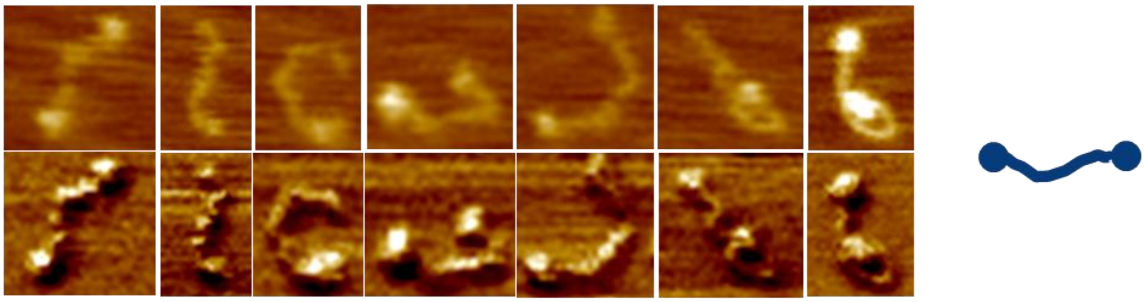

Figure 4.12. Magnified AFM height (left upper) and phase (left lower) images of linear polymer chains and illustration scheme for dumbbell structure (right).

Table 4.3. Numbers of linear and macrocyclic chains of crosslinked $C_{60}D_{476}C_{60}$ in different pH. The number of chains was counted from the AFM images. The polymer chains were quaternized with BBBV.

pH	0.41		0.61		0.77		0.93		1.13-1.63	
AFM	C[a]	L[b]	C	L	C	L	C	L	C	L
#1	11	111	8	55	3	27	3	71	0	-
#2	8	63	18	184	4	30	4	107	0	-
#3	6	56	4	37	5	60	4	75	0	-
Yield$_{cyclic}$	9.8%		9.8%		9.3%		4.1%		0%	

[a] C represents macrocyclic chains. [b] L represents linear chains.

The cyclization yields, determined by counting the number of chains in the AFM images, are given in Table 4.3. At each pH, three AFM images with areas of 1 μm× 1μm were used to count the numbers of linear and macrocyclic chains quaternized with

BBBV. The cyclization yield was calculated as the sum of the macrocyclic chains in all three images divided by the total number of polymer chains observed in the three images.

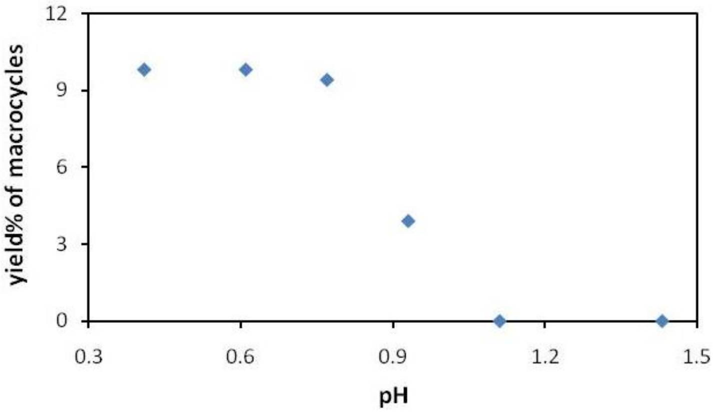

Figure 4.13. Percentage yield of macrocycles in the crosslinked $C_{60}D_{476}C_{60}$ products obtained from aqueous HCl solutions with different pH values. The number of chains was counted from the AFM images.

Even if the optimized conditions were used to prepare the macrocyclic chains from $C_{60}D_{476}C_{60}$, the cyclization yield of the crosslinked product determined from the AFM images was only 10%, which was lower than that obtained from the SEC results. The yields of the crosslinked macrocycles of $C_{60}D_{476}C_{60}$ obtained in aqueous hydrochloric acid solutions at different pH values are shown in the graph in Figure 4.13. At lower pH (<0.8) values, the cyclization yield was about 10%. As the pH was increased, a transition was observed between pH = 0.8 and 1.1. Once the pH was above 1.1, no macrocycles were formed and the cyclization yield decreased to 0%.

4.3.7 Comparison of the Cyclization Yields Obtained from SEC and AFM

The cyclization yields of the crosslinked products obtained from $C_{60}D_{476}C_{60}$ aqueous HCl solutions at different pH values were obtained from both SEC and AFM analysis. Both results were summarized in Figure 4.14 for comparison. From Figure 4.14, the cyclization yield of $C_{60}D_{476}C_{60}$ obtained from both SEC and AFM analysis shared the same trend when plotted against the pH. From the SEC results (the blue dots shown in Figure 4.14), the yield of the macrocyclic product remained near 35% when the pH of the solution was below 0.9 and the yield decreased to ~20% when the pH value was increased above 0.9. In contrast, the yield of macrocyclic chains determined by AFM characterization (around 10%) is much lower than that based on SEC analysis. However, the overall trend was similar in the two results, in that the cyclization yield remained relatively high when the pH was below 0.9, but decreased suddenly when the pH value was increased above 0.9.

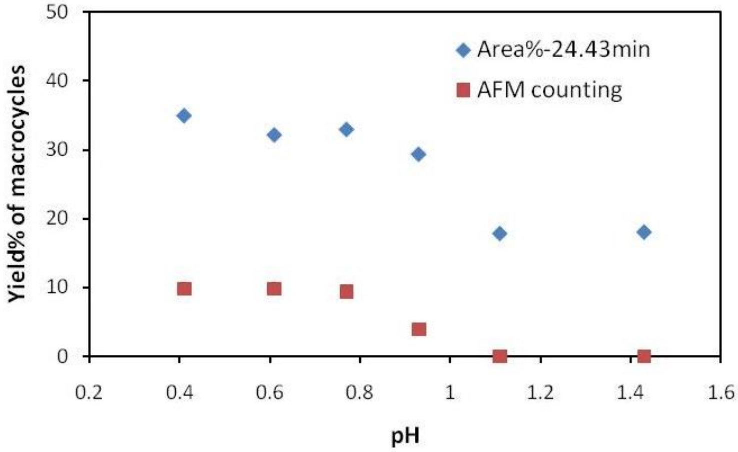

Figure 4.14. Comparison of the cyclization yields of the $C_{60}D_{476}C_{60}$ macrocycles obtained from SEC and AFM analysis.

As mentioned at the beginning of this chapter, SEC is the most widely-used technique for the characterization of macrocycles. However, SEC provides poor resolution. Columns are used to separate the sample particles according to their differences in size, and the stationary has pores with different sizes. When a particle sample is passed through a column, the larger particles are less likely to become entrapped within the pores, and thus will pass through the column more quickly. Meanwhile, the smaller particles are more likely to become embedded within the pores, and will thus pass through the column more slowly. However, in the real situation, the pore sizes of the stationary phase of a column are not well defined, which results in multiple paths that an analyte may follow. In addition, the volumes of the sample particles are not fixed either. These situations result in a broad SEC peak, even for a narrowly dispersed sample. Thus, SEC requires a large molecular weight difference for complete resolution between different samples. However, the apparent molecular weight difference between the macrocycles and their precursor is only 20%. In addition, the apparent molecular weight difference between the macrocycles and the PCP chains is even smaller. These criteria make it very difficult to differentiate the macrocyclic and linear chains by SEC analysis.

Furthermore, the columns separate particles by their size only when there are no interactions between the stationary phase and the particles. Undesired interactions between the column materials and the particles may lead to an asymmetric curve shape, and unreliable results. This is particularly true for samples bearing certain functional groups. In our study, the D block bears tertiary amine side-groups, which requires the addition of salts to the mobile phase to eliminate the interactions between the column and the tertiary amines. However, it still remains in question whether the interactions have been fully eliminated, or were merely suppressed. Last but not least, the RI detector is very sensitive to changes of temperature and pressure. The usage of an RI detector, which is a universal detector for SEC systems, leads to a diminished reproducibility of the calculated molecular weight. A change of the flow rate as small as 0.1% will cause a 10% error in the calculated molecular weight.[11] As a consequence of these limitations, SEC provides a less reliable method to determine the purity of the macrocycles. Based on this reason, cyclization yields based solely on SEC analysis are not reliable.

As shown in the above section, the cyclization yields determined from SEC traces do not agree with the yields calculated by AFM analysis. We believe that the results determined by AFM observation are more reliable, since AFM provides a more direct method, in which the yield is obtained by counting the individual linear and macrocyclic structures in the AFM images. Meanwhile, the SEC method is only useful for showing a trend of the macrocyclic composition changes.

4.3.8 Possible Reasons for the Low Cyclization Yield

The low yield of macrocycles can be attributed to several reasons. As shown in Scheme 4.3, the PCP chains are in equilibrium with the unimer macrocycles.

Thermodynamically, two energies were involved in the formation of the macrocyclic conformation, the interfacial energy of the collapsed C block and the bending energy of the D block. To prepare unimer macrocycles as the major product, the interfacial free energy reduction resulting from the fusion of the C end-blocks of the unimer chain needs to overwhelm the bending energy of the D block. However, the extraordinarily low composition of unimer macrocycles suggests that the unimer macrocycles are not the thermodynamically favoured species. This might be due to that the bending energy of the D block is too high, so that it dictates the chain conformation, and thus PCPs form the predominant structure.

If the effect of the interfacial free energy reduction encountered when the collapsed C blocks merge to form a unimer macrocycle is negligible, the polymer chain CDC can be considered to behave as a homopolymer, D. Jacobson and Stockmayer derived the probability[43] (P_r) at any given instant for finding chain ends in a Θ solvent:

$$P_r = (\frac{3}{2\pi})^3 \frac{v_e}{{R_n}^3} \tag{4.6}$$

where v_e is the reaction volume, in which the end coupling reaction occurs effectively. The term R_n is the root-mean-square end-to-end distance of the polymer chain. In this study, v_e remains the same for all of the end coupling reactions for the C block, and thus:

$$P_r \propto \frac{1}{{R_n}^3} \tag{4.7}$$

When the AFM images (in Figure 4.10) of the crosslinked sample were examined closely, it became apparent that most of the macrocyclic chains were prepared from the $C_{60}D_{476}C_{60}$ copolymer, with relatively short D chains. Meanwhile, the lengths of the PCP chains were much longer (approximately 2 times longer) than those of the macrocyclic chains.

The precursory polymer $C_{60}D_{476}C_{60}$ is a polydisperse sample, with a polydispersity index (PDI) 1.05. The number average molecular weight (M_n) of $C_{60}D_{476}C_{60}$ is calculated as 10^5 g/mol from Table 4.1. The molecular weight distribution of the copolymer can be considered as a Gaussian distribution, and the standard deviation (σ) of the distribution is related to M_n and PDI:[44]

$$\sigma = M_n(\mathrm{PDI} - 1)^{0.5} \tag{4.8}$$

Thus even a small polydispersity index may represent a wide distribution in the chain lengths. For $C_{60}D_{476}C_{60}$, with M_n and PDI values of 10^5 g/mol and 1.05, respectively, the standard deviation σ can be calculated as 22360 g/mol. This represents the molecular weights of the polymer ranging from 3×10^3 to 1.7×10^5 g/mol from points 1 to 7 in Figure 4.15.

According to Equation 4.5, the ratio of the probabilities for finding chain ends for polymer chains with molecular weight marked in Figure 4.15 can be derived as:

$$\frac{P_1}{P2} = (\frac{R_2}{R1})^3 = (\frac{N_2}{N_1})^{3/2} = (\frac{M_{w2}}{M_{w1}})^{3/2} \tag{4.9}$$

where N_1 and N_2 are the numbers of repeat units in Polymers 1 and 2, respectively. Meanwhile, M_{w1} and M_{w2} represent the molecular weights of Polymers 1 and 2, respectively. If the probability of the chain ends of polymers of Point 6 (M_n = 55280 g/mol) in Figure 4.15 contacting each other was set as 100%, the corresponding probabilities for the polymers at Points 2-5 can be calculated as 68, 42, 30 and 24%, respectively. The polymers at Point 1 and 7 were not taken into consideration, since amount of polymer that they represent is very small. This helps to explain the effect of the D block's length on the cyclization yield. With this in mind, the cyclization yield will substantially decrease with increasing length of the D block.

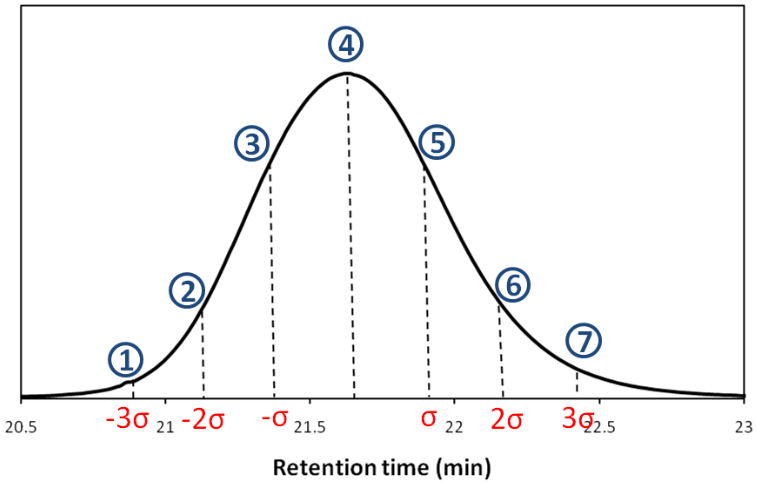

Figure 4.15. SEC trace of a fractionated sample of $C_{60}D_{476}C_{60}$. The interval between the dashed line represents the width of the standard deviation, σ.

The main reason for the low cyclization yield is the stiff backbone of the protonated D block. In acidic aqueous solutions (pH < 5.5), the D block is protonated to form a PE. To the best of our knowledge, attempts to cyclize PEs have not been previously reported. The persistence length is a physical property to indicate the stiffness of a polymer chain, and stiffer chains possess longer persistence lengths. For PE chains, even if high ionic strength (pH down to 0.4) is applied to screen the charges, the persistence length of a PE chain is still much larger than that of a traditional coil polymer chain.

The total persistence length of a PE chain is the sum of the bare persistent length (l_0) and the electrostatic persistence length (l_e).[45] For the D block, l_0 is 0.85 nm, as calculated from the following equation:[46]

$$l_0 = \frac{b}{2} = \frac{(C_\infty + 1)l}{2} \tag{4.10}$$

where b is the Kuhn length, C_∞ is the characteristic ratio of block D (11.0), and l is the bond length of a C-C bond (0.154 nm). The electrostatic persistence length l_e can be as high as tens of nanometers[47] in water with low ionic strength. For intrinsically flexible PE chains, l_e is proportional to the Debye screening length κ:[47,48]

$$l_e \propto \kappa^{-1} \propto I^{-0.5} \sim (c + 2c_s)^{-0.5} \tag{4.11}$$

where I is the ionic strength of the system, while c and c_s are the molar concentrations of the PE and the salt molecules, respectively. Debye and Huckel derived that, for an ideal perfect gas of ions:

$$\kappa_{DH}{}^2 = 4\pi l_B I \tag{4.12}$$

where l_B is the Bjerrum length.

According to Equation 4.11, the ratio of l_e values at different ionic strengths can be calculated with c = 0.05 mg/mL at different values of c_s. The results are summarized in Table 4.4. The expression of $(c + 2c_s)^{-0.5}$ shows how greatly l_e will be depressed by increases of the salt concentration. If the salt concentration is increased from 0.16 to 0.08 mol/mL, which is comparable to changes encountered in this study as the pH was changed from 0.8 to 1.1. l_e decreases by a factor of ~1.4. This stiffness difference can also contribute to the transition region lying between pH = 0.8 and 1.1, as shown in Figure 4.14.

Table 4.4. Calculated $(c + 2c_s)^{-0.5}$ at different c_s values.

c_s (M)	0	0.08 (pH=1.1)	0.16 (pH = 0.8)
$(c + 2c_s)^{-0.5}$ ($M^{-0.5}$)	684.6	2.5	1.8

4.3.9 Conclusions

Described in this chapter is the preparation and characterization of macrocycles from the triblock copolymers CDC. Macrocycles were prepared by photo-crosslinking the pre-associated C blocks of the CDC triblock copolymer in selective solvents for the central D block. The product was characterized by SEC and AFM techniques. By comparing the cyclization yields from both methods, it was found that the yield obtained from SEC analysis was much higher than that calculated from AFM. It was proposed that SEC was an unreliable method for macrocycle characterization and reasons supporting this were raised. Despite this, the two results still shared a similar trend. When the pH was below 0.8, a higher yields were obtained, and they would decrease dramatically when the pH was increased from 0.8 to 1.1. Several possible explanations for the low cyclization yields were discussed.

References

(1) Ragnetti, M.; Geiser, D.; Hocker, H.; Oberthur, R. C. *Makromol. Chem., Macromol. Chem. Phys.* **1985**, *186*, 1701-1709.

(2) Dodgson, K.; Sympson, D.; Semlyen, J. A. *Polymer* **1978**, *19*, 1285-1289.

(3) Dagger, A. C.; Semlyen, J. A. *Polymer* **1999**, *40*, 3243-3245.

(4) Roovers, J.; Toporowski, P. M. *Macromolecules* **1983**, *16*, 843-849.

(5) Lutz, P.; McKenna, G. B.; Rempp, P.; Strazielle, C. *Makromol. Chem. Rapid Comm.* **1986**, *7*, 599-605.

(6) Nagaoka, S.; Akashi, R. *Biomaterials* **1990**, *11*, 419-424.

(7) Mori, S., Barth, H.G. *Size Exclusion Chromatography*; Springer-verlag: Berlin, **1999**.

(8) Cooper, A. R. *Determination of Molecular Weight*; Wiley: New York, **1989**; Vol. 103.

(9) Barth, H. G. *Modern Methods of Polymer Characterization*; Wiley-Interscience: New York, **1991**.

(10) Yau, W. W. K., J. J. *Modern Size-Exclusion Liquid Chromatography: Practice of Gel Permeation and Gel Filtration Chromatography*; Wiley-Interscience: New York, **1979**.

(11) Letot, L.; Lesec, J.; Quivoron, C. *J. Liq. Chromatogr.* **1980**, *3*, 1637-1655.

(12) Blais, J. C.; Tessier, M.; Bolbach, G.; Remaud, B.; Rozes, L.; Guittard, J.; Brunot, A.; Marechal, E.; Tabet, J. C. *Int. J. Mass Spectrom. Ion Processes* **1995**, *144*, 131-138.

(13) Montaudo, G.; Montaudo, M. S.; Puglisi, C.; Samperi, F. *J. Polym. Sci., Part A: Polym. Chem.* **1996**, *34*, 439-447.

(14) Pasch, H.; Gores, F. *Polymer* **1995**, *36*, 1999-2005.

(15) Adachi, K.; Takasugi, H.; Tezuka, Y. *Macromolecules* **2006**, *39*, 5585-5588.

(16) Tezuka, Y.; Ohtsuka, T.; Adachi, K.; Komiya, R.; Ohno, N.; Okui, N. *Macromol. Rapid Comm.* **2008**, *29*, 1237-1241.

(17) Wollheim, T.; Kricheldorf, H. R.; Altstadt, V.; Koning, C. E.; Buning, G. H. W. *High Perform. Polym.* **2001**, *13*, 119-132.

(18) Rader, H. J.; Schrepp, W. *Acta Polym.* **1998**, *49*, 272-293.

(19) Poggi, M. A.; Gadsby, E. D.; Bottomley, L. A.; King, W. P.; Oroudjev, E.; Hansma, H. *Anal. Chem.* **2004**, *76*, 3429-3443.

(20) Magonov, S. N. *Atomic Force Microscopy in Analysis of Polymers*; John Willey and Sons Ltd, **2000**.

(21) Sheiko, S. S.; Moller, M. *Chem. Rev.* **2001**, *101*, 4099-4123.

(22) Vinograd, J.; Lebowitz, J.; Radloff, R.; Watson, R.; Laipis, P. *Proc. Natl. Acad. Sci. U.S.A.* **1965**, *53*, 1104-&.

(23) Klinov, D. V.; Neretina, T. V.; Prokhorov, V. V.; Dobrynina, T. V.; Aldarov, K. G.; Demin, V. V. *Biochem.-Moscow* **2009**, *74*, 1150-1154.

(24) Minko, S.; Roiter, Y. *Curr. Opin. Colloid. Interface Sci.* **2005**, *10*, 9-15.

(25) Prokhorov, V. V.; Nitta, K. H.; Terano, M. *Macromol. Chem. Phys* **2004**, *205*, 179-186.

(26) Gallyamov, M. O.; Khokhlov, A. R.; Moller, M. *Macromol. Rapid Comm.* **2005**, *26*, 456-460.

(27) Kumaki, J.; Nishikawa, Y.; Hashimoto, T. *J. Am. Chem. Soc.* **1996**, *118*, 3321-3322.

(28) Pastre, D.; Pietrement, O.; Fusil, P.; Landousy, F.; Jeusset, J.; David, M. O.; Hamon, C.; Le Cam, E.; Zozime, A. *Biophys. J.* **2003**, *85*, 2507-2518.

(29) Abu-Lail, N. I.; Camesano, T. A. *Biomacromolecules* **2003**, *4*, 1000-1012.

(30) Minko, S.; Kiriy, A.; Gorodyska, G.; Stamm, M. *J. Am. Chem. Soc.* **2002**, *124*, 10192-10197.

(31) Schappacher, M.; Deffieux, A. *Angew. Chem., Int. Ed.* **2009**, *48*, 5930-5933.

(32) Schappacher, M.; Deffieux, A. *J. Am. Chem. Soc.* **2008**, *130*, 14684-14689.

(33) Liu, G. J., *Ph.D. thesis*, University of Toronto, **1989**.

(34) Dou, H. J.; Hong, L. Z.; Liu, G. J. *Macromolecules*, **2010**, *43*, 4629-4637.

(35) Nakahama, S.; Hirao, A. *Prog. Polym. Sci.* **1990**, *15*, 299-335.

(36) Guo, A.; Liu, G. J.; Tao, J. *Macromolecules* **1996**, *29*, 2487-2493.

(37) Gao, H. F.; Matyjaszewski, K. *Macromolecules* **2006**, *39*, 7216-7223.

(38) Hu, J. W.; Zheng, R. H.; Wang, J.; Hong, L. Z.; Liu, G. J. *Macromolecules* **2009**, *42*, 4638-4645.

(39) Rehfeldt, F.; Steitz, R.; Armes, S. P.; Von Klitzing, R.; Gast, A. P.; Tanaka, M. *J. Phys. Chem.B* **2006**, *110*, 9171-9176.

(40) Casella, G. B., R. L. *Statistical Inference (2Ed.)*; Duxbury, **2001**.

(41) Minko, S.; Kiriy, A.; Gorodyska, G.; Stamm, M. *J. Am. Chem. Soc.* **2002**, *124*, 3218-3219.

(42) Schappacher, M.; Deffieux, A. *Science* **2008**, *319*, 1512-1515.

(43) Jacobson, H.; Beckmann, C. O.; Stockmayer, W. H. *J. Chem. Phys.* **1950**, *18*, 1607-1612.

(44) Schriemer, D. C.; Li, L. *Anal. Chem.* **1997**, *69*, 4169-4175.

(45) Ha, B. Y.; Thirumalai, D. *Macromolecules* **1995**, *28*, 577-581.

(46) Dentini, M.; Rinaldi, G.; Risica, D.; Barbetta, A.; Skjak-Braek, G. *Carbohydr. Polym.* **2005**, *59*, 489-499.

(47) Skolnick, J.; Fixman, M. *Macromolecules* **1977**, *10*, 944-948.

(48) Odijk, T. *J. Polym. Sci. Pt. B* **1977**, *15*, 477-483.

(49) Russell, W.R., Burkitt, M.J., Chesson, A. *Bioorg. Chem.* **1999**, *27*, 339-350.

Chapter 5

Conclusions and Future Work

5.1 Conclusions

Triblock copolymers, in comparison with their diblock copolymer counterparts, have more diverse structural, interactional, and compositional variables, and thus yield a greater diversity of micellar morphologies. Because of the complexity of triblock copolymer systems, the current understanding of triblock copolymer self-assembly behaviour is still in its infancy. This thesis is aimed at understanding the self-assembly behaviour of triblock copolymers in solution, and focuses on two aspects: the aggregation of multiple polymer chains (micellar behaviour) and the assembly of single polymer chains (or the assembly of unimer structures).

In the first aspect, ABC triblock copolymers bearing a mesogen-ordering block were studied. Our purpose was to understand the effect of the liquid crystalline block on the formation of the micellar morphologies. Block copolymers bearing mesogenic blocks behave differently from their amorphous counterparts, due to the special chain packing of the mesogen groups. Among coil-coil block copolymers, cylinders are formed only over a very narrow block composition window.[1-5] Coil-crystalline diblock copolymers tend to form bilayer structures when the two blocks have similar compositions, since the crystalline blocks usually fold in two dimensions.[6,7] The formation of cylindrical micelles has been reported for only a small number of coil-crystalline systems, in which the coil block is much longer than the crystalline block.[7-11] However, limited work has been devoted to the formation cylindrical micelles from mesogen containing block copolymer systems.[12]

Triblock copolymers can form the core-shell-corona micelles. Core-shell-corona cylinders with a crosslinkable shell are of interest, because nanotubes can be readily derived by crosslinking the shell block and removing the core block from these cylinders.[13] Subsequently filling these tubular cores with magnetic and semi-conducting inorganic nanoparticles yields solvent-dispersible polymer/inorganic hybrid nanofibers.[14,15] Cutting across core-shell-corona triblock copolymer nanofibers exposes the core chains at the end(s) of a shortened nanofiber. These nanofibers can be readily grafted onto solid substrates.[16] Alternatively, they can be coupled with nanospheres, to yield super-surfactants,[17] or they can be coupled to other types of nanofibers to yield nanofiber multiblocks,[18] which can be hierarchically assembled into supermicelles.

To the best of our knowledge, there have been no reports describing the mesogen-driven formation of core-shell-corona cylindrical micelles from triblock copolymers. Therefore, the first part of this thesis explored the micellization of linear triblock copolymers, ACF and BCF (PAA-*b*-PCEMA-*b*-PF and PtBA-*b*-PCEMA-*b*-PF), which consisted of two coil blocks and one mesogenic block. Several new discoveries were made from this study and solid evidence supporting these discoveries was also provided.

Firstly, a facile route for the preparation of core-shell-corona block copolymer cylindrical micelles was discovered. The core-shell-corona cylindrical micelles were readily formed from the linear triblock copolymers $A_{53}C_{44}F_{13}$, $A_{105}C_{86}F_{19}$, and $B_{53}C_{44}F_{13}$ in various solvent mixtures including TFT/MeOH, TFT/EtOH, and TFT/iPOH over a wide range of solvent composition.

Secondly, the mesogen-ordering of the F block was shown to be a crucial factor for the formation of cylindrical micelles. Direct evidence of mesogen-ordering in the cylindrical micelles was obtained from DSC and WAXS analysis, which revealed the characteristic transitional temperature and the characteristic periodicity, respectively, corresponding to the mesogen-structure of the F block. It was also found that well-defined cylindrical micelles could be prepared by firstly heating the solution to 70 ^{o}C and then slowly cooling the solution to 25 ^{o}C. The mesogenic phase of the F block was in the isotropic phase above 70 ^{o}C, and the slow cooling procedures allowed the F blocks to rearrange themselves into a mesogen-ordered phase, yielding well-defined cylindrical micelles. In addition, the ACF micelles were shown to undergo morphological transitions from large composite micelles or vesicles at high temperatures to cylindrical micelles when they were cooled below the isotropic-to-smectic A phase transition temperature of the F blocks. For the $A_{53}C_{44}F_{13}$ copolymer, this morphological transition was reversible, as observed when heating and cooling cycles were repeated. This demonstrated unambiguously that mesogen-packing-driven cylindrical micelle formation had occurred.

Thirdly, detailed analysis of the TEM images of the ACF cylindrical micelles indicated that the C shell chains were radially compressed compared to their unperturbed dimensions. Also, the coronal A chains were sparsely distributed, so that they did not form a uniform film covering the C shells. Instead, the corona chains aggregated to form ridges to reduce their radial compression and to avoid excessive configurational entropy loss. These features all arose from the mesogen-ordering of the F block, which yielded cylindrical micelles possessing abnormal thicknesses of the shell and corona layers. This is believed to be the first report of micelles with sparsely distributed corona chains.

In the second project, AFM was used to record images of the single-chain structures of CDC (PCEMA-*b*-PDMAEMA-*b*-PCEMA) copolymers with collapsed C end-blocks, and also their cyclized products. These triblock copolymers consisted of a long, hydrophilic central D block, with short hydrophobic C blocks attached at each end. In selective solvents for the D block, the hydrophobic C blocks collapsed, so that the

CDC copolymer yielded pompom-coil-pompom (PCP) structures or macrocycles. The collapsed C blocks formed the pompoms at the ends of the PCP structures. Meanwhile macrocycles were formed if two collapsed C blocks from the same polymer chain merged together into one globule, thus closing the polymer chain. The effect of the pH of the solution on the cyclization yield was studied, and the cyclization yields obtained from SEC- and AFM-based calculations were compared and discussed. A number of conclusions were drawn from this study, as will be summarized in the next few paragraphs.

Firstly, three different reagents were used to quaternize the D block. In addition to introducing cationic charges to the D block, the incorporation of these quaternization agents also enlarged the backbone, and thus enhanced the quality of their AFM images. AFM imaging of single polymer chain is challenging, because of the small diameters and high mobility of individual polymer chains. Three different quaternization reagents, benzyl bromide, BBC, and BBBV were reacted with the D block of the precursory copolymer PHEMA-*b*-PDMAEMA-*b*-PHEMA, and the AFM images of the quaternized products were compared. It was found that polymer chains that were quaternized with BBBV provided the best contrast in the AFM images, since the heights of the chains increased greatly after quaternization with this reagent. Under the same conditions, the polymer chains that were quaternized with BBBV were also less coiled than the polymer chains that were quaternized with either benzyl bromide or BBC. Thus the “artificial macrocycles”, e.g. the end C blocks collapsed with each other instead of connected with each other via covalent bonds, would be greatly reduced in the AFM images if BBBV was used as the quaternization reagent.

Secondly, the end-cyclization of CDC chains was studied in aqueous HCl solutions at different pH values. In selective solvents for the central D block, the two C end-blocks of the unimer chain associated together and ring-like structures were formed. The structures of these macrocycles were covalently locked by photo-crosslinking the C blocks. The pH effect (or equally, the effect of the ionic strength) on the cyclization yield was also studied in detail. The cyclization yield underwent a transition between pH = 0.8 and pH = 1.0. The cyclization yield decreased from pH = 0.8 to pH = 1.0.

Thirdly, both AFM and SEC techniques were used to characterize the end-cyclized CDC structures that were obtained in aqueous HCl solutions at various pH values. Low cyclization yields (~10% and ~30% based on AFM and SEC analysis, respectively) were observed among all of the samples. The AFM results implied that CDC copolymers with shorter D blocks formed macrocycles more readily than those with longer D blocks. The relatively rigid backbone of the polyelectrolyte chain may be a possible reason for these low cyclization yields.

Finally, the cyclization yields based on SEC and AFM characterization were compared. In comparison with AFM analysis, it was found that SEC provided a less reliable method for determining the distribution between macrocycles and linear PCP chains in the end-cyclized product. This was mainly attributed to the low resolution and low reproducibility of the calculated molecular weight of the SEC method. The poor resolution provided by SEC was exacerbated by the relatively small differences between the apparent molecular weight/retention time of the linear and macrocyclic products. In contrast, AFM analysis provided a direct method to observe the distribution between the macrocycles and PCP chains, and subsequently calculate the cyclization yield.

5.2 Future Research

5.2.1 Future Studies on the Mesogen-Driven Morphologies of ACF and BCF Copolymers

Cylindrical micelles from several different copolymers, including ACF and BCF copolymer systems, have been studied in various solvent mixtures of TFT and alcohols. The cylindrical micelles were well-characterized and it has been demonstrated here that mesogen-ordering is crucial for the formation of cylindrical micelles. However, as a unique case of micelles, there are more experiments can be explored on this mesogen-driven formation of cylinders to fully understand it.

Firstly, the role of corona chain in the cylinder structure is still ambiguous. Based on the classic theory of micelles, the corona chains should form a dense layer to avoid the inter-fusion of micelles, which stabilizes the micelles. According to the AFM and TEM images of the ACF cylinders, the corona chains on the surface of the cylinder are scarcely distributed. Meanwhile, the stability of the cylinder is still good. This does not agree with the classic theory for micelles. To understand the relation between the corona chain and the micelle stability, a set of experiments can be performed by varying the length of the corona chain. A series of ACF polymers should be synthesized with fixed C and F block length and different A block length. Under the same solvent conditions of TFT and methanol mixture, the morphology of the micelles formed by different ACF polymers can be observed and compared. Hypothetically, when block A is too short, the corona layer can not stabilize the cylinders and a cluster of cylinders or even a morphological transition might be observed. From this set of experiment, the critical length of block A to stabilize the cylinder can be obtained, which might help us to understand the molecular model of mesogen-driven formation of micelles.

Secondly, the role of middle block in cylinder formation is unclear. A simple experiment to do is to remove the middle block C from the triblock copolymer ACF and examine the micellar morphologies under the same solvent condition (e.g. TFT and methanol mixtures). A new diblock copolymer AF should be made first for the purpose of comparison. If both AF and ACF polymers show similar mesogen-driven cylinder morphologies, then we can conclude that block C does not play an important role in the mesogen-driven morphologies. Otherwise, if block C is demonstrated to be crucial in the mesogen-driven morphologies, further experiments can be done. For example, modify the middle block as C’, which is soluble in the desired solvent mixtures and study the micelle morphologies. This experiment can uncover that if the mesogen-ordering energy can still control the micellar morphologies when the solvophobic and solvophilic block ratio is changed. Besides, the length of the middle block can be changed as well, to see how the middle block length affects the micelle morphologies.

Thirdly, the role of core block in cylinder formation can be further explored. Use of a non-mesogenic (amorphous) block as the core-forming block and fixed the volume fraction of the three blocks the same as the ACF triblock copolymers. Comparison of the micelle morphologies of the amorphous triblock copolymer and ACF triblock copolymer might clarify the role of mesogenic block in the process of cylinder formation.

Fourthly, the kinetics of the cylinder formation are not fully understood. Different cooling rates, for example, may result in cylinders with different lengths or even topologies. Detailed studies on the kinetics of the cylinder formation may be helpful in preparation of cylinders with controllable lengths, which would be of great fundamentally interest. Furthermore, living polymerization of blocky cylinders has been observed in semicrystalline diblock copolymer systems.[8] It would also be interesting to investigate the on-site growth of mesogen-driven cylinders as well.

Lastly, during the experiments, toroidal micelles were occasionally observed as a major product in the TFT/alcohol solutions when the solutions were cooled to an moderate temperature (around 50 ^{o}C). Toroidal micelles are frequently encountered in natural systems, but are scarcely observed among synthetic polymers.[19] If successful, this would represent the first report of the preparation of toroidal micelles from liquid crystalline block copolymers.

5.2.2 Improving the Cyclization Yields of the CDC Copolymers

In the second part of the thesis, we demonstrated that the single polymer chains and unimer macrocycles could be successfully prepared from their linear precursors and observed by AFM. The unimer macrocycles were prepared by photo-crosslinking the pre-associated CDC triblock copolymers. However, the cyclization yields were low for all of the copolymers in the different solvent mixtures examined.

Some possible methods are proposed to improve the cyclization yield of the CDC copolymers. Firstly, triblock CDC copolymers with shorter D blocks could be used. As discussed in Section 4.3.9, a protonated D block is much more rigid than a traditional coil block, and thus requires a higher bending energy. A shorter D block would decrease the end-to-end distance of the polymer chain, and consequently increase the probability (P_r) of the C end-blocks contacting one another. Our AFM results also suggested that unimer macrocycles were obtained from CDC copolymers with relatively short D blocks. Secondly, macrocyclic polyelectrolytes (PEs) can be produced from an alternate approach. Instead of directly end-coupling the PE chains, macrocyclic PEs can also be produced by modifying pre-made macrocycles. Many groups have reported the successful synthesis of macrocycles following this approach.[20] Introducing tertiary amines to a polymer chain is useful for enhancing the quality of its AFM images. However, pendant tertiary amines hamper a polymer chain's ability to form macrocycles. Therefore, macrocycles could be prepared first from the polymer chains before the tertiary amines are incorporated, and subsequently the macrocyclic products may be decorated with tertiary amines. Thirdly, macrocycles can also be modified and magnified by various other methods, such as grafting polymer chains[21] onto the backbone of the unimer macrocycle, or by mineralization.[22]

References

(1) Zhang, L. F.; Eisenberg, A. *Science* **1995**, *268*, 1728-1731.

(2) Shen, H. W.; Eisenberg, A. *J. Phys. Chem. B* **1999**, *103*, 9473-9487.

(3) Srinivas, G.; Discher, D. E.; Klein, M. L. *Nat. Mater.* **2004**, *3*, 638-644.

(4) Jain, S.; Bates, F. S. *Science* **2003**, *300*, 460-464.

(5) Jain, S.; Bates, F. S. *Macromolecules* **2004**, *37*, 1511-1523.

(6) Lin, E. K.; Gast, A. P. *Macromolecules* **1996**, *29*, 4432-4441.

(7) Massey, J. A.; Temple, K.; Cao, L.; Rharbi, Y.; Raez, J.; Winnik, M. A.; Manners, I. *J. Am. Chem. Soc.* **2000**, *122*, 11577-11584.

(8) Wang, X. S.; Guerin, G.; Wang, H.; Wang, Y. S.; Manners, I.; Winnik, M. A. *Science* **2007**, *317*, 644-647.

(9) Gadt, T.; Ieong, N. S.; Cambridge, G.; Winnik, M. A.; Manners, I. *Nat. Mater.* **2009**, *8*, 144-150.

(10) Zhang, J.; Wang, L. Q.; Wang, H. J.; Tu, K. H. *Biomacromolecules* **2006**, *7*, 2492-2500.

(11) Lazzari, M.; Scalarone, D.; Vazquez-Vazquez, C.; Lopez-Quintela, M. A. *Macromol. Rap. Commun.* **2008**, *29*, 352-357.

(12) Li, M. H.; Keller, P. *Soft Matter* **2009**, *5*, 927-937.

(13) Stewart, S.; Liu, G. *Angew. Chem. Int. Ed.* **2000**, *39*, 340-+.

(14) Yan, X. H.; Liu, G. J.; Liu, F. T.; Tang, B. Z.; Peng, H.; Pakhomov, A. B.; Wong, C. Y. *Angew. Chem. Int. Ed.* **2001**, *40*, 3593-3596.

(15) Yan, X. H.; Liu, G. J.; Haeussler, M.; Tang, B. Z. *Chem. Mater.* **2005**, *17*, 6053-6059.

(16) Koh, K.; Liu, G. J.; Willson, C. G. *J. Am. Chem. Soc.* **2006**, *128*, 15921-15927.

(17) Liu, G. J.; Yan, X. H.; Li, Z.; Zhou, J. Y.; Duncan, S. *J. Am. Chem. Soc.* **2003**, *125*, 14039-14045.

(18) Yan, X. H.; Liu, G. J.; Li, Z. *J. Am. Chem. Soc.* **2004**, *126*, 10059-10066.

(19) Pochan, D. J.; Chen, Z. Y.; Cui, H. G.; Hales, K.; Qi, K.; Wooley, K. L. *Science* **2004**, *306*, 94-97.

(20) Hu, J. W.; Zheng, R. H.; Wang, J.; Hong, L. Z.; Liu, G. J. *Macromolecules* **2009**, *42*, 4638-4645.

(21) Schappacher, M.; Deffieux, A. *Science* **2008**, *319*, 1512-1515.

(22) Minko, S.; Kiriy, A.; Gorodyska, G.; Stamm, M. *J. Am. Chem. Soc.* **2002**, *124*, 10192-10197.

Appendix A

Radius of Gyration and Viscosity of Macrocycles Relative to the Corresponding Linear Chain

Generally speaking, the conformation of a macrocycles is more compact than that of a linear polymer chain of the same polymerization degree. The constraint of the conformation, together with the absence of chain ends causes macrocycles to behave considerably differently from linear chains. Some of the physical properties of macrocycles are introduced in the following pages.

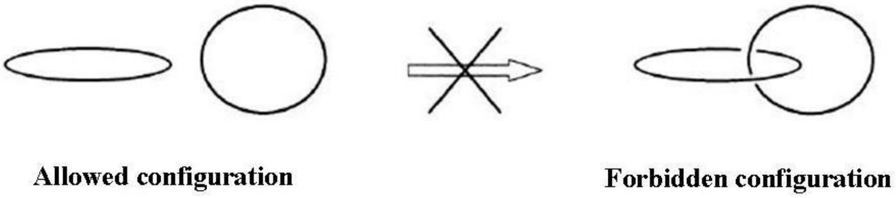

Figure AA.1. Scheme of the topological restriction on macrocycic polymers: non-concatenation.

The Θ condition is a key feature of dilute polymer solutions, in which the polymer chain behaves as an ideal chain. Experimental studies[1-4] on intermolecular second viral coefficients (or Flory Θ coefficient) A_2 for macrocyclic polymer-solvent systems show that the Θ temperature (the condition where $A_2 = 0$) of a macrocyclic is

4~6 °C lower than that of a corresponding linear polymer. However, theoretical studies[5,6] point out that intermolecular repulsion exists between macrocyclic polymers in such Θ solvents, due to the topological constraints, such as the non-concatenation or non-knotted restrictions,[7] (because the bonds of rings are not allowed to cross each other, Figure AA.1). Another theoretical study[8] suggests that the Θ temperatures for macrocyclic and linear polymers may be practically identical, even though the second viral coefficients vanished at different temperatures.

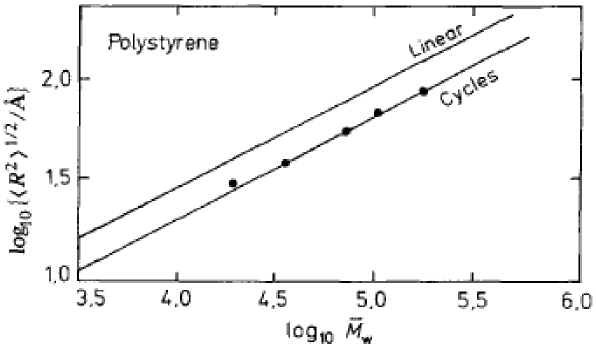

Figure AA.2. Logarithmic plot of the root mean square radius $<R^2>^{0.5}$ versus the molecular weight of macrocyclic and linear polystyrene under Θ conditions.[3]

The dimensions of polymers in the dilute solution are measured by the radius of gyration. The mean-square radius of gyration of macrocyclic polymers under Θ conditions are estimated to be exactly half those of linear polymers, which is $\frac{\langle s_r{}^2\rangle}{\langle s_l{}^2\rangle} = 0.5$.[8-15] Here, $\langle s_r{}^2\rangle$ and $\langle s_l{}^2\rangle$ are the mean-square radius of gyration of the macrocyclic and linear chains. This prediction is in close agreement with experimental results (Figure AA.2).[2,3] This ratio implies that macrocyclic polymers are more compact than the linear polymers with the same contour length under Θ conditions. A few experiments[3,16] that were carried out in a good solvent found that the ratio of radius of gyration between the macrocyclic polymers and linear polymers is 0.53. The larger ratio observed in good solvents than in Θ solvents may indicate that the ability of a macrocyclic polymer to expand is greater than that of a linear chain in a good solvent. However, the presence of 10% linear contaminants could also lead to the same value, which makes this claim questionable.

The intrinsic viscosity of polymers in dilute solution can be expressed by the Mark-Houwink relationship:

$$[\eta]=k\times M_v^a \tag{AA.1}$$

where $[\eta]$ is the intrinsic viscosity, k is a constant, M_v is the viscosity average molecular weight, a is the Mark-Houwink exponent. For linear polymers, k and a are constants for a particular polymer-solvent pair at a particular temperature.

Experimental results[2] have shown that the Mark-Houwink exponent a remains nearly unchanged for macrocyclic and liner polymers under the same conditions (Figure AA.3). Under Θ conditions, the exponent a is 0.5 for both macrocyclic and linear polymers (bottom of Figure AA.3). While in a good solvent the exponent a is approximately 0.7[3] (top of Figure AA.3). However, the intrinsic viscosities of macrocyclic polymers are actually lower than those of the corresponding linear polymers by a factor of 0.66 at Θ temperatures.[2,3,17] Higher ratios of the intrinsic viscosities between macrocyclic and linear polymers were determined by various research groups[2,3,17,18] to be between 0.71 and 0.74, indicating that the expansion of a macrocyclic polymer in a good solvent is greater than that of a linear polymer.

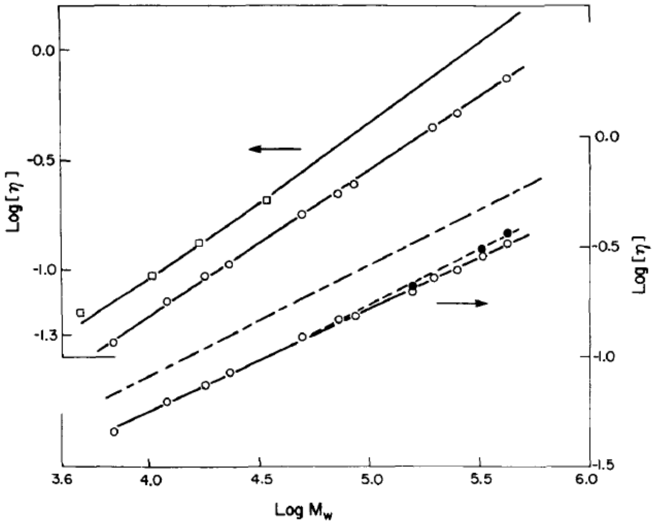

Figure AA.3. Log-log plot of the intrinsic viscosity of polystyrene versus the molecular weight at Θ temperature.[2] Top: in toluene, square-linear chains, circle-macrocycles; Bottom: in cyclohexane, dashed line-linear chains, circle-macrocycles. The slope represents the Mark-Houwink exponent *a*, which is nearly the same for the ring and linear polymers under the same conditions. The intercept represents *logk*, which indicates that the intrinsic viscosity of a ring polymer is lower than that of a linear polymer.

References

(1) Roovers, J.; Toporowski, P. M. *Macromolecules* **1983**, *16*, 843-849.

(2) Roovers, J. *J. Polym. Sci., Part B: Polym. Phys.* **1985**, *23*, 1117-1126.

(3) Lutz, P.; McKenna, G. B.; Rempp, P.; Strazielle, C. *Makromol. Chem. Rapid Comm.* **1986**, *7*, 599-605.

(4) Hild, G.; Strazielle, C.; Rempp, P. *Eur. Polym. J.* **1983**, *19*, 721-727.

(5) Frankkamenetskii, M. D.; Lukashin, A. V.; Vologodskii, A. V. *Nature* **1975**, *258*, 398-402.

(6) Iwata, K. *Macromolecules* **1985**, *18*, 115-116.

(7) Pakula, T.; Geyler, S. *Macromolecules* **1988**, *21*, 1665-1670.

(8) Rubio, A. M.; Freire, J. J.; Bishop, M.; Clarke, J. H. R. *Macromolecules* **1995**, *28*, 2240-2246.

(9) Edwards, C. J. C.; Richards, R. W.; Stepto, R. F. T.; Dodgson, K.; Higgins, J. S.; Semlyen, J. A. *Polymer* **1984**, *25*, 365-368.

(10) Edwards, C. J. C.; Rigby, D.; Stepto, R. F. T.; Dodgson, K.; Semlyen, J. A. *Polymer* **1983**, *24*, 391-394.

(11) Kramers, H. A. *J. Chem. Phys.* **1946**, *14*, 415-424.

(12) Casassa, E. F. *J. Polym. Sci., Part A: General Papers* **1965**, *3*, 605-&.

(13) Zimm, B. H.; Stockmayer, W. H. *J. Chem. Phys.* **1949**, *17*, 1301-1314.

(14) Boots, H.; Deutch, J. M. *Macromolecules* **1977**, *10*, 1163-1164.

(15) Prentis, J. J. *J. Chem. Phys.* **1982**, *76*, 1574-1583.

(16) Ragnetti, M.; Geiser, D.; Hocker, H.; Oberthur, R. C. *Makromol. Chem. Macromol. Chem. and Phys.* **1985**, *186*, 1701-1709.

(17) Rader, H. J.; Schrepp, W. *Acta Polym.* **1998**, *49*, 272-293.

(18) Higgins, J. S.; Ma, K.; Nicholson, L. K.; Hayter, J. B.; Dodgson, K.; Semlyen, J. A. *Polymer* **1983**, *24*, 793-799.

Appendix B

Studies on Aggregation Morphologies of $B_{105}C_{86}F_{19}$

This appendix includes a preliminary morphological study on micelle-like aggregates (MAs) from a linear triblock terpolymer. $PtBA_{105}$-*b*-$PCEMA_{86}$-*b*-$PFOEMA_{19}$ ($B_{105}C_{86}F_{19}$). As demonstrated in Chapter 3, the morphologies of $B_{105}C_{86}F_{19}$ micelles in TFT/MeOH solvent mixtures might not be determined by the mesogenic F block, since morphological transitions of the $B_{105}C_{86}F_{19}$ micelles were observed according to changes of the solvent composition. This work is focused on the micellization of the $B_{105}C_{86}F_{19}$ block terpolymer, which contains a fluorinated block and forms micelles in the absence of a mesogen ordering effect.

The morphologies of the $B_{105}C_{86}F_{19}$ MAs reported here include not only the traditional core-shell-corona spherical, cylindrical, and vesicular MAs, but also hamburger-like structures and ellipse-in-ellipse MAs, which are very unusual morphologies for linear ABC triblock block copolymers. Although the morphologies of hydrocarbon-based linear triblock copolymers have been extensively studied (reviewed in Chapter 1 and references therein), those of the fluorocarbon ones were not well studied yet. The micellization of triblock terpolymers containing fluorinated blocks has been reported by some groups.[1-4] The micellization of poly(perfluorooctylethyl methacrylate)-

bearing[5] or poly(perfluorohexylethyl methacrylate)-bearing[6,7] diblock copolymers has also been studied.

B.1 Solubility Tests for B, C, and F Homopolymers in Various Solvents

Due to the lack of a common solvent for all three blocks of the BCF copolymer, all of the solvents used for the morphological study were selective for at least one of the blocks. Therefore, we performed solubility tests on the homopolymers of each of the three blocks. Since TFT was used in all the solvent combinations, we also determined the volume fraction of TFT (f_{TFT}) at which the polymer solution became visually turbid. We used the visual change toward turbidity as an indication that the homopolymer had become insoluble, and the volume fractions used for this morphological study were not increased beyond these values. The turbidity tests were performed by firstly dissolving the polymer in the good solvent and then add the bad solvent dropwisely. The results of the solubility test are shown in Table AB.1. For each homopolymer, the left column shows the solubility of the polymer in a pure solvent, and the values in the right column indicate the f_{TFT} at which the polymer solution became turbid.

Table AB.1. Solubilities of homopolymers in selected solvents. The left column shows the solubility of the polymer in a pure solvent, and the values in the right column indicate the f_{TFT} at which the polymer solution became turbid.

Solvent	B		C		F	
TFT	S	N.A.	IS	N.A.	S	N.A.
hexanes	S	N.A.	IS	N.A.	IS	67%
acetone	S	N.A.	S	45%	IS	67%
diethyl ether	S	N.A.	IS	N.A.	IS	50%
PFMCH	IS	50%	IS	N.A.	S	N.A.

S: soluble, IS: insoluble, PFMCH: perfluoro(methyl-cyclohexane), N.A.: Not applicable.

B.2 Aggregation Morphologies of $B_{105}C_{86}F_{19}$ Observed in Various Solvent Systems.

Due to the lack of a common solvent for all three blocks, all of the solvents we used were selective solvents for at least one of the three blocks. Consequently, our system was more complex complicated than many other hydrocarbon-based micelle systems. Due to this solubility issue, all of the samples were heated at 50 ^{o}C for at least 4 days in an oil bath, and thus the thermodynamically stable structures may have been the major species observed. According to our previous results, this extended heating period would not cause noticeable crosslinking of the C block.[8] For TEM analysis, the samples were aero-sprayed immediately after they were removed from the oil bath, so that the solvent would evaporate very quickly and the morphologies of the samples would remain unchanged from those in the heated solution. Specimens for TEM analysis were stained with OsO_4, which is a selective staining agent for the C block. Therefore, in the TEM images, the C domains would appear darker due to the staining, while the F and B domains would appear light gray or invisible.

B.3 MAs of $B_{105}C_{86}F_{19}$ Prepared in TFT/Hexanes Solvent Mixtures.

In the first solvent mixture of TFT and hexanes, we prepared several samples with f_{TFT} values of 40%, 20% and 10%. As discussed above, B was always soluble and C was insoluble. Meanwhile, F, was insoluble when f_{TFT} was below 67%. Thus, among all of these samples, the B block was soluble, while the C and F blocks were both insoluble. The TEM images of the resultant MAs are shown in Figure AB.. At f_{TFT} = 40% (Figure AB.a), the resultant MAs are mostly ellipsoidal in shape, and some of the MAs have a spherical shape. Some of the spheres showed a light gray stripe across their center and others showed a light gray circle. At f_{TFT} = 20%, the resultant MAs appeared as two hemi-spheres attached together, as shown in Figure AB.b. When f_{TFT} was decreased further to 10%, mostly spherical structures were observed, and also prolonged structures with a gray core and dark shell were observed as a minor species (Figure AB.c).

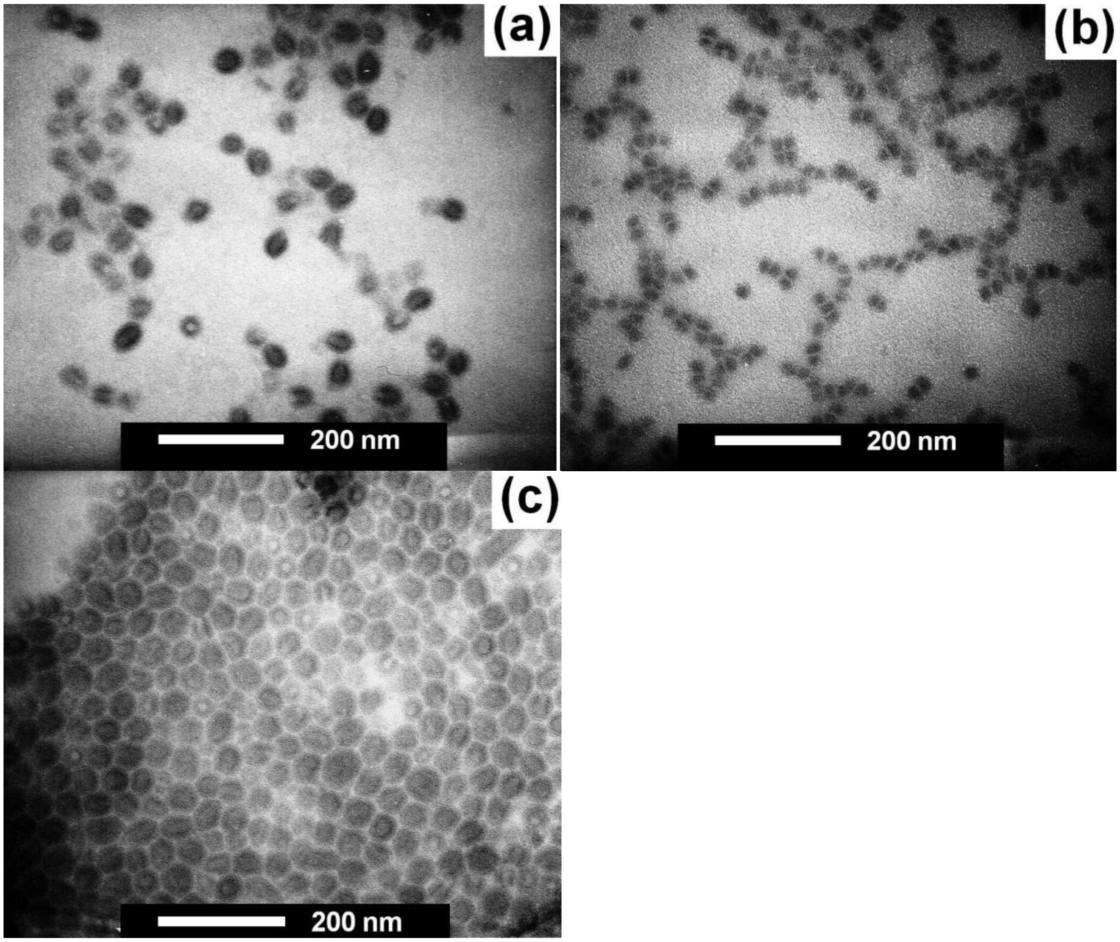

Figure AB.1. TEM images of $B_{105}C_{86}F_{19}$ in TFT/hexanes mixtures with f_{TFT} = 40% (a), 20% (b), and 10% (c).

The structure of the MAs at f_{TFT} = 40% is proposed to be an ellipsoidal structure, as illustrated in Scheme AB.a. The B domain is located on the surface of the ellipse as it is soluble in this solvent system. The C domains form the major component of the ellipse interior that is encapsulated by the B domain and surrounds the F domain. This C domain appears dark in the TEM images. Meanwhile, the F block forms the ellipsoidal core inside the C ellipse. When the major-axis (long-axis) of the ellipse was parallel to the incident electron beam under TEM, the projection of the MAs would appear as a sphere with a dark shell and a light spherical light. Meanwhile, if the major-axis was not parallel to the incident electron beam, the projection would appear as a dark ellipse with a light stripe in the center. All of these different structures observed in the TEM images essentially resulted from the different projection angles of the individual ellipsoidal structures with the incident electron beam. Therefore, although many of the structures appeared differently in the TEM image, they had the same ellipse-in-ellipse structure, as illustrated in Scheme AB.1b and c. Imae's group has reported the observation of ellipsoidal MAs from a diblock copolymer bearing a fluorinated block.[9] They claimed the ellipsoidal structure was due to the ellipsoidal core formed by the fluorinated block, which has too great steric hindrance to become closely packed. In another paper, Lodge, Hillmyer and co-workers also reported the preparation of ellipsoidal MAs from a fluorinated triblock copolymer.[10] They attributed these ellipsoidal MAs to the strong phase-segregation between the fluorinated core-forming block and the hydrocarbon-based shell-forming block, but no detailed explanation was provided. The situation encountered in our case is similar to those described by these other researchers. The F block formed an ellipsoidal core in the center, since it was highly incompatibility with the C domain. This ellipsoidal core induced the outside C block to also form an ellipse to accommodate the core.

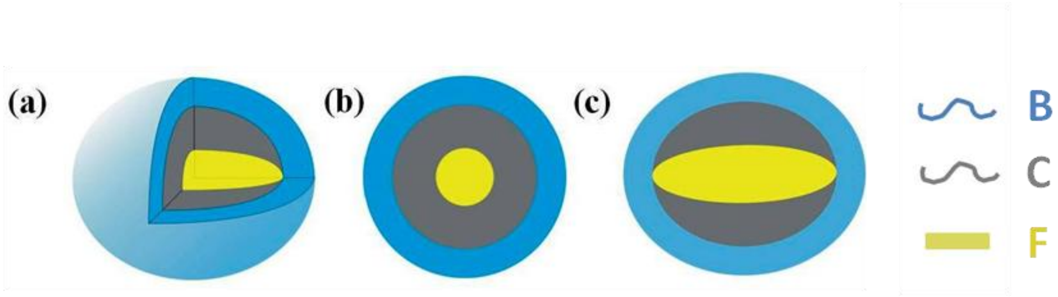

Scheme AB.1. Schematic representations of the ellipsoidal $B_{105}C_{86}F_{19}$ MAs as a 3D cartoon structure (a), as a 2D structure viewed from the x-axis (b), and as a 2D structure viewed from the z-axis (c).

When the TEM images shown in Figure AB.1 were closely compared, a very interesting feature was found, in that the cores of the MAs in image Figure AB.1.1b were light, and Figure AB.1c were gray, respectively, but some of those shown in Figure AB.1a are gray and the others are light. The core of the hamburger-like structure is composed of the F domain, which is not stained. Thus, it is understandable that the cores of the hamburger-like MAs were lighter in color when compared with the C shell domain under TEM observation. Meanwhile, when the F block forms the core of a core-shell-corona spherical MA, as shown in Figure AB.1c, the core of the resultant MA should appear gray under TEM, due to the surrounding C block. However, for the ellipse-in-ellipse structure, when the major-axis is parallel to the incident electron beam, the internal F ellipse would only appear as a light spherical domain. Meanwhile, when the incident beam is not parallel with the longer axis, the F would appear as a gray stripe in the centre, due to the C domain surrounding the F core. In other words, the path of the incident electron beam penetrating the F domain core would also include a greater amount of the C domain if the incident beam was not aligned with the axis of the ellipse. Therefore, the F domain would appear gray since a significant amount of the C domain was also part of the incident beam's pathway. In contrast, very little of the C domain was included in the paths of the electron beams passing through the F domain if the ellipsoidal axis was aligned with the incident beam.

Initially at a relatively high f_{TFT} (40%), the interfacial tension between F domain and the solvent may be lower than that between the C domain and the solvent, and ellipses were the dominant product. Thus the F core is not completely surrounded by the C shell. Instead of forming a core-shell-corona structure, both the C and F blocks are exposed to solvent and form an ellipse-in-ellipse structure. When f_{TFT} was decreased to 20%, the solvation conditions for C became worse than for F, and MAs with hamburger-like morphologies appeared (Figure AB.1b). In these structures, the F domain formed the "ham" or "meat" filling, and the C domains formed the hamburger "bun" (Scheme AB.2).

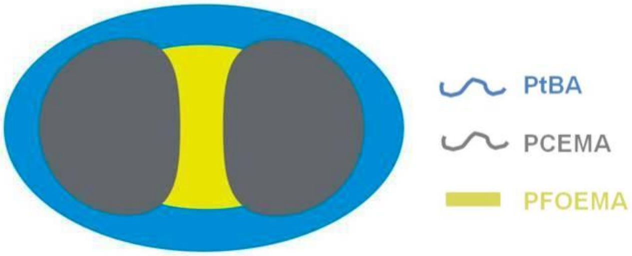

Scheme AB.*2*. Schematic representation of hamburger-like MAs.

When f_{TFT} reached 10%, the solvation conditions became worse for the F block, and thus it isolated itself further from the solvent to decrease the interfacial energy. Thus a core-shell-corona structure was formed. Due to the high steric hindrance of the F block, the resultant core-shell-corona MAs were not perfectly spherical in shape, and some elongated spheres also appeared in Figure AB.c.

These morphologies were not confirmed to be the thermodynamically favoured morphologies. The core-shell-corona spheres, ellipses, and hamburgers coexisted at all of the solvent compositions. However, the population of one structure was dominant over the other morphologies at each of the three compositions.

B.4 MAs of $B_{105}C_{86}F_{19}$ Prepared in Mixtures of TFT and Acetone.

In the solvent mixtures system of TFT and acetone, the morphologies of the MAs changed from core-shell-corona spheres to core-shell-corona cylinders when the f_{TFT} was changed from 10% to 0.5%, as shown in Figure AB.2. In these solvent mixtures, the F block is insoluble, the C and B blocks are soluble. Again, the gray and dark domains in the TEM images are attributed to F and C domains, respectively. When $f_{\mathrm{TFT}} = 10\%$, the polymer formed mostly spherical MAs, as shown in Figure AB.2a. Meanwhile, when $f_{\mathrm{TFT}} = 2\%$, a mixture of spherical and cylindrical MAs was observed (Figure AB.2b), and when f_{TFT} was decreased further to 0.5%, the MAs were mostly cylindrical (Figure AB.2c).

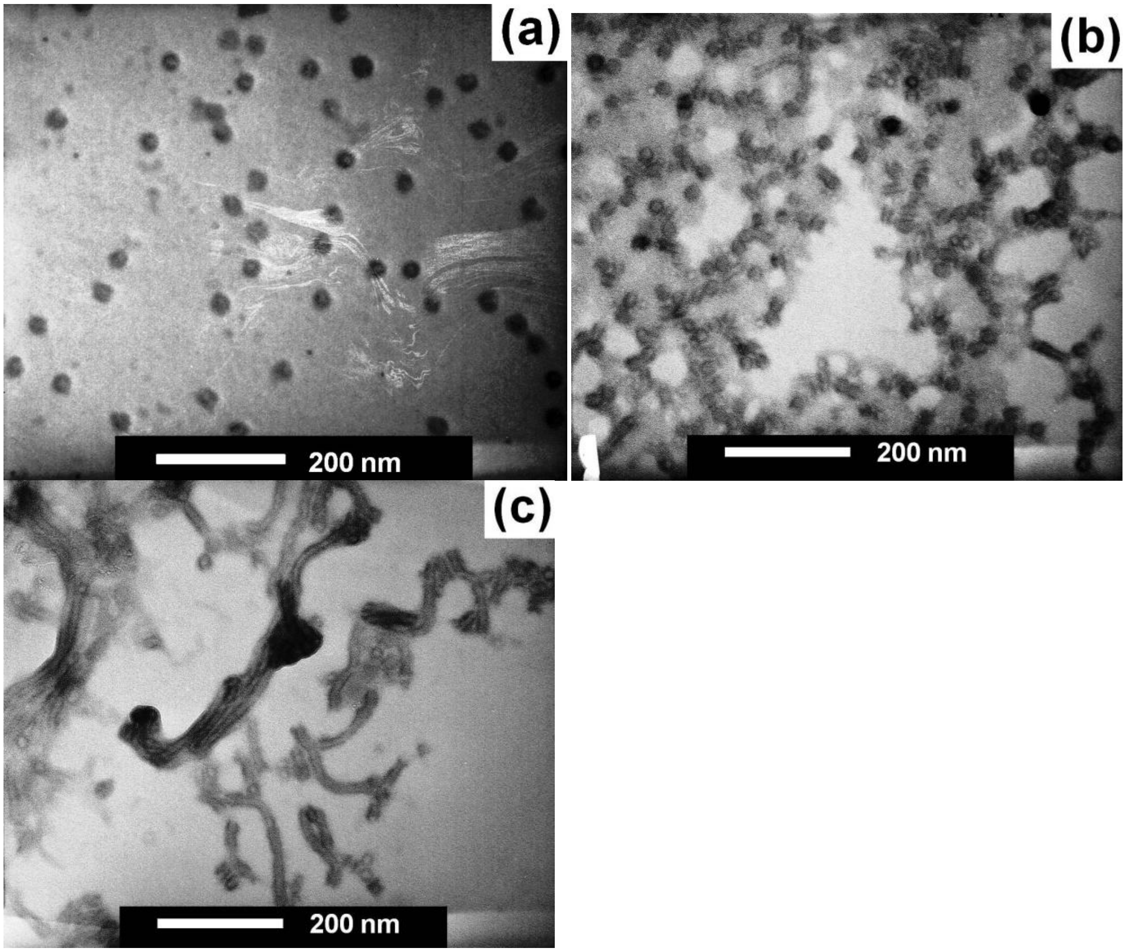

Figure AB.2. TEM images of $B_{105}C_{86}F_{19}$ in TFT/acetone mixtures with f_{TFT}= (a) 10% (a), 2% (b), and 0.5% (c).

Interestingly, this trend coincides with the theory of diblock copolymer micelles,[11] that with increasing content of selective solvent, the resultant MAs can undergo morphological transition from spherical, to cylindrical, and then to vesicular structures. When f_{TFT} is decreased, F becomes more and more insoluble and the resultant MAs underwent a morphological transition from spheres to cylinders. This transition would allow a larger aggregation number for the resultant MAs, and would lead to a reduced interfacial area between the F core and the solvent, and also a higher chain stretching energy of the core-forming block. Consequently, the total energy of the system will be reduced.

B.5 MAs of $B_{105}C_{86}F_{19}$ Prepared from Mixtures of TFT and Diethyl Ether

MAs were also produced in solvent mixtures of TFT and diethyl ether. As shown in Figure AB.3, the morphology of the MAs changed from an ellipse-in-ellipse structure to a mixture of worm-like and spherical structures when the $f_{\mathbf{TFT}}$ was decreased from 30% to 21%. When $f_{\mathbf{TFT}}$ was further decreased to 5%, the MAs had undergone conversion to core-shell-corona spheres.

Initially, when f_{TFT} is 30%, the polymer forms an ellipse-in-ellipse structure for the same reason described for the TFT/hexanes solvent mixtures. Under these conditions, the solvent was as poor for the F block as for the C block. Thus, both the C and F blocks were exposed to the solvent, resulting in an ellipse-in-ellipse structure, as shown in Scheme AB.1. Some of the MAs displayed a light stripe appearing in the middle of a dark particle, and the other MAs appeared as a dark spherical particle with a light core. These two apparent structures were actually of the same morphology but were viewed from different angles. One noteworthy feature is that in comparison with the ellipsoidal particles shown in Figure AB.1a, the particles obtained from the mixture of TFT/diethyl ether are smaller in size and their shape is mainly spherical rather than ellipsoidal.

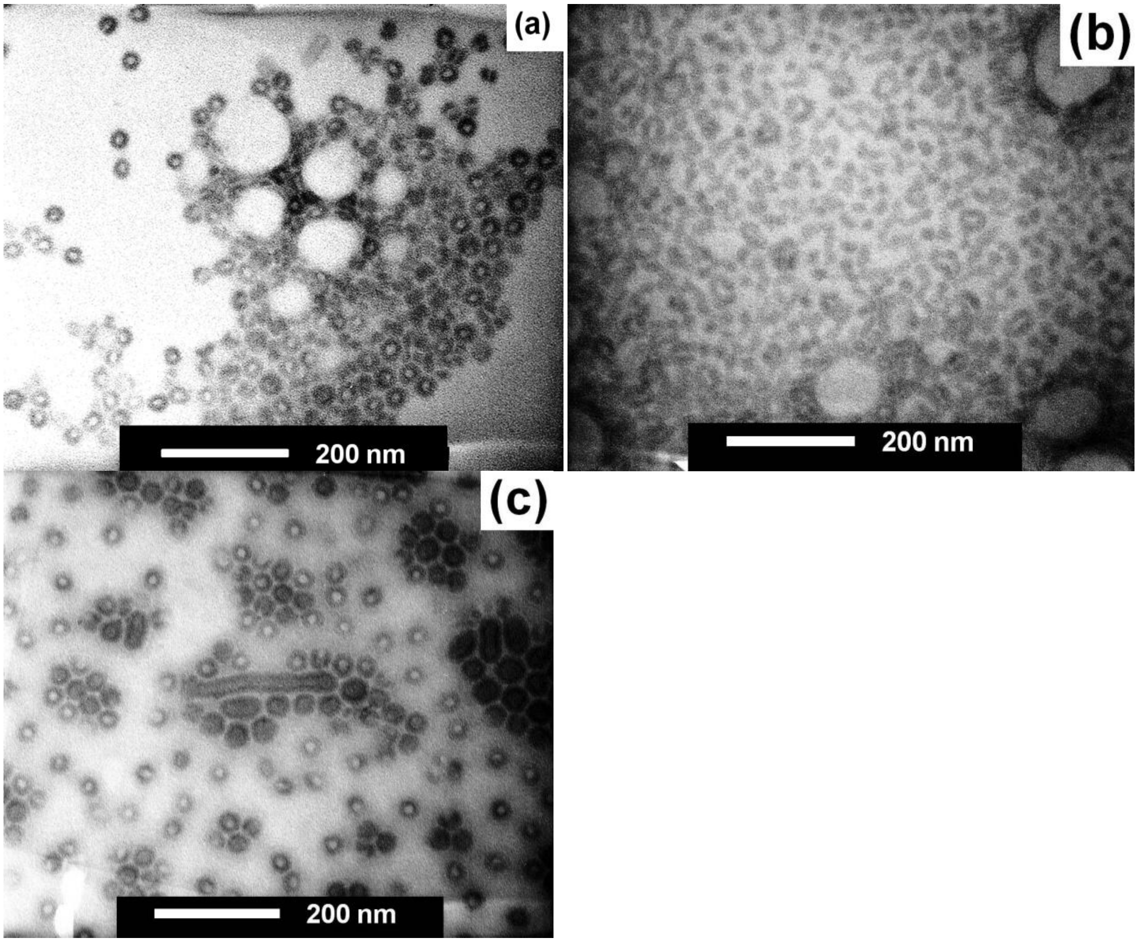

Figure AB.3. TEM images of $B_{105}C_{86}F_{19}$ MAs prepared in TFT/ether mixtures with f_{TFT} = 30% (a), 21% (b), and 5% (c).

Meanwhile, when f_{TFT} was decreased to 21%, the solvation conditions may have became worse for C than for F, so that the F domain migrated to the exterior and the C domain formed the core. However, when f_{TFT} was decreased to 5%, as showed in Figure AB.3c, the solvation conditions became worse for F than C. Thus, the F block had then formed the micellar core. Again, due to the high steric hindrance of the F domain, the resultant core-shell-corona MAs were not perfectly spherical in shape, and some elongated spheres were also seen in Figure AB.3c. These two transitions occurring with changing solvation conditions were very interesting and unexpected. The usage of two selective solvents for the copolymer blocks increased the complexity of this system, and also provides more possible combinations for this study.

B.6 MAs of $B_{105}C_{86}F_{19}$ Prepared from Mixtures of TFT and PFMCH.

In this solvent combination, the situation is different from the systems discussed above. In both of the solvents, TFT and perfluoro(methyl cyclohexane) (PFMCH), the F block is soluble and the C block is insoluble. Meanwhile, the B block becomes insoluble when the content of TFT is below 50 wt.%. Thus, in contrast to the other solvent systems, the C block would form the core of the resultant MAs, as shown in Figure AB.3.

When f_{TFT} is high, most of the MAs adopted a spherical morphology, with C forming the core and the B and F blocks forming the corona, as shown in Figure AB.3a.

With decreasing f_{TFT}, the C block remained in the micellar core, but as could be seen from Figure AB.3b, most of the MAs adopted a cylindrical morphology under these solvent conditions. As f_{TFT} was decreased further, the resultant MAs appeared as disk-like structures, which are shown in Figure AB.3c. Due to the lack of contrast, it was difficult to tell if the B block collapsed as a shell layer, or if it was still was soluble and stretched into the solvent. However, the C blocks, which were represented as the dark domain in image Figure AB.3a and Figure AB.3b, were clearly distributed in the cores of the MAs.

The average diameters of the spherical MAs shown in Figure AB.3a (prepared at f_{TFT} = 60%) were measured as 18 ± 2 nm, and of the MAs shown in Figure AB.3b (prepared at f_{TFT} = 43%) was measured as 17 ± 2 nm. These two values are very close, indicating that the C domain remained in the core when f_{TFT} was decreased from 60% to 43%. According to a previous study involving C homopolymers,[12] the characteristic ratio of C is 12.6 in a theta solvent. Based on this value, we calculated the unperturbed root-mean-square end-to-end distance to be 7.2 nm for the C block of the original triblock copolymer. This value is comparable to the radii of the MAs from Figure AB.3a and Figure AB.3b.

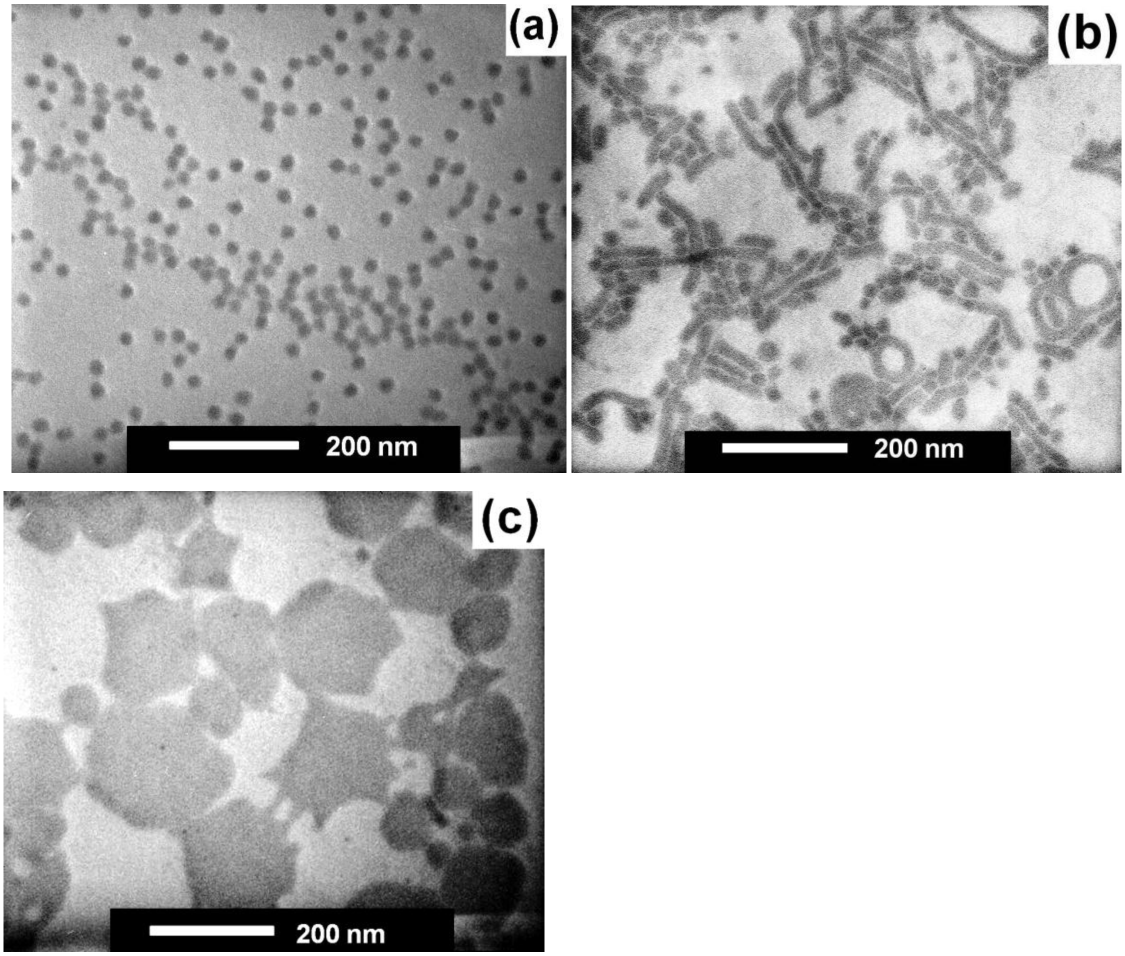

Figure AB.3. TEM images of MAs prepared from $B_{105}C_{86}F_{19}$ in TFT/PFMCH mixtures with f_{TFT} = 60% (a), 43% (b), and 30% (c).

Since the F and B blocks were on the surfaces of the spherical and cylindrical MAs, it is very likely that the two different blocks were segregated from each other and formed different domains. AFM was thus used to investigate the surface morphologies of these MAs. The images shown in Figure AB.4 are both height and phase images of the spherical and cylindrical MAs. From the height images (Figure AB.4a and c), it can be seen that the morphologies of the MAs were similar to those observed in the TEM images (Figure AB.4a and b). The aggregation of the MAs probably resulted from the poor compatibility between the solvents and the surfaces of the silicon wafers, which are hydrophobic (containing a fluorinated solvent) and hydrophilic (due to the -OH groups on the silicon wafer surface), respectively. However, no noticeable phase contrast was observed on the surfaces of either the spherical or cylindrical MAs in the phase images (Figure AB.4b and d). Since fluorinated polymers are generally incompatible with most hydrocarbon-based polymers, this finding was unexpected. One possible explanation is that the length of the F block is much shorter than that of the B block. As shown below, we performed a simple calculation showing that the length (unperturbed end-to-end distance) of the B block is approximately 8 nm, while the length of the F block is approximately 4 nm.

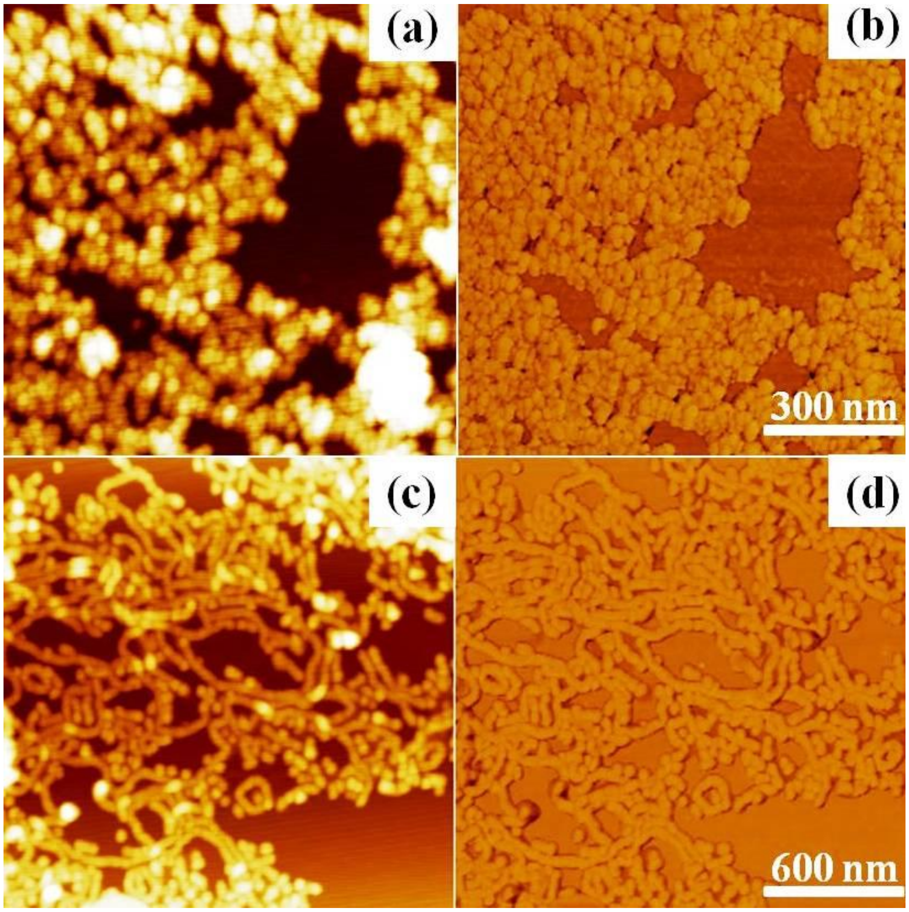

Figure AB.4. AFM images of the $B_{105}C_{86}F_{19}$ micelles sprayed from TFT/PFMCH mixtures. Shown are height (a) and phase (b) images of samples that were sprayed from TFT/PFMCH mixtures with $f_{TFT} = 50\%$. Height (c) and phase (d) images are also shown of samples that were sprayed from TFT/PFMCH mixtures with $f_{TFT} = 43\%$.

The block length of B is:

$$\sqrt{2 * l * C_\infty} * l_0 = \sqrt{2 * 105 * 12.8} * 0.154nm \approx 8\ nm \qquad \text{(AB.1)}$$

The block length of F is:

$$n * l_0 * \sin\left(\frac{\pi}{3}\right) = \left(19 * 0.154 * \sin\left(\frac{\pi}{3}\right)\right)nm \approx 5nm \qquad \text{(AB.2)}$$

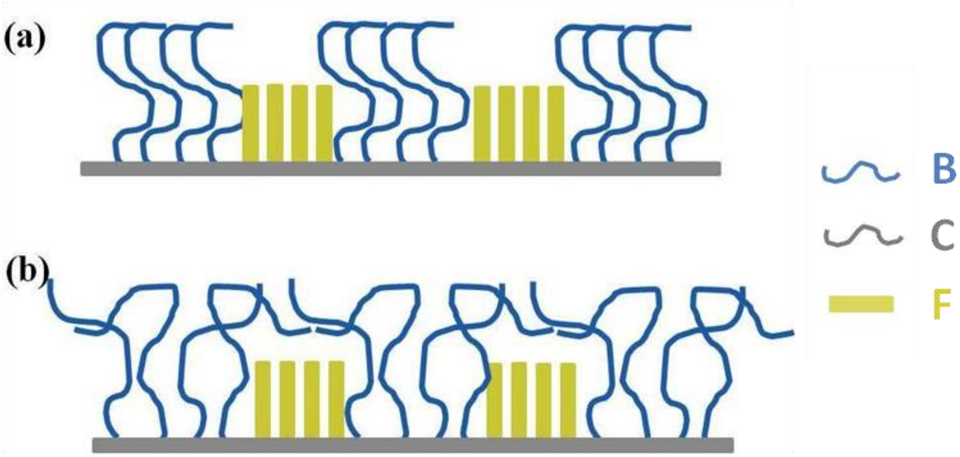

Scheme AB.3. Cartoon diagrams of the surface of $B_{105}C_{86}F_{19}$ MAs in TFT/PFMCH mixtures with f_{TFT} = 50% or 43%. Image (a) shows an ideal phase segregation of the B and F blocks. Image (b) shows a smooth MA surface forming after the B chains had collapsed onto the F domains as the MAs were dried.

Thus, it is highly possible that the B chains are long enough to shield the F chains from exposure to the surface in the dry state, and thus the surfaces of the MAs appear smooth in the AFM images. As shown in Scheme AB.3a, in an ideal case, the B and F chains would become segregated into different domains. However, because the B chains are much longer than the F chains, as the MAs were dried, the B chains collapsed on top of the F chains. Consequently, the MA surfaces appeared smooth layer, as shown in Scheme AB.3b.

The morphological transition from spherical to cylindrical micelles agrees with the theory of self-assembly of diblock copolymers in block-selective solvents.[11] With increasing content of selective solvent, the aggregation number of the resultant MAs increased and the structure of the resultant MAs changed from spheres, to cylinders, and then vesicles.

However, when the content of TFT was increased even further, instead of forming vesicles, the resultant MAs adopted a flattened disk-like structure. In these disk-like MAs, the core chains are fully stretched and form a flat interface, which minimizes the interfacial surface area. As a consequence of the decreased interfacial surface area, the coronal chains become much more crowded on the surfaces of the disk-like MAs than they are on the surfaces of other MAs, such as spherical or cylindrical MAs. Disk-like MAs were reported from the polymers containing crystalline blocks,[13] or also from the close-packing of rod blocks in the core.[14] Among coil-coil block copolymers, this morphology was reported only from systems reaching the "superstrong segregation limit" (SSSL) between the distinct blocks.[15] According to Lodge, Hillmyer and coworkers,[15] a "superstrong segregation" between a core and shell block results in a high interfacial energy, which overwhelms the conformational entropy loss that results from the crowding of coronal chains.[16,17] Lodge et al. have reported disk-like MAs obtained from the diblock copolymer 1,2-polybutadiene-*b*-poly(hexafluoropropylene oxide) (PB-*b*-PFPO),[15] and disk-like MAs with segregated cores from μ-EOF miktoarm star-terpolymers, where E represents polyethylethylene, O represents poly(ethylene oxide), and F represents either perfluorinated polyether or poly(perfluoropropylene oxide).[4] For both of these systems, a fluorinated block was involved. The high degree of incompatibility between the fluorophilic block and the oleophilic and hydrophilic block might have generated this SSSL-regime behaviour.

In our study, the disk-like MAs were also formed from the SSSL between the F block in the corona and B and C blocks in the core. In a TFT/PFMCH solvent mixture with f_{TFT} = 30%, both the B and C blocks are insoluble, while F is soluble. Therefore, from a solvation standpoint, the B forms the core and C forms the shell, while F should form the corona (Scheme AB.4). As with Lodge's system, the superstrong segregation between the fluorinated block and the hydrocarbon block allows the interfacial energy to overwhelm the chain crowding energy. In addition, the low weight fraction of the F block, e.g. 22 wt.%, requires the resultant MAs to have small curvatures. Since the coronal F chains were significantly shorter than the core and shell chains, "crew-cut" disk-like MAs were formed from our system.

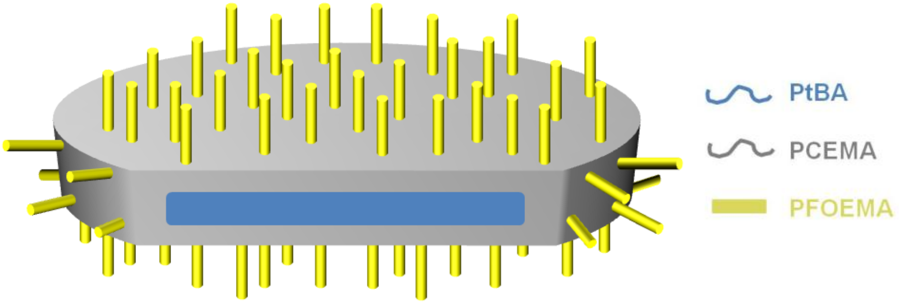

Scheme AB.4. Cartoon diagram showing the structure of a disk-like morphology.

References

(1) Li, Z. B.; Kesselman, E.; Talmon, Y.; Hillmyer, M. A.; Lodge, T. P. *Science* **2004**, *306*, 98-101.

(2) Hirao, A.; Hayashi, M.; Loykulnant, S.; Sugiyama, K. *Prog. Polym. Sci.* **2005**, *30*, 111-182.

(3) Skrabania, K.; von Berlepsch, H.; Bottcher, C.; Laschewsky, A. *Macromolecules* **2010**, *43*, 271-281.

(4) Li, Z. B.; Hillmyer, M. A.; Lodge, T. P. *Nano Lett.* **2006**, *6*, 1245-1249.

(5) Imae, T.; Tabuchi, H.; Funayama, K.; Sato, A.; Nakamura, T.; Amaya, N. *Colloids Surf. A* **2000**, *167*, 73-81.

(6) Lim, K. T.; Lee, M. Y.; Moon, M. J.; Lee, G. D.; Hong, S. S.; Dickson, J. L.; Johnston, K. P. *Polymer* **2002**, *43*, 7043-7049.

(7) Krupers, M. J.; Sheiko, S. S.; Moller, M. *Polym. Bull.* **1998**, *40*, 211-217.

(8) Njikang, G.; Han, D. H.; Wang, J.; Liu, G. J. *Macromolecules* **2008**, *41*, 9727-9735.

(9) Ito, H.; Imae, T.; Nakamura, T.; Sugiura, M.; Oshibe, Y. *J. Colloid. Interface Sci.* **2004**, *276*, 290-298.

(10) Zhou, Z. L.; Li, Z. B.; Ren, Y.; Hillmyer, M. A.; Lodge, T. P. *J. Am. Chem. Soc.* **2003**, *125*, 10182-10183.

(11) Zhang, L. F.; Eisenberg, A. *Science* **1995**, *268*, 1728-1731.

(12) Hong, L. Z.; Liu, G. J. *Macromolecules*, *43*, 3941-3946.

(13) Nakano, M.; Matsumoto, K.; Matsuoka, H.; Yamaoka, H. *Macromolecules* **1999**, *32*, 4023-4029.

(14) Wu, J.; Pearce, E. M.; Kwei, T. K.; Lefebvre, A. A.; Balsara, N. P. *Macromolecules* **2002**, *35*, 1791-1796.

(15) Edmonds, W. F.; Li, Z. B.; Hillmyer, M. A.; Lodge, T. P. *Macromolecules* **2006**, *39*, 4526-4530.

(16) Semenov, A. N.; Nyrkova, I. A.; Khokhlov, A. R. *Macromolecules* **1995**, *28*, 7491-7500.

(17) Nyrkova, I. A.; Khokhlov, A. R.; Doi, M. *Macromolecules* **1993**, *26*, 3601-3610.

Appendix C

Characterization of $C_{60}D_{476}C_{60}$ and its Cyclized Products

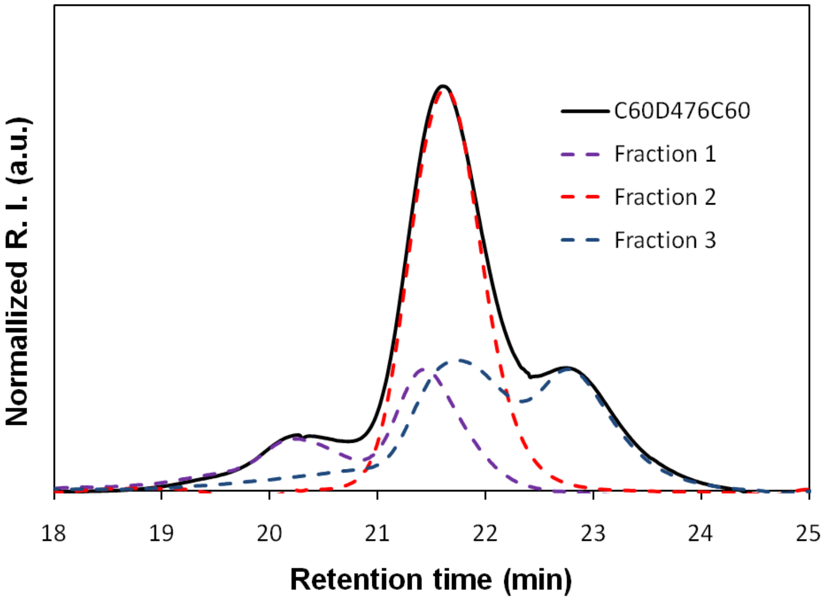

Figure AC.1. SEC traces of the triblock copolymer $C_{60}D_{476}C_{60}$ before fractionation (solid line) and three portions obtained after SEC fractionation: a high molecular weight impurity (fraction 1, purple dashed line), $C_{60}D_{476}C_{60}$ (fraction 2, red dashed line) and a low molecular weight impurity $D_{238}C_{60}$ (fraction 3, blue dashed line).

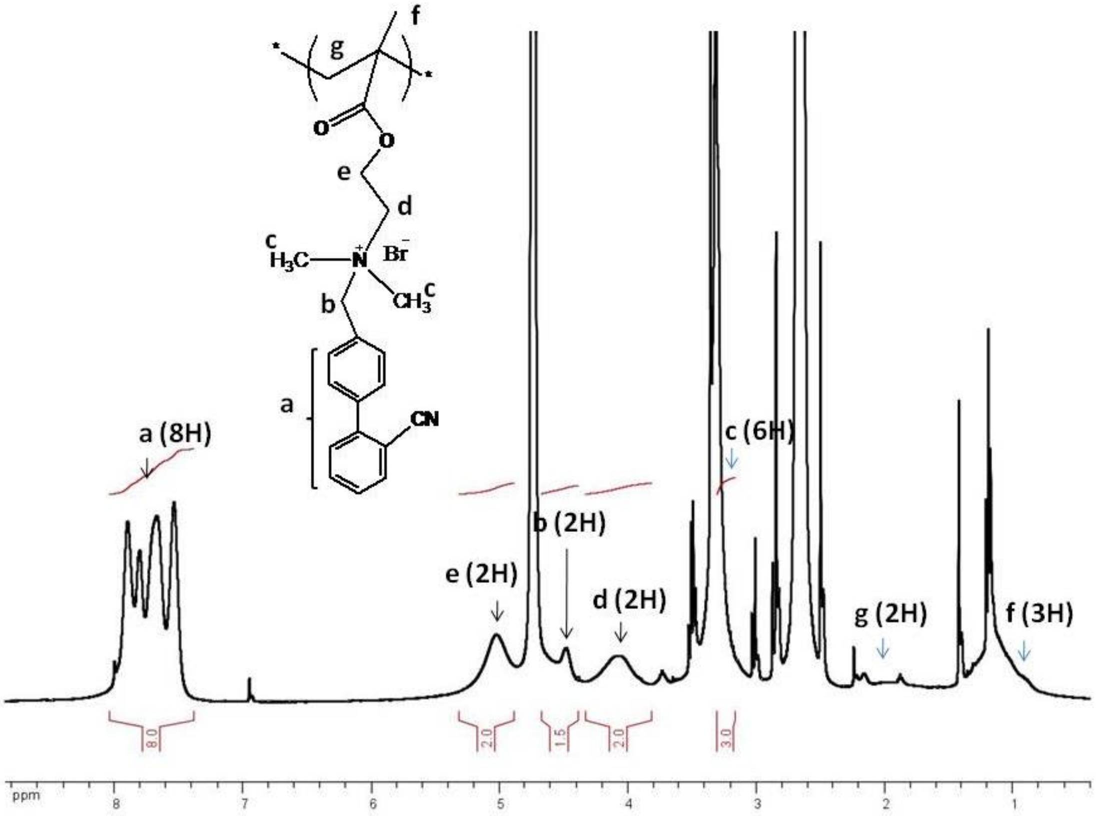

Figure AC.2. ^{1}H NMR spectrum of $C_{60}D_{476}C_{60}$ after quaternization with BBC.

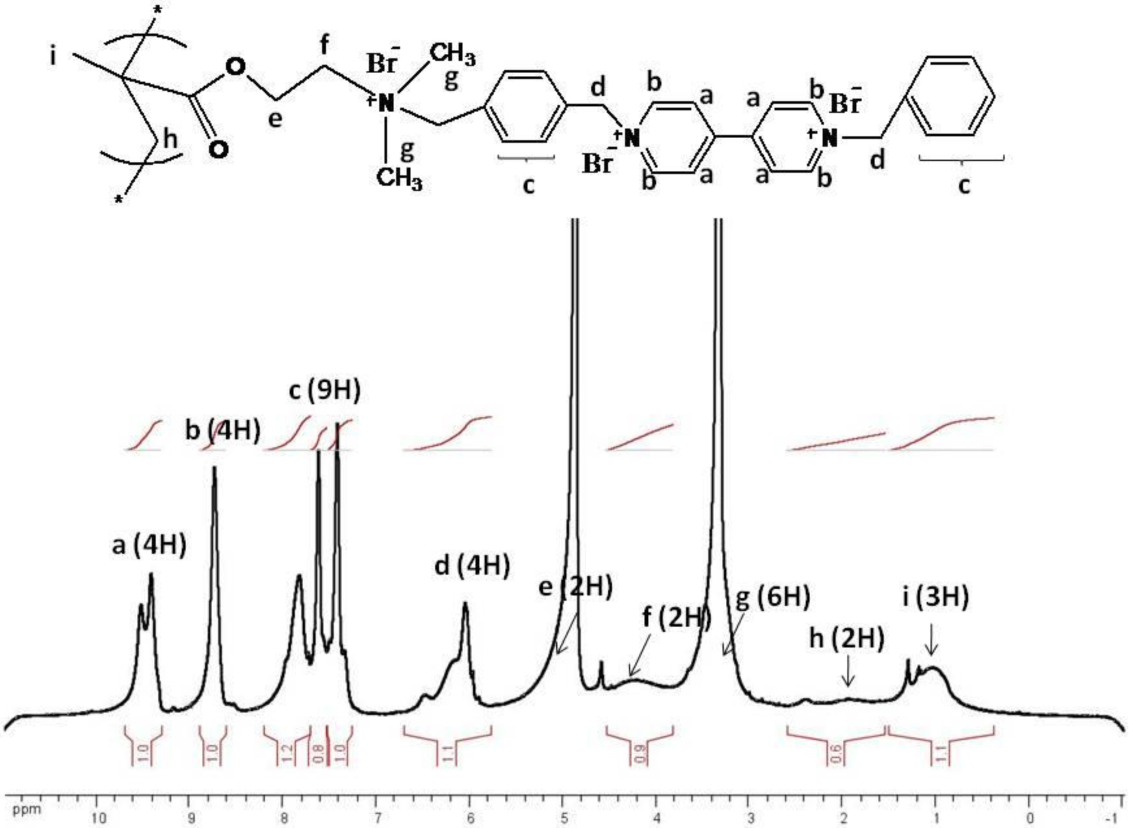

Figure AC.3. ^{1}H NMR spectrum of $C_{60}D_{476}C_{60}$ quaternized with BBBV.

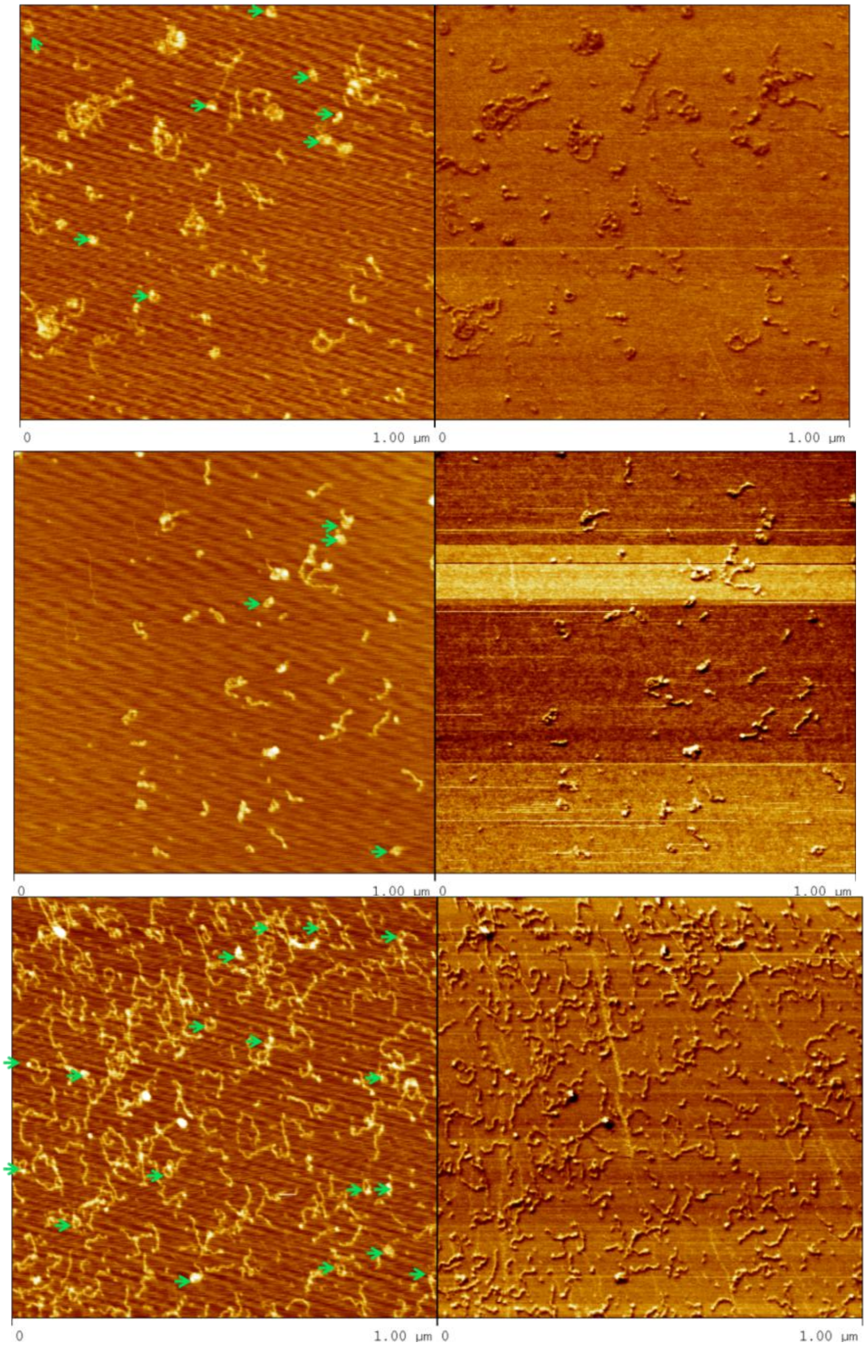

Figure AC.4. AFM height (left) and phase (right) images of specimens prepared by dropping a methanol solution of the crosslinked $C_{60}D_{476}C_{60}$ copolymer that was modified by BBBV quaternization onto a mica substrate. The crosslinked products were obtained from an aqueous HCl solution with a pH of 0.61. The images were obtained by scanning different locations of the same mica substrate. Green arrows are highlight the macrocyclic chains.

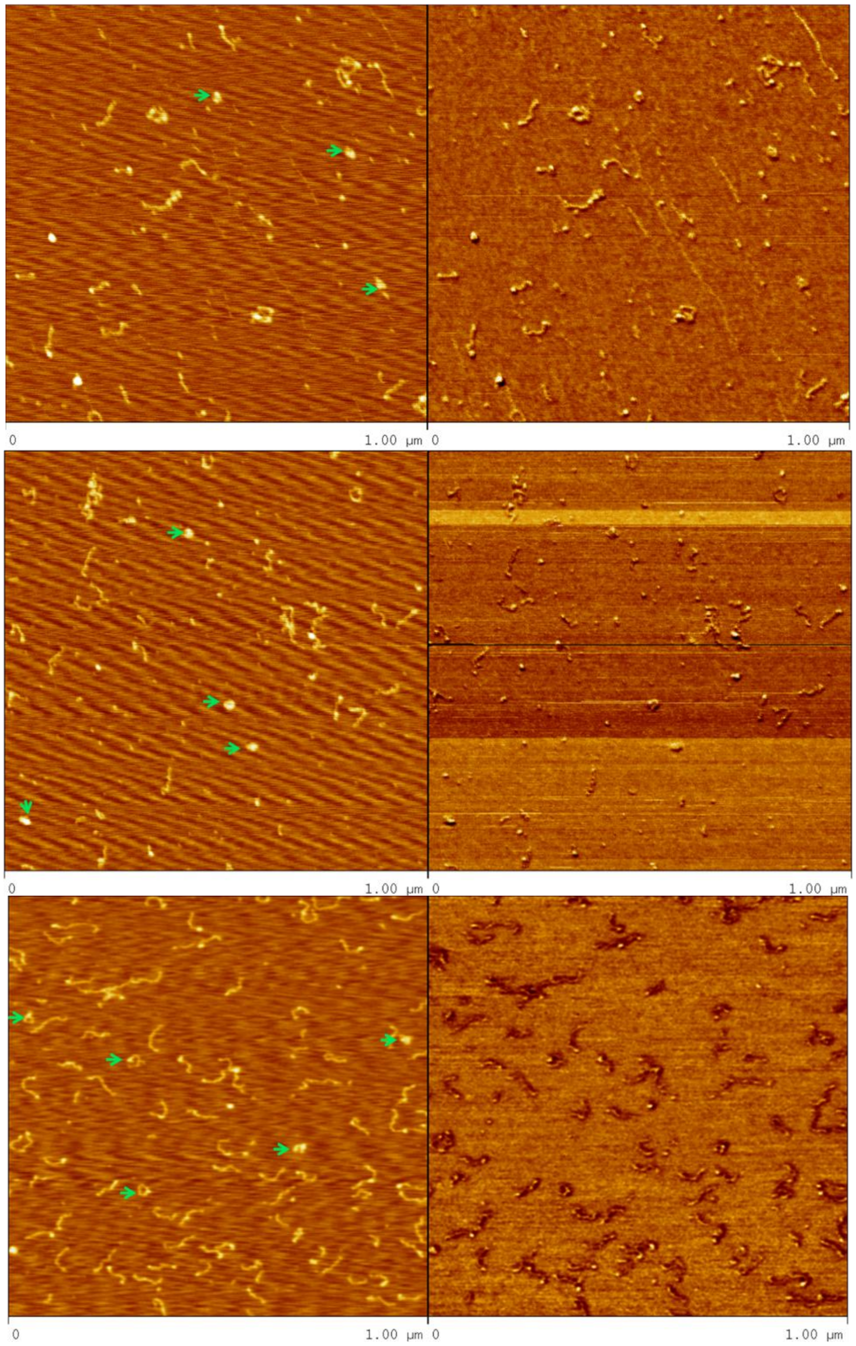

Figure AC.5. AFM height (left) and phase (right) images of specimens prepared by dropping a methanol solution of the crosslinked $C_{60}D_{476}C_{60}$ copolymer that modified by BBBV quaternization onto a mica substrate. The crosslinked products were obtained from an aqueous HCl solution with a pH of 0.77. The images were obtained by scanning different locations of the same mica substrate. Green arrows highlight the macrocyclic chains.

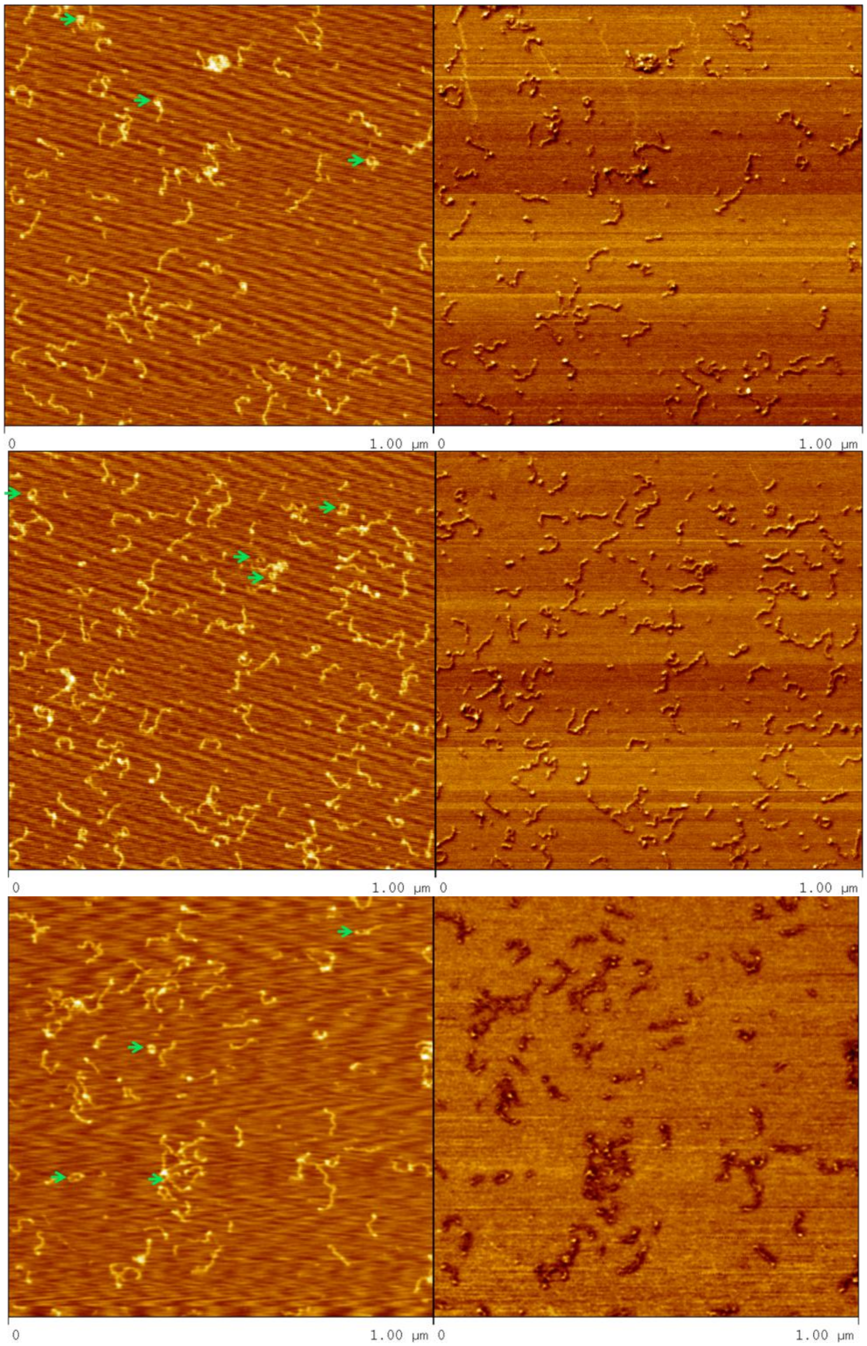

Figure AC.6. AFM height (left) and phase (right) images of specimens prepared by dropping a methanol solution of the crosslinked $C_{60}D_{476}C_{60}$ copolymer that was modified by BBBV quaternization onto a mica substrate. The crosslinked products were obtained from an aqueous HCl solution with a pH of 0.93. The images were obtained by scanning different locations on the same mica substrate. Green arrows highlight the macrocyclic chains.

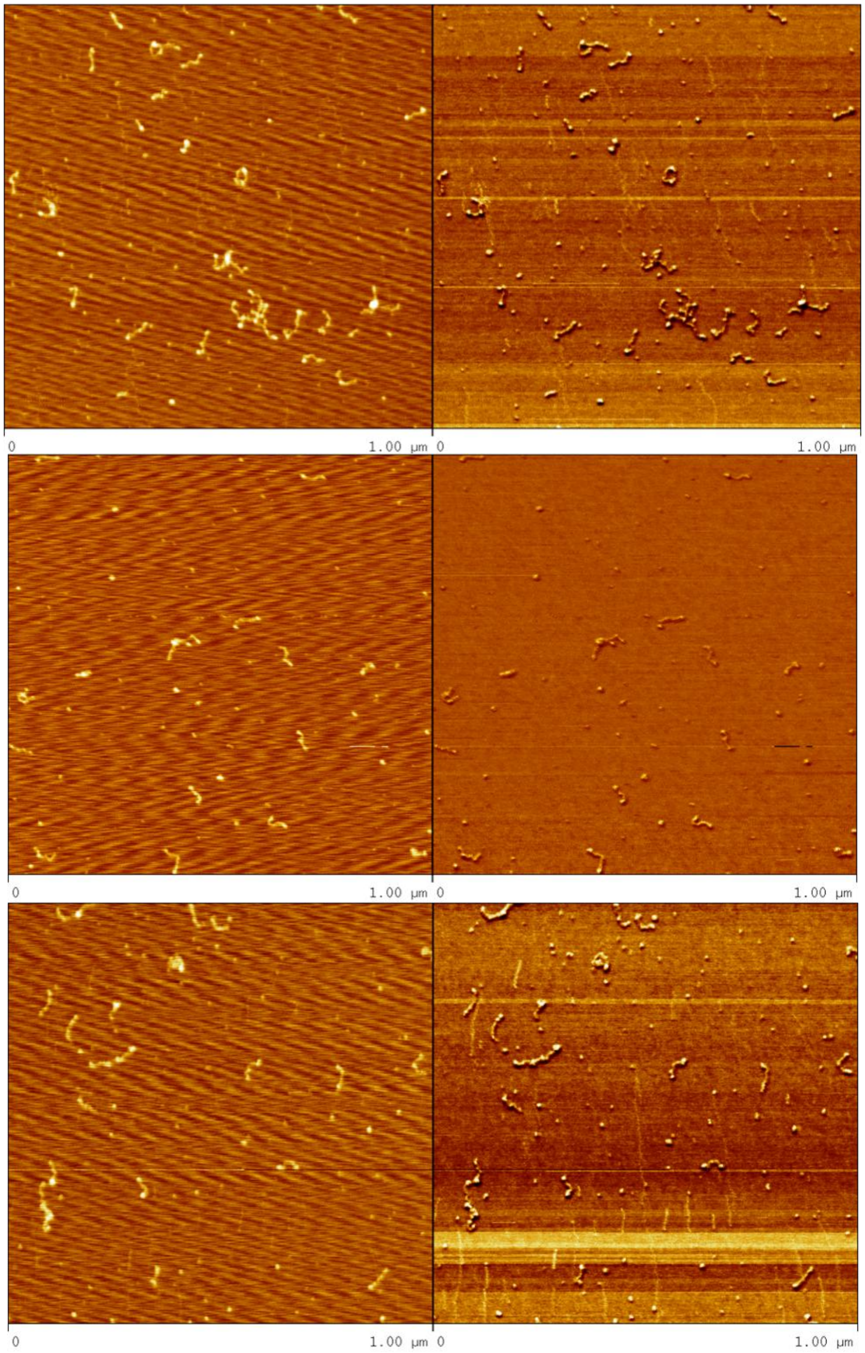

Figure AC.7. AFM height (left) and phase (right) images of specimens prepared by dropping a methanol solution of the crosslinked $C_{60}D_{476}C_{60}$ copolymer that was modified by BBBV quaternization onto a mica substrate. The crosslinked products were obtained in an aqueous HCl solution with a pH of 1.63. The images were obtained by scanning different locations of the same mica substrate.

Appendix D

Optimization of the Cyclization Conditions for the CDC Copolymer

D.1 Optimization of the Solvent Conditions

Various solvents and solvent combinations were tested to cyclize the $C_{49}D_{391}C_{49}$ copolymer. It was found that in $pH < 0$ acidic aqueous solutions, where D forms cationic chains, the retention time of the crosslinked product was 0.8 minutes shorter than that of the precursor, $C_{49}D_{391}C_{49}$. From the SEC traces, the apparent molecular weight reduction before and after crosslinking, was calculated as ~33%, indicating the formation of macrocycles. The conditions were optimized by using aqueous HCl solutions with different pH values (Figure AD.1). The SEC results indicated that the formation of macrocyclic products was most favourable among aqueous solutions at pH = 0.6 (Figure AD.2).

All results obtained in Appendix-IV were obtained from a completely different SEC system. The μ-Styragel columns of this system were Waters HT 5 and HT 4 columns. The mobile phase used was THF, with a 2% volume fraction of triethylamine. In addition, a different UV lamp was used to perform the photo-crosslinking. this lamp had a much weaker intensity, and probably also had a different light spectrum compared with the lamp used in other experiments. Consequently, only the trends of the results obtained from these measurements were taken into account.

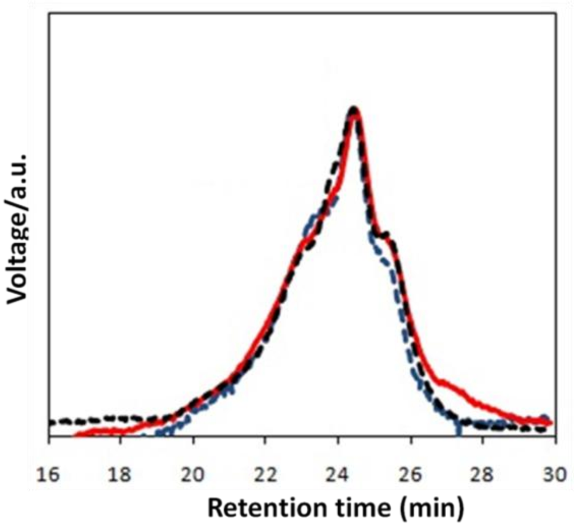

Figure AD.1. SEC traces of the crosslinked $C_{49}D_{391}C_{49}$ copolymer in an aqueous HCl solution at: pH = 0.5 (blue dotted line), pH = 0.6 (red solid line), and pH = 0.9 (black dotted line).

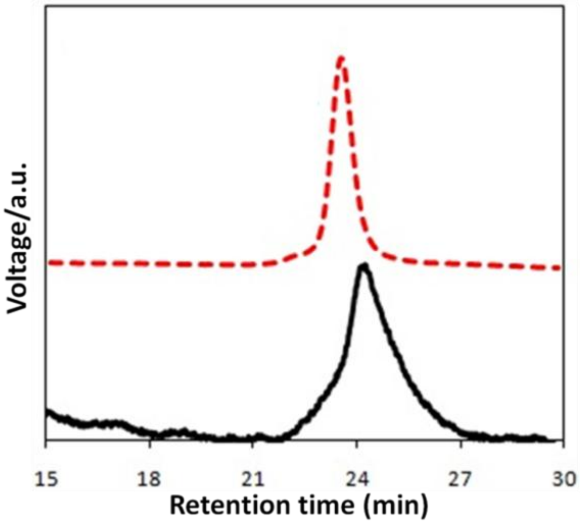

Figure AD.2. SEC traces of precursory $C_{49}D_{391}C_{49}$ (solid line) and crosslinked $C_{50}D_{400}C_{50}$ in an aqueous HCl solution at pH = 0.6 (dotted line).

Some organic solvents were also tested during the cyclization experiments, in which PDMAEMA was neutral. SEC analysis of the crosslinked products of $C_{49}D_{391}C_{49}$ in MeOH and in MeOH mixed with triethylamine is shown in Figure AD.3. Under both solvent conditions, the retention time was delayed by only 0.2 min and the apparent molecular weight decreased by 14% after crosslinking. Such a small apparent molecular weight decrease usually indicates the formation of the PCP species instead of the macrocyclic species.

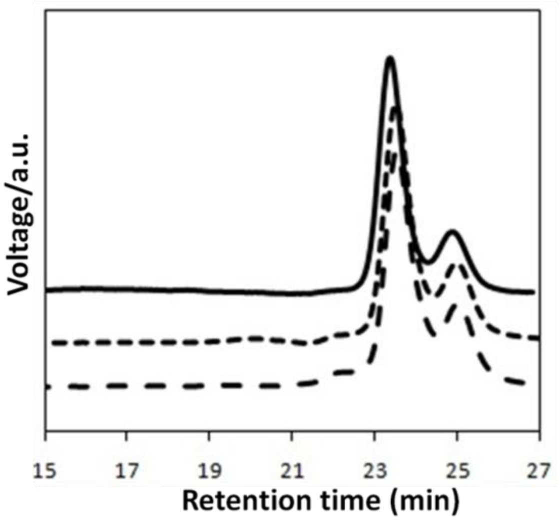

Figure AD.3. SEC traces of precursory $C_{49}D_{391}C_{49}$ (solid line), crosslinked $C_{49}D_{391}C_{49}$ in MeOH (dotted line), and crosslinked $C_{49}D_{391}C_{49}$ in MeOH with 3% triethylamine (dashed line).

A systematic study of a newly-synthesized triblock copolymer, $C_{60}D_{476}C_{60}$, was performed recently. This study focused on the differences among the crosslinked polymer structures produced under different acidity conditions. The molecular volume reductions of the samples observed at different pH values is included in Table AD.1.

Table AD.1. Hydrodynamic Volume reductions of $C_{60}D_{476}C_{60}$ before and after crosslinking under different acidity conditions, based on SEC analysis.

$C_{60}D_{476}C_{60}$	pH	Peak elution time (min)	Mp $/\times 10^{-4}$ conventional calibration (g/mol)	Mp ratio	Hydrodynamic volume reduction ratio
Precursor-0.61/0.71		21.66	6.1	-	-
pH = 0.61	0.61	22.16	4.8	77%	64%
pH = 0.71	0.71	21.86	5.4	89%	82%
Precursor-0.35		21.51	6.5	-	-
pH = 0.35	0.35	21.98	5.1	78%	65%

The data were plotted (Figure AD.4) as the delay time of the crosslinked product versus the pH of the aqueous solution in which the copolymer was crosslinked. Schematic diagrams are shown in the graph to demonstrate the possible structures of the crosslinked product in each pH range. When the pH is above 0.9, the ionic strength of the solution is not high enough to screen all of the cations on the polymer chains. Therefore, the D block behaves as a semi-rigid chain, and it is unlikely for the C end-blocks to become fused together. Instead, the terminal C blocks collapse individually and a PCP product is produced after crosslinking. This was verified by the short delay time (~ 0.2 min) observed among the corresponding SEC traces, which suggested that the PCP structure had formed. As the pH decreases and ionic strength increases, more cations on the polymer chains are screened, and the ratio of macrocycles in the crosslinked product increases. This trend is comparable with the increasing length of the delay time encountered between pH = 0.6 and 0.9. However, when the pH is below 0.6, the delay time becomes shorter as with decreasing of pH values. This can be explained by micelle formation, which was also verified by the difficulties encountered when passing the samples through a 0.4 um filter. Thus, the optimized cyclization conditions for the CDC triblock copolymer occur in aqueous HCl at pH ~ 0.6.

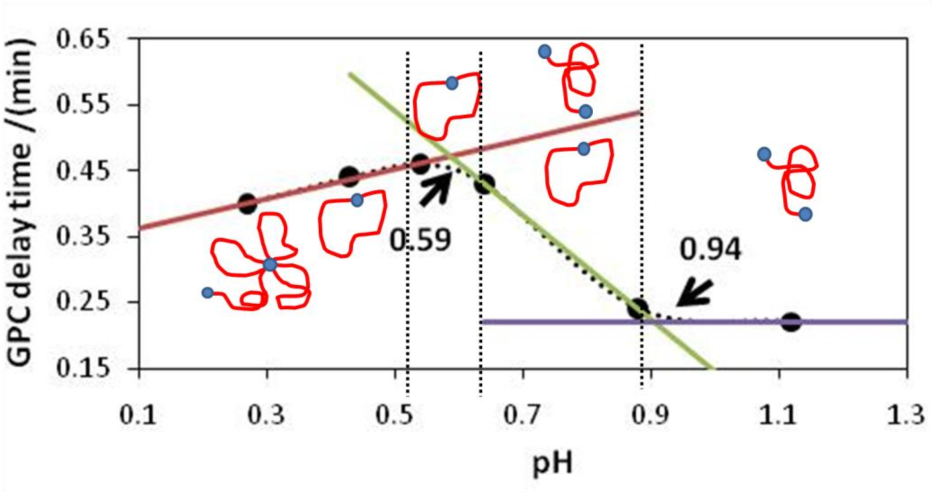

Figure AD.4. Plot of the delay times (relative to their precursor) of crosslinked $C_{60}D_{476}C_{60}$ copolymers versus the pH of the aqueous HCl solutions in which the triblock copolymer was crosslinked. The schematic diagrams shows the possible structures formed in different pH ranges.

D.2 Optimization of the C block length

Three CDC triblock copolymers with different C block lengths were used for the optimization. The same cyclization conditions were used for all three triblock copolymers. Generally, the copolymer was dissolved into an aqueous HCl solution (pH = 0.4) at a final concentration of 1.0 mg/mL. The solution was then irradiated with UV-light. The degree of crosslinking of the C block was determined by the UV-visible spectroscopy, and was between approximately 70 and 80%.

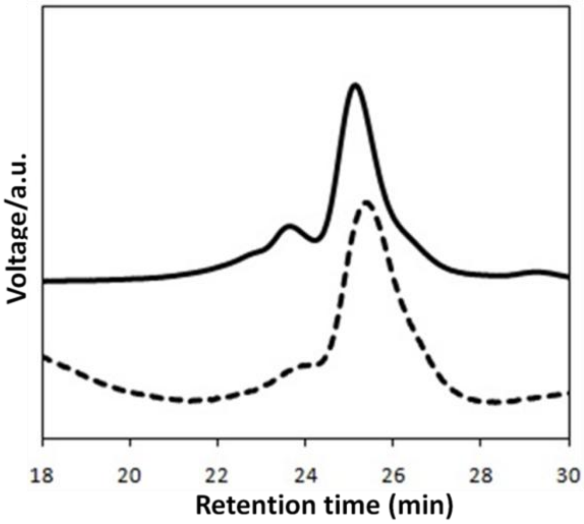

Figure AD.5. SEC traces of precursory $C_{12}D_{246}C_{12}$ (solid line) and crosslinked $C_{12}D_{246}C_{12}$ in aqueous HCl at pH = 0.6 (dotted line).

The results from the SEC analysis of two crosslinked triblock copolymers, $C_{12}D_{246}C_{12}$ and $C_{17}D_{414}C_{17}$, are shown in Figure AD.5 and Figure AD.6, respectively. For both of the triblock copolymers, the retention time delays of the crosslinked products from those of their precursors were less than 0.2~0.3 min. This indicates that under these cyclization conditions, the triblock copolymer did not form macrocycles when it had C block lengths of either 12 or 17 repeat units.

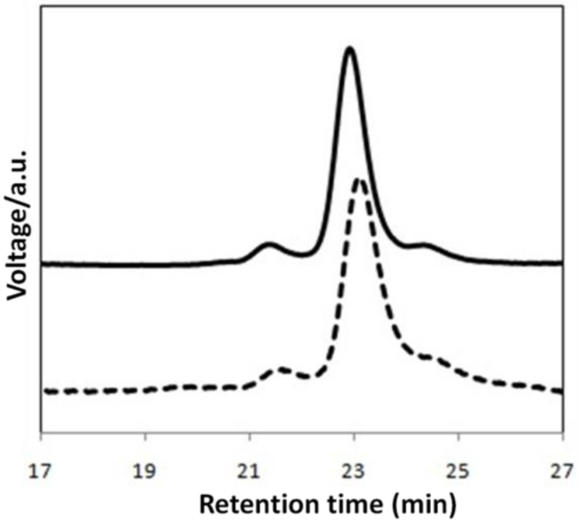

Figure AD.6. SEC traces of $C_{17}D_{414}C_{17}$ (solid line) and crosslinked $C_{17}D_{414}C_{17}$ in aqueous HCl at pH = 0.6 (dotted line).

Another triblock copolymer, $C_{40}D_{300}C_{40}$, was synthesized by Dr. Liangzhi Hong in Dr. Liu's group. Dr. Hong claimed that this triblock copolymer could not be cyclized using the conditions described above. Therefore, a conclusion can be drawn from the results discussed above: the minimum length of the C block required for the successful cyclization of a CDC triblock copolymer with a central D block length of 400 repeat units in aqueous HCl at pH = 0.6, is about 50 units.

The reasons why CDC triblock copolymers with short C chains cannot be cyclized are simple. Firstly, from an energetic standpoint, the interfacial energy decrease observed during macrocycle formation needs to compensate for the energy change arising from the compression of the polymer chain, which causes an entropy loss. The decrease of the interfacial energy (Equation AD.1) is related to the molecular weight of the C block (M_e). If M_e is too small, the decrease of the interfacial energy is smaller in magnitude than the increase of the compression energy, and the PCP structure becomes more thermodynamically stable than the macrocyclic structure.

$$\Delta F_A = 1.685 \times 10^8 \gamma ({}^{M_e}/_{\rho})^{2/3} \tag{AD.1}$$

Secondly, the crosslinking reactions between the C side chains can take place only when the distances between the two functional groups are within 0.4 nm. If the C block is short, it is not sufficiently coiled to arrange its side-chains into the correct position for the dimerization reaction to take place between CEMA units of the two end-blocks. Therefore, in this case, the crosslinking reaction between the two end-blocks cannot take place effectively.